

Development of Extended-Depth Swept Source Optical Coherence Tomography for  
Applications in Ophthalmic Imaging of the Anterior and Posterior Eye

by

Al-Hafeez Zahir Dhalla

Department of Biomedical Engineering  
Duke University

Date: \_\_\_\_\_

Approved:

\_\_\_\_\_  
Joseph A. Izatt, Supervisor

\_\_\_\_\_  
David J. Brady

\_\_\_\_\_  
Sina Farsiu

\_\_\_\_\_  
Anthony N. Kuo

\_\_\_\_\_  
Adam P. Wax

Dissertation submitted in partial fulfillment of  
the requirements for the degree of Doctor  
of Philosophy in the Department of  
Biomedical Engineering in the Graduate School  
of Duke University

2012

ABSTRACT

Development of Extended-Depth Swept Source Optical Coherence Tomography for  
Applications in Ophthalmic Imaging of the Anterior and Posterior Eye

by

Al-Hafeez Zahir Dhalla

Department of Biomedical Engineering  
Duke University

Date: \_\_\_\_\_

Approved:

\_\_\_\_\_  
Joseph A. Izatt, Supervisor

\_\_\_\_\_  
David J. Brady

\_\_\_\_\_  
Sina Farsiu

\_\_\_\_\_  
Anthony N. Kuo

\_\_\_\_\_  
Adam P. Wax

An abstract of a dissertation submitted in partial  
fulfillment of the requirements for the degree  
of Doctor of Philosophy in the Department of  
Biomedical Engineering in the Graduate School  
of Duke University

2012

Copyright by  
Al-Hafeez Zahir Dhalla  
2012

## Abstract

Optical coherence tomography (OCT) is a non-invasive optical imaging modality that provides micron-scale resolution of tissue micro-structure over depth ranges of several millimeters. This imaging technique has had a profound effect on the field of ophthalmology, wherein it has become the standard of care for the diagnosis of many retinal pathologies. Applications of OCT in the anterior eye, as well as for imaging of coronary arteries and the gastro-intestinal tract, have also shown promise, but have not yet achieved widespread clinical use.

The usable imaging depth of OCT systems is most often limited by one of three factors: optical attenuation, inherent imaging range, or depth-of-focus. The first of these, optical attenuation, stems from the limitation that OCT only detects singly-scattered light. Thus, beyond a certain penetration depth into turbid media, essentially all of the incident light will have been multiply scattered, and can no longer be used for OCT imaging. For many applications (especially retinal imaging), optical attenuation is the most restrictive of the three imaging depth limitations. However, for some applications, especially anterior segment, cardiovascular (catheter-based) and GI (endoscopic) imaging, the usable imaging depth is often not limited by optical attenuation, but rather by the inherent imaging depth of the OCT systems. This inherent imaging depth, which is specific to only Fourier Domain OCT, arises due to two factors: sensitivity fall-off and

the complex conjugate ambiguity. Finally, due to the trade-off between lateral resolution and axial depth-of-focus inherent in diffractive optical systems, additional depth limitations sometimes arises in either high lateral resolution or extended depth OCT imaging systems. The depth-of-focus limitation is most apparent in applications such as adaptive optics (AO-) OCT imaging of the retina, and extended depth imaging of the ocular anterior segment.

In this dissertation, techniques for extending the imaging range of OCT systems are developed. These techniques include the use of a high spectral purity swept source laser in a full-field OCT system, as well as the use of a peculiar phenomenon known as coherence revival to resolve the complex conjugate ambiguity in swept source OCT. In addition, a technique for extending the depth of focus of OCT systems by using a polarization-encoded, dual-focus sample arm is demonstrated. Along the way, other related advances are also presented, including the development of techniques to reduce crosstalk and speckle artifacts in full-field OCT, and the use of fast optical switches to increase the imaging speed of certain low-duty cycle swept source OCT systems. Finally, the clinical utility of these techniques is demonstrated by combining them to demonstrate high-speed, high resolution, extended-depth imaging of both the anterior and posterior eye simultaneously and *in vivo*.

If your knowledge of fire has been turned to certainty by words alone, then seek to be cooked by the fire itself. Don't abide in borrowed certainty. There is no real certainty until you burn; if you wish for this, sit down in the fire.

Rumi

# Contents

Abstract .....	iv
Contents.....	vii
List of Tables.....	ix
List of Figures .....	x
Acknowledgements .....	xvi
1. General Background and Significance .....	1
1.1. Optical Coherence Tomography .....	1
1.2. Full-Field OCT .....	6
1.3. Imaging Depth Limitations in OCT .....	19
1.4. Sweep Buffering in Swept Source OCT .....	33
1.5. Anterior Segment Biometry with OCT.....	39
1.6. Research Aims.....	43
2. Extended-Depth Full-Field OCT .....	45
2.1. Speckle Reduction and Crosstalk Rejection in Full-Field OCT.....	46
2.2. Extended-Depth Full-Field Swept Source OCT .....	58
3. Coherence Revival in Swept Source OCT.....	80
3.1. Theoretical Development of SSOCT .....	81
3.2. Coherence Revival-based Heterodyne SSOCT.....	102
3.3. Dispersive Optical Delay Lines in Coherence Revival SSOCT .....	136
4. Sweep Buffering in Swept Source OCT.....	143

4.1.	Sweep Buffering in SSOCT using a Fast Optical Switch.....	144
4.2.	Sweep Buffering and Coherence Revival.....	165
5.	Towards “Whole-Eye” OCT .....	169
5.1.	Challenges in Realizing Whole-Eye OCT.....	170
5.2.	Simultaneous SSOCT of the Anterior and Posterior Eye.....	176
6.	Conclusions and Future Directions .....	189
6.1.	Field-Deployable, Handheld SSOCT System for Sequential Anterior/Posterior Ocular Imaging .....	190
6.2.	Intrasurgical OCT imaging with extended-depth SSOCT .....	198
6.3.	Time and polarization –encoded dual depth SSOCT .....	202
6.4.	Design of an optimal coherence revival laser.....	205
6.5.	Ultrahigh resolution SDOCT using supercontinuum lasers .....	207
	References .....	210
	Biography.....	241

## List of Tables

Table 2.1: Fibers used for SCI and SII and relevant parameters.....	52
Table 2.2: FWHM of PSF at various locations throughout the field of view.....	65

## List of Figures

Figure 1.1: Schematic of a time-domain OCT system .....	2
Figure 1.2: Simulated TDOCT signal of a single reflector showing raw “fringe burst” and demodulated signal .....	2
Figure 1.3: Schematic of SDOCT and SSOCT systems.....	5
Figure 1.4 - Representation of data acquisition in FDOCT systems, demonstrating the acquired spectral interferogram (left) and resulting depth profile (right). Two artifacts unique to FDOCT are depicted: the DC artifact and the complex conjugate.....	5
Figure 1.5: Schematic of a typical FFOCT system, from [58] .....	7
Figure 1.6: Schematic representation of crosstalk in FFOCT .....	9
Figure 1.7: Schematic representation of parallel FDOCT encoding schemes .....	15
Figure 1.8: Schematic of an LF-SDOCT system, from [76] .....	16
Figure 1.9: Schematic of a FFSSPM system, from [78]. SLD: Superluminescent diode. FFP: Fiber Fabry-Perot filter. L <sub>C</sub> , L <sub>BS</sub> , L <sub>CCD</sub> and L <sub>OBJ</sub> : collimating, beamsplitter, camera and objective lenses, respectively. BS: Beamsplitter. CCD: Charge coupled device 2D array camera. R: Reference reflection off of cover glass. ....	17
Figure 1.10: SDOCT retinal B-scan corrupted with a complex conjugate artifact. ....	21
Figure 1.11: SDOCT image of cornea and iris with complex conjugate artifact (A), and with the artifact resolved (B), from [105].....	25
Figure 1.12: Cross-sectional intensity distribution of an ideal Bessel beam .....	31
Figure 1.13: Schematic of a FDML laser, from [149]. FFP-TF: fiber Fabry-Perot tunable filter. ISO: isolator. SOA: semiconductor optical amplifier.....	34
Figure 1.14: Schematic of a buffered, unidirectional FDML laser, from [149].....	36
Figure 1.15: Buffered 200 kHz SSOCT system using an Axsun Technologies 100 kHz swept source laser with a duty cycle of ~50%, from [158].....	37

Figure 1.16: Buffered SSOCT system with polarizer and amplification stage, from [160]38	
Figure 2.1: Coherence area and coherence gate definitions .....	48
Figure 2.2: System schematic. SLD, superluminescent diode; SMF, single mode fiber; MMFL, multimode fiber launch; MM, mode mixer & fiber spool; L1-4, lenses; BS, beam splitter; ND, neutral density filter; M, reference mirror on PZA. Dashed boxes represent interchangeable configurations for SCI and SII .....	51
Figure 2.3: Phase resolved image of 1951 USAF test chart showing groups 4, 5, 6 and 7.54	
Figure 2.4: USAF 1951 test chart imaged through water (top), 6mfp (middle) & 8mfp (bottom) scattering solutions.....	55
Figure 2.5: MTF's from images taken beneath water, 6mfp and 8mfp solutions for both SCI and SII.....	56
Figure 2.6: OCT projections of a <i>Drosophila melanogaster</i> summed over 100 $\mu$ m, centered at 100 $\mu$ m (top) and 200 $\mu$ m (bottom) from top surface using SCI (left) and SII (right) .....	56
Figure 2.7: Schematic of prototype FF-SSOCT system.....	63
Figure 2.8: ZEMAX ray diagram of the illumination optics (top), reference arm collection optics (middle), and sample arm collection optics (bottom). .....	64
Figure 2.9: Schematic of all-fiber MZI k-clock .....	66
Figure 2.10: Processed k-clock signal from the fiber Mach-Zehnder interferometer. ....	66
Figure 2.11: Flowchart showing hardware interconnects .....	67
Figure 2.12: Sensitivity fall-off and axial resolution measurements.....	72
Figure 2.13 Left: Representative B-scan image of the bullet surface extracted from 3D FF-SSOCT dataset (linear scale). Right: Corresponding bullet surface segmented. ....	74
Figure 2.14: Three-dimensional reconstructed surface renderings of a 0.45 caliber slug acquired with from four rotations .....	75
Figure 2.15: Axial resolution measured at ~4mm and ~6mm imaging depth in air and behind 25mm of water .....	77

Figure 3.1: Time and Fourier domain representations of coherence revival. The ideal interferogram is convolved with the instantaneous source spectrum to yield the measured spectral interferogram, which is the Fourier transform of the observed A-scan. Equivalently, the ideal sample reflectivity is multiplied by the fall-off function, resulting in the observed A-scan. .... 113

Figure 3.2: Schematic of SSOCT systems tested. Laser was either an 840nm or 1040nm ECTL. BR: Balanced receiver. PM: power meter. BD: beam dump. UP: Unused port. G: galvanometer. .... 118

Figure 3.3: (A-C) Fall-off plots from a numerical simulation of a coherence revival SSOCT system with a stationary cavity for 0, +1 and +2 cavity length offsets, respectively. Note that no shift in the peak sensitivity position is observed. (D) Fall-off profile demonstrating coherence revival peaks centered at 80mm and 160mm. .... 122

Figure 3.4: Fall-off plots from a numerical simulation of a coherence revival SSOCT system with a cavity whose pathlength varies linearly in wavelength with a slope of  $2\mu\text{m}/\text{nm}$ , +1 (A) and +2 (B) cavity length offsets. The expected axial position shifts of the peak sensitivity positions of 2.1 and 4.2mm are observed. .... 122

Figure 3.5: A and B: Fall-off plots from a numerical simulation of a coherence revival SSOCT system with a cavity whose pathlength varies linearly in frequency with an *average* slope of  $2\mu\text{m}/\text{nm}$ , for +1 and +2 cavity length offsets, respectively. The expected axial position shifts of the peak sensitivity positions are observed, but the axial PSFs are severely degraded due to the non-linear phase modulation. C and D show the same data as A and B after applying dispersion compensation. .... 123

Figure 3.6: Fall-off measurements from the 840nm system for 0 (A), +1 (B) and +2 (C) cavity length offsets. The physical separations between the peak sensitivity position from 0 to +1 and from +1 to +2 were both 66.1mm. .... 126

Figure 3.7: Fall-off measurements from the 1040nm system for -1 (A), 0 (B) and +1 (C) cavity length offsets. The physical separations between the peak sensitivity positions of the -1 and 0 and the 0 and +1 offsets were 115.0mm and 114.8mm, respectively. .... 127

Figure 3.8: Comparison images taken on the 840nm, 8kHz (Thorlabs SL850-P16 laser) system with 0 (A) and +1 (B) cavity length offsets. Both images comprise 1000 (lateral) x 1300 (axial) pixels spanning 13 mm (lateral) x 5.3 mm (axial), the latter scaled to account for refractive index. Each image represents 5 averaged frames obtained over 0.6s. The locations of the ZPD and +1 offset positions are indicated. .... 129

Figure 3.9: Comparison images taken on the 1040nm, 100kHz (Axsun Technologies laser) system with 0 (A) and +1 (B) cavity length offsets. Both images comprise 2000 (lateral) x 2300 (axial) pixels spanning 14 mm (lateral) x 6.9 mm (axial), the latter scaled to account for refractive index. Each image represents 5 averaged frames obtained over 100msec. The locations of the ZPD and +1 offset positions are indicated.....	130
Figure 3.10: Volume projections of the same eye acquired with the 840nm (left) and 1040nm (right) systems. The 840nm volume consisted of 1300 (axial) x 500 x 200 samples, acquired in 12.5 seconds. The 1040nm volume consisted of 2304 (axial) x 500 x 200 samples, acquired in 1 second.....	131
Figure 3.11: Schematic of the optical delay line. $L_{col}$ : Collimating lens, DG: Diffraction grating, LODL compound achromatic lens with focal length $f_{ODL}$ , M: gold mirrors, $\theta$ , mirror angle. Red, green and blue lines represent ray traces at wavelengths of 1090nm, 1040nm, and 990nm respectively.....	137
Figure 4.1: Schematic of buffering stage. PC: Polarization controllers. UP: Unused port .....	148
Figure 4.2: Schematic of SSOCT system. BR: Balanced receiver. AL: Aiming laser. BD: Beam dump. UP: Unused port. PC: Polarization controller. L1,L2: Lenses. G: Galvanometers.....	149
Figure 4.3: Traces of original (blue) and buffered (magenta) sweeps. Green vertical lines denote the start of each sweep, while red vertical lines denote the end.....	150
Figure 4.4: Timing and triggering in buffered SSOCT (simulated) .....	152
Figure 4.5: SSOCT A-scans of a mirror in the presence of PMD. A: Switch only in source arm. B: Spool only in source arm. C: Switch and spool in source arm. D: Same as C but corrected with polarization controllers.....	156
Figure 4.6: A-scans of a mirror using (A) the original sweep, (B) the buffered sweep processed with the original clock, and (C) the buffered sweep processed with the transformed clock .....	160
Figure 4.7: <i>In vivo</i> B-scan of fovea acquired before optimization of polarization controller. Image consists of 1600 A-scans x 5 averaged frames. Total acquisition time was 40msec.....	162
Figure 4.8: Enlargement of top left corner of Figure 4.7.....	163

Figure 4.9: In vivo B-scan of fovea acquired after optimization of polarization controller. Image consists of 1600 A-scans x 5 averaged frames. Total acquisition time was 40msec. ....	163
Figure 4.10: Enlargement of top left corner of Figure 4.9.....	163
Figure 4.11: Schematic of buffered, extended-depth SSOCT system. BR: Balanced receiver. BD: Beam dump. UP: Unused port. PC: Polarization controller. L1, L2: Lenses. G: Galvanometers.....	165
Figure 4.12: In vivo B-scan of anterior segment. Image consists of 1600 A-scans x 5 averaged frames. Total acquisition time was 40msec.....	167
Figure 4.13: Enlargement of apex of cornea from Figure 4.12 .....	167
Figure 4.14: Enlargement of iris and anterior lens from Figure 4.12 .....	167
Figure 5.1: Schematic of human eye showing regions of interest for whole-eye OCT. Anterior segment (red) and posterior eye (blue). Modified from [220] .....	171
Figure 5.2: Schematics of optical designs typically used for OCT imaging of the anterior segment (left) and retina (right). SM: scanning mirror. L1,L2: lenses. ....	174
Figure 5.3: Sample arm design of sequential imaging of anterior (red) and posterior eye (blue). G: galvanometers. DM: dichroic mirror for fixation target (not shown). L1: Identical compound achromatic lenses. L2: Aspherical lens. M: Fixed mirrors. FM: Flip mirrors. ....	174
Figure 5.4: SSOCT system schematic. BR: Balanced receiver. PM: power meter. UP: Unused ports, PC: polarization controller. Sample arm: Red and blue lines depict the retinal and anterior segment imaging paths, respectively. Overlapping paths are shown in purple. L: Lens. HWP: half-wave plate. PBS: Polarizing beamsplitter. FM: fold mirror. G: Galvanometers.....	178
Figure 5.5: Sensitivity fall-off profiles for the retinal (top) and anterior segment (bottom) imaging channels. Red horizontal lines are drawn at -6dB sensitivity from the peak....	183
Figure 5.6: Simultaneously acquired anterior segment and retinal images. A: A single frame as acquired before cropping and dispersion compensation, consisting of 2000 (lateral) x 2304 (axial) samples, acquired in 20msec. ZPD: Zero pathlength difference position, +1CL: Cavity length offset position. B and C: Separated anterior segment and	

retinal images, averaged over 5 frames. Scale bars are 1mm, 1mm x 1mm and 250 $\mu\text{m}$ x 1° in A, B and C, respectively.....	185
Figure 5.7: 3D rendering of simultaneously acquired anterior segment and retinal volumes. Total acquisition consisted of 2304 x 500 x 200 samples, acquired in 1 s.....	186
Figure 5.8: SSOCT B-scans taken with the OCT system aligned with the volunteer's visual axis (left) and optical axis (right). Each pair of images consists of 1600 (lateral) by 2304 (axial) samples x 5 averaged frames, acquired in 40 msec each.....	187
Figure 6.1: Schematic of rapidly switchable dual reference arm configuration based on a MEMS fiber optic switch.....	193
Figure 6.2: Top: Schematic of a switchable sample arm design showing retinal imaging (blue) and anterior segment imaging (red) states. G: Galvanometers. DM: Dichroic mirror (for fixation target, not shown). L1: Compound achromatic lenses. L2: Aspherical lens. M: Fixed mirrors. FM: Flip mirrors. Bottom: 3D rendering of the same sample arm design.....	195
Figure 6.3: Existing design of the intrasurgical MM-SDOCT system, from [233].....	199
Figure 6.4: Schematic of a time and polarization encoded dual-depth sample arm. Red and blue lines depict the retinal and anterior segment imaging paths, respectively. Overlapping paths are shown in purple. FOS: Fast optical switch. L: Lens. HWP: half-wave plate. PBS: Polarizing beamsplitter. FM: fold mirror. G: Galvanometers .....	203

## Acknowledgements

This work would not have been possible without the support and guidance of the many friends and mentors who helped me over the years.

First and foremost, I would like to thank my advisor, Professor Joseph Izatt, for teaching, guiding, trusting and, most of all, inspiring me. I could not have asked for a better mentor, role model or advocate.

I also want to thank the members of my committee for their guidance and advice. Thank you, Professor Brady, for teaching me the fundamentals of the field and always being available to answer my questions. Thank you, Professor Farsiu, for challenging me and always believing in me. Thank you, Dr. Kuo, for being an invaluable resource of clinical insight and brilliant ideas. And thank you, Professor Wax, for your advice and mentorship over the years.

I also want to acknowledge the many other clinicians, colleagues and friends who have contributed to my development as a scientist. Dr. Cynthia Toth has been amazing in her support of translational research. Professor Bing Yu and Dr. Karthik Vishwanath introduced me to biomedical optics as an undergraduate, and continue to serve as mentors and friends. Richard Nappi taught me everything I know about machining and fabrication. And lastly, Professor Mike Choma and Professor Audrey Ellerbee have been invaluable sources of knowledge, experience and advice.

Thank you, also, to my fellow students, both past and present, for sharing the journey with me.

To my parents, thank you for your unwavering love, support and guidance. The sacrifices you made and the values you instilled in me made this possible.

And lastly, to Elisabeth, thank you for standing by me through it all, and for reminding me that there is more to life than OCT.

As I am a strong advocate for giving credit where credit is due, acknowledgements for specific contributions to the work presented in this thesis are included in the introduction to each chapter. Very specific contributions are acknowledged in footnotes.

# **1. General Background and Significance**

## **1.1. *Optical Coherence Tomography***

Optical coherence tomography [1], or OCT, is an optical imaging modality that enables volumetric imaging of tissue microstructure with micron-scale resolution and millimeter-scale penetration. Since its inception in 1991, OCT has been used in numerous research and clinical applications. Initial success in ophthalmic imaging of retina [1-7] lead to the commercialization of first-generation OCT systems by Carl Zeiss Meditec, as well continued research into applications in anterior segment imaging [8-11], endoscopic imaging of the gastro-intestinal tract [12-14], small animal imaging [15-17], and catheter-based imaging of coronary arteries [18-23]. OCT has also seen limited use in imaging of non-biological samples, such as artwork [24-26], fingerprints [27-29] and integrated circuits [30, 31].

### **1.1.1. Time Domain Optical Coherence Tomography**

OCT systems function as coherence gated interferometers wherein low coherence light is directed towards and collected from a sample in an epi-illumination scheme (Figure 1.1). At the photodetector, light returning from the sample interferes with light returning from a reference arm; interference fringes are only observed from reflectors in the sample arm whose optical pathlength is within a coherence length of the reference pathlength. By scanning the reference arm position axially, a series “fringe bursts” are

observed at the photodetector, corresponding to reflectors in the sample arm. After demodulation of the photodetector signal, a depth profile, or A-scan, is recovered with an axial resolution equal to the coherence length of the source.

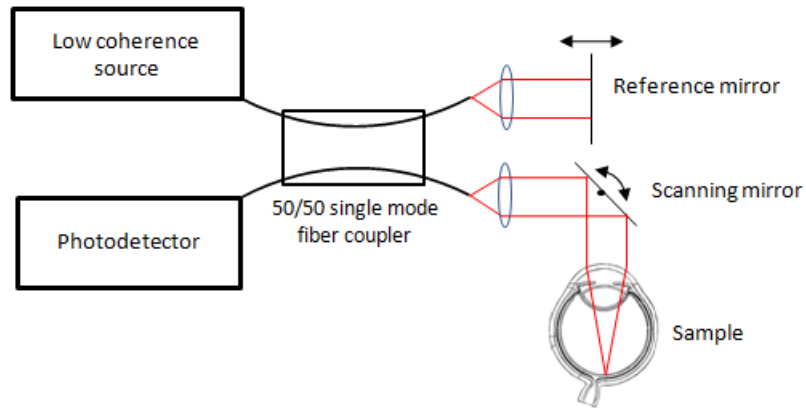


Figure 1.1: Schematic of a time-domain OCT system

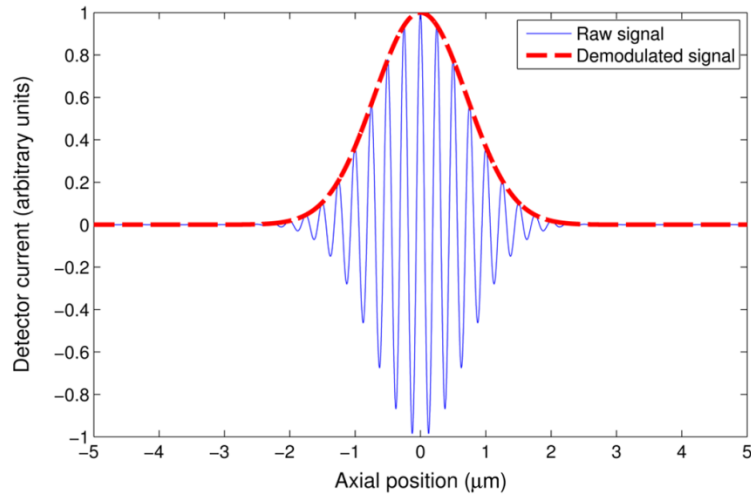


Figure 1.2: Simulated TDOCT signal of a single reflector showing raw “fringe burst” and demodulated signal

The first generation of OCT instruments, retroactively referred to as “time-domain” OCT or TDOCT, acquired A-scans by mechanically translating the reference mirror axially to build up a depth scan. Two-dimensional images (B-scans) and three-dimensional volumes could then be built up by raster scanning the sample beam using scanning mirrors. Due to mechanical limitations of how fast the reference mirror could be scanned, early OCT systems were limited to A-scans rates of a few hundred hertz. The development of the rapid scanning optical delay line (RSOD) [12, 32, 33], based on Fourier domain pulse shaping techniques [34-37], enabled A-scan rates of a few kilohertz, thereby enabling “video rate” OCT. These were the fastest iterations of TDOCT before the widespread adoption of Fourier Domain OCT.

### **1.1.2. Fourier Domain Optical Coherence Tomography**

Fourier Domain Optical Coherence Tomography (FDOCT) is an alternative approach to OCT that is based on spectral interferometry [38]. Despite demonstrations of the technique dating back as early as 1995 [39-46], and even mathematical derivations of the sensitivity advantage of FDOCT by Andretzky in 1998 [47] and by Mitsui in 1999 [48], it was not until 2003 that the sensitivity advantage Fourier Domain OCT was widely recognized. It was then that three nearly-simultaneous publications [49-51] directly comparing the sensitivity of FDOCT to TDOCT showed that FDOCT was

theoretically 20~30dB better. This realization also implied that the potential imaging speed of FDOCT could be 100 to 1000 times faster than TDOCT.

In FDOCT, the reference arm of the OCT interferometer is not scanned, but rather held stationary. Light returning from the sample and stationary reference is combined and the resulting broadband interference pattern is measured with spectrally separated detectors. That is, the power spectral density of the interfering light is measured as a function of optical frequency. Due to the Fourier relationship between the autocorrelation function and the power spectral density (the Wiener-Khintchine theorem [52, 53]), the A-scan (depth profile) can then be retrieved by simply taking the inverse Fourier transform of the “spectral interferogram”. A complete theoretical development of FDOCT is presented in Section 3.1.

FDOCT can be realized in two ways, referred to as spectral-domain, or SDOCT, and swept-source, or SSOCT. These two types of systems are depicted in Figure 1.3. In SDOCT, a conventional broadband source (usually a superluminescent diode or femtosecond laser) is used, but the photodetector is replaced with a spectrometer. Conversely, in SSOCT, the broadband source is replaced with a rapidly sweeping laser that typically has a narrow instantaneous linewidth but a broad tuning bandwidth. A photodetector is still used, although typically these systems will require photodetectors much more bandwidth than their TDOCT counterparts.

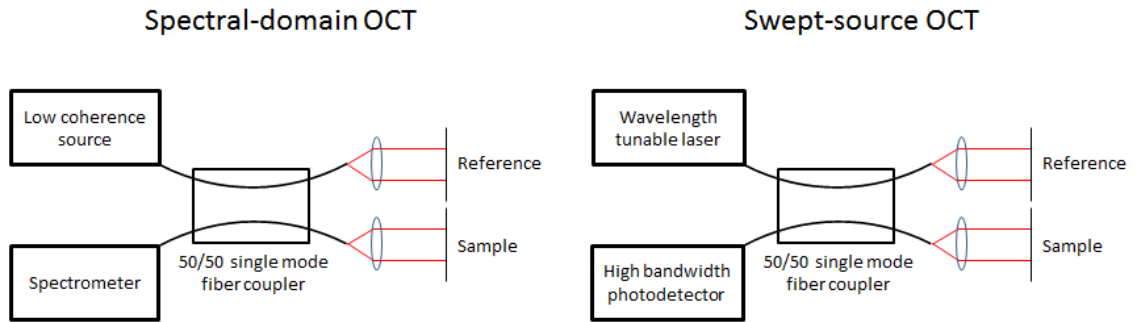


Figure 1.3: Schematic of SDOCT and SSOCT systems.

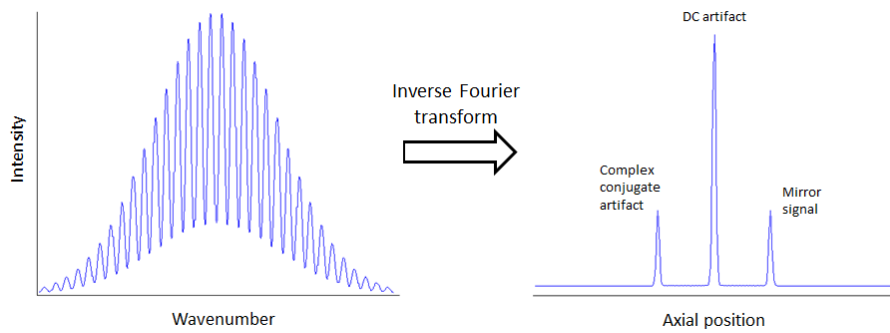
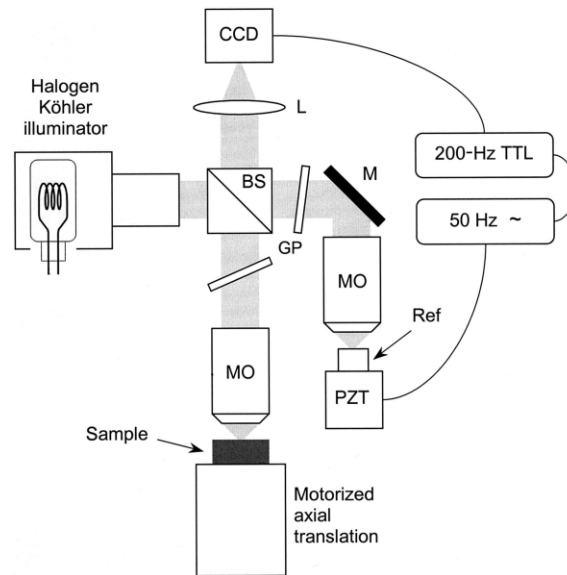


Figure 1.4 - Representation of data acquisition in FDOCT systems, demonstrating the acquired spectral interferogram (left) and resulting depth profile (right). Two artifacts unique to FDOCT are depicted: the DC artifact and the complex conjugate.

## 1.2. Full-Field OCT

Full-field optical coherence tomography (FFOCT), also referred to as full-field optical coherence microscopy (FFOCM), wide-field OCT, parallel OCT or *en face* OCT, refers to a technique wherein an entire *en face* slice of an OCT volume is acquired simultaneously, by using a 2D array camera as the detector in a wide-field Michelson interferometer. The technique is similar to traditional time-domain OCT techniques, except that the reference mirror does not scan rapidly. Instead, quadrature components of the interference signal are extracted using either phase stepping interferometry [54] or sinusoidal phase modulation [55]. A schematic of an FFOCT system, in the commonly used Linnik configuration, is provided in Figure 1.5. The system depicted employs a PZT to allow phase stepping for extraction of quadrature components. However, several other hardware configurations have been used to extract quadrature components, especially photoelastic modulators paired with two linear polarizers [55, 56].

While the technique was first reported by Beaufrepaire [55], the idea of such an “interference microscope” had been suggested by Dyson as early as 1950 [56]. Furthermore, what was essentially a FFOCT system was demonstrated by Kino and Chim in 1990 [57], but was referred to as a Mirau correlation microscope and employed a Mirau interferometer configuration.



**Figure 1.5: Schematic of a typical FFOCT system, from [58]**

The system described by Beurepaire employed an LED with a coherence length of  $20\ \mu\text{m}$ , but achieved an axial resolution of  $8\ \mu\text{m}$  due to the tight focus of the microscope objective. In 2002, Dubois et al [59] presented an FFOCT system in a Linnik configuration. This system was also based on an LED, and achieved comparable resolution. The LED was then quickly replaced by a thermal light source with a much broader bandwidth in two nearly simultaneously published papers [60, 61]. Coincidentally, both papers reported nearly identical performance, including an isotropic resolution of  $\sim 1\ \mu\text{m}$  at frame rates of up to 50Hz for  $256 \times 256$ -pixel images.

While later publications focused on additional characterization [58] and applications [62-64] of FFOCT, few substantial technical improvements have since been reported in time domain embodiments of FFOCT, perhaps due to the discovery of the

dramatic sensitivity advantage of FDOCT over TDOCT in 2003 [49-51] and the implementation challenges in implementing Fourier domain techniques in FFOCT (discussed in section 1.2.4).

### **1.2.1. Coherent Artifacts in Full-Field OCT**

An important consideration in the design of FFOCT systems is the management of coherent artifacts, specifically speckle and crosstalk. Crosstalk originates in scattering samples when multiply scattered light reaches the detector and interferes with singly-scattered light originating from the coherence gated imaging depth in the sample. In point-scanning OCT, the confocal aperture of the single mode fiber largely rejects multiply scattered light. However, full-field OCT systems must be implemented in free space, and thus lack this confocal aperture. Therefore, multiply scattered photons are detected by the camera, and a subset of these multiply scattered photons will have travelled the correct optical pathlength to interfere with the reference field. In order for multiply scattered light to travel the appropriate optical pathlength to be coherent with the reference field, the first scattering event must occur in a specific region of the sample, which we call the “crosstalk region”. This region can be described as a spherical cap with a depth equal to the coherence gated depth in the sample, and a base radius equal to twice that depth (see Figure 1.6). As the volume of this crosstalk region grows with the depth into the sample cubed, crosstalk artifacts to become significantly worse with

increasing depth into the sample. For further details on the origins of crosstalk in FFOCT, Karamata et al have provided a detailed discussion of coherent artifacts and the effects of multiple scattering in OCT in reference [65].

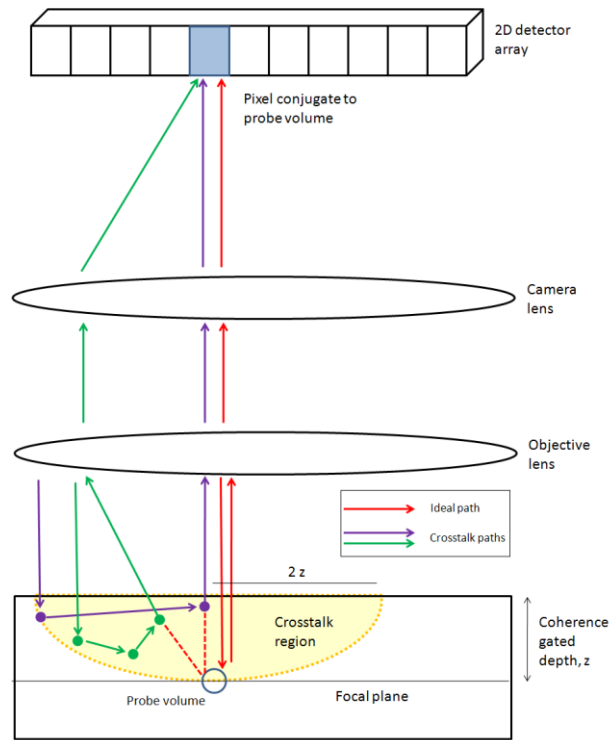


**Figure 1.6: Schematic representation of crosstalk in FFOCT**

### 1.2.2. Coherent vs. Incoherent Illumination

The coherence properties of the illumination field in an imaging system can have important consequences on the system's optical transfer function. This is addressed at

length in a dedicated chapter of Joseph Goodman's *Fourier Optics* [66], and thus only the key points from that discussion will be addressed here.

For the purpose of this discussion, a “coherent imaging system” refers to a system for which the illumination is highly *spatially* coherent, without regard to the *temporal* coherence properties of the illumination (which indeed may be either coherent or incoherent). Similarly, an “incoherent system” refers to a system for which the illumination is spatially incoherent, again without regard to its temporal coherence properties. It should be noted, however, that for a purely monochromatic source, it would be impossible to create a spatially incoherent illumination field.

By definition, then, a coherent imaging system is one for which the impulse responses in the image plane are correlated, and as such, will produce a response that is linear in complex amplitude. It can be shown that for such a coherent imaging system, this amplitude response (or amplitude transfer function, ATF) is simply given by a scaled Fourier transform of the pupil function, specifically [66]:

$$\text{ATF}(f_x, f_y) = P(\lambda z_i f_x, \lambda z_i f_y) \quad (1.1.1)$$

Conversely, an incoherent system is one for which the impulse responses in the image plane are completely uncorrelated, and thus will produce a response that is linear in intensity. As the intensity is simply given by the square of the field, the response of such

a system is given by the square of the amplitude response in the space domain (i.e. the incoherent PSF is equal to the square of the coherent PSF). Thus, the incoherent transfer function (or optical transfer function, OTF) is given by the auto-correlation of the same scaled Fourier transform of the pupil function, i.e. [66]:

$$\text{OTF}(f_x, f_y) = P(\lambda z_i f_x, \lambda z_i f_y), P(\lambda z_i f_x, \lambda z_i f_y) \quad (1.1.2)$$

If we consider a simple 1D coherent imaging system with a rectangular pulse as the pupil, the ATF would simply be a scaled version of that rectangular pulse, with some cutoff frequency  $f_c$ . The OTF of an analogous 1D incoherent system would be the auto-correlation of that rectangular pulse: a triangular pulse, with a non-zero response extending out to  $2 f_c$ . It is tempting, therefore, to conclude that since the OTF extends twice as far in frequency space as the ATF, that incoherent systems would have twice the resolution. However, at least presently, it is impossible to directly measure the amplitude of an optical field, and thus the only measurable quantity is its intensity (with so-called square-law detectors). If we define  $H(f_x, f_y)$  as the scaled Fourier transform of the pupil function of an imaging system, and  $G(f_x, f_y)$  as the complex amplitude of the object of interest, the resulting image spectra for the coherent and incoherent cases are given by [66]:

$$F_{\text{coherent}}(f_x, f_y) = HG^*HG \quad (1.1.3)$$

$$F_{\text{incoherent}}(f_x, f_y) = [H^*H][G^*G] \quad (1.1.4)$$

For the incoherent case, the measured intensity is given by the multiplication in Fourier space of the OTF (i.e.  $H^*H$ ) and the auto-correlation of the object's amplitude spectrum. Thus, the system's intensity response is given by the OTF. We can also define an intensity point spread function that is simply the Fourier transform of the OTF. Both the OTF and the intensity PSF are independent of the sample.

For the coherent case, the system response is intimately linked with the complex amplitude of the object. As such, no frequency response or point spread function can be defined with respect to intensity. Indeed, the system's intensity response depends on the phase distribution of the object being investigated.

An interesting observation is that for point-scanning imaging systems, such as traditional OCT, the acquisition of different lateral positions in the sample is separated in time. Thus, the impulse responses of adjacent points on the image plane are not correlated, even if coherent light is used. As a result, scanning imaging systems will exhibit transfer functions analogous to an incoherent imaging system<sup>1</sup>. In the case of traditional point-scanning OCT, then, the axial direction of the image will exhibit

---

<sup>1</sup> Credit to Shwetadwip Chowdhury for this observation. A complete mathematical derivation of the incoherent-like properties of scanning imaging systems will be presented in an upcoming paper.

properties of a coherent imaging system (because all axial depths are illuminated simultaneously, even in TDOCT), but the lateral direction will be incoherent.

### **1.2.3. Spatially Incoherent Illumination in Full-Field OCT**

Previous studies have demonstrated crosstalk rejection and speckle reduction in full-field OCT by using spatially incoherent illumination (SII) from a thermal source [60, 65, 67]. It was demonstrated in [67] that reduction of these coherent artifacts occurs as a result of the thermal source's low spatial coherence, and is unrelated to temporal coherence. However, the average number of photons within a coherence volume of blackbody radiation is always on the order of unity [68], which limits the speed and sensitivity of OCT systems employing thermal sources [67, 69, 70]. A strategy to overcome this limit, while still achieving crosstalk rejection, is to reduce the spatial coherence of a coherent source, such as an SLD or femtosecond laser. The theoretical basis of this approach has been explored previously with the aid of dynamic mode mixing [70, 71]. In section 2.1, we demonstrate how carefully selected multimode fibers can be used to realize SII with partially coherent sources without the need for dynamic mode mixing.

#### 1.2.4. Parallel Fourier Domain OCT

In recent years, the speed of traditional (point-scanning) FDOCT imaging systems has grown at a tremendous pace, with the fastest FDOCT systems to date operating at A-scan rates of a few megahertz [72-74]. Most of these high speed systems employ an SSOCT configuration, but swept source lasers capable of comparable sweep rates have not been developed in the 800nm regime, which provides the highest axial and lateral resolution among the three commonly used OCT bands (800nm, 1.0 $\mu$ m and 1.3 $\mu$ m). Meanwhile, high speed silicon-based array cameras have recently achieved frame rates as high as one million frames per second at 316 x 260 megapixel resolution (Photron USA, Inc, San Diego, CA). With sufficient optical power, these cameras could support A-scan rates exceeding 100MHz.

These advancements in silicon-based array camera technology have made possible the development of high speed parallel OCT systems in the 840nm regime, using either line-field spectral domain (LF-SDOCT) [75-77] or full-field swept source (FF-SSOCT) [28, 78, 79] configurations. A schematic of these encoding schemes is shown in Figure 1.7.

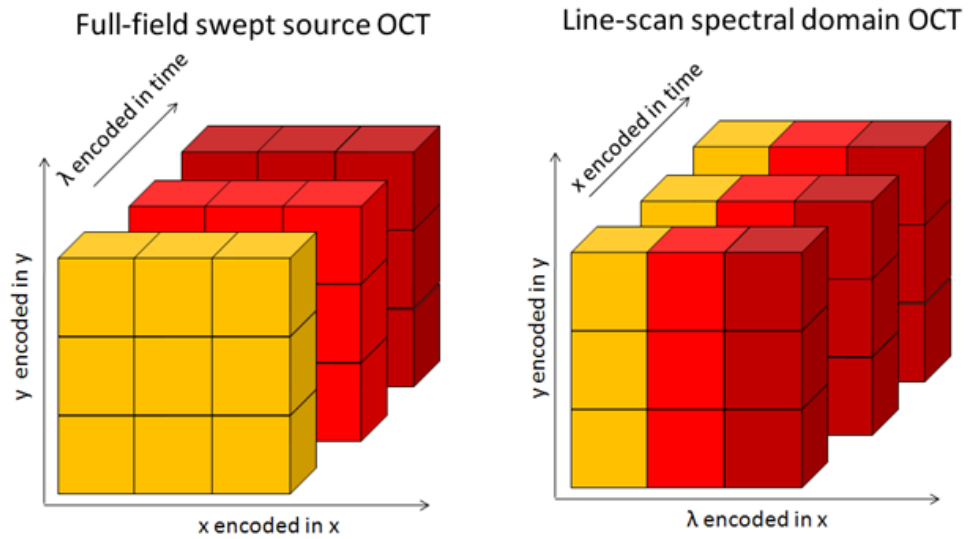


Figure 1.7: Schematic representation of parallel FDOCT encoding schemes

LF-SDOCT systems operate by imaging a focused line onto the sample, and (after combining the returning line with reference light), dispersing that focused line across a high speed 2D array detector. Thus, each frame capture acquires all of the information required to produce a B-scan, and volumes can be built up by scanning the focused line across the sample in one dimension. A schematic of a LF-SDOCT system is shown in Figure 1.8.

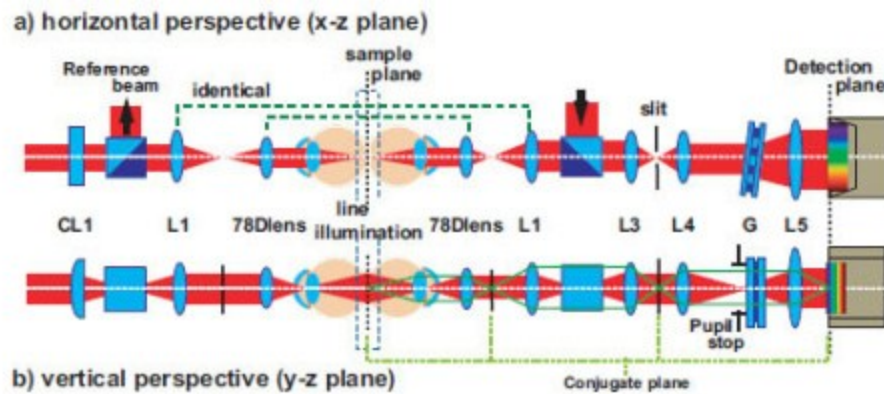
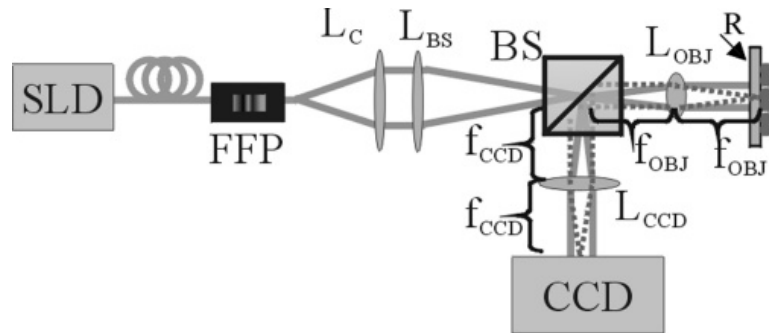


Figure 1.8: Schematic of an LF-SDOCT system, from [76]

FF-SSOCT systems are much more similar to time domain FFOCT systems in that a standard Linnik, Mirau, or common-path interferometer design can be used. However, these systems employ a tunable laser (or a broadband source with a tunable filter) instead of a broadband source. For each wavelength that the source tunes to, an *en face* image of the sample is combined with the reference field, and a 2D interference image is acquired. After a complete acquisition (consisting of several hundred camera frames), a spectral interferogram corresponding to each pixel can be extracted from the stack of acquired frames, and thus the entire data set can be processed to obtain a full OCT volume. A schematic of a full-field swept source phase microscopy (FFSSPM) system (which is essentially a phase stable FF-SSOCT system) is shown in Figure 1.9.



**Figure 1.9: Schematic of a FFSSPM system, from [78]. SLD: Superluminescent diode. FFP: Fiber Fabry-Perot filter.  $L_C$ ,  $L_{BS}$ ,  $L_{CCD}$  and  $L_{OBJ}$ : collimating, beamsplitter, camera and objective lenses, respectively. BS: Beamsplitter. CCD: Charge coupled device 2D array camera. R: Reference reflection off of cover glass.**

FF-SSOCT confers advantages over time-domain FFOCT techniques in that it has no moving parts and does not require precise alignment of the focal plane and confocal gate. However, because each acquired frame contributes only a single spectral channel, the integration time for each A-scan is relatively long, equal to the number of spectral channels per A-scan times the integration time of the camera. Even for high speed cameras, this integration time is prohibitively long to image non-stationary samples.

While both of these configurations enable high sensitivity and high speed volumetric imaging, they also lack the confocal aperture of the single mode fiber that is present in traditional point-scanning OCT. Furthermore, because they are spectrally resolved, each spectral channel has a very narrow spectral bandwidth and thus very high temporal coherence. As a result, these techniques are prone to speckle and crosstalk, which further limits their applicability for imaging biological tissues. LF-

SDOCT can be made somewhat less sensitive to coherent imaging artifacts by reimaging the focused line onto a confocal slit (as shown in Figure 1.8). However, crosstalk may still occur between A-scans across the line, which in practice limits the usable imaging depth to a few hundred microns when used with coherent sources [76]. Incoherent sources are compatible with LF-SDOCT, but these sources typically lack sufficient power spectral density to enable high-speed imaging [75].

FF-SSOCT techniques are even more sensitive to coherent imaging artifacts, as substantially more potential crosstalk paths are present with the 2D illuminated field. Also, neither confocal apertures nor incoherent sources are compatible with the technique. As such, FF-SSOCT techniques are more suitable for imaging non-scattering samples, such as thin specimens on microscope slides [78] and non-biological specimens [28, 30].

In section 2.2, we describe an application of extended-depth FF-SSOCT system designed for wide field-of-view (both lateral and axial) surface topography applications. This system employs a high spectral purity swept source, enabling a long imaging range, and employs a high speed camera that supports net A-scan rates of up to 1.4MHz.

### **1.3. *Imaging Depth Limitations in OCT***

The imaging depth of OCT systems is most often limited by one of three factors: optical attenuation, sensitivity fall-off, or depth-of-focus. The first of these, optical attenuation, stems from the limitation that OCT only detects singly-scattered light. This is because interference between the sample and reference fields requires a strict phase relationship, and phase information is lost after multiple scattering [80]. In homogeneously (or pseudo-homogeneously) scattering media, the proportion of photons that remain unscattered falls off exponentially with distance into the sample. Thus, beyond a certain penetration depth, essentially all of the incident light will have been multiply scattered, and can no longer be used for OCT imaging. For imaging of biological tissues at NIR optical wavelengths, optical attenuation typically limits the usable imaging range to 1 to 2 mm. Thus, for many applications (especially retinal imaging), optical attenuation is the most restrictive of the three imaging depth limitations. However, for some applications, especially anterior segment, cardiovascular (catheter-based) and GI (endoscope-based) imaging, the usable imaging depth is often not limited by optical attenuation, due to the presence of large regions of low scattering around the tissue of interest (e.g. the ocular anterior chamber, or the lumen of a coronary artery or GI tract). For these systems, the imaging range is often limited by the inherent imaging depth of the OCT systems. This inherent imaging depth, which is specific to

only Fourier Domain OCT systems, arises due to two factors: sensitivity fall-off and the complex conjugate ambiguity, and is discussed in section 1.3.

Finally, due to the trade-off between lateral resolution and axial depth-of-focus inherent in diffractive optical systems, additional depth limitations sometimes arise in either high lateral resolution or extended depth OCT imaging systems. This limitation is most apparent in applications such as adaptive optics (AO-) OCT of the retina [81-84], and extended depth imaging of the ocular anterior segment [85-88]. Depth-of-focus limitations will be discussed extensively in section 1.3.4.

### **1.3.1. Inherent imaging depth limitations in FDOCT**

Both FDOCT techniques suffer from an inherent, sample-independent limited imaging depth range, typically between 1 and 5mm. However, since the signal in OCT is derived only from backscattered ballistic photons, and biological tissue is generally highly scattering at optical wavelengths, optical attenuation from absorption and scattering typically restrict the usable imaging depth to less than 2mm. Thus, for many applications this inherent imaging range is not the limiting factor in determining the practical imaging depth. However, several important OCT applications would benefit from extended imaging depths, including ophthalmic imaging of the anterior segment, intrasurgical imaging, small animal imaging, endoscopic imaging of the gastrointestinal tract, and catheter imaging of coronary arteries.

The inherent limited imaging depth range is due to two factors. The first of these stems from the fact that FDOCT extracts depth information from the inverse Fourier transform of a spectral interferogram. As the spectral interferogram can only be recorded as a real signal, its Fourier transform is necessarily Hermitian symmetric about the zero pathlength difference position (ZPD), which occurs at electronic DC after Fourier transformation of the spectral interferogram. Consequently, positive and negative displacements about the ZPD position cannot be unambiguously resolved, which gives rise to mirror image artifacts. These artifacts can be avoided by placing the zero pathlength difference position outside of the sample, which results in two non-overlapping mirror images of the sample being acquired in the positive and negative frequencies. This technique resolves the complex ambiguity, but at the expense of halving the usable imaging range. Also, adjustment of the reference delay is required to ensure that distracting “wrapping” artifacts do not occur if the sample moves across the ZPD position, as shown in Figure 1.10.

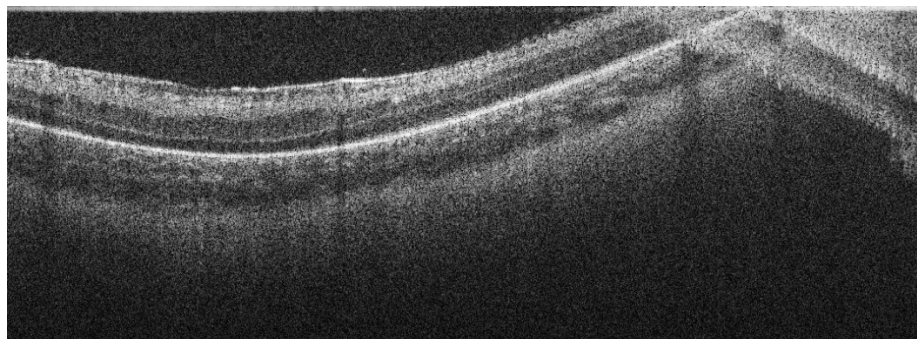


**Figure 1.10: SDOCT retinal B-scan corrupted with a complex conjugate artifact.**

The complex conjugate ambiguity would not pose such a problem if it were not for the fact that the total imaging range is also limited by a phenomenon known as sensitivity fall-off. In SSOCT, the instantaneous linewidth of the swept laser can be thought of as a sampling function that interrogates the intrinsic spectral interferogram. The spectral interferogram is sampled by, and thus convolved with, the instantaneous laser linewidth, which results in reduced fringe visibility when the fringe period approaches the linewidth. As smaller fringe periods (i.e. higher fringe frequencies) correspond to deeper imaging depths, this reduced visibility results in decreasing sensitivity with increasing imaging depth. In SDOCT, the spectral bandwidth detected by each pixel of the spectrometer is analogous to the laser linewidth in SSOCT, and likewise results in reduced fringe visibility with increased imaging depth.

The combination of the complex conjugate ambiguity and sensitivity fall-off results in a depth sensitivity profile that is well approximated by the “single-sided” Fourier transform of the average instantaneous linewidth of the laser over an entire sweep (or the average spectral bandwidth corresponding to a spectrometer pixel in SDOCT). Assuming a central wavelength of  $\lambda_0$  and a spectral resolution with a full-width at half-max (FWHM) of  $\delta_r\lambda$ , the depth at which the sensitivity is reduced by one half,  $z_{6dB}$ , is given by [89]:

$$Z_{6\text{dB}} = \frac{\ln(2)}{\pi} \frac{\lambda_0^2}{\delta_r \lambda} \quad (1.1.5)$$

For complex conjugate resolved SDOCT techniques, the sensitivity profile is given by the two-sided Fourier transform, and ranges from  $-Z_{6\text{dB}}$  to  $+Z_{6\text{dB}}$ , thus doubling the usable imaging range. The deepest resolvable single-sided depth,  $Z_{\text{max}}$ , is determined by the spectral sampling interval,  $\delta_s \lambda$ , and the central wavelength,  $\lambda_0$ , according to the relation [89]:

$$Z_{\text{max}} = \frac{\lambda_0^2}{4\delta_s \lambda} \quad (1.1.6)$$

In an ideal SDOCT system, the spectral resolution  $\delta_r \lambda$  would be equal to the spectral sampling interval  $\delta_s \lambda$ , and  $Z_{6\text{dB}}$  would occur at approximately  $0.88 Z_{\text{max}}$ . However, for the spectral sampling interval to be equal to the spectral resolution, the resolution of the spectrometer must be “pixel-limited”, and not diffraction or aberration limited. As most OCT spectrometers have several thousand pixels that are only a few microns wide, it is a challenging optical design problem to construct a spectrometer that is pixel-limited over the entire spectral range. As a result, most practical SDOCT spectrometers have a spectral resolution that is worse than the spectral sampling interval, and thus  $Z_{6\text{dB}}$  is usually only a small fraction of  $Z_{\text{max}}$ .

In SSOCT, the relationship between the spectral sampling interval and the spectral resolution is much less restricted. The spectral sampling interval depends only on the laser sweep speed and digitization rate. Specifically, the average spectral sampling interval is simply the ratio of the average wavelength sweep speed (in nm/s) and the digitization rate (in samples/s). The spectral resolution, however, is typically limited by the instantaneous laser linewidth, which has little dependence on the laser sweep speed or digitization rate. As a result, the ratio of  $z_{\max}$  and  $z_{6\text{dB}}$  can vary widely. In fact, some state-of-the-art SSOCT systems have demonstrated  $z_{6\text{dB}}$  values that exceed their  $z_{\max}$  value [88], meaning that the entire digitized imaging range is usable with high sensitivity.

### **1.3.2. Complex Conjugate Resolved Optical Coherence Tomography**

Extending the imaging depth range of FDOCT by resolving the complex conjugate ambiguity has been an area of interest for which a number of techniques have been developed [42, 90-104]. These techniques include phase shifting using a PZT-mounted reference arm [42] or electro-optic phase modulator [92], heterodyne techniques in both swept-source [90, 91, 93] and spectral-domain [94] implementations, instantaneous acquisition of phase separated interferograms using 3x3 interferometers [95] or polarization encoding [97], harmonic lock-in detection of phase modulation [96], imparting a phase ramp across a B-scan with B-M mode scanning [98, 105] and pivot-

offset scanning [99, 100, 102], sinusoidal phase modulation [101], dispersion encoding [104, 106]. An example of a complex conjugate corrupted image, and a corresponding complex conjugate resolved image is shown in Figure 1.11.

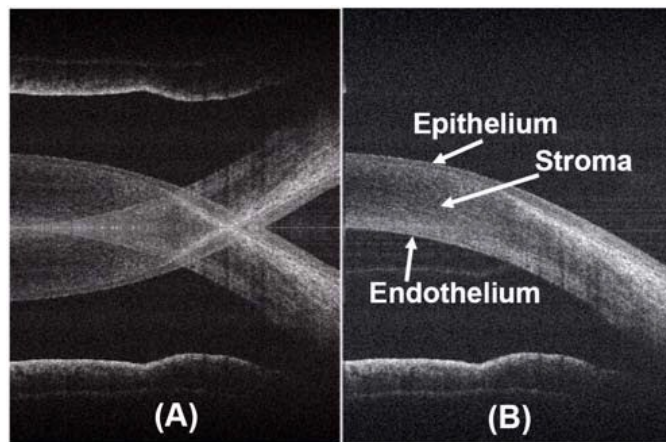


**Figure 1.11: SDOCT image of cornea and iris with complex conjugate artifact (A), and with the artifact resolved (B), from [105]**

Unfortunately, all of these techniques are accompanied by significant drawbacks including reduced sensitivity, reduced axial resolution, reduced imaging speed, required lateral oversampling, increased system complexity, increased cost and/or increased signal processing overhead. In addition, most of these techniques produce incomplete suppression of the complex conjugate artifact, resulting in distracting “ghost” images.

### 1.3.3. Heterodyne Swept Source Optical Coherence Tomography

One of the most effective methods for resolving the complex conjugate ambiguity is heterodyne complex-conjugate resolved SSOCT. This technique resolves the ambiguity by shifting the peak sensitivity position away from electronic DC, such that positive and negative displacements from that position can be discerned. As this technique shifts, rather than suppresses, the complex conjugate, it completely resolves the artifact. In addition, heterodyne SSOCT does not result in any reduction in imaging speed or require lateral oversampling. In this method, one or two active elements acting as frequency shifters, usually acousto-optic modulators (AOM's) [90, 91] (though electro-optic modulators (EOM's) have been used [93]) are used to apply a differential modulation frequency between the sample and reference arm light. While effective, this technique is limited in that such modulators are expensive and require careful alignment. More significantly, active frequency shifters tend to have appreciable insertion losses, resulting in reduced sensitivity, and restricted optical bandwidth, resulting in spectral distortion leading to distortion and broadening of the axial point-spread function (PSF). In addition, processing of the acquired data requires either hardware demodulation [91] or significant additional post-processing steps [90]. We have recently developed a very simple and cost effective method for realizing heterodyne SSOCT which exploits a phenomenon known as coherence revival [107]. This work is the subject of Chapter 3.

### 1.3.4. Depth-of-focus limitations in OCT

The optical design of most OCT systems is in many ways analogous to that of a typical confocal scanning laser confocal imaging system, except that most OCT systems use a relatively low numerical aperture (NA). Thus, as with confocal imaging systems, the lateral resolution in OCT is determined by the NA of the objective lens, and is given by [89, 108]:

$$\delta x = \frac{0.37\lambda_0}{NA} \quad (1.1.7)$$

However, unlike in confocal microscopy, the axial resolution in OCT is determined only by the “roundtrip” coherence length of the source, and is thus completely decoupled from the lateral resolution of the system and largely independent of the optical design. The coherence length of the source depends on its spectral bandwidth, with broader bandwidths corresponding to tighter coherence lengths. The roundtrip coherence length of a source with a Gaussian bandwidth with a FWHM of  $\Delta\lambda$ , centered at  $\lambda_0$ , can be computed as [89]:

$$l_c = \frac{2\sqrt{\ln(2)}}{\pi} \frac{\lambda_0^2}{\Delta\lambda} \quad (1.1.8)$$

In contrast to traditional confocal microscopy, where the axial confocal gate determines the axial sectioning thickness, in OCT, the axial confocal gate actually determines the axial field-of-view, which is given by [89]<sup>2</sup>:

$$FOV_{axial} = \frac{0.221\lambda_0}{\sin^2\left(\frac{\sin^{-1}(NA)}{2}\right)} \quad (1.1.9)$$

Because of the decoupling of the lateral and axial resolution, OCT systems usually employ small NA objectives selected to match the lateral resolution of the confocal imaging system to the axial resolution of the OCT source, thereby providing isotropic imaging resolution over a relatively deep imaging range [89]. Nevertheless, there are applications in which high NA objectives are used with OCT, and these systems are commonly referred to optical coherence microscopy (OCM) systems [55, 110-113].

### 1.3.5. Extended depth-of-focus strategies in OCT

A number of techniques and strategies have been proposed to extend the depth-of-focus of OCT imaging systems. These methods can be grouped into three general

---

<sup>2</sup> Note that the prefactor in this expression for axial FOV has been corrected as compared to the expression in reference [89]. Credit to Derek Nankivil for this correction, which will be updated in the upcoming second edition of [109]

categories: multiple focal plane techniques, beam-shaping and aperture apodization techniques, and digital refocusing strategies.

Perhaps most straightforward extended depth-of-focus techniques involve using multiple focal planes, for example, by translating the objective during an acquisition or between sequential acquisitions. The former technique, known as dynamic focus tracking [114-118], refers to systems wherein the objective lens is translated simultaneously with the reference arm, which keeps the coherence gated imaging depth coincident with the objective focus. Of course, this technique is only applicable to time-domain OCT systems. A similar technique applicable to both time-domain and Fourier-domain OCT systems is “zone focusing”, wherein a series of images are acquired sequentially with the focal plane shifted and then combined in post processing [119-121]. Recently, this technique was extended further in the development of “dual focus” OCT systems for imaging multiple depths within a sample by combining two SDOCT systems that simultaneously image different depths within the eye [122, 123]. We have recently developed a polarization encoded technique that enables simultaneous imaging of the anterior and posterior eye with a single SSOC system [124]. This work is the subject of Chapter 5.

The second category of techniques includes different methods of beam-shaping aperture apodization, especially the use approximations of Bessel beams. A Bessel beam is a field of electromagnetic radiation whose amplitude is described by a Bessel function

of the first kind. Bessel beams are of particular interest in extended-depth imaging applications because of the fact that true Bessel beams do not diffract (i.e. do not spread out) and because they are “self-healing” (meaning that an obstruction in the beam path does not block light from reaching objects downstream).

Although the mathematical foundations of Bessel beams had been laid out as early as 1915 (see references [125-127] for a more complete historical perspective), these early solutions required beams with infinite spatial extent and infinite energy, and thus were not physically realizable. It was not until 1986 that Durnin et al first suggested [128, 129] and then later demonstrated [130] that approximations of Bessel beams (called quasi-Bessel beams) could be experimentally realized. And while these beams were not truly non-diffracting, they demonstrated a substantially longer depth-of-field than Gaussian beams of a comparable beam waist.

Quasi-Bessel beams are not without drawbacks, however. Most notably, because the cross-sectional intensity distribution of a Bessel beams contains many sidelobes that contain most of the transmitted power [125, 127, 131, 132], illumination and collection efficiencies of OCT sample arms that employ Bessel beams are typically very low.

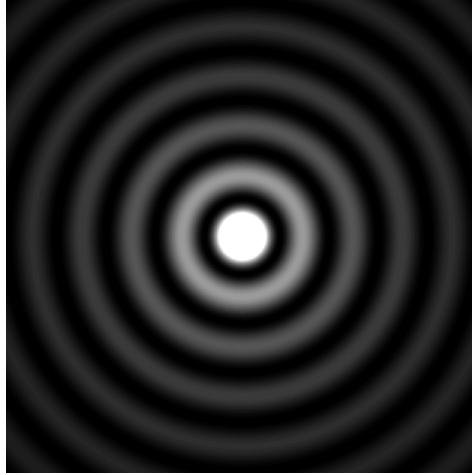


**Figure 1.12: Cross-sectional intensity distribution of an ideal Bessel beam**

Despite this drawback, there has been considerable interest in using Bessel beams in OCT. The use of Bessel beams in OCT has been largely aided by the development of the so-called “axicon lens” [133], which enables the formation of a quasi-Bessel beam from a collimated Gaussian beam with much higher efficiency than an annular pupil. Ding et al reported the first use of OCT with an axicon lens in 2002 [134] using a TD-OCT system. While the extended depth of focus of the system was confirmed, a large drop in imaging sensitivity was also observed (although not quantified). In 2006, Leitgeb et al [132] improved upon this technique by using a much more sensitive SDOCT system, and also by using an axicon for illumination but a conventional lens for detection. This scheme avoids the “intensity-critical” double-pass through the axicon lens, but the use of a conventional for collection lens reduces the depth-of-field enhancement somewhat. Nevertheless, this system still achieved an

impressive  $1.5\mu\text{m}$  resolution over a  $200\mu\text{m}$  axial range. In 2008, Lee and Rollan [135] performed a similar measurement to that performed by Ding et al [134], but with an SDOCT system and a custom micro-optic axicon lens. They achieved lateral resolution of  $8\mu\text{m}$  over a  $4\text{mm}$  axial range. However, a careful characterization of the system efficiency revealed a 21dB sensitivity penalty, which is approximately equivalent to the sensitivity gain achieved by averaging 7 acquisitions. More recently, in 2011, Blatter et al [136] improved upon the “Bessel illumination/Gaussian detection” technique first presented by Leitgeb [132] by using a high speed (440kHz) SSOCT system. They achieved a  $5.5\mu\text{m}$  resolution over an  $8\text{mm}$  axial range, and also quantified the sensitivity loss in the “Bessel illumination/Gaussian detection” scheme to be only 7dB as compared to a system using conventional lenses. In addition to the use of axicon lenses, phase masks [137] and rod lenses [138] have also been used to for annular apodization to generate extended depth-of-focus beams.

The third category of extended depth-of-focus OCT strategies can be broadly defined as digital refocusing, and includes deconvolution techniques [139-143], interferometric synthetic aperture microscopy (ISAM) [71, 144-146] and holographic methods [147]. These techniques have been applied with varying degrees of success, but have yet to see significant adoption in clinical settings. As these techniques are computational, and not optical, in their implementation, they are beyond the scope of this dissertation and will not be discussed in detail here.

## **1.4. Sweep Buffering in Swept Source OCT**

Sweep buffering in SSOCT refers to the use of long spools of optical fiber (typically hundreds to thousands of meters long) to delay and interlace swept source laser sweeps. Although the specific implementations details vary, buffering is generally used to increase the effective sweep frequency of swept source lasers that have duty cycles of less than 50%.

### **1.4.1. Fourier Domain Mode Locker Lasers**

The first applications of sweep buffering in SSOCT were applied to Fourier Domain Mode Locked (FDML) lasers [148], which will be described briefly here.

Perhaps the most commonly used swept source lasers are external cavity tunable lasers (ECTL's), which employ a semiconductor gain chip and rapidly swept external filter to create a narrow laser line that can be rapidly swept over a broad bandwidth. While these lasers have been shown to operate at rates up to 115kHz [149, 150], achieving sweep speeds faster than this is challenging because of the finite buildup time of lasing from spontaneous emission [149].

FDML lasers obviate the need to build up each new wavelength sweep from spontaneous emission by keeping a copy of the laser sweep inside the cavity itself. A schematic of an FDML laser is shown in Figure 1.13. These lasers typically comprise a semiconductor optical amplifier (SOA), two isolators, and a rapidly tunable piezoelectric

fiber Fabry-Perot filter (FFP) in a fiber ring cavity with a very long fiber spool. The FFP filter is then sinusoidally driven at a frequency that is precisely the reciprocal of the roundtrip cavity time, such that a pair of bi-directional wavelength sweeps is generated for each period. A fiber coupler is used to pick off a small portion of the circulating laser sweeps, but because a large portion of the sweep remains in the cavity, buildup from spontaneous emission is not required. This design permits the generation of laser sweeps with narrow linewidths, broad tuning bandwidths and repetition rates exceeding 1MHz [73, 151]. Since their invention in 2006, FDML lasers have been demonstrated in a variety of OCT applications at continually improving and record-breaking speeds [24, 72, 73, 86, 113, 136, 148, 149, 151-157]

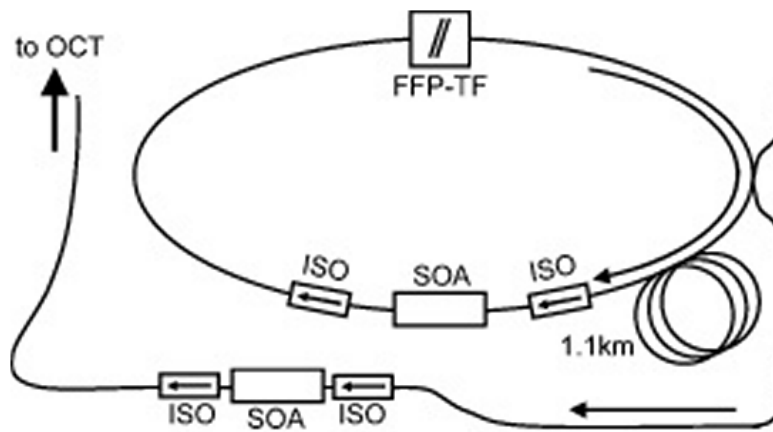


**Figure 1.13: Schematic of a FDML laser, from [149]. FFP-TF: fiber Fabry-Perot tunable filter. ISO: isolator. SOA: semiconductor optical amplifier**

### 1.4.2. Intra-cavity Buffering in FDML lasers

Because FDML lasers store a circulating copy of the laser sweep in the long fiber spool, the entire FDML cavity is, in a sense, a form of buffer. However, FDML lasers have also been demonstrated using two fiber spools inside the cavity to create unidirectional laser sweeps. This is desirable as it has been observed that the “backward” sweep of an FDML laser (i.e. long wavelength to short wavelength) has superior noise and linewidth characteristics as compared to the “forward” sweep [148, 149]. A schematic of a buffered, unidirectional FDML is shown in Figure 1.14. This laser differs from the laser shown in Figure 1.13 in that the long fiber spool has been broken up into two shorter fiber spools, with output couplers placed in between them. To enable unidirectional sweeping, the drive current to the SOA is modulated such that forward sweep is suppressed, and is thus replaced by the buffered “copy” of the backward sweep.

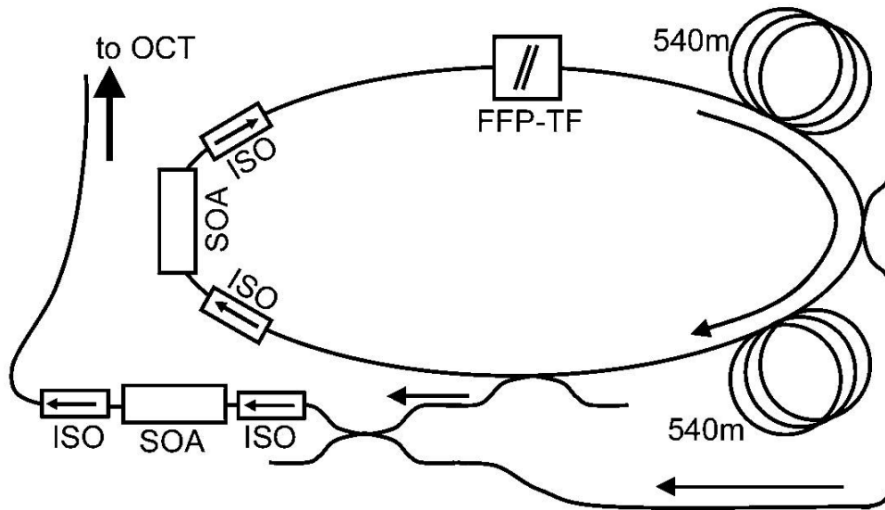


Figure 1.14: Schematic of a buffered, unidirectional FDML laser, from [149]

### 1.4.3. Extra-cavity Buffering

Similar to the use of buffer spools within the FDML cavity, buffering can also be implemented with fiber spools outside of the laser cavity. This extends the applicability of buffering techniques to non-FDML laser sources, especially ECTL's. Buffering stages with multipliers as high as 16x have been demonstrated with high speed, low duty-cycle FDML's to realize A-scan rates as high as 5 MHz [73]. However, ECTL's and other commonly used SSOCT lasers typically do not have duty cycles much below 50%, and thus buffering stages with multipliers greater than 2x have not been demonstrated with non-FDML sources.

The Axsun technologies 1060nm SSOCT laser is a good candidate for buffering. This commercially available turnkey ECTL has a sweep rate of 100 kHz, tuning

bandwidth of  $>100$  nm, but a specified duty cycle of only  $\sim 45\%$ . The low duty cycle is due to the fact that the laser uses a MEMS-based tunable filter, and during the backward sweep of the filter, the laser is turned off [158]. Potsaid et al [158] used a 2x buffer stage to increase the sweep rate of this laser to 200 kHz. A schematic of the buffer stage used is shown in Figure 1.15. One drawback of this design, however, is its optical inefficiency at the 50/50 fiber coupler, as half of the light is lost at port 3 (in Figure 1.15). In one configuration, Potsaid et al used the light from both port 2 and port 3 to create a dual spot OCT system that effectively operated at 400 kHz. However, this approach significantly complicates the design of the OCT system, while also halving the ANSI-limited power [159] that each spot can use.

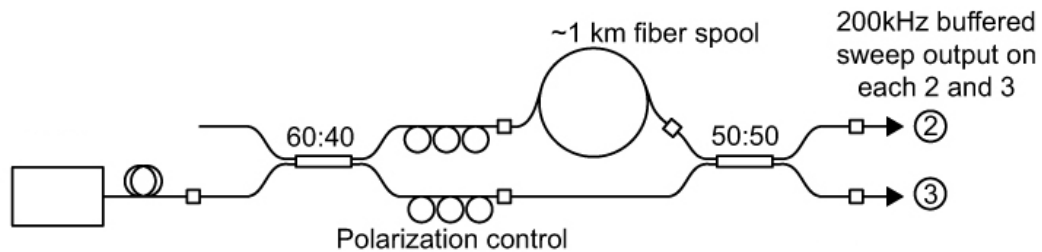


**Figure 1.15: Buffered 200 kHz SSOCT system using an Axsun Technologies 100 kHz swept source laser with a duty cycle of  $\sim 50\%$ , from [158]**

Another drawback of this approach is the potential for polarization mode dispersion (PMD) in the buffered output due to birefringence in the fiber spool. This is especially problematic for retinal imaging, where the sample beam traverses birefringent ocular

tissues such as the cornea and retinal nerve fiber layer [160], resulting in the creation of ghost images and phase artifacts. Beumann et al [160] address this concern by adding a polarizer after recombination of the original and buffered sweep. However, the losses through the fiber polarizer, coupled with the inefficiency of the 50/50 coupler used to recombine the two sweeps, result in substantial optical attenuation. To compensate for these power losses, an amplification stage consisting of an SOA and two isolators was added. A schematic of this configuration is shown in Figure 1.16. This amplification stage produced several undesirable effects. First, it reduced the spectral bandwidth of the source from 103nm to 70nm, broadening the axial PSF and degrading axial resolution. Second, the SOA produced significant broadening of the laser linewidth [161], resulting in a sensitivity fall-off of 4.2dB/mm. This is substantially worse than the ~1dB/mm fall-off we have measured in similar systems employing the same laser model (Chapter 3). Lastly, the SOA requires its own drive electronics and TEC, resulting in increased system cost and complexity.

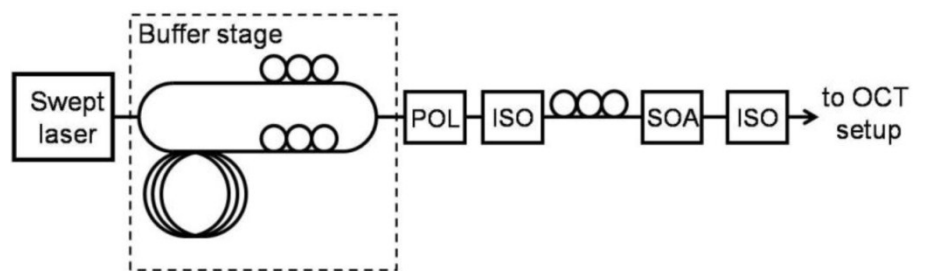


Figure 1.16: Buffered SSOCT system with polarizer and amplification stage, from [160]

Another consideration related to buffering is the technique used for performing wavenumber recalibration. Many turnkey SSOCT lasers, such as the Axsun laser, contain an optically integrated Mach-Zehnder Interferometer clock, or k-clock, that provides a clocking signal for wavenumber recalibration. Both external cavity buffering schemes described above [158, 160] are incompatible with the use of this internal k-clock, at least for the buffered sweep, and thus required the construction of a second clock for wavenumber recalibration.

In chapter 4, we describe an alternative buffering technique with superior optical power efficiency than previously reported methods. We also describe strategies to mitigate PMD without the use of lossy polarizers, and to use the wavenumber calibration from the original sweep (such as would be generated by an integrated k-clock) to recalibrate the buffered sweep.

### **1.5. Anterior Segment Biometry with OCT**

The clinical success of OCT for imaging the retina and diagnosing diseases of the posterior eye has been well documented [5-7, 162]. OCT imaging of the anterior eye, first demonstrated by Izatt et al in 1994 [8], also showed initial promise as a technique for measuring corneal topography, angle evaluation (especially for narrow-angle glaucoma) and anterior chamber biometry [80]. However, anterior segment OCT has seen comparatively less clinical adoption than retinal OCT, perhaps due to the

accessibility of the anterior eye for direct examination, and the existence of established clinical tools such as placido-ring topography and Scheimpflug photography. In addition, because the applications of OCT in the anterior eye are primarily quantitative in nature (as opposed to primarily morphological, as with retinal imaging), the slow acquisition rates of early time-domain OCT systems resulted in significant motion artifacts that precluded the use of OCT for quantitative biometry [163, 164].

Although the development of FDOCT in the early 2000's dramatically increased the imaging speed of retinal OCT systems, most early FDOCT systems were limited to imaging ranges of 1~2mm due to sensitivity fall-off and the complex conjugate ambiguity. While this imaging range is sufficient for retinal imaging, the anterior segment spans approximately 8mm in physical length [165] (~11mm in optical pathlength), and thus far exceeded the imaging range of early SDOCT systems.

Despite these limitations, however, anterior segment OCT remained of interest because of its ability to completely characterize the optical system of the anterior eye. This characterization can be carried out through measurements of several biometric parameters, including curvature of the anterior and posterior corneal surfaces, corneal refractive power, corneal thickness, anterior chamber depth, crystalline lens curvature, crystalline lens optical power, crystalline lens thickness, and axial eye length [88, 123, 124, 166-172]. Existing clinical methods for evaluation of these parameters are limited to measurement along a single axis and do not accurately account for off-axis variations

and aberrations. With the ability to rapidly acquire densely sampled 2D images and 3D volumes, OCT offers the potential to perform substantially improved characterization of the refractive properties of the anterior eye. This would enable improvements in customized modeling of patient eyes, which in turn would enhance intraocular lens customization and refractive surgical interventions, and also facilitate the correction of optical distortions due aberrations in patient optics in retinal OCT diagnostics.

Patient motion presents an additional complication in achieving accurate, quantitative anterior segment biometry with OCT. This motion can be categorized into axial motion (parallel to the OCT beam) and lateral motion (transverse to the OCT beam). Lateral motion occurs due to voluntary and involuntary movement of the patient's eye or head due to saccades, micro-saccades, tremors and the like. Prior works have established that most lateral motion is band-limited to frequencies less than 100 Hz [173, 174]. However, Zhao et al [168] have previously demonstrated that quantitative anterior segment biometry is far more sensitive to errors due to axial motion as compared to lateral motion. Recently, McNabb et al showed that axial eye motions, which occur primarily due to head movement, cardiac pulsations and breathing, are band-limited to 50Hz for motions larger than 1  $\mu\text{m}$ . Thus, acquisition of "motion-free" B-scans requires frame acquisition rates exceeding 100 Hz, although under-sampling techniques can be used to acquire motion-free images, even with relatively slow clinical systems [175].

The continuing development of FDOCT, especially with respect to increases in imaging depth (as discussed above) and imaging speed [74, 88, 148, 150, 151, 155-157, 176, 177], combined with the development of motion compensation strategies [178, 179] and refraction correction algorithms [168, 169, 180, 181], has recently made possible the extraction of corneal power from OCT images of the anterior segment [164, 168, 170, 175, 182, 183]. Other recent advances towards realizing “whole eye OCT” [88, 123, 124, 172] have enabled the measurement of other biometric parameters, including axial eye length, through simultaneous measurement of the anterior and posterior eye. While these achievements are a significant step towards the realization of complete and accurate quantitative characterization of the entire optical system of the eye, continued advances in imaging speed and imaging depth, as well as additional clinical validation, are necessary before widespread clinical translation is feasible.

## **1.6. Research Aims**

The objective of the work presented in this thesis was the development of advanced techniques for extending the imaging range and increasing the imaging speed of swept source optical coherence tomography systems. While the primary motivation for the development of these techniques was for applications in ophthalmology, specifically in anterior segment biometry, the techniques developed may also have applications in cellular and non-biological imaging, as well as in other medical applications of OCT outside of ophthalmology. The specific aims of this work are outlined as follows:

*Specific Aim 1:* The development of extended-depth full-field optical coherence tomography techniques. This aim is addressed in Chapter 2.

*Specific Aim 2:* The development of extended-depth swept source optical coherence tomography techniques, especially through resolving the complex conjugate ambiguity. This aim is addressed in Chapter 3.

*Specific Aim 3:* The development of high-speed swept source optical coherence tomography techniques, particularly through the development of sweep buffering techniques. This aim is addressed in Chapter 4.

*Specific Aim 4:* The development of depth-multiplexed optical coherence tomography techniques, especially “whole-eye OCT”, i.e. the simultaneous imaging of the entire optical system of the eye. This aim is addressed in Chapter 5.

## 2. Extended-Depth Full-Field OCT

Despite a handful of examples to the contrary [28, 30, 78, 79], most embodiments of full-field (FF-) OCT have been time domain systems employing thermal light sources [58, 60-64, 184, 185]. Thermal light sources are used primarily because of their low spatial coherence, which dramatically reduces coherent imaging artifacts such as speckle and crosstalk. However, the average number of photons within a coherence volume of blackbody radiation is always on the order of unity [68], which limits the speed and sensitivity of OCT systems employing thermal sources [67, 69, 70], and also precludes their use with Fourier domain OCT.

The use of spatially coherent sources, such as SLD's and femtosecond lasers, is desirable as they can have much higher output powers, enabling improved sensitivity, and can be efficiently coupled into optical fibers, reducing system complexity. Unfortunately, depth-dependent signal degradation due to coherent "crosstalk" precludes the use of spatially coherence sources, at least for imaging of highly scattering samples such as biological tissues. In addition, crosstalk also limits the utility of full-field swept source OCT (FF-SSOCT), as swept source lasers are typically spatially coherent.

In section 2.1, we describe a technique to reduce the spatial coherence of partially coherent sources, which are commonly used on TDOCT and SDOCT. Reducing the spatial coherence of the illumination field suppresses crosstalk and speckle in much the same way as employing a thermal source does.

In section 2.2, we describe the development of an extended-depth FF-SSOCT system. It should be noted that this system is not compatible with the technique described in section 2.1, and thus would suffer from appreciable coherent artifacts if used for imaging biological specimens. However, the system is ideal for (and in fact was designed for) large field-of-view imaging of non-turbid samples, such as in surface topography applications. The system utilized a high spectral purity swept source and a high speed CMOS, which together enabled very large axial and lateral field-of-view imaging at A-scan rates of up to 1.4MHz.

Justin Migacz contributed to the work presented in this chapter, aiding with the construction, data acquisition and data analysis of both systems.

## **2.1. Speckle Reduction and Crosstalk Rejection in Full-Field OCT**

### **2.1.1. Theory**

For a step-index multimode fiber, the complex degree of mutual coherence of two points on the fiber endface at the same instant in time is given by [186]:

$$g(\Delta r) = \frac{2 J_1(k_0 \text{ NA } \Delta r)}{k_0 \text{ NA } \Delta r} \quad (2.1.1)$$

where  $\Delta r$  is the separation,  $J_1$  is a Bessel function of the first kind,  $k_0$  is the wavenumber, and NA is the fiber numerical aperture. The coherence area is commonly defined as the region over which the complex degree of coherence exceeds 0.88, i.e. when the argument of the Bessel function in equation (2.1.1) less than unity [187]. However, for the purpose of determining the effectiveness of a spatial coherence gate to reject multiply scattered photons, we follow the definition in [186] and, in analogy to the Rayleigh criterion for resolution, define a spatial coherence gate radius,  $\Delta r_{SCG}$ , that extends to the first minimum of the Bessel function in equation (2.1.1) [69, 186]:

$$\Delta r_{SCG} = \frac{1.22\pi}{k_0 \text{ NA}} \quad (2.1.2)$$

The relationship between these two definitions is depicted in Figure 2.1. If the coherence gate radius of the illumination on the sample is smaller than the system resolution, the illumination can be treated as spatially incoherent [71].

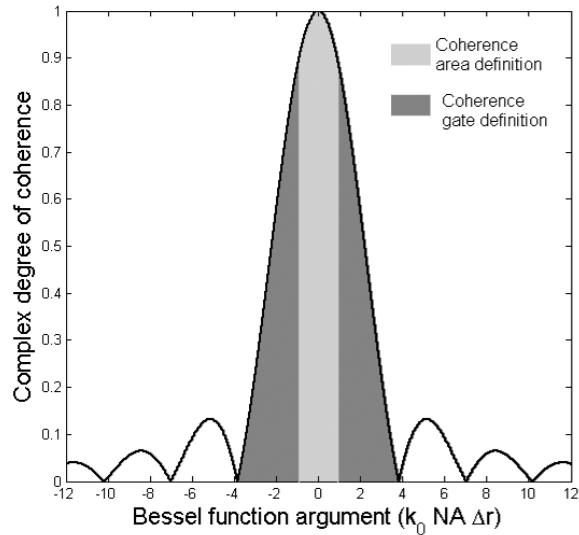


**Figure 2.1: Coherence area and coherence gate definitions**

Equation (2.1.1) is only valid if intermodal interactions are negligible; that is, modes propagating in the fiber must be mutually incoherent. This assumption is valid for fibers that are sufficiently long such that the intermodal delay between all supported modes exceeds the source coherence length [186], but not so long that they approach the mode coupling length [188]. The mode coupling length is length beyond which appreciable mode mixing occurs due to defects in the fiber, such as impurities and microbends. For typical silica-clad step-index fibers, this length is on the order of 1 km [189].

We can meet this first condition by ensuring that the intermodal delay between the fundamental mode and the highest order mode is greater than the source coherence length multiplied by the number of supported modes:

$$\left| L_{fiber} N_{high} - L_{fiber} N_{low} \right| > l_c M \quad (2.1.3)$$

where  $L_{fiber}$  is the length of the fiber,  $N_{high}$  and  $N_{low}$  are the group indices of the highest order and fundamental mode,  $l_c$  is the source coherence length, and  $M$  is the number of modes supported. For a step-index multimode fiber, the difference in group index between the fundamental and highest supported modes is given by [190]:

$$N_{high} - N_{low} = N_1 \frac{\Delta n}{n_{core}} \quad (2.1.4)$$

where  $N_1$  is the core group index,  $\Delta n$  is the refractive index step between the core and cladding, and  $n_{core}$  is the refractive index of the core. The number of modes supported by a weakly guiding multimode fiber with core radius  $a$  is given by  $M = 16a^2 (NA)^2 / \lambda^2$  [190]. Thus, the condition in equation (2.1.3), coupled with the requirement that the fiber be shorter than the mode coupling length, can be expressed as:

$$L_{coupling} \gg L_{fiber} > L_{min} = \frac{16 a^2 (NA)^2 l_c n_{core}}{\lambda^2 N_1 \Delta n} \quad (2.1.5)$$

If this condition is met, the tip of the multi-mode fiber can be treated as a spatially incoherent extended source. The fiber tip can then be imaged onto the sample to realize SII, in analogy to critical illumination in microscopy. Alternatively, light emerging from the fiber can be collimated and directed to the sample, in analogy to Koehler illumination. It has been shown that both of these illumination schemes yield identical spatial coherence properties [191].

### **2.1.2. Methods**

For a proof of principle experiment, we implemented the FFOCT system depicted in Figure 2.2 using a Linnik interferometer configuration. Major system components included an SLD ( $\lambda_c=828\text{nm}$ ,  $\Delta\lambda=50\text{nm}$ ,  $P=6\text{mW}$ ), a 1.3MP CMOS camera (Pixelink A741), and a reference mirror mounted on a piezoelectric actuator (Thorlabs AE0505D16F). The system had a field of view of 2.1mm and lateral resolution of  $6.9\mu\text{m}$  (Airy diameter).

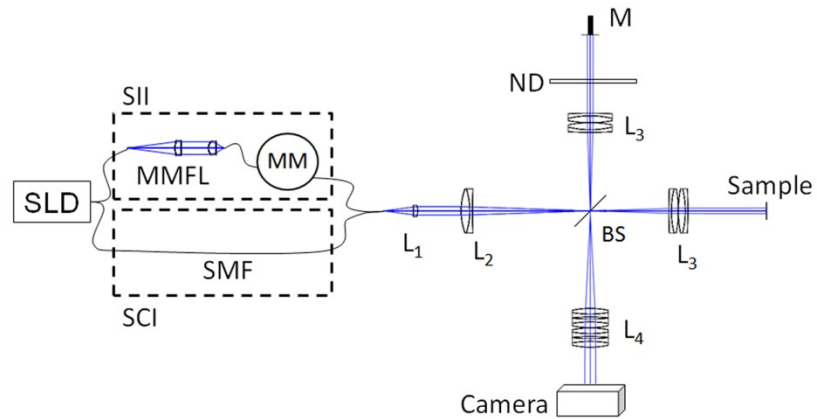


**Figure 2.2: System schematic. SLD, superluminescent diode; SMF, single mode fiber; MMFL, multimode fiber launch; MM, mode mixer & fiber spool; L1-4, lenses; BS, beam splitter; ND, neutral density filter; M, reference mirror on PZA. Dashed boxes represent interchangeable configurations for SCI and SII.**

Two illumination schemes were used: spatially coherent illumination (SCI) was used to demonstrate crosstalk artifacts, and SII was used to demonstrate crosstalk rejection and recovery of resolution. For SCI, a single mode fiber was used to couple light directly from the SLD into the setup. For SII, the source was coupled into one of three multimode fibers with varying core diameters and NA's (see table 1). For fiber 4, the coherence area is smaller than the system lateral resolution, and thus the illumination is essentially spatially incoherent.

**Table 2.1: Fibers used for SCI and SII and relevant parameters**

Fiber #	a	NA	$L_{\min}$	$L_{\text{fiber}}$	M	$\Delta r_{\text{SCG}}$
1	8 $\mu\text{m}$	0.13	-	1m	1	-
2	200 $\mu\text{m}$	0.22	4.4m	5m	~12,500	24.7 $\mu\text{m}$
3	200 $\mu\text{m}$	0.48	3.9m	20m	~53,800	11.3 $\mu\text{m}$
4	400 $\mu\text{m}$	0.48	16m	80m	~215,000	5.65 $\mu\text{m}$

a – core diameter, NA – numerical aperture,  $L_{\min}$  – min fiber length,  $L_{\text{fiber}}$  – actual fiber length, M – supported modes,  $\Delta r_{\text{SCG}}$  coherence gate radius (at sample)

To resolve *en face* OCT images, we acquired four images in 90-degree phase steps. Amplitude and phase maps were then extracted as described in [54]. The integration time was dynamically adjusted to account for varying coupling efficiency and sample reflectivity, and ranged between 100 $\mu\text{s}$  to 1ms. To demonstrate crosstalk rejection, we imaged a 1951 USAF resolution test chart beneath 2mm solutions of water and 1 $\mu\text{m}$  polystyrene microspheres, containing either 0 (control), 6 or 8 mean free paths (mfp) of roundtrip scattering. Using the test chart images, the modulation transfer function (MTF) can be estimated as:

$$\text{MTF}(f) = \frac{I_{\max}(f) - I_{\min}(f)}{I_{\max}(f) + I_{\min}(f)} \quad (2.1.6)$$

where  $f$  is the known spatial frequency of the test chart bars,  $I_{max}$  is the average image intensity in the bright region of the bars, and  $I_{min}$  is the average image intensity in the dark region of the bars. To quantify the image enhancement for high spatial frequencies under SII, the MTF was measured for fibers 1 and 4 under all three solutions. To demonstrate the feasibility of this method for imaging biological specimens, we also imaged an immobilized *Drosophila melanogaster* sample using fibers 1 and 4. Volumes were acquired by stepping the sample stage in 5 micron axial steps over a range of 300 $\mu\text{m}$ .

### **2.1.3. Results**

To demonstrate the phase stability and field flatness of our system, we first imaged a 1951 USAF test chart in air, as shown in Figure 2.3. The system phase stability was measured by taking the standard deviation of the phase in a region of the test chart image where the test chart was expected to be an optical flat. We measured a phase stability of 93.3 mrad, corresponding to a flatness of 6.16nm. The true stability of the system may in fact be better than this, as the specified flatness of the test target was only 0.0001" (2.54  $\mu\text{m}$ ).

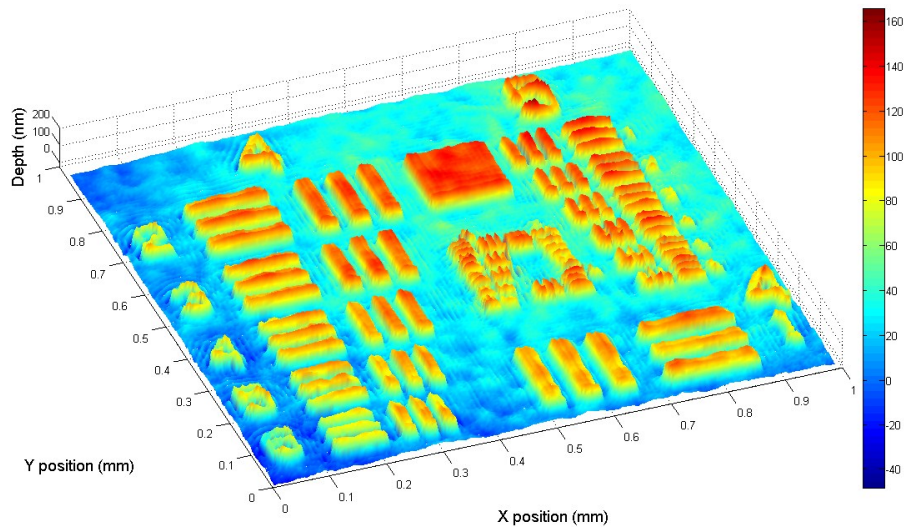


**Figure 2.3: Phase resolved image of 1951 USAF test chart showing groups 4, 5, 6 and 7.**

Images of groups 5, 6 and 7 of the test chart under all phantoms and illumination schemes are shown in Figure 2.4. For the 6 and 8 mfp solutions, a clear improvement in resolution is seen as the spatial coherence is decreased. MTF plots derived from images corresponding to fibers 1 and 4 are shown in Figure 2.5. We define the effective resolution at an MTF visibility of 0.09, as implied by the Rayleigh criterion. For the SCI case, crosstalk results in a significant loss in resolution, degrading from 95 lp/mm in water to 60 lp/mm in the 6 mfp solution and 55 lp/mm in the 8 mfp solution. At high spatial frequencies, the MTF is almost completely recovered using SII, for which the resolution is 90 lp/mm for both 6 mfp and 8 mfp. At lower spatial frequencies, the image from the 8 mfp solution suffered some loss of contrast, likely caused by the reduced signal-to-noise ratio that resulted from the additional scattering.

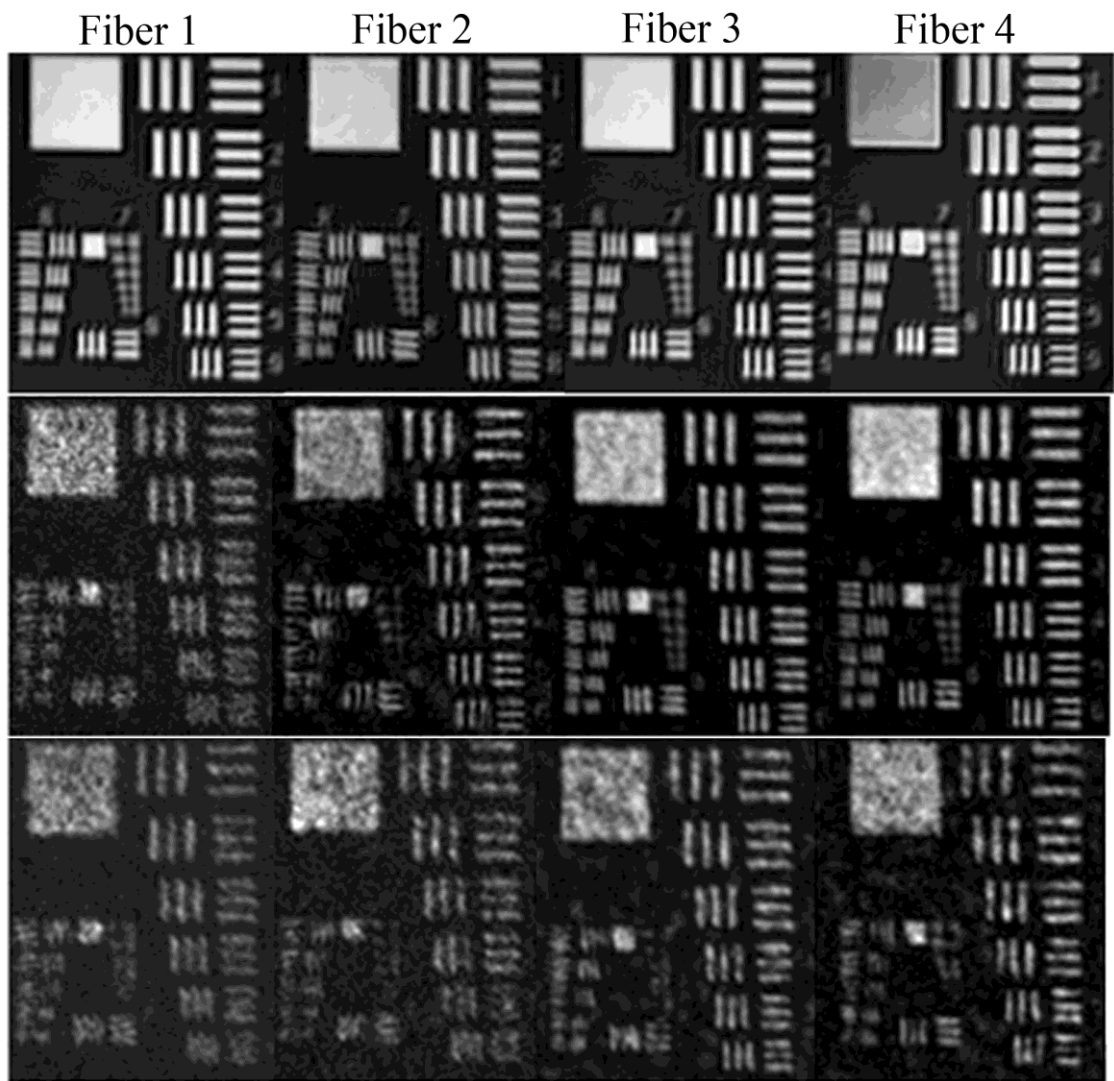


Figure 2.4: USAF 1951 test chart imaged through water (top), 6mfp (middle) & 8mfp (bottom) scattering solutions

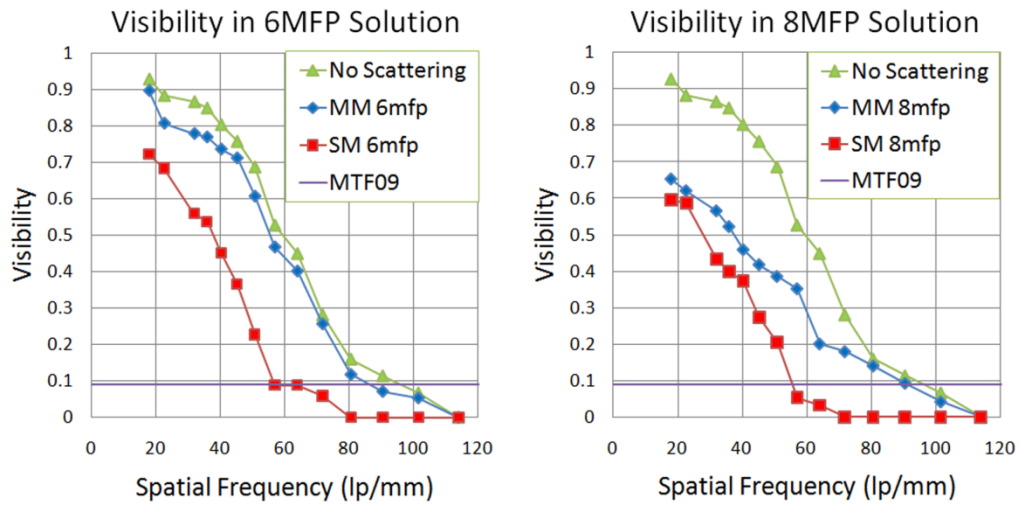


Figure 2.5: MTF's from images taken beneath water, 6mfp and 8mfp solutions for both SCI and SII

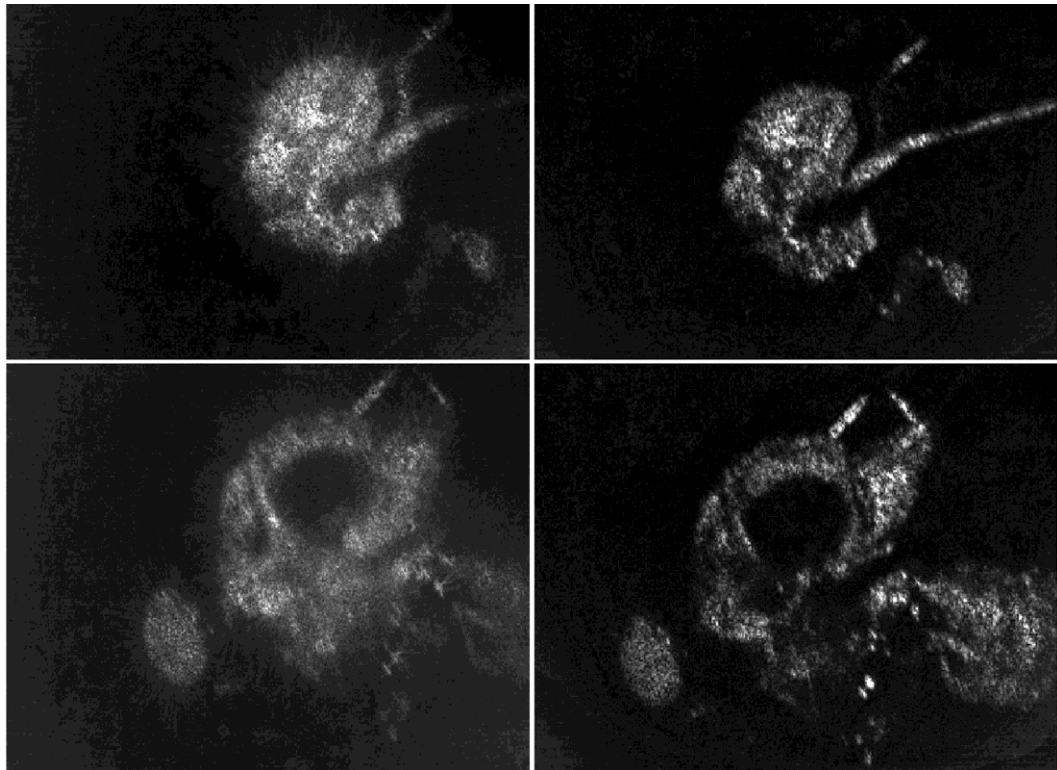


Figure 2.6: OCT projections of a *Drosophila melanogaster* summed over 100µm, centered at 100µm (top) and 200µm (bottom) from top surface using SCI (left) and SII (right)

Representative *en face* projections of the fruit fly, summed over  $100\mu\text{m}$ , are shown in Figure 2.6. These results show degradation of image quality due to crosstalk artifacts in the SCI case, and effective rejection of these artifacts and a clear improvement in resolution in the SII case.

#### **2.1.4. Discussion**

In summary, we have demonstrated a technique to reduce the spatial coherence of broadband, temporally coherent source by employing multimode fiber, and shown that this method is effective in preventing resolution loss caused by crosstalk artifacts in turbid samples. This resolution improvement was verified quantitatively with MTF measurements, and practically by imaging a fruit fly. This technique demonstrates a solution to a major obstacle in implementing parallel acquisition OCT with spatially coherent sources, but may also be valuable in other fields.

Since the contents of this section was first published in 2010 [192], there has been a fair amount of interest in the generation of sources with moderate temporal coherence and low spatial coherence that would maintain the large power spectral density associated with coherent. Redding et al [193] recently demonstrated the use of a “random laser” that exhibited moderate temporal coherence with low spatial coherence and used this source to demonstrate “speckle-free” laser imaging. Similarly, Manni and Goodman [188] recently investigated the potential for using the modal dispersion of

multimode fiber to reduce speckle in cinematic laser projector applications, performing a careful analysis of the properties of the fiber required to achieve a speckle contrast of less than 1%. The technique we have presented confers all of the same advantages as the techniques described by Redding et al [193], and is essentially identical to the technique described by Manni and Goodman [188], and thus would appear to have many potential applications beyond OCT.

## **2.2. *Extended-Depth Full-Field Swept Source OCT***

In this section, we describe the design and development of a high speed and very wide field-of-view FF-SSOCT system for surface topography applications. The system is capable of imaging over a 10 mm x 10 mm x 10 mm field-of-view with 45  $\mu\text{m}$  lateral and 30  $\mu\text{m}$  axial resolution, and supports a net A-scan rates of up to 1.4 MHz. The system is also sufficiently robust against dispersion to image through several centimeters of water or ice without appreciable degradation of axial resolution. Furthermore, the design is scalable to enable imaging over substantially longer depths, and to be tolerant of very large amounts of dispersion. This work was performed under contract FA8650-09-C-7932 with the Defense Advanced Research Projects Agency and the U.S. Air Force Research Laboratory.

### 2.3.1. Introduction and Motivation

Traditional implementations of OCT provide lateral and axial resolution of a few microns, limited by diffraction and available light source bandwidths, respectively. For imaging of biological tissues, the imaging depth range is limited to a few millimeters due to strong elastic scattering at the NIR wavelengths used. Because of these factors, the imaging depth dynamic range is typically on the order of 1000.

In FDOCT, spectral interference between the sample and a reference is recorded over multiple spectral channels, either sequentially using a swept-frequency laser source (SSOCT) or simultaneously by dispersing the mixed light fields across a receiver array (SDOCT). Following Fourier transformation, the maximum imaging depth obtainable corresponds to the coherence length associated with each spectral channel (the laser linewidth in SSOCT or the spectrometer resolution in SDOCT), the depth sampling corresponds to the spacing between spectral channels, and the depth resolution corresponds to the coherence length of the composite spectrum. For biomedical imaging over millimeter depth scales and with  $\sim 1000$  depth dynamic range, the spectral channel resolution required is  $\sim 0.1$  nm and a detector array with 1000 elements must be used.

For imaging with increased depth range but without loss of resolution, both the spectral resolution and the number of spectral channels must be increased. In an extreme case, a depth range of 10 meters would require a spectral resolution of 0.03 pm (10 MHz), and  $10^6$  spectral channels would need to be acquired to maintain 10 micron

resolution (assuming a center wavelength of 800 nm). These requirements would be difficult to meet using available dispersive spectrometers and detector arrays, and thus are not practically realizable with SDOCT. Furthermore, the spectral purity required to achieve this kind of imaging range in SSOCT has only been demonstrated with tunable lasers that tune at speeds on the order of 100nm/s or less. This is several orders of magnitude slower than commonly used SSOCT lasers, and is prohibitively slow for practical imaging in traditional scanning OCT implementations.

Management of sample dispersion in traditional FDOCT systems is relatively easily addressed because the amount of second-order dispersion (group velocity dispersion, or GVD) and higher order dispersion (HOD) within the limited sample depth of 1~2mm is typically small compared to material dispersion mismatches between sample and reference arms. Thus, so long as the amount of glass in both arms can be controlled within a few millimeters, the amount of chirp induced across the spectrum will be negligible compared to the spectral channel width, and would not appreciably degrade the axial resolution. Furthermore, any remaining amount of dispersion mismatch between the arms, as well as dispersion within the sample, may be corrected via numerical post-processing [176]. However, advanced system designs for increased depth range (such as imaging through several meters of ice or water) must be tolerant of much more significant spectral chirp.

In the remainder of this chapter, we present a novel FF-SSOCT system design that offers several advantages over traditional FDOCT systems, outlined below.

1. The system employs a type of very high spectral purity tunable laser developed for the telecommunications industry. These lasers can provide  $< 10\text{MHz}$  linewidths (capable of supporting  $> 10$  meters of SSOCT imaging depth) with  $> 10$  nm tuning range (delivering  $< 30$   $\mu\text{m}$  depth resolution) over a wide range of available center wavelengths (600-1800 nm). The primary limitation on sources available presently is tuning rate and accuracy.
2. These tunable lasers also feature adjustable tuning speeds, which provide the agility to sample at any desired spectral interval. This provides precise and dynamic control over the depth dynamic range, a feature that is not realizable with traditional FDOCT systems.
3. Due to the decoupling between frequency channel width and spacing, swept-sources lasers with sufficient tuning agility can be constructed with greatly increased tolerance to large amounts of sample dispersion by tuning the spectral channel spacing to match the anticipated nonlinear spectral chirp. This process can be done either prospectively, if an estimate of the

anticipated thickness of dispersive media is available, or iteratively. Having appropriately sampled the chirped spectral interference data, sample dispersion can then be compensated using numerical spectral phase adjustment, as is commonly performed in FDOCT.

4. Swept-source systems can take advantage of modern fast 2D cameras capable of multi-kHz megapixel frame rates, delivering the equivalent of multi-MHz A-scan SSOCT imaging capability despite the relatively slow tuning speed of the laser.

### **2.3.2. System Design**

As a demonstration of this increased depth range FF-SSOCT system design, we constructed a prototype system based on a commercially available tunable laser source and a high-speed CMOS camera.

The laser source used was a Thorlabs INTUN laser (Model TL780-B), which operated with a center wavelength of 780 nm, 15 nm tuning range, 1.8 pm tuning resolution and 1 pm wavelength repeatability. The effective linewidth of the laser was 4 MHz, and the maximum scanning speed was 80nm/s. Based upon these source parameters, the predicted FF-SSOCT system performance included an axial resolution of 30 $\mu$ m, and a  $z_{6dB}$  range of 16.5m. The high-speed CMOS camera utilized was a Photron

model SA4, which was capable of acquiring 3600 frames per second at 1024x1024 pixel resolution, with sufficient sensitivity to support this faster imaging speed.

A schematic of the full-field swept-source imaging system is illustrated in Figure 2.7. The design exclusively used off-the-shelf lenses, which were sourced from Thorlabs. Two plano-convex cylindrical lenses were used to reshape the elliptical output beam of the INTUN laser into a (nearly) circular beam, which was then fiber-coupled into a single mode fiber (SM-800) using an achromatic doublet. Single mode fiber coupling was performed to limit feedback into the laser (due to the poor coupling efficiency of back reflected light), and to facilitate coupling into the fiber k-clock (discussed below).

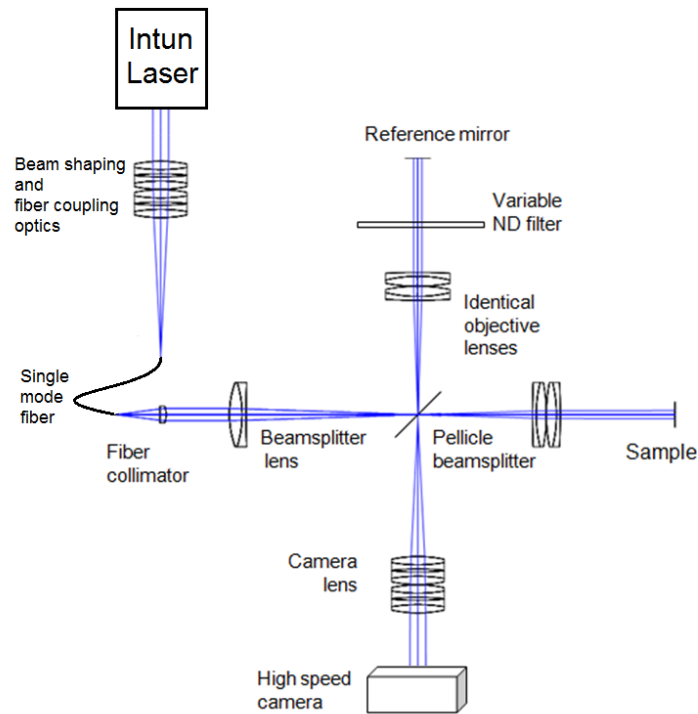


**Figure 2.7: Schematic of prototype FF-SSOCT system.**

The interferometer was constructed in a Linnik configuration, as shown. Imaging optics were optimized using ray-tracing optical design software (ZEMAX) to provide a diffraction-limited performance of  $< 45\mu\text{m}$  PSF FWHM across nearly the entire  $1\text{cm} \times 1\text{cm} \times 1\text{cm}$  design field-of-view. Figure 2.8 shows ZEMAX ray diagrams of the illumination optics, the reference arm collection optics, and the sample arm collection optics, respectively. The ZEMAX estimated FWHM of PSF cross-sections at several locations throughout the field-of-view are listed in Table 2.2.

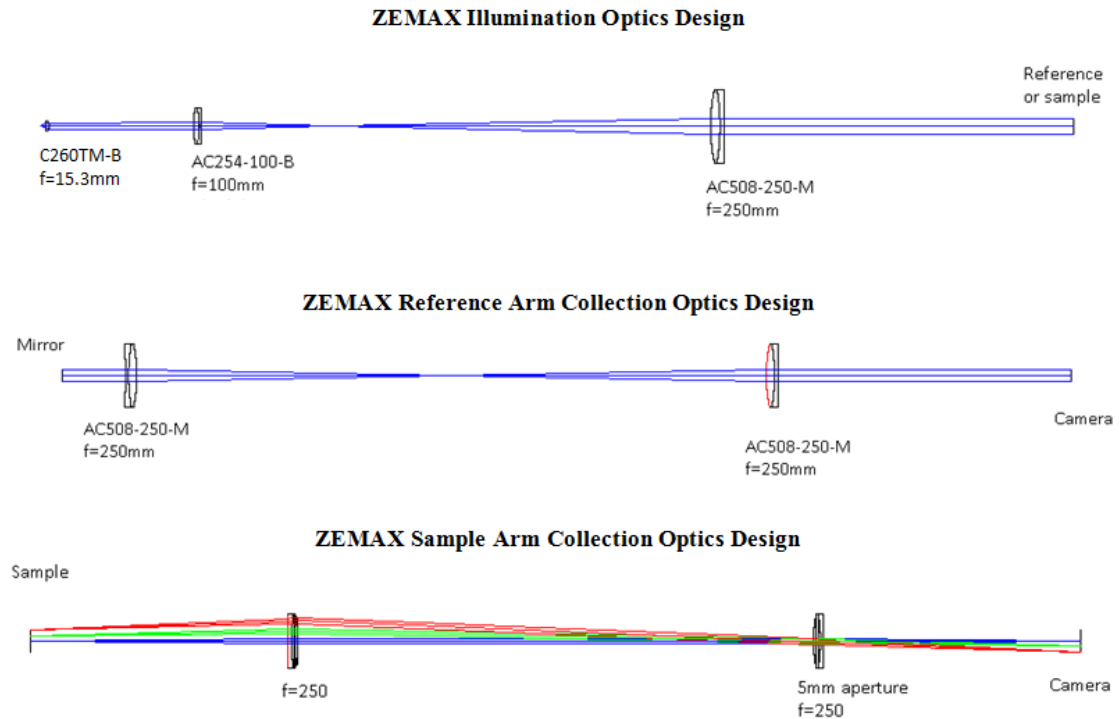


Figure 2.8: ZEMAX ray diagram of the illumination optics (top), reference arm collection optics (middle), and sample arm collection optics (bottom).

**Table 2.2: FWHM of PSF at various locations throughout the field of view**

Axial position	(+5,+5)mm	(+2.5,+2.5)mm	(0,0)mm	(-2.5,-2.5)mm	(-5,-5)mm
5.0mm in front	45.8 $\mu\text{m}$	48.5 $\mu\text{m}$	54.4 $\mu\text{m}$	48.5 $\mu\text{m}$	45.8 $\mu\text{m}$
Focal plane	44.3 $\mu\text{m}$	44.3 $\mu\text{m}$	45.4 $\mu\text{m}$	44.3 $\mu\text{m}$	44.3 $\mu\text{m}$
5.0mm behind	47.2 $\mu\text{m}$	44.8 $\mu\text{m}$	44.3 $\mu\text{m}$	44.8 $\mu\text{m}$	47.2 $\mu\text{m}$

Wavenumber calibration was performed using a custom built, all-fiber “k-clock”, as shown in Figure 2.9. Although not shown in Figure 2.7, the k-clock was connected to the single mode fiber via a 90/10 fiber coupler. The k-itself clock consisted of two 50/50 fiber couplers with a  $\sim 7\text{mm}$  optical pathlength offset, arranged in Mach-Zehnder interferometer (MZI) configuration. The outputs of the second coupler were connected to a balanced photoreceiver, and the resulting signal was digitally bandpass filtered and then used to resample the acquired spectral data. An example of the processed output of this calibration system is shown in Figure 2.10.

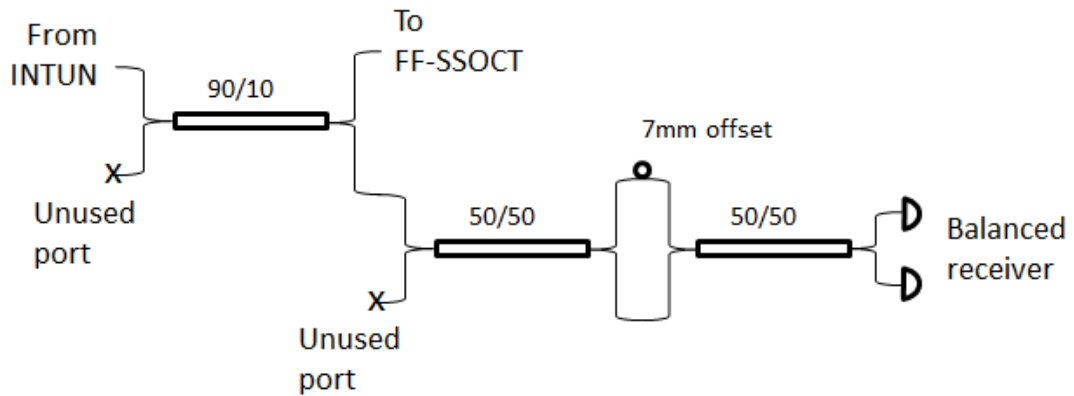


Figure 2.9: Schematic of all-fiber MZI k-clock

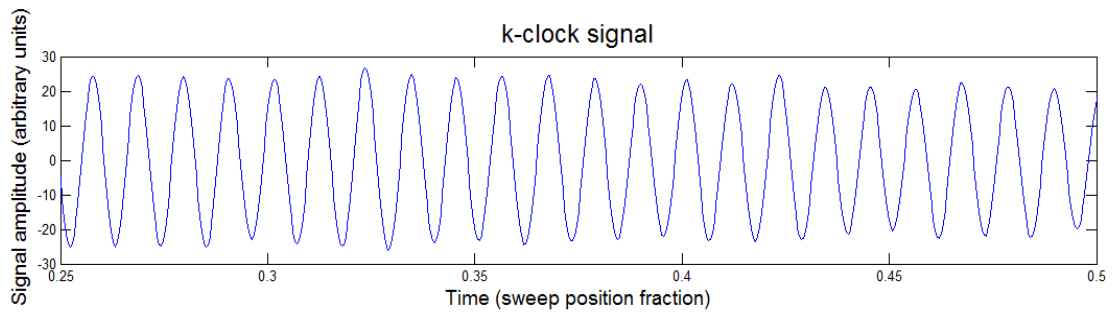
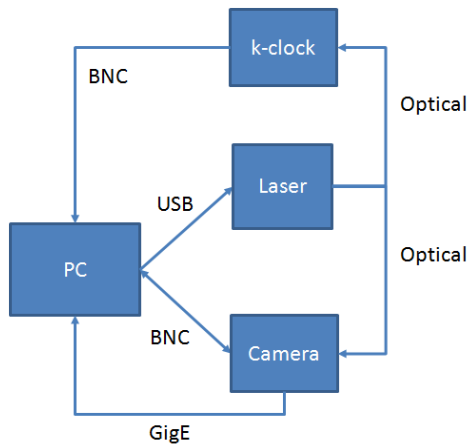


Figure 2.10: Processed k-clock signal from the fiber Mach-Zehnder interferometer.

Hardware interfacing between the computer and various hardware components is illustrated in the flowchart in Figure 2.11. The computer communicated with the INTUN laser through a USB interface, and with the k-clock receiver and high speed camera through a National Instruments (NI) DAQ connector block (BNC). Data

acquired with the camera was stored on the camera's on-board memory and read off via a GigE interface.



**Figure 2.11: Flowchart showing hardware interconnects**

Data acquisition was driven by a custom developed LabVIEW program, which operated as follows. Upon user request via a button click, a start acquisition trigger was sent nearly simultaneously to the laser via the USB interface and to the camera via the NI DAQ board. The laser would then perform a single, unidirectional sweep and the camera would free-run at a preset frame rate to acquire a preset number of frames. The camera also fired a TTL pulse at the start of the integration of each frame. The TTL pulse, along with the signal from the k-clock balanced receiver, was digitized using the same DAQ board. At the conclusion of the acquisition, data was streamed from the on-board memory of the camera via a GigE interface and written to a solid state drive.

Post-processing processing algorithms were developed in MATLAB, and functioned as follows. Each pixel of the camera was treated as a separate A-scan, with each frame corresponding to a single spectral channel. Wavenumber linearization was performed by detecting the zero crossings of the k-clock signal and interpolating the acquired spectral data corresponding to each pixel of the 2D array to be linear with those zero-crossings. Standard OCT processing techniques, including DC subtraction and spectral windowing, were then applied before Fourier transformation.

### **2.3.3. System Performance**

The imaging speed, sensitivity, and axial resolution of the FF-SSOCT were carefully characterized, as follows.

At the maximum sweep rate, the INTUN laser tuned over the entire 15 nm tuning range in 280 milliseconds. Thus, with 1024 x 1024 A-scans acquired over 280 milliseconds, a net A-scan rate of 3.74 MHz was achievable. However, due to the Gaussian power distribution of the beam, only approximately 37% of the camera's pixels had sufficient optical power to measure a usable signal. This usable portion of the sensor area was approximately 625 x 625 pixels, and corresponded to a field-of-view on the sample of about 12.5mm x 12.5mm. Thus, the maximum net A-scan rate of the system was 1.4 MHz.

For the imaging experiments performed, however, the sweep speed was reduced to increase the system sensitivity and to allow enough spectral samples to be acquired to support an imaging depth > 10mm. The FOV was also reduced to limit the acquisition of data outside of the desired 10mm x 10mm lateral field-of-view. Thus, we used 512 x 512 pixels and a sweep period of either 0.52 seconds or 1.872 seconds, corresponding to net A-scan rates of 524 kHz and 140 kHz.

Assuming shot-noise limited performance, the theoretical system sensitivity can be calculated using a modified form of the technique described by Choma et al [51]. For a particular pixel of interest and assuming integration over the entire frame period, the sensitivity is given by:

$$SNR = \frac{\rho R_s S_{avg}}{4 e B_{ssoct}} \quad (2.2.1)$$

Here,  $q$  is the detector responsivity,  $R_s$  is the sample reflectance, and  $e$  is the elementary charge.  $S_{avg}$  is a parameter related to average power reaching the pixel of interest and the number of spectral channels, and can be approximated by:

$$S_{avg} = M P_{source} / N \quad (2.2.2)$$

where  $M$  is the number of spectral channels,  $P_{\text{source}}$  is the average source power reaching the sample, and  $N$  is the number of illuminated detector elements. Also,  $B_{\text{ssoct}}$  is the OCT signal bandwidth, given by:

$$B = (\Delta k \Delta x_{\text{max}}) / (\pi \Delta t) \quad (2.2.3)$$

where  $\Delta k$  is the total source bandwidth, in wavenumber,  $\Delta x_{\text{max}}$  is the deepest resolvable depth, and  $\Delta t$  is the sweep period.

Given the manufacturer specified detector responsivity of 0.6, and assuming a sample reflectivity of 1 (for a mirror), source power of 4mW (maximum incident power on the sample), and 1872 spectral channels acquired over 0.52 seconds with 512 x 512 active pixels, we predict a sensitivity of 101.5 dB. It is important to note that this is the expected average sensitivity, and the actual sensitivity will vary from pixel-to-pixel

The actual sensitivity was measured by calculating the peak signal-to-noise ratio of the signal from a mirror positioned near the zero pathlength position (DC), with sufficient attenuation to prevent saturation of the camera. Attenuation was achieved both by placing a calibrated ND filter in the sample arm and reducing the camera integration time. The peak signal-to-noise ratio was then determined by taking the ratio

of the largest A-scan peak to the standard deviation of the noise floor with the sample arm blocked.

Using this technique, we measured a signal-to-noise ratio of 61dB with a total of 34dB of attenuation, yielding a sensitivity of 95dB. It is important to note that the sensitivity varied across the field-of-view due to the Gaussian power distribution of the source. The sensitivity measured was the peak value, whereas the calculated value was the average expected sensitivity. Thus the true discrepancy between the theoretical and measured sensitivities would be even larger than 6dB. However, the predicted sensitivity assumed shot-noise limited detection. The large discrepancy between the predicted and measured sensitivities suggests that noise contributions from digitization round-off, receiver noise and/or relative intensity noise (RIN) were appreciable.

Axial resolution was measured by acquiring volumes of an attenuated mirror placed at the various depths through the axial field-of-view. The central 100 x 100 A-scans of each volume were averaged, and the axial resolution was then measured as the FWHM of the averaged mirror peak.

An estimate of the sensitivity fall-off can also be measured from this experiment. It should be noted that due to the extremely narrow linewidth of the laser, the observed sensitivity fall-off is not due to the linewidth of the laser, but rather due to the bandwidth over which the linewidth tunes during the integration of each frame. Thus, by reducing the camera's integration time, the sensitivity fall-off could be extended.

However, this would either require a camera capable of a faster framerate, or would come at the cost of system sensitivity. For these measurements, the camera integration time was set to maximum, which was approximately the reciprocal of the framerate (3600 Hz). Results of the axial resolution and sensitivity measurement are shown in Figure 2.12. The mirror signal at each depth is plotted, and the measured FWHM of each peak is shown above. Figure 2.12. The mirror signal at each depth is plotted, and the measured FWHM of each peak is shown above. peak is shown above.

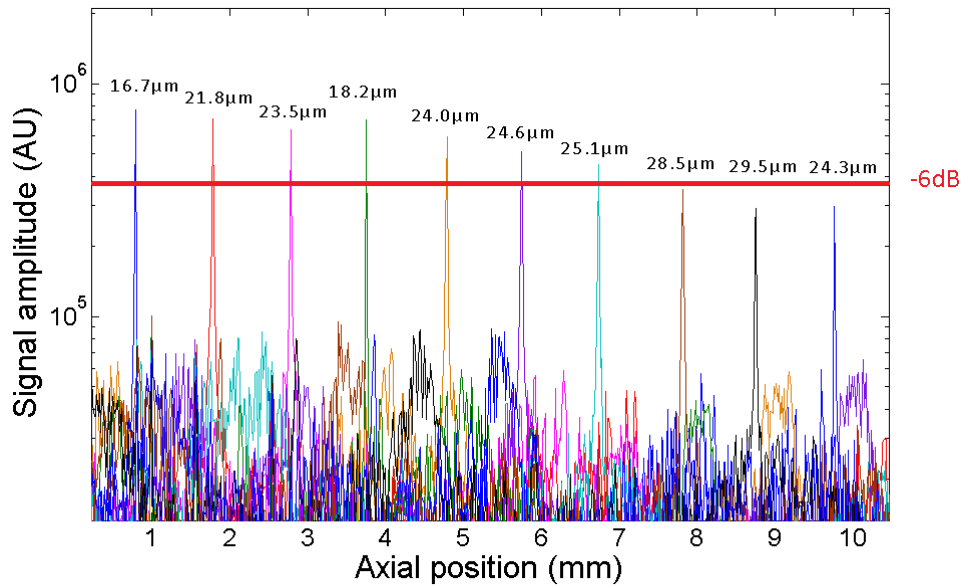


**Figure 2.12: Sensitivity fall-off and axial resolution measurements**

The axial resolution was better than 30 $\mu$ m throughout the 10mm extended axial imaging range, with the measured axial resolution varying between approximately 16 and 29 microns. The degradation in axial resolution may be explained by the presence

of clocking errors due to the relatively short etalon length of the k-clock as compared to the imaging range (7mm), as well as the reduced SNR with increased imaging depth.

Sensitivity fall-off is often characterized by the -6dB imaging range, which for this system was approximately 8mm (red line in Figure 2.12). As discussed above, this sensitivity fall-off is due to the spectral sampling of the laser, and not the linewidth of the laser itself.

#### **2.3.4. Imaging Results**

The FF-SSOCT system was used to image the topography of a .45 caliber slug scavenged from a shooting range. As the slug itself was opaque, it was mounted on a rotation stage (Thorlabs, CR1-Z7) to facilitate imaging from multiple angles. Due to the large field of view of this system, the entire slug was imaged in only four rotations, rotating the sample 90 degrees between acquisitions. Volumes of 512 x 512 lateral samples and 1872 axial samples were collected over 1.872s each, corresponding to an A-scan rate of 140kHz. Thus, the total imaging time was approximately 7.5 seconds. The entire acquisition process took approximately 20 minutes, limited by the rate at which data could be read from the camera.

Image segmentation was performed in post-processing to locate the surface of the bullet, using a modified graph-cut segmentation algorithm originally developing for segmenting corneal OCT images [181, 194]. A representative B-scan image of the bullet cross-section and the corresponding segmentation data are illustrated in Figure 2.13.

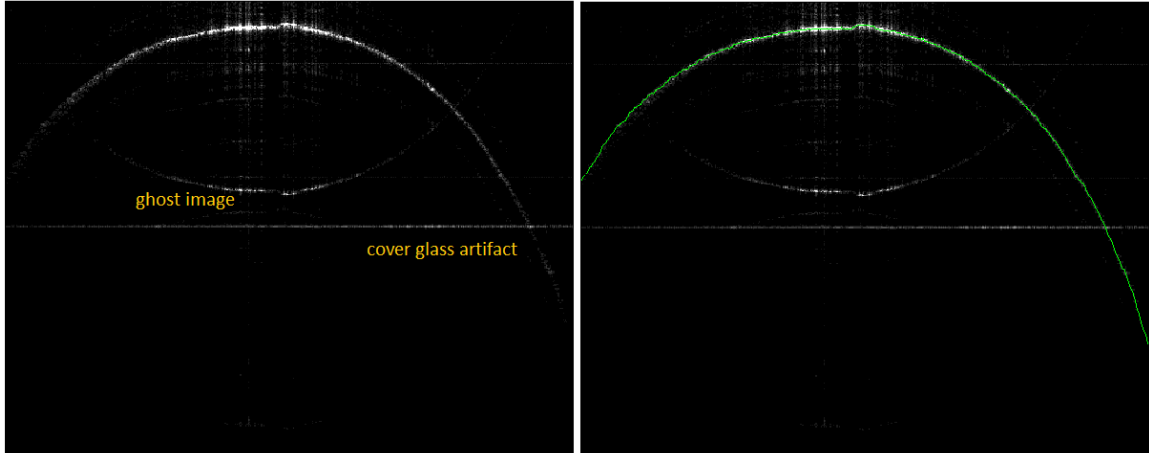


**Figure 2.13 Left: Representative B-scan image of the bullet surface extracted from 3D FF-SSOCT dataset (linear scale). Right: Corresponding bullet surface segmented.**

Due to the bright boundary at the bullet surface, these images had a sufficiently narrow dynamic range to permit display on a linear scale (as opposed to a logarithmic scale, which is commonly used for viewing OCT images). Two types of artifacts are identified in the left image. These artifacts were seen in all of the FF-SSOCT images, and were due to the presence of a  $\sim 2$  mm thick cover glass over the image sensor. Although the cover glass was AR coated, the coating was for visible wavelengths and did not perform well at the NIR wavelengths used in this system. As a result, a portion of the light reflecting off of the sensor would reflect back off of the glass/air interface. While these cover glasses are typically not a concern for time domain FFOCT implementations (where the source coherence length is only a few microns), the instantaneous source coherence

length in FF-SSOCT is sufficiently long for interference fringes to be observed from these reflections off of the cover glass. As a result, the cover glass produced a sharp horizontal line in the image as well as other weaker horizontal streaks, and also resulted in the appearance of ghost images from the cross-correlation of the multiply-reflected reference fields and the sample light. Fortunately, the segmentation algorithm was sufficiently robust to ignore these ghost images, but the presence of a cover glass on camera sensors may be a concern for future applications of FF-SSOCT.

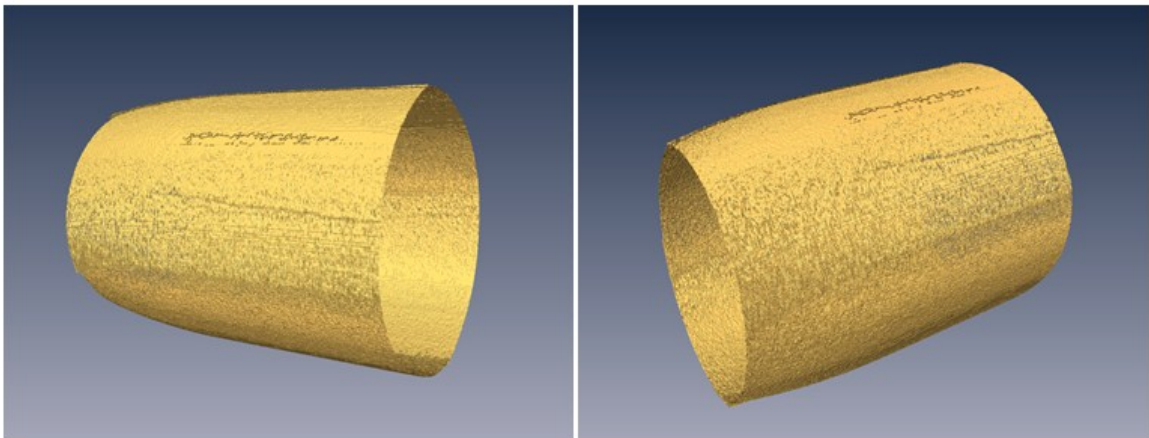


**Figure 2.14: Three-dimensional reconstructed surface renderings of a 0.45 caliber slug acquired with from four rotations**

Surfaces extracted from the segmentation algorithm were used to create surface renderings of the bullet sample. The four surfaces were combined using *a priori* knowledge of their relative rotations, and then manually adjusted. Renderings of the final reconstructed surface are shown in Figure 2.14. Rifling marks on the surface on the

bullet are clearly discernible in both renderings. Upon very close inspection, slight discontinuities can be discerned at the borders between each of the 4 volumes. These were likely due to very slight field curvature in the imaging plane. Though not performed here, techniques for correcting field curvature in OCT images have been used for corneal biometry applications [168].

### **2.3.5. Dispersion Tolerance**

The FF-SSOCT system design described here is inherently much more tolerant to dispersion than standard OCT systems. This tolerance arises from three factors. First, the entire reference and sample arm are free space and dispersion matched. The only components of the system that employ fiber, which often gives rise to dispersion in OCT systems, are common to both paths and thus do not degrade the image resolution. Second, this system uses a narrower bandwidth than commercial OCT systems. The optical pathlength difference over the optical bandwidth is therefore reduced, further reducing dispersion artifacts. Finally, the relatively coarse axial resolution of the system diminishes the significance of the dispersion that remains. For example, for this system, a sample located beneath 10mm of water would give rise to only approximately  $8\mu\text{m}$  of roundtrip lateral resolution broadening. This would broaden the system resolution to between 24 and 34 microns, an increase of only 33%. However, for an ultrahigh

resolution OCT system with a resolution of 2 microns, a similar amount of PSF broadening would correspond to an 800% increase.

To quantitatively demonstrate the dispersion tolerance of this system, we imaged a mirror both in air and behind a 25mm thick water cell at imaging depths of 4mm and 6mm. By evaluating the broadening of the coherence function (axial resolution) in each case, we can track the effect of dispersion on image quality. The results of these measurements are shown in Figure 2.15.

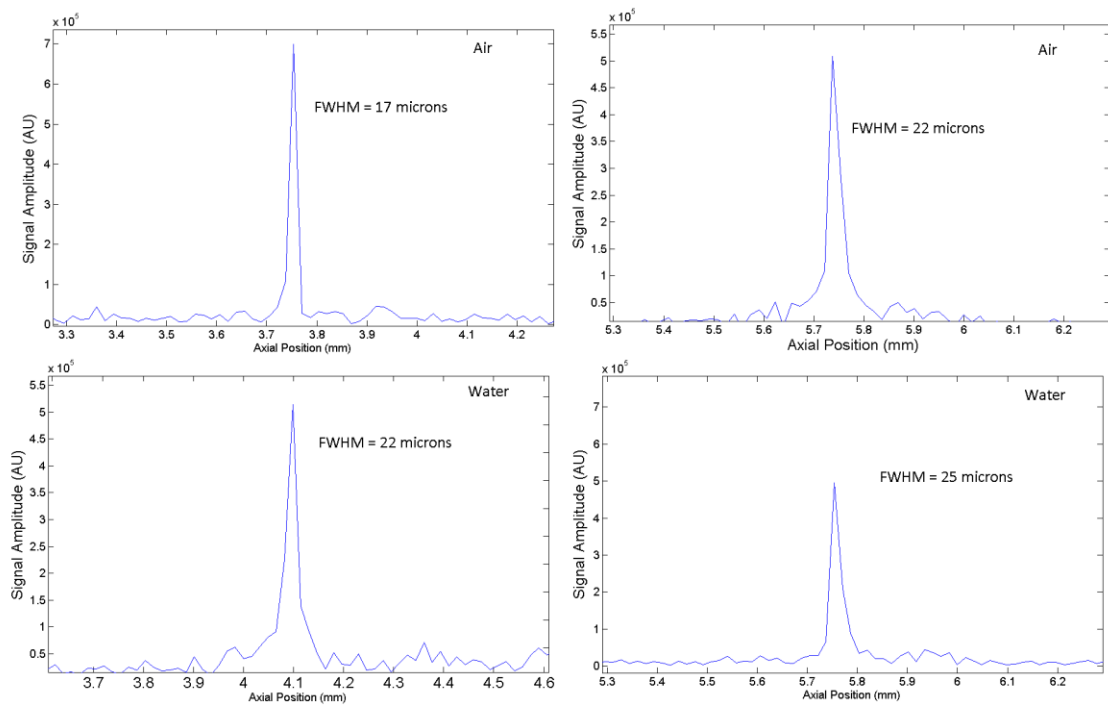


**Figure 2.15: Axial resolution measured at ~4mm and ~6mm imaging depth in air and behind 25mm of water**

In both cases, the FWHM of the observed coherence function degraded by less than 5 microns, without the use of numerical dispersion compensation.

Correction for additional dispersion can be achieved through software dispersion compensation. Even very large amounts of dispersion can be corrected in software if sufficient spectral samples are taken, or if, as described earlier, the laser sweep is deliberately chirped to facilitate denser spectral sampling at shorter wavelengths. However, for samples with only small to moderate amounts of dispersion, such as a bullet located within a few millimeters of water or ice, the dispersion tolerance inherent to this system design may be sufficient.

### **2.3.6. Summary**

SSOCT system designs offer several advantages over conventional, commercially available SDOCT systems for extended-depth imaging applications, primarily because of the decreased axial sensitivity fall-off effect afforded by lasers with narrow instantaneous linewidths. By implementing SSOCT systems in a full-field configuration employing high frame rate CMOS cameras, the drawback of long imaging times due to the relatively low sweep rate of some very long coherence length lasers is mitigated. In this work, we provided a proof of principle demonstration of this concept by constructing a novel FF-SSOCT system capable of better than 30  $\mu\text{m}$  axial resolution and 50 micron lateral resolution over a 1cm x 1cm x 1cm isotropic field of view, achieving

dispersion-tolerant, 0.5 GVoxel volumetric imaging in under 2 seconds. While this technique may be limited to imaging of non-biological samples due to its high spatial coherence, it is well suited for surface topography applications of large objects that exceed the field-of-view of traditional OCT systems.

### 3. Coherence Revival in Swept Source OCT

In this chapter, we introduce coherence revival SSOCT, a simple and low-cost implementation of heterodyne SSOCT (introduced in section 1.3.3) that is compatible with certain swept source lasers. This technique effectively resolves the complex conjugate ambiguity, and thus can double the usable imaging range of SSOCT systems.

Although heterodyne SSOCT techniques have been used since 2004 [90, 91, 93], a complete mathematical derivation describing how this technique actually resolves the complex conjugate ambiguity has not been published. This is perhaps due to the fact that such a description requires an understanding of the role of phase and group delay in the SSOCT signal, which has also not been published. Hee [195] has previously derived the time-domain OCT signal in the presence of dispersion using a Taylor expansion of the propagation constant, and Izatt and Choma [89] have previously derived the FDOCT signal in non-dispersive media, which is valid for both SDOCT and SSOCT. However, to our knowledge, no description of the FDOCT or SSOCT signal in dispersive media has been developed.

Thus, we begin this chapter by following Hee's derivation of the TDOCT signal in dispersive media for SSOCT, but adapting this treatment for SSOCT. We then extend this treatment to describe how heterodyne SSOCT resolves the complex conjugate. Next, we describe the phenomenon of coherence revival and demonstrate its use for extended depth imaging of the anterior segment. Finally, we investigate the use of

dispersive optical delay lines (DODL's) as a means of creating a large group delay and mitigating axial PSF degradation in these systems.

Derek Nankivil aided in the system construction and data acquisition for the coherence revival experiments. Professor Andrew Rollins contributed substantially to the development of the expressions for group and phase delay in RSOD's with swept source lasers.

### **3.1. Theoretical Development of SSOCT**

#### **3.1.1. Derivation of SSOCT Signal in a Non-Dispersive Medium**

We begin by following Hee's derivation of the time-domain OCT signal in a non-dispersive medium<sup>1</sup> [195]. Consider a Michelson interferometer illuminated with coherent, monochromatic light (Figure 1.1). Light returning from the sample and reference arms produces, at the detector, two monochromatic electric field components:

$$E_R = A_R e^{(-j(2\beta_R l_R - \omega t))} \text{ and } E_S = A_S e^{(-j(2\beta_S l_S - \omega t))} \quad (3.1.1)$$

---

<sup>1</sup> The entire development of the TDOCT signal, up to equation (3.1.13), is reproduced from [195]. It is included here for completeness. Our original treatment of the problem (i.e. the derivation of the SSOCT signal) begins with equation (3.1.14).

where  $E_R$  and  $E_S$  are the electric fields returning from the reference and sample, respectively,  $A_R$  and  $A_S$  are the field amplitudes,  $l_R$  and  $l_S$  are the reference and sample reflector positions, and  $\beta_R$  and  $\beta_S$  are the propagation constants in each arm. If the detector used is a square-law detector, the time-averaged photocurrent at the detector will be given by:

$$I = \left\langle \frac{\eta e}{h\nu} \left( \frac{|E_R + E_S|^2}{2\eta_0} \right) \right\rangle \quad (3.1.2)$$

where  $\eta$  is the detector responsivity,  $e$  is the electronic charge,  $h\nu$  is the photon energy, and  $\eta_0$  is the intrinsic impedance of free space. Combining these equations yields:

$$I = \frac{\eta e}{2h\nu\eta_0} \left( |A_R|^2 + |A_S|^2 + 2A_R A_S \cos\left(2\pi \frac{\Delta l}{\lambda/2}\right) \right) \quad (3.1.3)$$

where we have assumed the sample and reference are in free space, and  $\Delta l$  is the difference between the sample and reference reflector pathlengths. We now consider a broadband source illuminating the same Michelson interferometer. The sample and reference fields then become functions of optical frequency:

$$E_R(\omega) = A_R(\omega) \exp\{-j(2\beta_R(\omega)l_R - \omega t)\} \quad (3.1.4)$$

$$E_S(\omega) = A_S(\omega) \exp\{-j(2\beta_S(\omega)l_S - \omega t)\} \quad (3.1.5)$$

The interference signal at the detector is proportional to the sum of the interference due to each monochromatic component of the broadband light, and is thus given by:

$$I \propto \text{real} \left\{ \int_{-\infty}^{\infty} E_S(\omega) E_R(\omega)^* \frac{d\omega}{2\pi} \right\} = \text{real} \left\{ \int_{-\infty}^{\infty} S(\omega) \exp[-j\Delta\phi(\omega)] \frac{d\omega}{2\pi} \right\} \quad (3.1.6)$$

where we have used the definitions:

$$S(\omega) = A_S(\omega) A_R(\omega)^* \quad (3.1.7)$$

$$\Delta\phi(\omega) = 2\beta_S(\omega)l_S - 2\beta_R(\omega)l_R \quad (3.1.8)$$

$S(\omega)$  is (in general) equal to the power spectral density of source. The phase term  $\Delta\phi(\omega)$  represents the phase mismatch at the detector for each frequency component. Assuming the propagation constants are the same in each arm,  $\beta$  can be expanded using a first order Taylor series expansion:

$$\beta(\omega) = \beta(\omega_0) + \beta'(\omega_0)(\omega - \omega_0) \quad (3.1.9)$$

Thus, the phase mismatch term becomes:

$$\Delta\phi(\omega) = \beta(\omega_0)(2\Delta l) + \beta'(\omega_0)(\omega - \omega_0)(2\Delta l) \quad (3.1.10)$$

Combining equations (3.1.6) and (3.1.10) then yields the detector photocurrent in a TDOCT system:

$$I \propto \text{real} \left\{ \exp[-j\omega_0\Delta\tau_p] \int_{-\infty}^{\infty} S(\omega - \omega_0) \exp[-j(\omega - \omega_0)\Delta\tau_g] \frac{d(\omega - \omega_0)}{2\pi} \right\} \quad (3.1.11)$$

where  $\Delta\tau_p$  and  $\Delta\tau_g$  are the phase and group delay differences between the sample and reference, given by:

$$\Delta\tau_p = \frac{\beta(\omega_0)}{\omega_0} 2\Delta l \quad (3.1.12)$$

$$\Delta\tau_g = \beta'(\omega_0) 2\Delta l \quad (3.1.13)$$

For SSOCT, we can consider each spectral channel as a separate, single-depth TDOCT measurement. Each of these channels is centered at some instantaneous central frequency  $\omega_c$  and has a finite linewidth described by a linewidth function  $\Delta\nu(\omega - \omega_c)$ .

Thus, we can modify the equation (3.1.11) in the following ways to make it appropriate for a description of SSOCT:

1. All of the  $\omega_0$  terms become  $\omega_c$ , as we are treating each spectral channel as a separate OCT measurement centered at  $\omega_c$  with a finite bandwidth described by the linewidth  $\Delta\nu(\omega)$ .
2. The source term inside the integral becomes  $S(\omega-\omega_0)\Delta\nu(\omega-\omega_c)$ , as the “source” for each wavelength channel is the linewidth function centered at  $\omega_c$  multiplied by the source function evaluated at  $\omega_c$ . The  $S(\omega-\omega_0)$  term accounts for the shape of the swept source laser’s tuning bandwidth, and will ultimately determine the axial resolution. We assume that each spectral channel is sufficiently narrow such that  $S(\omega-\omega_0)$  remains constant across the channel.
3. The phase and group delays are now a function of  $\omega_c$ , and must be evaluated for each spectral channel.

Making these changes, the SSOCT signal in a non-dispersive medium becomes:

$$I(\omega_c) \propto \text{real} \left\{ S(\omega_c - \omega_0) \exp[-j\omega_c \Delta\tau_p(\omega_c)] \right. \\ \left. \times \int_{-\infty}^{\infty} \Delta\nu(\omega - \omega_c) \exp[-j(\omega - \omega_c) \Delta\tau_g(\omega_c)] \frac{d(\omega - \omega_c)}{2\pi} \right\} \quad (3.1.14)$$

For simplicity, let us assume we have a Gaussian linewidth function:

$$\Delta\nu(\omega - \omega_c) = \left( \frac{2\pi}{\sigma_w^2} \right)^{\frac{1}{2}} \exp \left[ -\frac{(\omega - \omega_c)^2}{2\sigma_w^2} \right] \quad (3.1.15)$$

This Gaussian linewidth profile has been normalized to integrate to unity, and has a standard deviation of  $2\sigma_w$ . Substituting this into our expression for the SSOCT signal and solving the definite integral yields:

$$I(\omega_c) \propto \text{real} \left\{ S(\omega_c - \omega_0) \exp[-j\omega_c \Delta\tau_p(\omega_c)] \exp \left[ -\frac{\Delta\tau_g^2(\omega_c)}{2\sigma_t^2} \right] \right\} \quad (3.1.16)$$

Note that the Gaussian in this expression has a standard deviation of  $2\sigma_t$ , which is related to the standard deviation of the linewidth profile ( $2\sigma_w$ ) by [195]:

$$2\sigma_t^2 = \frac{2}{\sigma_w^2} \quad (3.1.17)$$

It is important to note that, contrary to Hee's treatment where  $\sigma_t$  was the characteristic width of the axial PSF, in this case,  $\sigma_t$  is the characteristic width of the fall-off function. The expression above describes the SSOCT signal as a function of the instantaneous frequency. As we are considering a non-dispersive material, the phase and group delays are actually equal and independent of frequency. Accounting for this, we have:

$$I(\omega_c) \propto \text{real} \left\{ S(\omega_c - \omega_0) \exp[-j\omega_c \Delta\tau] \exp\left[-\frac{\Delta\tau^2}{2\sigma_t^2}\right] \right\} \quad (3.1.18)$$

The desired A-scan is then achieved by Fourier transformation over  $\omega_c - \omega_0$ :

$$i(t) \propto \left[ s(t) * \frac{1}{2} (\delta(t - \Delta\tau) + \delta(t + \Delta\tau)) \right] \times \exp\left[-\frac{\Delta\tau^2}{2\sigma_t^2}\right] \cos(-\omega_0 \Delta\tau) \quad (3.1.19)$$

Here,  $s(t)$  is the Fourier transform of the source spectrum and represents the axial resolution. This axial resolution term is convolved with a pair of delta functions denoting the positive and negative positions of the sample reflector. The third term remains unchanged from before the Fourier transform as it does not depend on time or

frequency. This term represents the signal fall-off due to a loss of fringe visibility, and is only a function of the delay  $\Delta\tau$ . Finally, the cosine term represents a rapid modulation in depth that is analogous to the carrier frequency in TDOCT. This term is introduced because the Fourier transform is evaluated about  $\omega_0$  and not DC, and is included only for completeness. In practice, this modulation is not detected and has no significance.

### 3.1.2. Derivation of SSOCCT Signal in a Dispersive Medium

We now consider an SSOCCT signal in a medium with group velocity dispersion (GVD). In this analysis, we neglect higher order dispersion and assume the dispersion is constant throughout the sample. That is, we neglect sample dependent dispersion and only consider dispersion introduced by the interferometer, such as what would be created by a fiber length mismatch between the reference and sample arm. The Taylor expansion of the propagation constant from equation (3.1.9) then becomes:

$$\beta(\omega) = \beta(\omega_0) + \beta'(\omega_0)(\omega - \omega_0) + \frac{1}{2}\beta''(\omega_0)(\omega - \omega_0)^2 \quad (3.1.20)$$

As we are neglecting higher order dispersion, the third derivative of the phase propagation constant is presumed to be zero, and thus the second derivative  $\beta''$  is constant. The phase mismatch term then becomes:

$$\Delta\phi(\omega) = \beta(\omega_0)(2\Delta l) + \beta'(\omega_0)(\omega - \omega_0)(2\Delta l) + \frac{1}{2} \Delta\beta''(\omega_0)(\omega - \omega_0)^2(2L) \quad (3.1.21)$$

where  $\Delta\beta''$  is the GVD mismatch between the sample and reference paths over the mismatch length of  $2L$ , i.e.:

$$\Delta\beta''(\omega_0) = \beta_S''(\omega_0) - \beta_R''(\omega_0) \quad (3.1.22)$$

Inserting the new phase term from (3.1.21) into equation (3.1.6) yields the TDOCT signal in a dispersive medium:

$$I \propto \text{real} \left\{ \exp[-j\omega_0\Delta\tau_p] \int_{-\infty}^{\infty} S(\omega - \omega_0) \exp[-j(\omega - \omega_0)\Delta\tau_g] \right. \quad (3.1.23) \\ \left. \times \exp\left[-j\frac{1}{2}\Delta\beta''(\omega_0)(\omega - \omega_0)^2 2L\right] \frac{d(\omega - \omega_0)}{2\pi} \right\}$$

Casting equation (3.1.23) in its SSOCT form (as above) yields:

$$I(\omega_c) \propto \text{real} \left\{ S(\omega_c - \omega_0) \exp[-j\omega_c\Delta\tau_p(\omega_c)] \right. \quad (3.1.24) \\ \times \int_{-\infty}^{\infty} \Delta\nu(\omega - \omega_c) \exp[-j(\omega - \omega_c)\Delta\tau_g(\omega_c)] \\ \left. \times \exp\left[-j\frac{1}{2}\Delta\beta''(\omega_c)(\omega - \omega_c)^2 2L\right] \frac{d(\omega - \omega_c)}{2\pi} \right\}$$

Using the same Gaussian linewidth function as before, the definite integral can be evaluated:

$$I(\omega_c) \propto \text{real} \left\{ S(\omega_c - \omega_0) \exp[-j\omega_c \Delta\tau_p(\omega_c)] \left( \frac{\sigma_t}{\Gamma} \right) \exp \left[ -\frac{\Delta\tau_g^2(\omega_c)}{2\Gamma^2} \right] \right\} \quad (3.1.25)$$

Here, again following Hee [195], we have defined  $\Gamma$  as the characteristic width of the fall-off function in the presence of dispersion, a complex parameter given by:

$$\Gamma^2 = \sigma_t^2 + j\Delta\beta''(\omega_c)2L = \sigma_t^2 + j\tau_{\text{crit}}^2 \quad (3.1.26)$$

This expression makes use of a dispersion parameter,  $\tau_{\text{crit}}$ , given by:

$$\tau_{\text{crit}} = \left( \Delta\beta''(\omega_c)2L \right)^{1/2} \quad (3.1.27)$$

So far, this treatment has not yet addressed the key difference between SSOCT and TDOCT, namely that because SSOCT can be thought of as a train of single-point TDOCT measurements centered at different optical frequencies, the phase and group delay

terms can themselves be frequency dependent. In order to account for this, the frequency dependence of the phase and group delay terms must be incorporated.

We begin by replacing the phase and group delays by their definitions with respect to the propagation constant:

$$I(\omega_c) \propto \text{real} \left\{ \frac{\sigma_t}{\Gamma} S(\omega_c - \omega_0) \exp \left[ -j\omega_c \frac{\beta(\omega_c)}{\omega_c} 2\Delta l \right] \exp \left[ -\frac{(\beta'(\omega_c) 2\Delta l)^2}{2\Gamma^2} \right] \right\} \quad (3.1.28)$$

We now take Taylor expansions of  $\beta$  and  $\beta'$  about the center frequency of the sweep,  $\omega_0$ , modified to account for the fact that the GVD only exists over a length  $2L$ :

$$\beta(\omega_c) = \beta(\omega_0) + \beta'(\omega_0)(\omega_c - \omega_0) + \frac{1}{2} \Delta\beta''(\omega_0)(\omega_c - \omega_0)^2 \frac{2L}{2\Delta l} \quad (3.1.29)$$

$$\beta'(\omega_c) = \beta'(\omega_0) + \Delta\beta''(\omega_0)(\omega_c - \omega_0) \frac{2L}{2\Delta l} \quad (3.1.30)$$

As before, because we are neglecting higher order dispersion,  $\beta''$  is a constant. Thus the carrier component of the SSOCT signal becomes:

$$\begin{aligned} & \exp[-j\beta(\omega_c)2\Delta l] \tag{3.1.31} \\ & = \exp\left[-j2\Delta l\left(\beta(\omega_0) + \beta'(\omega_0)(\omega_c - \omega_0) + \frac{1}{2}\Delta\beta''(\omega_0)(\omega_c - \omega_0)^2 \frac{2L}{2\Delta l}\right)\right] \end{aligned}$$

We now define the phase and group delays at the center sweep wavelength:

$$\Delta\tau_{p0} = \frac{\beta(\omega_0)}{\omega_0} 2\Delta l \tag{3.1.32}$$

$$\Delta\tau_{g0} = \beta'(\omega_0) 2\Delta l \tag{3.1.33}$$

Substituting with the definitions of phase and group delay (defined at the center frequency of the sweep) yields:

$$\begin{aligned} & \exp[-j\beta(\omega_c)2\Delta l] \tag{3.1.34} \\ & = \exp\left[-j\left(\omega_0\Delta\tau_{p0} + \Delta\tau_{g0}(\omega_c - \omega_0) + \frac{1}{2}\Delta\beta''(\omega_0)(\omega_c - \omega_0)^2 2L\right)\right] \end{aligned}$$

Because we are neglecting higher order dispersion,  $\beta''$  is a constant, and thus the  $\tau_{\text{crit}}$  defined above applies here as well:

$$\tau_{\text{crit}} = \left(\Delta\beta''(\omega_c)2L\right)^{1/2} = \left(\Delta\beta''(\omega_0)2L\right)^{1/2} \tag{3.1.35}$$

$$\begin{aligned} & \exp[-j\beta(\omega_c)2\Delta l] \\ & = \exp\left[-j\left(\omega_0\Delta\tau_{p0} + \Delta\tau_{g0}(\omega_c - \omega_0) + \frac{1}{2}\tau_{\text{crit}}^2(\omega_c - \omega_0)^2\right)\right] \end{aligned} \quad (3.1.36)$$

Similarly, the Gaussian in the SSOCT signal becomes:

$$\exp\left[-\frac{(\beta'(\omega_c)2\Delta l)^2}{2\Gamma^2}\right] = \exp\left[-\frac{(\beta'(\omega_0)2\Delta l + \Delta\beta''(\omega_0)(\omega_c - \omega_0)2L)^2}{2\Gamma^2}\right] \quad (3.1.37)$$

Substituting with the definitions of group delay, the dispersion parameter and  $\Gamma$  yields:

$$\exp\left[-\frac{(\beta'(\omega_c)2\Delta l)^2}{2\Gamma^2}\right] = \exp\left[-\frac{(\Delta\tau_{g0} + \tau_{\text{crit}}^2(\omega_c - \omega_0))^2}{2(\sigma_t^2 + j\tau_{\text{crit}}^2)}\right] \quad (3.1.38)$$

Combining all of these terms yields a complete expression for the SSOCT signal in dispersive media:

$$\begin{aligned}
I(\omega_c) \propto \text{real} \left\{ S(\omega_c - \omega_0) \left( \frac{\sigma_t}{\Gamma} \right) \right. & \quad (3.1.39) \\
& \times \exp \left[ -j \left( \omega_0 \Delta \tau_{p0} + \Delta \tau_{g0} (\omega_c - \omega_0) + \frac{1}{2} \tau_{\text{crit}}^2 (\omega_c - \omega_0)^2 \right) \right] \\
& \left. \times \exp \left[ -\frac{(\Delta \tau_{g0} + \tau_{\text{crit}}^2 (\omega_c - \omega_0))^2}{2(\sigma_t^2 + j \tau_{\text{crit}}^2)} \right] \right\}
\end{aligned}$$

While this expression may seem initially daunting, several simplifications can be made.

The final exponential in equation (3.1.39) ultimately defines the falloff profile of the SSOCT signal. Focusing on and re-expressing the argument of this exponential:

$$\begin{aligned}
& -\frac{(\Delta \tau_{g0} + \tau_{\text{crit}}^2 (\omega_c - \omega_0))^2}{2(\sigma_t^2 + j \tau_{\text{crit}}^2)} & \quad (3.1.40) \\
& = -\frac{(\Delta \tau_{g0} + \tau_{\text{crit}}^2 (\omega_c - \omega_0))^2}{2} \left( \frac{\sigma_t^2}{\sigma_t^4 - \tau_{\text{crit}}^4} - j \frac{\tau_{\text{crit}}^2}{\sigma_t^4 - \tau_{\text{crit}}^4} \right)
\end{aligned}$$

Recalling that  $\sigma_t$  is the characteristic length of the sensitivity fall-off (typically several millimeters), and  $\tau_{\text{crit}}$  is the characteristic broadening of the axial PSF (which would be tens of microns in an extreme case), for all practical SSOCT systems,  $\sigma_t \gg \tau_{\text{crit}}$ , and therefore we can make the following simplification:

$$\begin{aligned}
& -\frac{(\Delta\tau_{g0} + \tau_{\text{crit}}^2 (\omega_c - \omega_0))^2}{2} \left( \frac{\sigma_t^2}{\sigma_t^4 - \tau_{\text{critical}}^4} - j \frac{\tau_{\text{critical}}^2}{\sigma_t^4 - \tau_{\text{critical}}^4} \right) \\
& \approx -\frac{(\Delta\tau_{g0} + \tau_{\text{crit}}^2 (\omega_c - \omega_0))^2}{2\sigma_t^2}
\end{aligned} \tag{3.1.41}$$

Similarly, in practical systems, this characteristic fall-off length,  $\sigma_t$ , will be much larger than any variance in the group delay created by the presence of GVD. Thus, we can assume the group delay is constant for the purposes of determining falloff.

$$-\frac{(\Delta\tau_{g0} + \tau_{\text{crit}}^2 (\omega_c - \omega_0))^2}{2\sigma_t^2} \approx \frac{-\Delta\tau_{g0}^2}{2\sigma_t^2} \tag{3.1.42}$$

Finally, this same observation allows for one additional simplification:

$$\text{real} \left\{ \frac{\sigma_t}{\Gamma} \right\} \approx 1 \tag{3.1.43}$$

Applying these simplifications, the expression for the SSOC signal becomes:

$$I(\omega_c) \propto \text{real} \left\{ S(\omega_c - \omega_0) \exp \left[ -\frac{\Delta \tau_{g0}^2}{2\sigma_t^2} \right] \right. \\ \left. \times \exp \left[ -j \left( \omega_0 \Delta \tau_{p0} + \Delta \tau_{g0} (\omega_c - \omega_0) + \frac{1}{2} \tau_{\text{crit}}^2 (\omega_c - \omega_0)^2 \right) \right] \right\} \quad (3.1.44)$$

Taking the Fourier transform over  $\omega_c - \omega_0$  yields:

$$i(t) = \exp \left[ -\frac{\Delta \tau_{g0}^2}{2\sigma_t^2} \right] \cos(-\omega_0 \Delta \tau_p) \\ \times \left[ s(t) * \frac{1}{2} \left( \delta(t - \Delta \tau_{g0}) + \delta(t + \Delta \tau_{g0}) \right) * \text{GVD}(t) \right] \quad (3.1.45)$$

Here, the first term represents the falloff and is a function of group delay. As before, the cosine term represents a rapid modulation that is introduced because the Fourier transform is evaluated about  $\omega_0$  and not DC and has no practical significance.

The  $s(t)$  term is the source function Fourier transform and represents the axial resolution.

The two delta functions are the reflector positions under Hermitian symmetry.  $\text{GVD}(t)$  is the Fourier transform of the quadratic phase function, and broadens the axial PSF in the presence of group velocity dispersion. Assuming the source function Fourier

transform  $s(t)$  is Gaussian with a standard deviation of  $2\sigma_r$ , the broadened PSF standard deviation after convolution with  $\text{GVD}(t)$  would be given by [195]:

$$2\sigma_r = 2\sigma_r \sqrt{1 + \left(\frac{\tau_{critical}}{\sigma_r}\right)^4} \quad (3.1.46)$$

Thus, as expected, the expression for the SSOCT signal in a dispersive medium is nearly identical to that of a non-dispersive medium, except that the axial PSF is degraded due to the GVD in the system.

### 3.1.3. Derivation of Heterodyne SSOCT Signal

Heterodyne SSOCT techniques work by adding a phase modulator (typically an acousto-optic modulator, or AOM) to both the reference arm and sample arm, or just the reference arm. In the former case, the two phase modulators are operated at different frequencies, and only the net modulation is of significance.

In order for heterodyne SSOCT to work, the AOM's must shift the interferometric fringe frequencies without shifting the fall-off profile. To understand how this is possible, we begin with a modified form of the SSOCT signal expression derived above:

$$I(\omega_c) \propto \text{real} \left\{ S(\omega_c - \omega_0) \exp[-j\omega_c \Delta\tau_p(\omega_c)] \right. \\ \left. \times \int_{-\infty}^{\infty} \Delta\nu(\omega - \omega_c) \exp[-j(\omega - \omega_c) \Delta\tau_g(\omega_c) - j\phi_{AOM}(t)] \frac{d(\omega - \omega_c)}{2\pi} \right\} \quad (3.1.47)$$

Here we have added a new term,  $\phi_{\text{AOM}}(t)$ , which accounts for the phase shift created by the AOM's. This term is expressed as a function of  $t$  to indicate that the phase shift varies in time. However, it is critical to note that the instantaneous phase shift produced by the AOM's at any given time is achromatic. Because the laser's output frequency is swept in time, both  $\omega_c$  and  $\phi_{\text{AOM}}$  vary in time, and we will eventually need to derive an expression for  $\phi_{\text{AOM}}$  that is a function of  $\omega_c$ . Nevertheless,  $\phi_{\text{AOM}}(t)$  is not a function of  $\omega$  and thus comes out of the integral here:

$$I(\omega_c) \propto \text{real} \left\{ S(\omega_c - \omega_0) \exp \left[ -j\omega_c \Delta\tau_p(\omega_c) - j\phi_{\text{AOM}}(t) \right] \right. \\ \left. \times \int_{-\infty}^{\infty} \Delta\nu(\omega - \omega_c) \exp \left[ -j(\omega - \omega_c) \Delta\tau_g(\omega_c) \right] \frac{d(\omega - \omega_c)}{2\pi} \right\} \quad (3.1.48)$$

The rest of the derivation follows as before, yielding:

$$I(\omega_c) \propto \text{real} \left\{ S(\omega_c - \omega_0) \exp \left[ -\frac{\Delta\tau_{g0}^2}{2\sigma_t^2} \right] \exp \left( -j\omega_0 \Delta\tau_{p0} - j\phi_{\text{AOM}}(t) \right) \right. \\ \left. \times \exp \left( -j\Delta\tau_{g0}(\omega_c - \omega_0) \right) \exp \left( -j\frac{\tau_{\text{crit}}^2}{2}(\omega_c - \omega_0)^2 \right) \right\} \quad (3.1.49)$$

For simplicity, we assume that the frequency sweep of the SSOCT laser is linear in time, and that the AOM produces a pure cosine modulation in time. We now express  $\phi_{\text{AOM}}(t)$  as a function of  $\omega_c$ :

$$\varphi_{AOM}(\omega_c) = \exp[-j(\omega_c - \omega_0)\Delta\tau_{AOM}] \quad (3.1.50)$$

Here,  $\Delta\tau_{AOM}$  relates the laser sweep speed and the AOM modulation frequency. After substituting this expression, Fourier transformation of the signal yields:

$$i(t) = \exp\left[-\frac{\Delta\tau_{g0}^2}{2\sigma_i^2}\right] \cos(-\omega_0\Delta\tau_p) \quad (3.1.51)$$

$$\times \left[ s(t) * \frac{1}{2} \left( \delta(t - \Delta\tau_{g0} - \Delta\tau_{AOM}) + \delta(t + \Delta\tau_{g0} + \Delta\tau_{AOM}) \right) * \text{GVD}(t) \right]$$

Here, the positive displacements have been shifted by  $+\Delta\tau_{AOM}$  and the negative displacements have been shifted by  $-\Delta\tau_{AOM}$ , yielding a separation between the conjugates of  $2\Delta\tau_{AOM}$ . Note that the group delay and the sensitivity fall-off are not affected. As a result, the zero pathlength difference position (ZPD, i.e. where the  $\Delta\tau_g = 0$ ) is now encoded at  $\Delta\tau_{AOM}$ . If  $\Delta\tau_{AOM} > \sigma_i$ , then the axial position shift created by the AOM's exceeds the characteristic fall-off distance, and the complex conjugate is effectively resolved.

### 3.1.4. Electronic Fall-off

A complete description of sensing depth limitations in SSOCT must also account for fall-off due to the electronic bandwidth of the electronic detection components, i.e. the "electronic fall-off". The electronic fall-off is similar to the optical fall-off in that it attenuates high fringe frequencies. However, the mechanism by which this occurs is fundamentally different. Optical (linewidth) fall-off occurs due to the loss of fringe visibility from the fringe signal being averaged over the instantaneous linewidth, whereas electronic fall-off arises because each spectral measurement occurs over some finite integration time, during which the wavelength of the laser output is not stationary.

The effects of electronic fall-off can be combined with optical fall-off, creating an "effective" linewidth. In order for such a treatment to be accurate, however, the electronic fall-off term must account for the bandwidth of all of the electronic components in the system, including the photodiode, the digitizer and any amplifiers or filters. Assuming all of these components have linear responses, the net frequency response is simply the product of the frequency responses of all of the electronic components.

Further analysis can be performed by taking the inverse Fourier transform of the total frequency response, which yields a temporal impulse response function. Assuming that the laser sweeps linearly in time, this impulse response can be converted from time to optical bandwidth by simply multiplying by the sweep speed of the laser. The

effective linewidth is then given by the convolution of this “electronic linewidth” and the laser linewidth. Fourier transformation of this effective linewidth then yields the effective fall-off. It should be noted that, in practice, neither the laser sweep speed nor the laser linewidth are constant, and typically both of these will depend on the output wavelength of the laser. Thus, the effective linewidth is actually a function of optical frequency.

In the preceding discussion, we assumed that the both the optical fall-off profile and the electronic profile were centered about the same point. That is, the optical fall-off profile was centered about the zero pathlength difference (ZPD) position, while the electronic fall-off position was centered at DC, and these two points were coincident.

In the case of heterodyne SSOCT, the optical fall-off remains centered about ZPD, but the fringe frequencies have been shifted to be centered about  $\Delta\tau_{\text{AOM}}$ . The combined effect of optical and electronic fall-off can no longer be computed as described above. Instead, the optical fall-off profile should be shifted to be centered about  $\Delta\tau_{\text{AOM}}$ , and an electronic fall-off profile should be computed from the Fourier transform of the electronic PSF. The product of these two profiles then yields the combined optical/electronic fall-off profile.

### **3.2. Coherence Revival-based Heterodyne SSOC**

Heterodyne SSOC resolves the ambiguity by creating a frequency shift that moves the peak sensitivity position away from DC, such that positive and negative displacements from that position can be discerned. A significant advantage of this technique is that it shifts the complex conjugate, rather than attenuating it, and thus does not result in distracting ghost images. This technique has previously been implemented using acousto-optic modulators (AOMs) and electro-optic modulators [93] to apply a differential frequency shift between the sample and reference arms [90, 91]. The drawbacks of the technique mostly stem from the use of these modulators, in that they typically have large insertion losses and restricted optical bandwidths, which results in reduced imaging sensitivity and reduced axial resolution. Furthermore, data processing in traditional implementations of heterodyne SSOC is significantly more complicated than in traditional SSOC, requiring either hardware demodulation [91] or complicated post-processing [90].

Here, we present a novel and extremely simple method of realizing heterodyne SSOC using a phenomenon referred to as coherence revival. This technique exploits the fact that some external cavity tunable lasers (ECTLs) used for SSOC automatically produce a phase modulated signal when used in an interferometer whose arms are mismatched by an integer multiple of the laser's cavity length. This technique has a number of advantages over traditional, AOM-based heterodyne SSOC in that it is

simple to implement, causes no reduction of axial resolution, and requires no additional hardware beyond a traditional SSOC system. Furthermore, the only additional processing step required is the use of a numerical dispersion compensation algorithm, which is an ordinary processing step in many SSOC systems.

### **3.2.1. Theory**

#### Coherence revival

Coherence revival refers to the phenomenon where interference fringes are observed in an interferometer illuminated by a light source with a comb-like spectrum not only when the reference and sample arms are matched in delay, but also when the two arms are mismatched at periodic intervals. These intervals can be several orders of magnitude longer than the source coherence length.

This phenomenon occurs if the light source in the interferometer is a laser simultaneously oscillating at multiple longitudinal modes. The period at which each set of interference fringes is observed is then equal to the reciprocal of the mode spacing, which is also equal to the roundtrip delay of the laser cavity. This phenomenon has been used to measure the mode spacing of multi-mode diode lasers, and is discussed extensively in [196].

Briefly, if such a laser oscillates at multiple longitudinal modes simultaneously, even if these modes have random phase relationships with respect to each other (i.e. the

laser is not mode locked), the multi-mode field emitted from the laser has a periodic waveform. This periodicity stems from the fact that the mode spacing is constant, or, equivalently, that the laser cavity length is fixed. The field outside the cavity is thus periodic with a period equal to the roundtrip cavity delay [196].

### Coherence revival in SSOCT

This phenomenon is important for SSOCT as many currently available and emerging commercial swept source lasers are external-cavity tunable lasers (ECTLs) that exhibit this behavior. These lasers typically contain a semiconductor gain chip inside a long external cavity (typically tens of millimeters). The long cavity provides very fine mode spacing, and because the semiconductor gain media is inhomogeneously broadened, several of these longitudinal modes can oscillate simultaneously [197]. These lasers then sweep by employing a tunable filter, located inside the cavity, that creates large loss at all but a small subset of these modes. As the filter tunes, the laser mode-hops between these finely spaced longitudinal modes, but because many of the finely spaced modes are excited simultaneously, the tuning appears smooth on a macro-scale.

An important consequence of this phenomenon is that interference fringes can be observed when the sample and reference arm are mismatched by an integer multiple of the laser cavity length. This effect can be understood as arising from the interference of sequential pulses emanating from a pulsed laser, where the first emitted pulse travels

through the reference arm, and the second emitted pulse travels through a shorter sample arm. Both pulses arrive at the receiver simultaneously and with a high degree of mutual coherence. Therefore, by mismatching the interferometer arms by one cavity length, the optical path delay of the laser cavity is effectively applied in the sample arm. This concept can be extended to place any integer number of virtual cavities in the sample arm.

#### Phase modulation in the virtual cavity

An important consequence of this virtual cavity effect is that the optical path delay of the cavity is effectively applied in the sample arm (under conditions of coherence revival). In an ordinary SSOCT system, effects such as dispersion and phase modulation that occur in the laser cavity are common to light propagating in both the sample and the reference arm, and thus do not affect the SSOCT signal. However, when coherence revival is used to place a virtual cavity in only one arm of the interferometer, this symmetry is broken, and the optical path delay of the cavity is applied in the sample arm only. Thus, any dispersion or phase modulation that is created in the laser cavity will then affect the SSOCT signal.

One of the challenges of previous heterodyne SSOCT systems is that the AOMs used are expensive, lossy, dispersive, and difficult to implement [90, 91]. A significant advantage of the virtual cavity effect is that it allows for the placement of a phase

modulator directly inside the laser cavity. In fact, we have observed that at least two different models of commercially available swept source lasers create phase modulation automatically when employed in a coherence revival configuration. We suggest that the source of this phase modulation is a frequency shift due to variation of the optical pathlength (OPL) of the laser cavity over the course of the laser sweep. This frequency shift may be due to a change in the physical length of the cavity, likely as part of the tuning mechanism, or a modulation of the refractive index of some element in the cavity, perhaps due to carrier-induced changes of the refractive index of the gain media [198].

To demonstrate mathematically how a variation in the laser cavity OPL results in phase modulation, we derive an expression for the SSOCT signal in a system where the OPL difference between the reference and the sample varies during the scan. The interferometric cross term of the SSOCT signal in a system where the length of one arm changes over the course of the sweep is given by [87, 199]:

$$i_n(t) \propto \cos(2k(t)[z_r - z_n(t)]) \quad (3.2.1)$$

where  $i_n(t)$  is the time dependent photocurrent due to the  $n^{\text{th}}$  sample reflector,  $k(t)$  is the wavenumber that is swept in time, and  $z_r$  and  $z_n(t)$  are the axial positions of the reference mirror and  $n^{\text{th}}$  reflector. The axial position of the sample reflector is allowed to vary in time during the sweep.

We initially assume that the change in the cavity OPL varies linearly with the instantaneous central wavelength of the laser sweep,  $\lambda_c$ . The reflector position can then be cast as a function of  $\lambda_c$ :

$$z_n(\lambda_c) = z_{n0} + M(\lambda_0 - \lambda_c) \quad (3.2.2)$$

where  $\lambda_0$  is the central wavelength of the sweep,  $z_{n0}$  is the mean position of the  $n^{\text{th}}$  sample reflector, and  $M$  is a parameter that describes the slope of the OPL change with wavelength (e.g. in mm/nm). We combine equations (3.2.1) and (3.2.2) and recast the photocurrent as a function of the instantaneous central wavenumber,  $k_c$ , to yield:

$$i_n(k_c) \propto \cos(2k_c(z_r - z_{n0} - M\lambda_0) + 4\pi M) \quad (3.2.3)$$

Here, the  $M\lambda_0$  term represents the axial position shift produced by the phase modulation, and the  $4\pi M$  term is a constant and unimportant phase shift. Thus, the axial position shift created by the cavity length variation,  $\Delta z$ , can be expressed as:

$$\Delta z = M\lambda_0 \quad (3.2.4)$$

It is important to note that this axial position shift is created as a phase delay only.

Group delay is given by the derivative of the instantaneous phase shift with respect to frequency, and although the laser cavity OPL changes over the course of the sweep, the cavity length is constant with respect to optical frequency at all times during the sweep.

Thus, the cavity OPL variation creates a phase delay without creating an offsetting group delay. It is this separation between phase and group delay that enables the separation between the real image and its complex conjugate [87, 199].

#### Coherence revival in the Fourier domain

The effects of the swept laser mode structure upon the observed SSOCT signal, including the loss of visibility in coherence revival, are readily understood in terms of simple Fourier relationships (Figure 3.1). The length and finesse of the Fabry-Perot resonator cavity determine the spacing and spectral purity of the resonator modes, respectively. The transmission function of the resonator is given by [200]:

$$T_{cavity}(\omega) = \frac{T_{max}}{1 + \left(\frac{2F}{\pi}\right)^2 \sin^2\left(\frac{\pi\omega}{\omega_{FSR}}\right)} \quad (3.2.5)$$

where  $T_{max}$  is the peak spectral density,  $F$  is the cavity finesse, and  $\omega_{FSR}$  is the angular free spectral range given by  $\omega_{FSR} = \pi c / n_{eff} L$ . Assuming the laser has at least moderate finesse,

( $F > 5$ ), this expression is well approximated by a series of Lorentzian functions, i.e. a Lorentzian convolved with a comb:

$$T_{cavity}(\omega) \approx \left( \frac{T_{\max}}{1 + (\tau\omega)^2} \right) * \left( \sum_{m=-\infty}^{\infty} \delta(\omega - m\omega_{FSR}) \right) \quad (3.2.6)$$

where  $\tau$  is given by  $\tau = 2F / \omega_{FSR}$  and is inversely proportional to the linewidth of the Lorentzian, and  $\delta$  denotes the Dirac delta function. The ECTL also has a tunable filter placed inside the cavity, with a passband that is much broader than the mode spacing, such that many modes will oscillate simultaneously. If we denote the transmission function of the tunable filter as  $T_{filter}$ , the instantaneous spectrum of this type of laser can be expressed as:

$$S_{inst}(\omega, \omega_c) = S_{source}(\omega) T_{filter}(\omega, \omega_c) \left[ \left( \frac{T_{\max}}{1 + (\tau\omega)^2} \right) * \left( \sum_{m=-\infty}^{\infty} \delta(\omega - m\omega_{FSR}) \right) \right] \quad (3.2.7)$$

where  $S_{source}(\omega)$  is the integrated power spectral density of the laser sweep, and  $T_{filter}$  also depends on  $\omega_c$ , the instantaneous central frequency of the laser that varies over sweep.

For each spectral channel of an SSOCT A-scan centered at a frequency  $\omega_c$ , the detected photocurrent is equal to the ideal spectral interferogram multiplied by the instantaneous spectrum  $S_{inst}(\omega, \omega_c)$  and then integrated over  $\omega$ . This is analogous to

convolving the ideal spectral interferogram with the instantaneous spectrum, and thus the sensitivity fall-off profile is related to the Fourier transform of the instantaneous spectrum. The ideal spectral interferogram is defined as that resulting from the sample structure only, absent any SSOCT instrument function. For simplicity, we assume that  $T_{filter}$  maintains a constant shape across the sweep, and thus the magnitude of its Fourier transform is constant. The fall-off profile is then given by directly taking the normalized magnitude of the Fourier transform of equation (3.2.7) with respect to  $\omega$ , and recasting in terms of the pathlength mismatch,  $z$ :

$$f_{falloff}(z) = f_{filter}(z) * \left[ \exp\left(-\frac{|z|}{\zeta}\right) \left( \sum_{m=-\infty}^{\infty} \delta(z - mn_{eff}L) \right) \right] \quad (3.2.8)$$

where  $z = tc / 2$ ,  $L$  is the physical cavity length,  $n_{eff}$  is the effective refractive index,  $\zeta$  is the characteristic decay distance given by  $\zeta = n_{eff}LF / \pi$ , and  $f_{filter}$  is the Fourier transform of  $T_{filter}$ . Because the source bandwidth is much broader than the filter's spectral bandwidth, after Fourier transformation, the contribution of the source to the fall-off profile is negligible and has thus been dropped.

The fall-off profile in equation (3.2.8) is composed of a comb with a period  $n_{eff}L$  that is multiplied by a double-sided exponential function with a characteristic decay distance  $\zeta$ . The comb is then convolved with  $f_{filter}$ , which is the magnitude of the Fourier

transform of the tunable filter passband. As with conventional SSOCT,  $f_{filter}$  defines the SSOCT fall-off profile. For coherence revival, this profile applies to each set of fringes, which are separated by the period of the comb. The exponential function, heretofore referred to as the *coherence revival fall-off envelope*, determines the loss of fringe visibility at increasing multiples of the cavity length. These relationships are all depicted in Figure 3.1.

Conventional fall-off profiles are typically specified by the pathlength mismatch that results in a 6dB loss in sensitivity. For comparison, we derived the characteristic distance at which this envelope is reduced by the same amount:

$$\Delta z_{-6dB} \approx 0.44 n_{eff} LF \quad (3.2.9)$$

This result suggests that, for ideal cavities with large finesse, the coherence revival fall-off envelope would allow the use of many cavity length offsets before fringe visibility is severely degraded.

### Non-linear cavity length variation

An important consideration that has not yet been addressed relates to the assumption that the cavity OPL changes linearly with wavelength. Equation (3.2.3) demonstrates that such a linear relationship would result in a pure phase modulation. In practice, however, the OPL change may not be linear in wavelength, and may instead

exhibit a non-linear relationship. This non-linear cavity length variation still creates phase modulation, but the modulation frequency is chirped rather than constant. This is analogous to different wavelengths experiencing different OPLs in the sample arm, a phenomenon that is closely related to material dispersion. Therefore, while a non-linear cavity length variation still creates phase modulation, it also results in distortion in the axial point-spread function (PSF). Fortunately, well-established numerical techniques used to correct dispersion in SSOCT [176] can also be used to correct this PSF distortion.

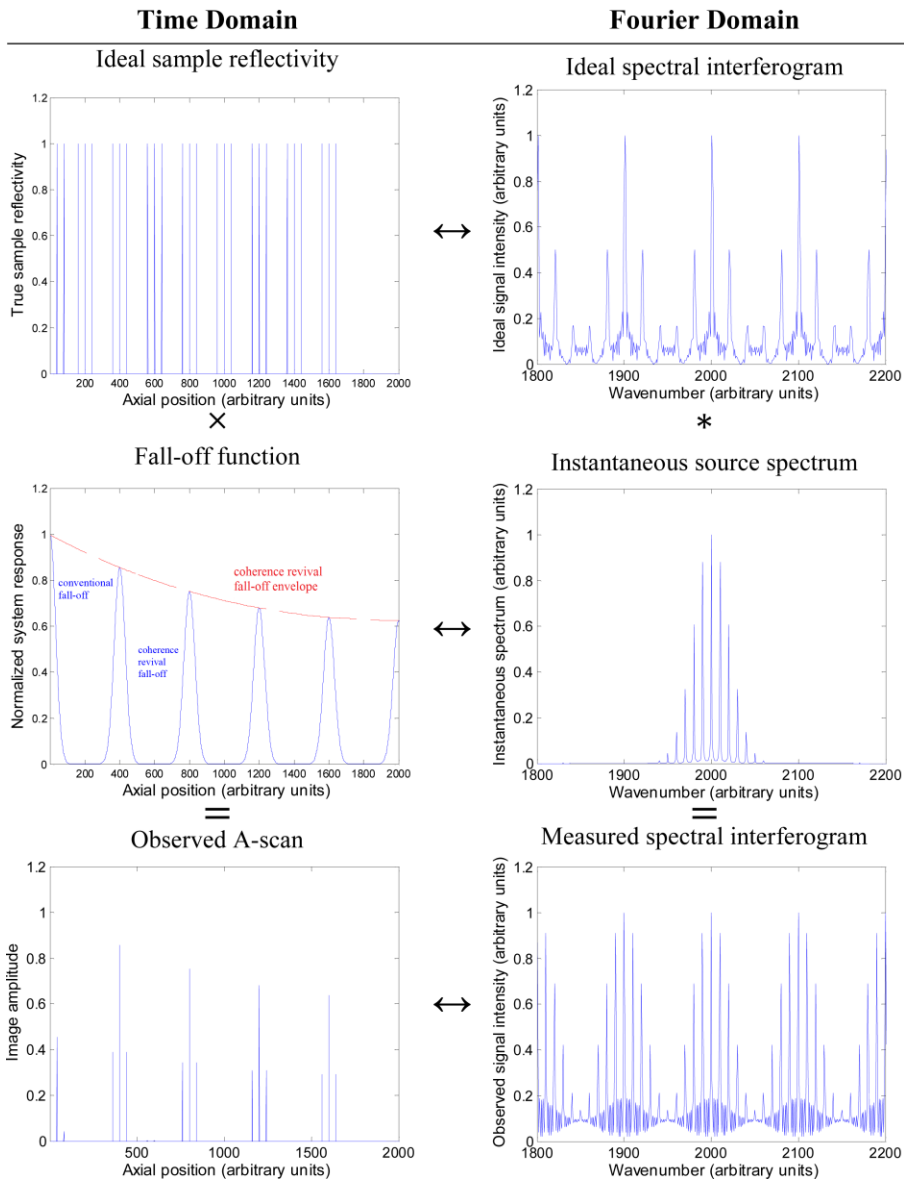


**Figure 3.1: Time and Fourier domain representations of coherence revival. The ideal interferogram is convolved with the instantaneous source spectrum to yield the measured spectral interferogram, which is the Fourier transform of the observed A-scan. Equivalently, the ideal sample reflectivity is multiplied by the fall-off function, resulting in the observed A-scan.**

### 3.2.2. Methods

#### Numerical simulations

To validate the theory developed above, we created a numerical simulation of a coherence revival SSOCT system in MATLAB. The simulation was designed to model an SSOCT system comprising an ECTL with a Gaussian-shaped tuning bandwidth centered at 1050nm, FWHM bandwidth of 50nm, cavity length of 80mm and cavity finesse of 25. These parameters were chosen to mimic the observed behavior of the Axsun laser. The  $S_{source}$  term from equation (3.2.7) was given by:

$$S_{source}(\omega) = S_0 \exp\left[\frac{(\omega - \omega_0)^2}{2\sigma_s^2}\right] \quad (3.2.10)$$

where  $S_0$  is a normalization term and  $\sigma_s$  is the standard deviation. The cavity transmission function from equation (3.2.5) was used, except that either the physical cavity length or the cavity index was allowed to vary over the sweep, resulting in the following expressions for  $\omega_{FSR}$ :

$$\omega_{FSR}(\omega_c) = \frac{\pi c}{n_{eff} L(\omega_c)} \quad \text{OR} \quad \omega_{FSR}(\omega_c) = \frac{\pi c}{n_{eff}(\omega_c) L} \quad (3.2.11)$$

These expressions allow the mode spacing and cavity transmission spectrum to vary as a function of the instantaneous central frequency. Finally, the tunable filter passband was modeled as a Gaussian with a FWHM of 0.05nm, which corresponds to a SSOCT fall-off profile similar to what is observed with commercially available lasers.

The tunable filter passband is thus given by:

$$T_{filter}(\omega - \omega_c) = \exp\left[-\frac{(\omega - \omega_c)^2}{2\sigma_{filter}^2}\right] \quad (3.2.12)$$

where  $\sigma_{filter}$  is the standard deviation of the Gaussian and  $\omega_c$  is the instantaneous central frequency of the sweep. Using these formulas, A-scans were simulated using 9216 spectral channels over a bandwidth equal to four times the source FWHM (200nm). For each spectral channel,  $T_{filter}$ ,  $\omega_{FSR}$  and  $T_{cavity}$  were computed for the corresponding instantaneous central frequency  $\omega_c$ , which was stepped linearly over the simulation bandwidth. The instantaneous source term was then computed using equation (3.2.7).

Each spectral channel of each A-scan was then computed as a single time-domain OCT measurement, as derived by Hee [195], but replacing the original source term with the instantaneous source term, and dropping the high frequency carrier:

$$I(\omega_c) \propto \text{real} \left\{ \int_{-\infty}^{\infty} S_{inst}(\omega, \omega_c) \exp[-j(\omega - \omega_c)\Delta\tau_g] \frac{d\omega}{2\pi} \right\} \quad (3.2.13)$$

where  $\Delta\tau_g$  is the group delay difference between the sample and reference reflectors.

This integral was computed for all 9216  $\omega_c$  values in the simulation to produce a spectral interferogram, which was then Fourier transformed to yield a depth scan.

Simulations were run for a stationary cavity, a cavity whose pathlength varied linearly with the instantaneous central wavelength, and a cavity whose pathlength was varied linearly with the instantaneous central frequency. In the latter two cases, the total cavity length variation was 100 $\mu\text{m}$  over the sweep FWHM (50nm), and 400 $\mu\text{m}$  over the entire simulation bandwidth (200nm), yielding a slope parameter M of approximately 2  $\mu\text{m}/\text{nm}$ .

For simulations where the cavity pathlength varied linearly in frequency, numerical dispersion compensation algorithms [176] were also applied to correct the degradation in the axial PSF. For each of these simulations, multiple A-scans were computed, modeling a single sample reflector at various delays. Fall-off profiles were then computed by plotting the peak of each as a function of the delay.

### SSOCT systems at 840nm and 1040nm

To demonstrate coherence revival SSOCT in practice, two SSOCT systems were constructed using different commercially available ECTLs (Figure 3.2). The first used a Thorlabs SL850-P16, with a central wavelength of 840nm, tuning bandwidth of 80nm, and repetition rate of 8kHz (forward sweep only). The balanced receiver used was a Thorlabs PDB120A, a Si receiver with 75MHz electronic bandwidth. The second system used an Axsun Technologies swept source laser with a central wavelength of 1040nm, tuning bandwidth of 100nm and repetition rate of 100kHz. The balanced receiver used in the 1040nm system was a Wieserlabs WL-BPD1GA, an InGaAs receiver with 1GHz electronic bandwidth. An RF amplifier (HD24388, HD Communications Corp.) was also used with the 1040nm system (not shown). An Alazar Technologies ATS9870 digitizer was used for both systems, operating at 250MS/s and 1GS/s for the 840nm and 1040nm systems, respectively. Both systems had identical topologies, and made use of the spectrally balanced interferometer configuration recently suggested by Klien et al [151]. While the fiber couplers and detectors differed between the two systems, the same digitizer and reference and sample arm optics were used. A very long motorized translator (SGSP46-400X, Sigma Koki) was used in the reference arm.

Sensitivity and fall-off measurements were made with both systems with the sample arms matched, and at various cavity length offsets. The cavity length of each laser was measured by placing an attenuated mirror in the sample arm and translating

the reference arm over its entire linear travel (400mm). The distance between the peak fringe visibility positions of each set of interference fringes was determined to be the cavity length. We use the terms +1 or -1 cavity length offset to refer to the situations in which the sample arm was longer or shorter than the reference arm by one cavity length, respectively.

For the 840nm source, fall-off measurements were taken with cavity length offsets of -2, -1, 0, +1 and +2. For the 1040nm source, only the -1, 0 and +1 cavity length offsets were used, because the phase modulation imparted by -2 and +2 offsets exceeded the electronic bandwidth of the digitizer. For each system, fall-off measurements were made using consistent levels of sample and reference power across all cavity length offsets, to allow the relative signal levels to be compared.

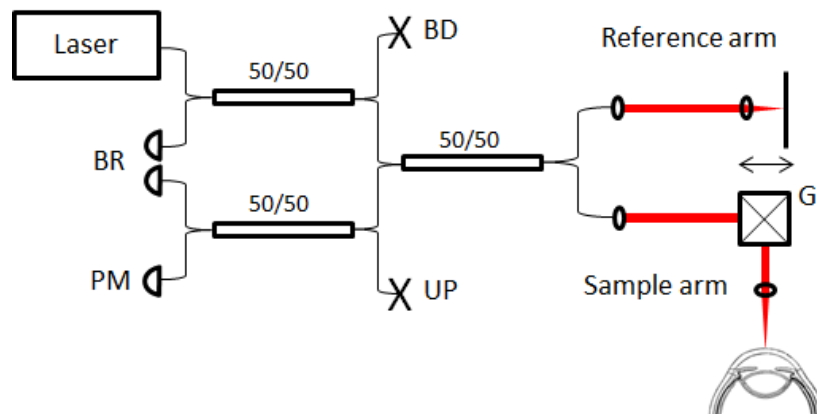


Figure 3.2: Schematic of SSOCT systems tested. Laser was either an 840nm or 1040nm ECTL. BR: Balanced receiver. PM: power meter. BD: beam dump. UP: Unused port. G: galvanometer.

Finally, to demonstrate the feasibility of this technique for *in vivo* imaging, the ocular anterior segments of healthy human volunteers were imaged. For these experiments, the powers incident on the patient cornea were  $600\mu\text{W}$  and  $1.8\text{mW}$  for the 840nm and 1040nm systems, respectively, which were within the limits of the ANSI Z136.1 standard [159]. To demonstrate the improved imaging depth with coherence revival CCR, both systems were used at both 0 and +1 cavity offsets. The sample arm used consisted of two galvanometers (Cambridge technologies) and a compound objective lens designed to provide sufficient depth of field to demonstrate the extended imaging range of the SSOCT systems [87].

#### Wavenumber recalibration and dispersion compensation

As the SSOCT signal was sampled linearly in time, and the lasers swept non-linearly in wavenumber, the acquired signal required resampling before Fourier transformation. Both lasers contained an internal Mach-Zehnder interferometer clock, whose signal was digitized along with the photoreceiver signal. The zero-crossings of the clock were detected and used to generate a linear-in-wavenumber recalibration vector that was used to resample the SSOCT signal linearly in wavenumber. However, because the clock signals were only intended for imaging depths of 2.9mm and 3.7mm (for the 840nm and 1040nm systems, respectively), the recalibration vector was first interpolated to increase the achievable imaging depth to 9.4mm and 12.4mm,

respectively. The photoreceiver signals were then resampled using this recalibration vector via linear interpolation.

The numerical simulations described above demonstrate how a non-linear-in-wavelength cavity length variation results in axial PSF degradation, analogous to the effects of material dispersion. In fact, we observed such an axial PSF degradation in our experiments. These dispersion-like effects, as well as true dispersion from unmatched optics and fiber lengths in the sample and reference arm, were corrected using a numerical dispersion compensation [176]. Briefly, after resampling to linearize the spectral interferogram in wavenumber, the spectral interferogram was multiplied by a complex phase function, given by:

$$DC(k) = \exp\left(-j\left(a_1(k - k_0)^2 + a_2(k - k_0)^3\right)\right) \quad (3.2.14)$$

where  $a_1$  and  $a_2$  are fitting parameters and  $k_0$  is the central wavenumber of the sweep. Optimal values of  $a_1$  and  $a_2$  were determined using an optimization algorithm to maximize the peak signal from a mirror.

### 3.2.3. Results

#### Numerical simulations results

Results from the numerical simulations are shown in Figure 3.3, Figure 3.4 and Figure 3.5. Figure 3.3 shows the results from the simulation with a fixed cavity, demonstrating coherence revival without a frequency shift. Figure 3.4 and Figure 3.5 show the results from simulations in which the cavity length varied linearly with the instantaneous central wavelength and instantaneous central frequency, respectively. For the linear-in-wavelength case, the slope of the cavity variation was precisely  $2\mu\text{m}/\text{nm}$ , while the linear in frequency case used an *average* slope of  $2\mu\text{m}/\text{nm}$ . From equation (3.2.4), the expected axial shifts for cavity offsets of 0, +1 and +2 are 0mm, 2.1mm and 4.2mm. To allow for relative comparisons, all simulation figures are plotted on the same vertical scale. Also, as the simulated spectral interferograms are real signals, their Fourier transform remain Hermitian symmetric. Thus, only positive (frequencies) displacements are shown. Furthermore, the abscissa in the fall-off plots is the axial position that is extracted from the Fourier transform, and thus does not represent the axial position of the reflector for coherence revival peaks. Conversely, the fall-off profile in Figure 3.3D was extracted by plotting the peak of the Fourier transformed SSOCT signals against the simulated reflector positions that generated the corresponding signals. Fall-off profiles for the simulations in which the cavity length varied are not shown but were identical to Figure 3.3D.

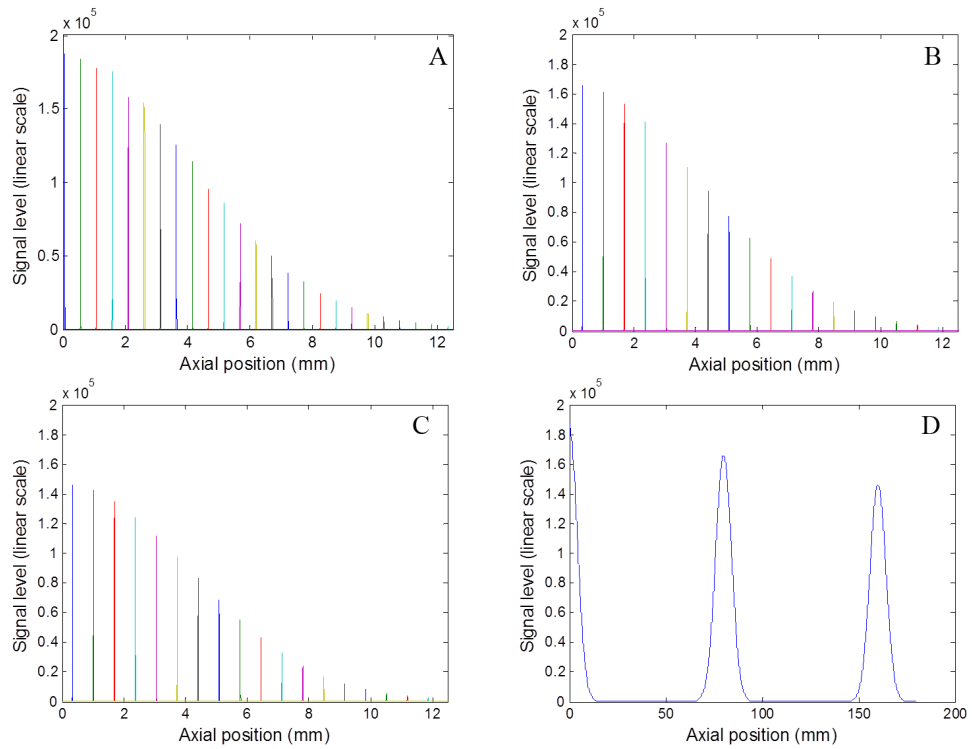


**Figure 3.3: (A-C) Fall-off plots from a numerical simulation of a coherence revival SSOCT system with a stationary cavity for 0, +1 and +2 cavity length offsets, respectively. Note that no shift in the peak sensitivity position is observed. (D) Fall-off profile demonstrating coherence revival peaks centered at 80mm and 160mm.**

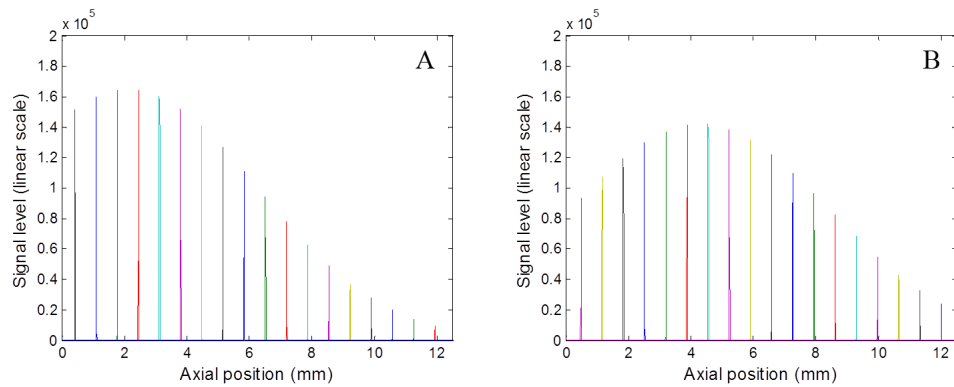


**Figure 3.4: Fall-off plots from a numerical simulation of a coherence revival SSOCT system with a cavity whose pathlength varies linearly in wavelength with a slope of  $2\mu\text{m}/\text{nm}$ , +1 (A) and +2 (B) cavity length offsets. The expected axial position shifts of the peak sensitivity positions of 2.1 and 4.2mm are observed.**

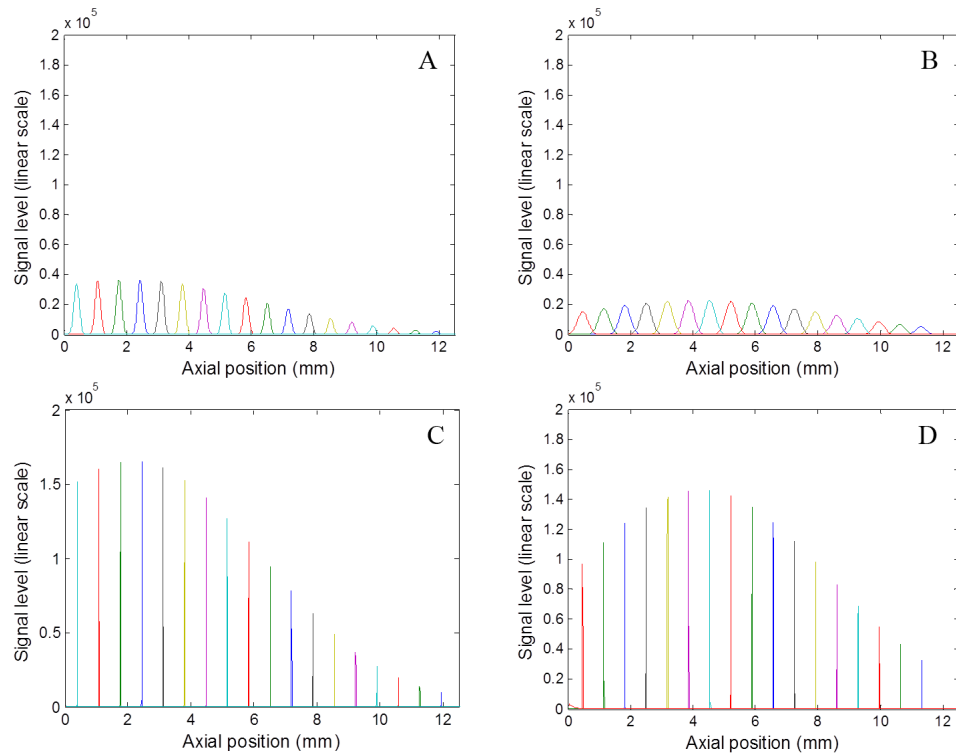


**Figure 3.5: A and B: Fall-off plots from a numerical simulation of a coherence revival SSOCT system with a cavity whose pathlength varies linearly in frequency with an *average* slope of  $2\mu\text{m}/\text{nm}$ , for +1 and +2 cavity length offsets, respectively. The expected axial position shifts of the peak sensitivity positions are observed, but the axial PSFs are severely degraded due to the non-linear phase modulation. C and D show the same data as A and B after applying dispersion compensation.**

### Experimental fall-off measurements

Fall-off profiles from the 840nm system are shown in Figure 3.6. A peak sensitivity of 95dB was measured near the 0 cavity offset with  $600\mu\text{W}$  incident on the sample. This was reduced from the theoretical shot noise limit of 104dB due to coupling losses, unbalanced RIN, and digitization noise due to the low effective number of bits of the digitizer (6.7 ENOB). Sensitivity relative to this peak value is plotted on the ordinates

of Figure 3.6. Results are shown for the 0, +1 and +2 cavity offsets. Measurements at -1 and -2 cavity offsets were also made, but the results have been omitted here as they were nearly identical to the results from +1 and +2 offsets, respectively. The physical pathlength difference between the peak visibility positions of the 0 and +1 offsets was 66.1mm. The physical pathlength difference between the peak visibility positions of the 0 and +2 offset was precisely double (within the resolution of the translation stage), at 132.2mm. Exactly the same distances were observed for the negative offsets. These measurements were in good agreement with the manufacturer's estimate of the cavity length as approximately 50mm of physical pathlength, without accounting for refractive index.

Fall-off profiles from the 1040nm system are shown in Figure 3.7. A peak sensitivity of 98dB was measured near the 0 cavity offset with 1.8mW incident on the sample. The theoretical shot noise limit for this system was also 104dB, and the discrepancy between the measured and theoretical sensitivity was due to the same factors discussed above, as well amplification noise from the RF amplifier. Sensitivity relative to this peak value is plotted on the ordinate of Figure 3.7. Results are shown for the -1, 0 and +1 cavity offsets; the -2 and +2 offsets could not be measured as, for those offsets, the phase modulation created by the laser cavity up-converted the spectral interferogram beyond the digitization bandwidth of the digitizer. The physical pathlength difference between the -1 and 0 and the 0 and +1 offsets were 115.0mm and

114.8mm, respectively. Again, this was in good agreement with the pathlength suggested by the manufacturer of approximately 80mm of fiber.

Because the sample and reference powers were kept constant during these measurements, we can determine the loss in peak sensitivity for each cavity length offset from the falloff profiles. Figure 3.6 shows that the peak sensitivity in the +1 and +2 offsets for the 840nm system were attenuated by 5dB and 10.5dB, respectively, from that of the pathlength matched case. If we define the usable imaging range as the depths over which the signal amplitude is reduced by less than 6dB, the imaging ranges for the 840nm were approximately 2.5mm, 5mm and 4mm for the 0, +1 and +2 offsets.

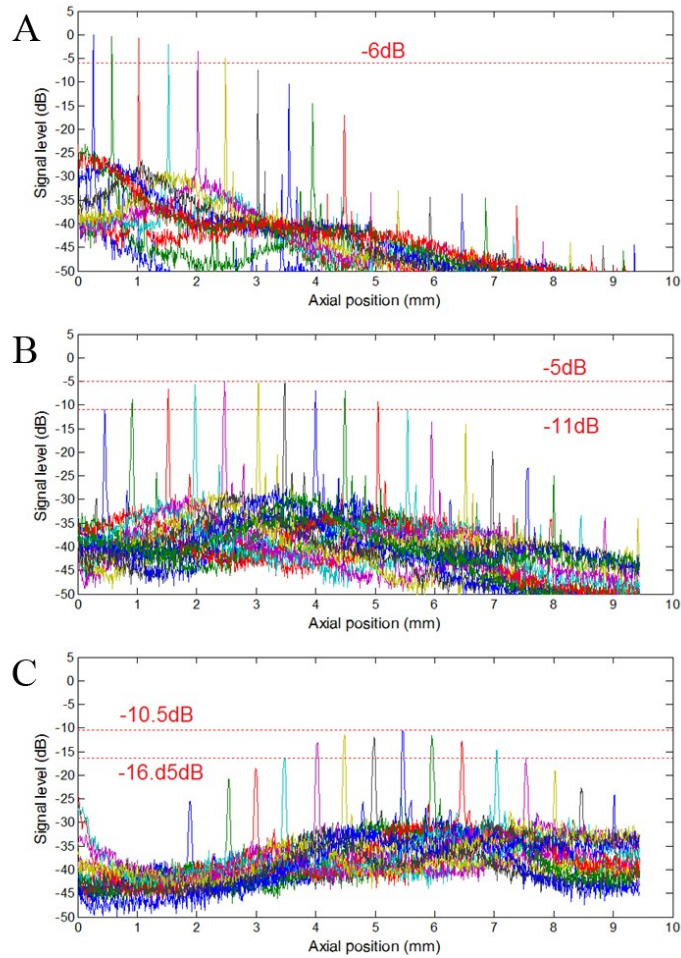


**Figure 3.6: Fall-off measurements from the 840nm system for 0 (A), +1 (B) and +2 (C) cavity length offsets. The physical separations between the peak sensitivity position from 0 to +1 and from +1 to +2 were both 66.1mm.**

Similarly, Figure 3.7 shows that the loss in sensitivity at the -1 and +1 offsets was only about 1dB, despite the considerably longer cavity length. From this, we infer that the finesse of the 1040nm laser was much higher than the finesse of the 840nm laser. The usable imaging ranges were 9mm, 5.5mm and 9mm for the -1, 0, and +1 offsets, respectively.

It is interesting to note that the optimal dispersion compensation phase functions were nearly identical between the +1 and -1 cavity length offsets for both systems. Furthermore, the phase function parameters  $a_1$  and  $a_2$  used to optimally correct measurements from -2 and +2 cavity length offsets (for the 840nm system) was precisely double that of the phase function used for the -1 and +1 cavity length offsets.

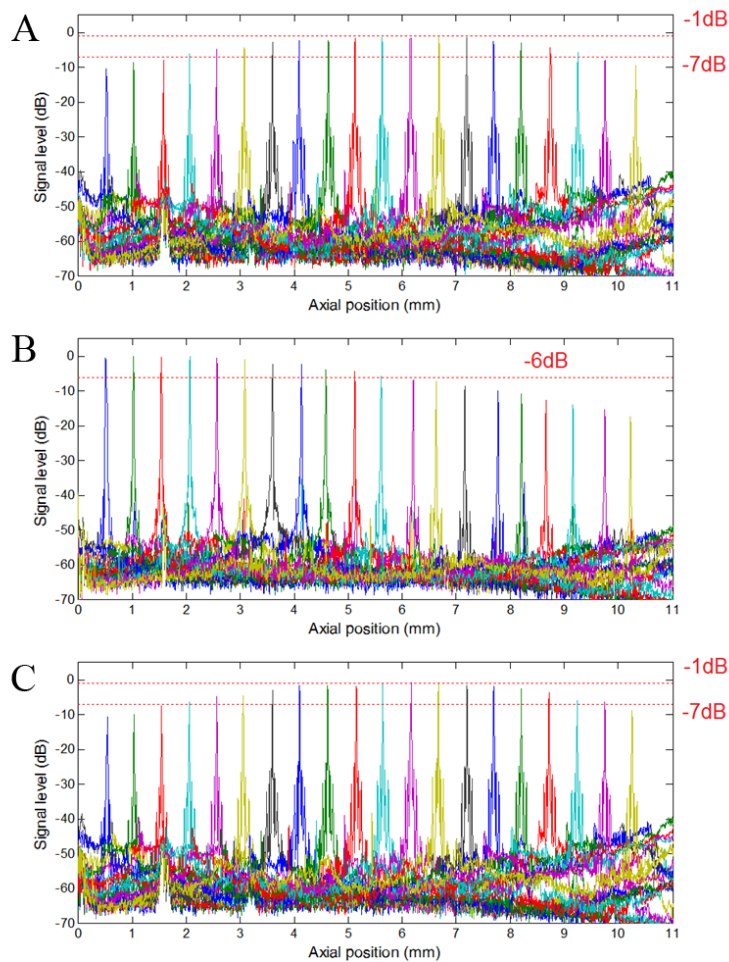


**Figure 3.7: Fall-off measurements from the 1040nm system for -1 (A), 0 (B) and +1 (C) cavity length offsets. The physical separations between the peak sensitivity positions of the -1 and 0 and the 0 and +1 offsets were 115.0mm and 114.8mm, respectively**

### Imaging Results

Figure 3.8 shows the results of two images of the same volunteer's ocular anterior segment for comparison. The image in A was taken with the reference and sample arms matched in pathlength, whereas the image in B was taken with the sample arm one cavity length longer than the sample arm. Both images were acquired on the 840nm system, and each image comprises five averaged frames. The locations of the zero pathlength difference (ZPD) position and the +1 offset position are indicated. Figure 3.9 shows the results of the same experiment conducted on the 1040nm system. Figure 3.10 shows two volume projections taken on the same eye with both the 840nm (left) and 1040nm (right) systems.

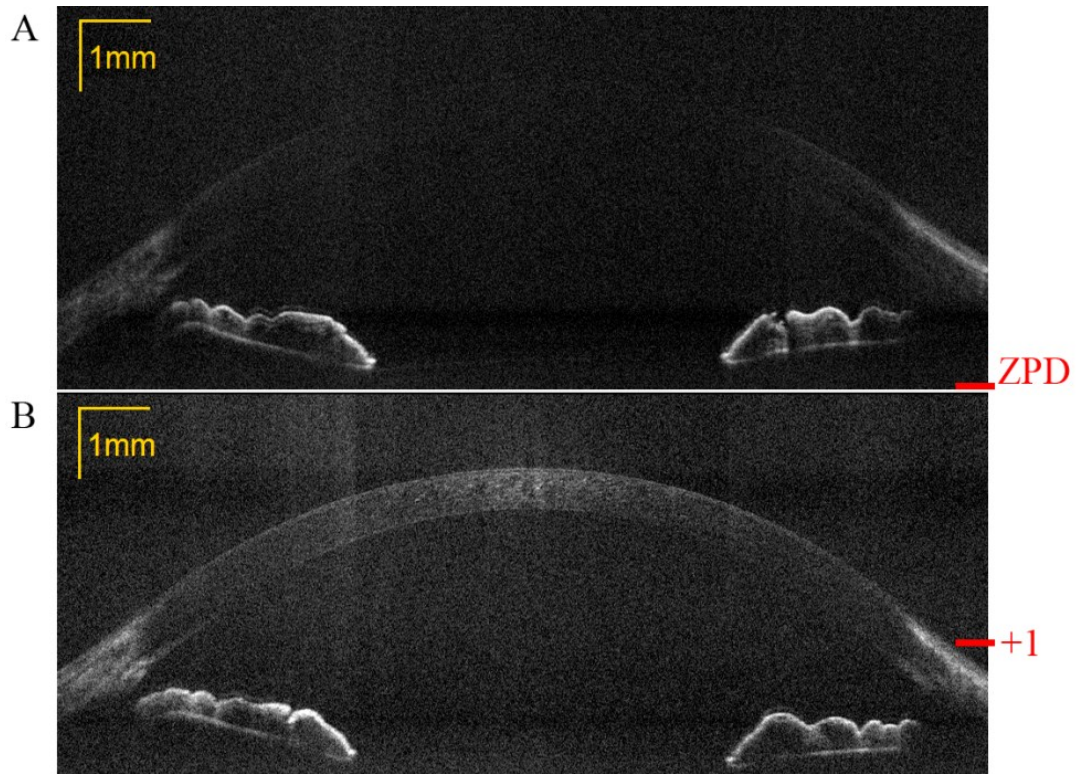
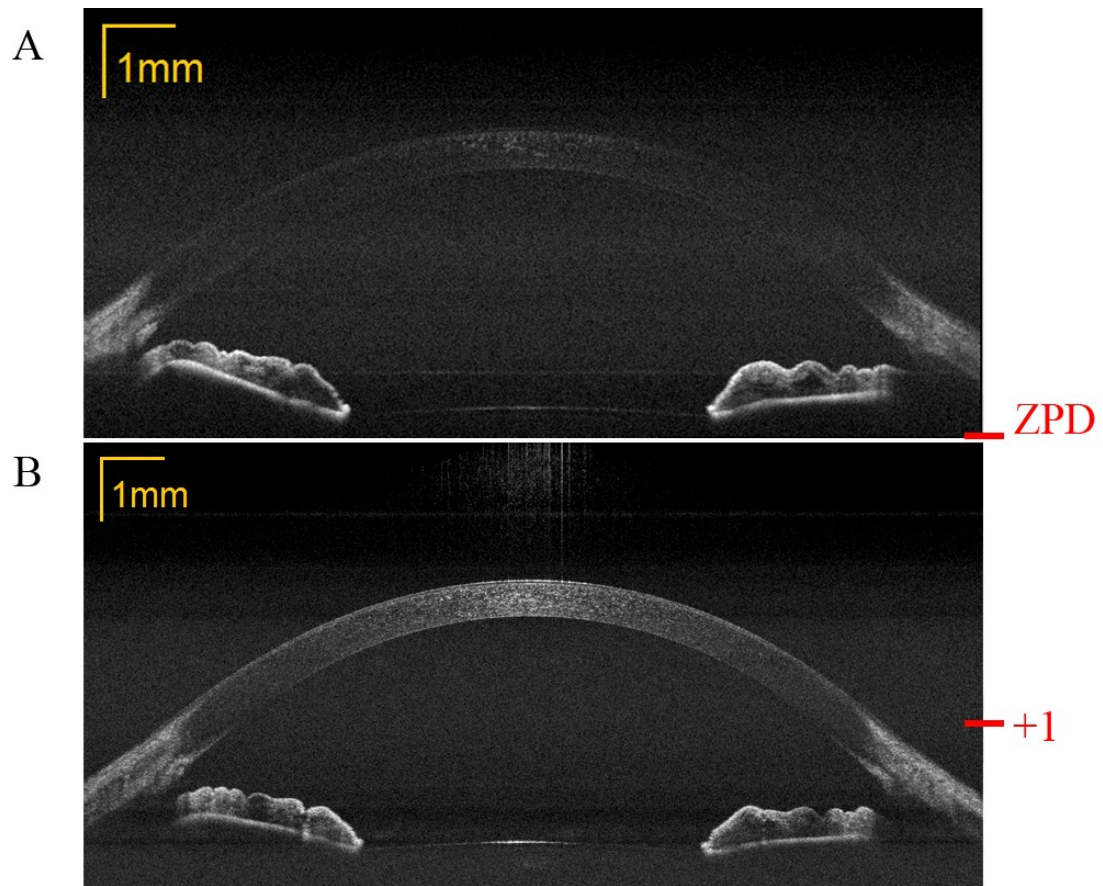
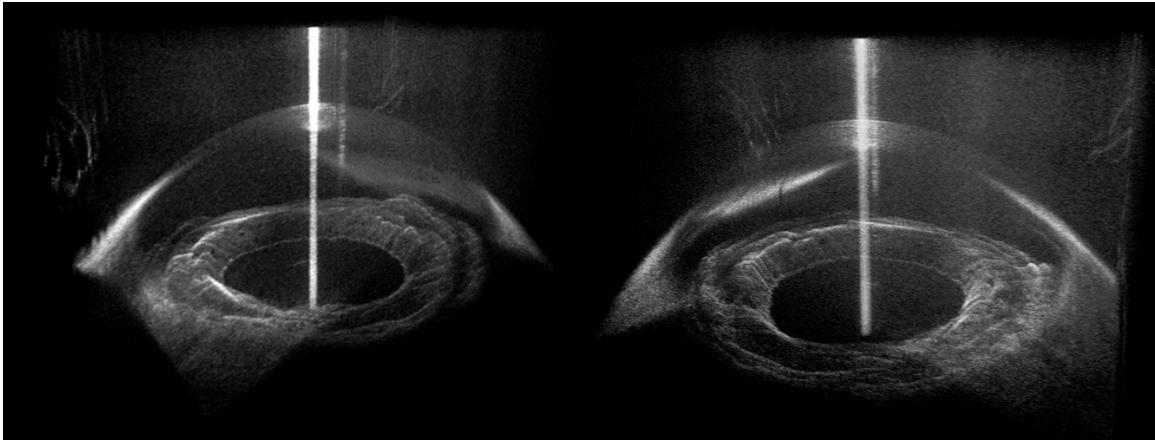


Figure 3.8: Comparison images taken on the 840nm, 8kHz (Thorlabs SL850-P16 laser) system with 0 (A) and +1 (B) cavity length offsets. Both images comprise 1000 (lateral)  $\times$  1300 (axial) pixels spanning 13 mm (lateral)  $\times$  5.3 mm (axial), the latter scaled to account for refractive index. Each image represents 5 averaged frames obtained over 0.6s. The locations of the ZPD and +1 offset positions are indicated.



**Figure 3.9: Comparison images taken on the 1040nm, 100kHz (Axsun Technologies laser) system with 0 (A) and +1 (B) cavity length offsets. Both images comprise 2000 (lateral) x 2300 (axial) pixels spanning 14 mm (lateral) x 6.9 mm (axial), the latter scaled to account for refractive index. Each image represents 5 averaged frames obtained over 100msec. The locations of the ZPD and +1 offset positions are indicated.**



**Figure 3.10: Volume projections of the same eye acquired with the 840nm (left) and 1040nm (right) systems. The 840nm volume consisted of 1300 (axial) x 500 x 200 samples, acquired in 12.5 seconds. The 1040nm volume consisted of 2304 (axial) x 500 x 200 samples, acquired in 1 second.**

### 3.2.4. Discussion

#### Summary

Coherence revival is an attractive implementation of heterodyne SSOC, and carries with it a number of advantages over traditional methods employing AOMs. First and foremost, the method is simple and inexpensive; in cases where the laser already exhibits phase modulation, all that is required is an adjustment of the reference arm length and an increase in the digitization speed. Second, while there is an associated loss in sensitivity, the magnitude of this loss depends on the laser design (primarily the cavity finesse). We have shown that, for at least one commercially available swept source laser, this loss in sensitivity is only about 1dB. Finally, no additional complicated signal processing or image processing techniques are required. The axial PSF

degradation observed in the coherence revival configurations can be managed using numerical dispersion compensation, a common processing step in SSOCT.

### Dispersion

The dispersion compensation algorithm used in our experiments, from equation (3.2.14), employed two fitting parameters,  $a_1$  and  $a_2$ , which are related to the group velocity dispersion (GVD) and third order dispersion (TOD), respectively. These fitting parameters can be used to quantify the GVD and TOD of the system [201], although it is important to note that the parameters were optimized to correct dispersion-like effects of coherence revival as well as true material dispersion due to unmatched optics and fiber lengths between the sample and reference arm. For the 1040nm laser, the group delay dispersion and total TOD of the system, when operated in a +1 cavity length offset configuration, were measured to be 9400 fs<sup>2</sup> and 55700 fs<sup>3</sup>, respectively. Assuming this dispersion occurs over the cavity length of 115 mm, and accounting for the index of refraction of the fiber in the cavity (Corning HI 1060,  $n \approx 1.47$ ), this implies a GVD of 60.0 fs<sup>2</sup>/mm (or -105 ps/nm/km) and a TOD of 356 fs<sup>3</sup>/mm. The manufacturer's reported value for GVD of HI1060 fiber is -38 ps/nm/km, suggesting that there is significantly more dispersion in the system than would be caused by the fiber in the cavity alone. For the 840nm laser, the group delay dispersion and total TOD of the system, when operated in a +1 cavity length offset configuration, were measured to be 5300 fs<sup>2</sup> and 22800 fs<sup>3</sup>,

respectively. Assuming the dispersion occurs over the 66.1mm cavity length offset and that the cavity is free-space, this implies a GVD of  $40.3 \text{ fs}^2/\text{mm}$  (or  $-108 \text{ ps/nm/km}$ ) and a TOD of  $172 \text{ fs}^3/\text{mm}$ .

### Digitization

Huber et al [149] and Goldberg et al [202] have demonstrated that, for SSOCT systems, 8-bit digitization results in only a marginal reduction in image quality and SNR as compared to digitization at higher bit depths. This is in large part due to the dynamic range that is conserved by the attenuation of the source's spectral shape using the spectrally balanced detection scheme discussed above.

However, even in cases where spectrally balanced detection is not possible, heterodyne SSOCT techniques are well suited to shallow bit-depth digitization because the signals of interest are shifted away from DC. Thus, residual DC artifact can be removed by high-pass filtering before digitization.

The required digitization rate depends on the laser sweep speed, desired imaging depth and the frequency of the phase modulation created by the ECTL. As the up-converted frequencies must be Nyquist sampled, the required digitization rate is equal to the digitization rate of a conventionally configured (i.e. non-heterodyne) SSOCT system plus twice the modulation frequency. For the lasers used in our experiments, this

resulted in approximately a two-fold increase in required digitization bandwidth as compared to conventional SS-OCT.

### Image Artifacts

We observed the generation of two distinct types of image artifacts when using this method. First, with the 840nm laser, we observed the appearance of faint but sharp “ghost images” in the fall-off plots, only at the deepest end of the imaging depth. These artifacts appeared even when the cavity length offset was zero, and can be clearly seen in Figure 3.3A, as faint reflectors between 6 and 10mm with amplitudes between -30 and -50 dB. However, these artifacts were not sufficiently bright to appear in biological images. The second type of artifact we observed was seen with both lasers, and was characterized by the appearance of highly dispersed ghost images near the deepest end of the imaging depth. The amplitudes of these artifacts were measured and compared to the amplitude of the desired signal. The relative artifact amplitude depended on the axial position of the true reflector signal, and ranged between -36.5dB and -42.5dB for the 1040nm laser and between -25.5dB and -33.5dB for the 840nm laser. Examples of these artifacts can be seen in Figure 3.8B and Figure 3.9B, at the top of the images, as faint ghosts of the pupil (in Figure 3.8B) and cornea (in Figure 3.9B).

We attribute these artifacts to two sources. First, non-linearity in the cavity length variation might give rise to multiple phase modulation frequencies, or even

harmonics of the phase modulation frequency that are then aliased into the passband of the system electronics. These higher order modulation frequencies would create additional “ghost” images centered at different depths. Second, the k-clocks used for the 840nm and 1040nm sources were designed for imaging depths of 2.9mm and 3.7mm, respectively, and were not intended to be interpolated out to 9.4mm and 12.4mm. Thus, the artifacts may also be caused by inaccuracies in the wavenumber recalibration.

In practice, these artifacts only appeared at the deepest imaging depths where the sensitivity was poor, and were also so faint that for biological imaging, they were only visible in the presence of very bright reflectors or averaged images. Nevertheless, the wavenumber recalibration issue can be easily addressed in future designs employing the same lasers by constructing a Mach-Zehnder interferometer with a longer mismatch, rather than using the lasers’ internal clock. Addressing the non-linearity of the cavity length variation is a more challenging problem, and may not be necessary as the artifacts were generally unobtrusive.

### **3.3. Dispersive Optical Delay Lines in Coherence Revival SSOCT**

The large amount of “dispersion-like” axial PSF degradation, as well as the large offset that must be generated between the sample and reference arm, can complicate the implementation of coherence revival-based heterodyne SSOCT systems. In this section, we describe the use of a dispersive optical delay line (DODL) that can provide large reference delays as well as hardware dispersion compensation in a relatively small footprint.

#### **3.2.1. Grating-based Dispersive Optical Delay Line**

Figure 3.11 below shows a ray-traced model of a grating-based D-ODL, which is similar in design to the rapid scanning optical delay lines (RSOD's) that were used in the fastest iterations of time-domain OCT systems [32, 33]. However, this D-ODL differs from an RSOD in that the scanning mirror in the image plane of the grating lens is replaced with a mirror at a fixed angle.

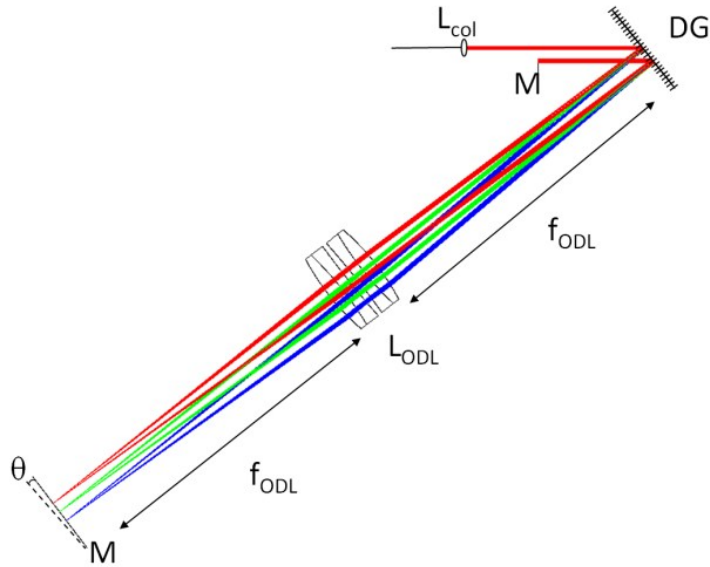


**Figure 3.11: Schematic of the optical delay line.  $L_{col}$ : Collimating lens, DG: Diffraction grating, LODL compound achromatic lens with focal length  $f_{ODL}$ , M: gold mirrors,  $\theta$ , mirror angle. Red, green and blue lines represent ray traces at wavelengths of 1090nm, 1040nm, and 990nm respectively.**

RSOD's have been used extensively in TDOCT due to their ability to provide rapidly scanned group delays, while also providing precise control of the Doppler frequency and dispersion compensation [32, 33, 35]. Design considerations are described in detail in reference [33], but were derived for time-domain OCT applications. Thus, we begin by deriving the group and phase delay through a DODL with a stationary mirror and swept wavelength source.

We define  $\lambda_0$  to be the center wavelength of the entire sweep,  $\lambda_c$  to be the center of the instantaneous linewidth, and  $\lambda$  to be any wavelength propagating through the

system. Then, following the derivation in [33], the phase shift for a single pass through the D-ODL (double pass of the grating) as a function of  $\lambda$  is given by:

$$\phi(\lambda) = \frac{4\pi\theta f_{ODL}(\lambda - \lambda_0)}{p\lambda} \quad (3.3.1)$$

where  $\theta$  is the mirror angle,  $f_{ODL}$  is the lens focal length and  $p$  is the grating pitch. This expression was derived using the grating equation and the small angle approximation. Specifically, this small angle approximation was used to compute the diffraction angle as a function of wavelength, as follows:

$$\theta_d(\lambda) = \arcsin\left(\frac{\lambda - \lambda_0}{p}\right) \approx \frac{\lambda - \lambda_0}{p} \quad (3.3.2)$$

It was found that the use of the small angle approximation introduces less than 0.02% error over the range of diffraction angles used in our experiments (-30mrad to 30mrad).

Next, equation (3.3.2) is expressed as a function of angular optical frequency:

$$\phi(\omega) = \frac{4\pi\theta f_{ODL}(\omega_0 - \omega)}{p\omega_0} \quad (3.3.3)$$

When expressed as a function of angular frequency, the phase shift can be used to determine the phase delay as follows:

$$t_{\phi} = \frac{\phi(\omega_c)}{\omega_c} \quad (3.3.4)$$

Note that the phase delay is defined according to the phase shift of the instantaneous central wavelength. Combining equations (3.3.3) and (3.3.4) yields:

$$t_{\phi}(\lambda_c) = \frac{2\theta f_{ODL}(\lambda_c - \lambda_0)}{pc} \quad (3.3.5)$$

The phase delay is thus a function of  $\lambda_c$ , which is swept rapidly in time. The free-space phase pathlength difference, relative to the central wavelength, is then also a function of  $\lambda_c$ :

$$\Delta l_{\phi}(\lambda_c) = \frac{2\theta f_{ODL}(\lambda_c - \lambda_0)}{p} \quad (3.3.6)$$

Thus, the free-space phase pathlength varies linearly with the instantaneous wavelength. The group delay can also be defined from the phase shift from the relation:

$$t_g = \frac{\partial \phi(\omega_c)}{\partial \omega_c} \quad (3.3.7)$$

Combining equations (3.3.3) and (3.3.7) yields:

$$t_g = -\frac{4\pi\theta f_{ODL}}{p\omega_0} = -\frac{2\theta f_{ODL}\lambda_0}{cp} \quad (3.3.8)$$

Thus, despite the fact that the phase delay varies over the course of the laser sweep, the group delay is constant with respect to the instantaneous optical frequency. As demonstrated in section 3.1.2, only the group delay factors in to the SSOCCT signal, and thus the dependence of phase delay on the instantaneous optical frequency is not a concern.

To clarify, the group delay computed in equation (3.3.8) is applied in a single pass through the D-ODL (double pass of the grating). However, because the double-pass mirror in the D-ODL will also serve as the reference mirror in the OCT interferometer, it is this “single pass” delay that is of interest. Equation (3.3.8) can be used to calculate the range of single-pass group delays achievable with a D-ODL given the lens focal length, grating pitch, central wavelength and the angular range through which the mirror can be tilted.

### 3.2.2. Hardware dispersion management

An additional advantage conferred by the use of RSOD's in time-domain OCT was the ability to manage dispersion in hardware. In fact, the RSOD design was based upon Fourier domain pulse shapers and pulse compressors, which were designed specifically for managing dispersion [34-37]. In the RSOD and D-ODL embodiments, dispersion management is achieved by simply displacing the grating from the focal plane of the lens. Positive dispersion is created when the grating-to-lens distance is less than  $f_{ODL}$ , and negative dispersion is created when the grating-to-lens distance is larger than  $f_{ODL}$ . In this way, RSOD's have been used to compensate for dispersion from EOM's [93] and relatively long lengths of fiber [32]. Fork et al [203] and Tearney [204] have previously derived expressions for the GVD in an RSOD with the grating displaced from the focal plane of the lens, and thus these expressions will not be re-derived here. Following their derivations, the GVD through an RSOD or D-ODL is given by:

$$\text{GVD} = \frac{-\lambda_0^3 (L - f_{ODL})}{\pi c^2 p^2} \cos(\theta_0)^{-\frac{3}{2}} \quad (3.3.9)$$

where  $L$  is the grating to lens distance,  $\theta_0$  is the diffraction angle of the central wavelength, and all other parameters are defined as above.

As an example, to compensate for the  $9400\text{fs}^2$  of GVD observed in the coherence revival PSF with the Axsun laser described in section 3.2.4, a D-ODL with a grating pitch

of  $1.67\mu\text{m}$  and focal length of  $100\text{mm}$  could be constructed. The diffraction angle of this D-ODL would be  $38.6$  degrees. Then, using equation (3.3.9), an offset of approximately  $4.5\text{mm}$  would be required to offset this dispersion.

## 4. Sweep Buffering in Swept Source OCT

In this chapter, we describe the development of advanced sweep buffering techniques that can increase the imaging speed of SSOCT systems employing low duty-cycle swept source lasers. These techniques are an improvement upon previously described buffering systems, conferring potential advantages in power efficiency, sensitivity, axial resolution and axial imaging range. Furthermore, these techniques are compatible with coherence revival, enabling the realization of SSOCT systems with both enhanced imaging depth and increased imaging speed.

In section 4.1, we describe the design considerations and evaluate the performance of a prototype buffered SSOCT system, and then demonstrate the use of this system to enable high speed, high resolution imaging of the posterior eye. In section 4.2, we describe the combining of sweep buffering techniques with coherence revival-based heterodyne SSOCT to achieve both increased imaging speed and extended imaging depth in the same system. This system is used to demonstrate high speed and high resolution imaging of the anterior eye.

Several of my colleagues contributed to the work presented in this chapter. Kevin Shia aided with the construction of the buffered SSOCT system, data acquisition and analysis. Hansford Hendargo and Derek Nankivil constructed the posterior eye and anterior eye sample arms, respectively, and also aided with data acquisition.

## **4.1. Sweep Buffering in SSOCT using a Fast Optical Switch**

### **4.1.1. Introduction**

The imaging speed of OCT systems has increased dramatically in recent years, with A-scan rates in the megahertz regime recently being demonstrated for *in vivo* imaging [73, 88, 151]. These fast acquisition rates confer important advantages in numerous clinical applications. For example, high speed imaging of the anterior segment minimizes artifacts due to patient motion (discussed in section 1.5), enabling improved accuracy in the extraction of biometric parameters [86, 164, 175, 182]. High speed imaging is also important for Doppler OCT imaging of retinal blood vessels [115, 160, 205-213], where fast acquisition speeds facilitate the resolving of high speed flows in the optic disc without fringe washout [214]. Finally, and perhaps most critically, high speed imaging techniques are valuable for catheter-based intravascular OCT imaging, where the imaging time is limited by the requirement of administering saline flushes to remove blood from the OCT catheter's field-of-view [21, 23].

While the fastest imaging speeds demonstrated to date have been achieved using swept source OCT lasers, many of these lasers operate with duty cycles of less than 50%, including some FDML's [148, 149], fiber ring lasers [215, 216] and ECTL's [150, 161, 217]. In section 1.4, we reviewed how sweep buffering can be used to increase the duty cycle of these low-duty lasers. The most straightforward buffering technique, as demonstrated by Potsaid et al [158], is to simply split the light emerging from the laser into two paths

using a fiber coupler, delay one path by the sweep period using an appropriately long spool of fiber, and then recombine the two using a second fiber coupler. This configuration is shown in Figure 1.15. Unfortunately, this technique is rather lossy, as only half of the light emerging from the buffer stage is used.

Furthermore, when imaging through birefringent tissues such as the cornea and retinal nerve fiber layer (RNFL), polarization mode dispersion (PMD) in the buffered output due to birefringence in the fiber spool can produce image artifacts and, for phase sensitive applications, corruption of the phase signal [160]. Beumann et al [160] demonstrated that the PMD through the fiber spool could be removed with the addition of a linear polarizer after recombining the original and buffered sweeps. However, the optical losses through the polarizer, coupled with the inefficiency of the buffered design, result in substantial optical attenuation. To mitigate this attenuation, an amplification stage consisting of an SOA and two isolators was added. A schematic of this configuration is shown in Figure 1.16. Unfortunately, the use of the SOA resulted in a narrower tuning bandwidth and broader linewidth, which degraded the axial resolution and axial imaging range, respectively.

One additional drawback of using fiber coupler to recombine the original and buffered sweeps is related to the difference between the “sampling” duty cycle and the “laser on” duty cycle of low duty cycle tunable lasers. The sampling duty cycle refers to the proportion of the sweep period where the wavelength sweep is linear (or pseudo-

linear). The laser on duty cycle refers to the proportion of the sweep period that the laser outputs appreciable power, but is not tuning linearly. For the specific case of the Axsun laser used in these experiments (which is presumably similar to the ones used in references [158] and [160]), the laser had a sampling duty cycle of 44% and a laser-on duty cycle of 62%. Thus, if a 50/50 coupler is used, the beginning and end of the buffered sweep will be corrupted by the end and beginning the original sweep, respectively, and vice versa. Thus, approximately 300ns of both the beginning and end of each 4.4 $\mu$ s sweep will be subject to this corruption, corresponding to 13% of the sampling duty cycle. In practice, this effect is mitigated by the fact that the spectral shaping windows that are often applied in SSOCT processing minimize the contribution the extreme ends of the sweep have on the processed A-scan. Nevertheless, this crosstalk between the beginning and end of opposite sweep types still results in an increase in shot noise, and also contributes to the ANSI limited power [159] that can be directed towards the patient eye. As a result of both of these effects, the system sensitivity would be reduced.

Here, we describe a novel buffering strategy that employs a very fast optical switch (< 60 ns switch time) instead of a 50/50 fiber coupler. The use of this switch allows the buffered OCT system to be substantially more power efficient than techniques employing 50/50 couplers, and prevents crosstalk between the beginning and end of opposite sweep types.

We also demonstrate a technique for transforming the wavenumber calibration signal from the original sweep (derived from the Axsun laser's integrated k-clock) signal for use with the buffered sweep that maintains transform-limited axial resolution without requiring the construction of a second interferometer.

Finally, we report on the results of a careful PMD analysis of the system, and devise a strategy to minimize polarization-related image artifacts without the use of lossy linear polarizers. Because of the overall power efficiency of this technique, booster SOA's are not required, and therefore the spectral narrowing and linewidth broadening associated with SOA's is avoided. As a result, the axial resolution and imaging range of the un-buffered system are preserved.

#### **4.1.2. Methods**

##### Buffering stage design

A schematic of the buffering stage is shown in Figure 4.1. The laser used was an Axsun Technologies swept source laser with a central wavelength of 1040nm, tuning bandwidth of 100nm and repetition rate of 100kHz. A 60/40 coupler was used to compensate the 1.5dB attenuation (~70% transmission) of the fiber spool such that both the original and buffered sweeps had similar power. The spool itself consisted of ~1000m of HI1060 fiber. Three polarization controllers are used to orient the polarization at the input of the fiber spool and at both inputs to the optical switch. A

custom optical switch produced by Boston Applied Technologies was used, based upon their Nanona FOS platform. The switch employs transparent electro-optic ceramics, which have been described previously [218], to produce a variable waveplate, which is then used in a polarization encoded Mach-Zehnder interferometer configuration to produce a 2x2 optical switch. Specified parameters of interest of the switch were an insertion loss of  $\sim 1.1$  dB (78% transmission) and switching time of 50 ns, both of which were verified experimentally. By tuning the output voltage of the switch driver, the crosstalk between the output channels can be varied up to a maximum crosstalk suppression of 21 to 26 dB (varied between channels). Thus, the crosstalk can be adjusted to achieve any splitting ratio from 99/1 to 50/50. By increasing the crosstalk, the second port of the switch could be used as a k-clock channel. However, as we employed the integrated k-clock in the Axsun laser for these experiments, the k-clock port was not used, and thus, the output voltage was adjusted for maximum crosstalk suppression.

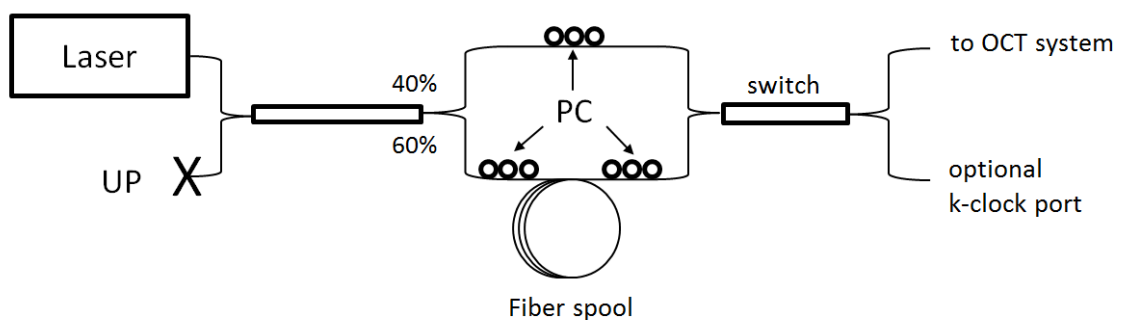


**Figure 4.1: Schematic of buffering stage. PC: Polarization controllers. UP: Unused port**

## SSOCT system design

A schematic of the SSOCT system used to demonstrate the buffering system described above is shown in Figure 4.2. The system made use of the spectrally balanced interferometer configuration suggested by Klien et al [151]. A sample arm adapted for retinal imaging and a conventional reference arm were constructed. In compliance with the ANSI z136.1 standard [159], power incident on the patient eye was limited to 1.8mW. A 635nm fiber coupled diode laser was also used as an aiming beam, but the power incident on the patient eye was limited to less than one microwatt and thus did not pose an exposure hazard. OCT light returning from the reference and sample arms was detected with a NewFocus 1807 balanced receiver, an InGaAs receiver with 120MHz electronic bandwidth. An Alazar Technologies ATS9870, operating at 1GS/s was used to record both the integrated k-clock signal from the Axsun laser and the interferometric signal from the balanced receiver.

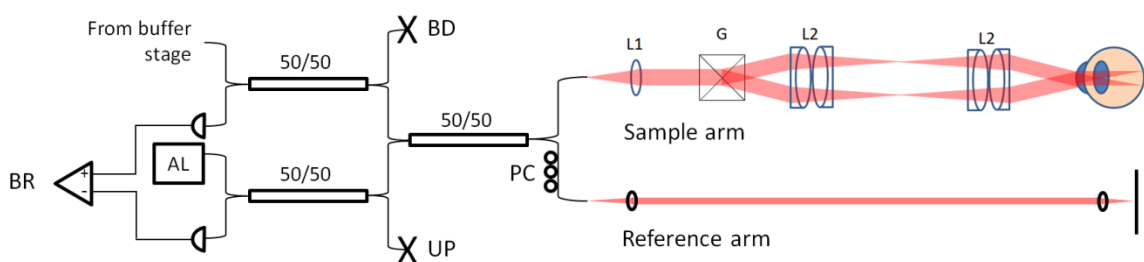


**Figure 4.2: Schematic of SSOCT system. BR: Balanced receiver. AL: Aiming laser. BD: Beam dump. UP: Unused port. PC: Polarization controller. L1,L2: Lenses. G: Galvanometers**

### Optical switch timing

The delay between the front sweep and buffered sweep was calculated by measuring the outputs from laser and the spool simultaneously on two separate photoreceivers. The peak of the cross-correlation of these two signals then corresponds to the optical delay in the fiber, which was measured to be  $4.911\mu\text{s}$ . A schematic of the data used to perform this cross-correlation is shown in Figure 4.3.

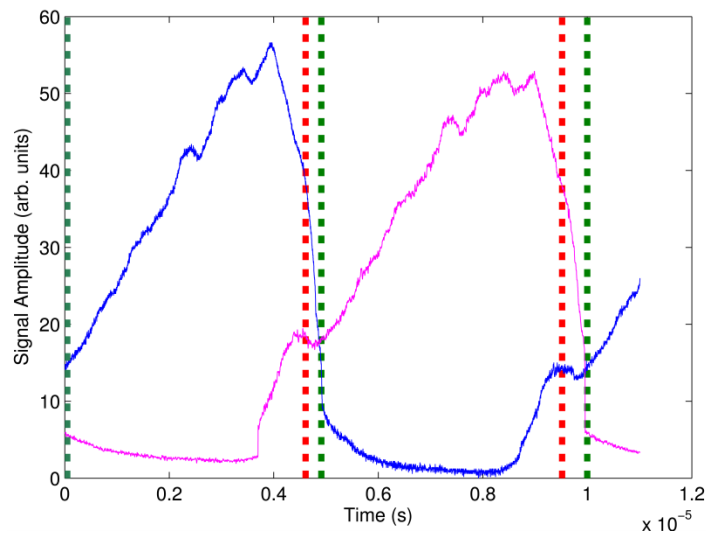


**Figure 4.3: Traces of original (blue) and buffered (magenta) sweeps. Green vertical lines denote the start of each sweep, while red vertical lines denote the end.**

The blue trace represents the original signal while the magenta trace represents the buffered sweep. For the purposes of data processing, the original sweep was deemed to occur between sample 1 and sample 4608, and the buffered sweep was deemed to occur between sample 4911 and 9519. In Figure 4.3, the beginnings of the original and buffered

sweeps are denoted by green vertical lines, whereas the end of each sweep is denoted by a red line. In normal operation, the green lines would denote the switching points of the optical switch. This figure also demonstrates the appreciable optical crosstalk that would occur between the two sweeps if a 50/50 coupler were used.

### Hardware triggering and timing

The hardware triggering of this system was slightly more complicated than that of a traditional SSOCT system, and was carried out as follows. First, because the laser only fired a single start trigger for each original sweep/buffered sweep pair, the digitizer was used to acquire a continuous stream of 9536 sample (9.5 $\mu$ s) for each sweep trigger, which thus contained both the original and buffered sweeps. The digitizer thus operated at a 95% duty cycle, and output a digital high (5V) on its auxiliary IO (auxIO) channel when integrating. The rising edge of this auxIO channel was used to trigger an SRS DS345 digital function generator, which was set to output a single square wave pulse at a frequency of 107.3kHz and initial phase of 22 degrees. This effectively produced a square wave that was low for the first half of the sweep period and transitioned to high just before at the start of the buffered sweep. This square wave was used as the control signal for the optical switch driver. Finally, a TGP110 pulse generator (Aim-TTi) was synchronized with the SRS function generator and set to create a doubled pulsed with a pulse delay of 4.911 $\mu$ s. The output from the pulse generator

was then fed into a National Instruments DAQ card (NI PCI-6221) and used as the sample clock for the drive waveform for the galvanometers. A schematic of the timing scheme is shown in Figure 4.4. Red vertical lines indicate the start of an original sweep, magenta lines represent the start of the buffered sweep and green lines represent the end of the buffered sweep.

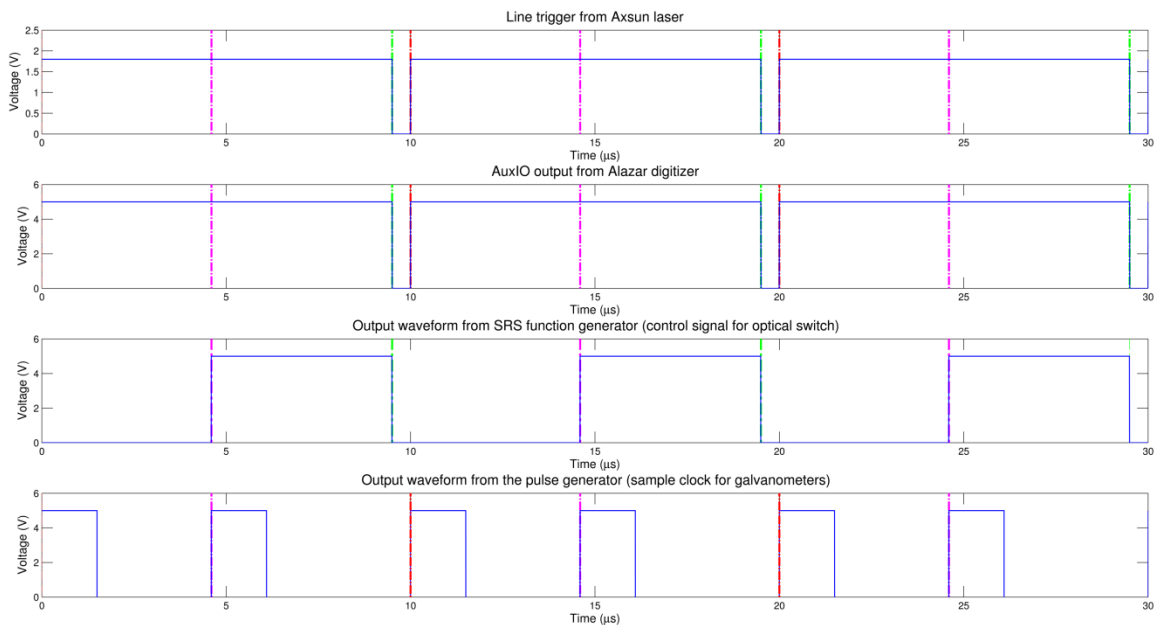


**Figure 4.4: Timing and triggering in buffered SSOCT (simulated)**

### Management of Polarization Mode Dispersion (PMD)

Both the fiber spool and the optical switch result in the generation of PMD, which in turn may result in the creation of image artifacts and ghosts when imaging a

birefringent sample. PMD (or, more precisely, differential group delay<sup>2</sup>) occurs in the fiber spool because “single mode” fibers actually support two orthogonally polarized modes. Due to imperfections and asymmetries in practical fiber, these two polarization modes will have different propagation velocities, resulting in a differential group delay between the two polarization modes. External forces on the fiber, such as bends, twists and compression, also induce birefringence, and PMD due to these effects often dominates over PMD due to the geometry of the fiber.

The generation of PMD in the optical switch occurs by a different mechanism. As described above, the optical switch functions by splitting incoming light into two polarization channels. An electro-optic device is then used as a tunable waveplate to impart either a 0 or 90 degree rotation of the polarization state in each channel. Two polarization channels are then combined and directed into either of the two output ports. As a result of the design of this system, even slight differences in the optical pathlengths of the two channels in the switch will result in the generation of appreciable PMD.

The combination of PMD from the spool and from the switch complicates matters further, especially if the fast and slow axes of the two components are not aligned. For example, if we consider a pulse of unpolarized light entering the system,

---

<sup>2</sup> The term PMD, in its usage here, is a misnomer. The transient difference in the group delay of the two orthogonal polarizations in a single mode fiber is commonly referred to as the differential group delay (DGD). DGD is a dynamic phenomenon that fluctuates in time, especially in deployed fiber, and thus is a statistical process. PMD refers to the length-normalized statistical average DGD for a given fiber type.

after traversing the spool, the light will be split into two differentially delayed pulses. After entering the switch, if the axes are not aligned, each of those two pulses may be split into two differentially delayed pulses, resulting in the generation of four propagating pulses of light, each of which is in a different polarization state. After entering the OCT interferometer, the four pulses will travel to the reference and sample arms before reaching the receiver. Depending on the orientation of the polarization axes and the amount of birefringence in the sample and reference arms, each of the four pulses in the reference arm will exhibit a varying degree of coherence with each pulse in the sample arm. Thus, in normal OCT operation, a single A-scan of a mirror will display not one, but several peaks corresponding to the interference between differentially delayed pulses in the reference and sample. If this system were used for imaging, its axial PSF would also have many peaks, resulting in severe image artifacts.

Fortunately, the PMD in this system can be managed through the use of fiber polarization controllers. For the buffered sweep, because the laser is partially polarized (we measured a degree of a degree of polarization of 66%, discussed in section 5.2.2), we used a polarization controller at the entrance of the spool to align the polarization axis of the laser output to one of the polarization axes of the spool. A second polarization controller was used to align the polarization of the light leaving the spool to the axes of the switch. Similarly, for the original sweep, a polarization controller was placed before the switch to align the polarization axis of the laser output to one of the axes of the

switch. While these polarization alignments cannot be perfect due to chromatic considerations, they significantly reduced the effects of PMD by largely restricting power in the system to only two of the four possible polarization states. Furthermore, these two dominant polarizations are orthogonal, and thus, in the absence of birefringence in the sample arm, each polarization state should only interfere with itself. This would result in a single peak, analogous to an OCT system without PMD.

The final consideration in polarization management is the potential presence of birefringence in the sample. By placing a polarization controller in the reference arm, birefringence can be introduced into the reference arm that offsets the birefringence in the sample arm. Thus, when imaging through birefringent tissue, such as the cornea or the RNFL, the reference arm polarization must be adjusted to optimize signal. As we demonstrate below, these polarization artifacts can be suppressed beneath the noise floor with careful adjustment of these polarization controllers.

To demonstrate the effects of these multiple polarization states, we performed the following measurements. First, we constructed an OCT system with the switch placed in the source arm, but without the fiber spool. Second, we replaced the fiber spool with the switch. Finally, we constructed the complete buffered system, with both the spool and switch. For each experiment, we acquired A-scans with only a mirror in the sample arm, and adjusted the polarization controllers to enable visualization of the

multiple peaks corresponding to interference between the various polarization states.

These A-scans are shown in Figure 4.5.

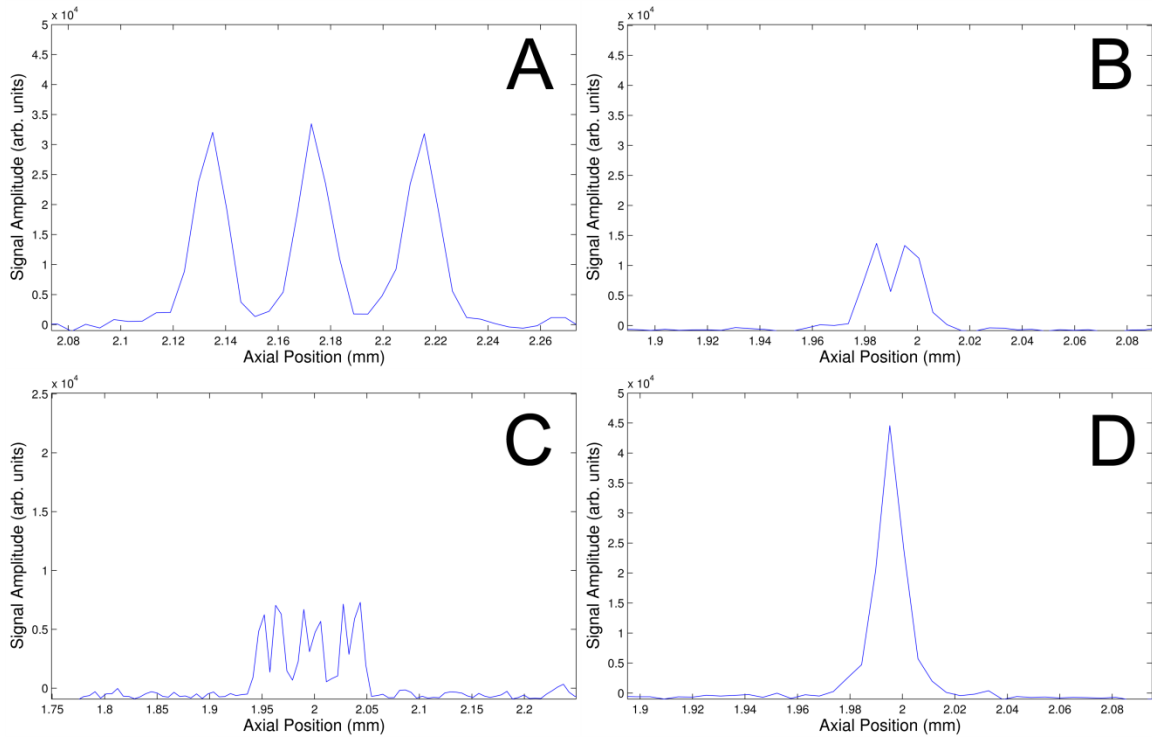


**Figure 4.5: SSOCT A-scans of a mirror in the presence of PMD. A: Switch only in source arm. B: Spool only in source arm. C: Switch and spool in source arm. D: Same as C but corrected with polarization controllers.**

Figure 4.5A shows an A-scan of a mirror with only the switch in the source arm, and contains three peaks each separated by approximately 40 microns. Figure 4.5B shows an A-scan of a mirror with only the spool in the source arm. Because the PMD through the spool is comparable to the axial resolution of the system, the expected three peaks overlap partially. Thus, the reference arm polarization controller was adjusted to

emphasize only the outer two peaks. These two outer peaks are separated by about 16 microns, implying that the separation between individual peaks was 8 microns, 5 times less than the peak separation through the switch. Figure 4.5C shows an A-scan of a mirror with both the spool and the switch in the source arm, and shows 3 pairs of split peaks. Each pair of peaks corresponds to the 3 peaks created by PMD in the switch, and the centers of the pairs are separated by approximately 40 microns, as expected. The splitting of the peaks is due to the PMD in the spool, and the separations between the paired peaks were all approximately 16 microns, as expected. Finally, Figure 4.5D shows the axial PSF once the polarization controllers have been optimized to maximize the central peak. While some residual sidelobes remain, the largest sidelobe peak is approximately -42 dB weaker than the central peak. For all of these measurements that used the fiber spool, wavenumber recalibration was performed as described below.

#### Wavenumber recalibration

For processing the original sweep, the signal from the integrated k-clock of Axsun laser was digitized and processed as previously described in section 3.2.2. Briefly, the zero-crossings of the clock were detected and used to generate a linear-in-wavenumber recalibration vector. This recalibration vector was interpolated such that the vector length matched the number of data samples in the original sweep (4608), which provided a  $Z_{\max}$  12.4mm. This interpolated vector was then used to resample the

portion of the photoreceiver signal corresponding to the original sweep (i.e. the first 4608 samples) to be linear in wavenumber.

By appropriately transforming the k-clock signal from the original sweep, the buffered sweep can also be resampled. Dispersion in the fiber spool causes short wavelengths to travel slower than long wavelengths, and because the laser sweeps from short wavelengths to long wavelengths, the entire laser sweep is compressed after travelling through the spool. If we were to direct this compressed laser sweep into the k-clock and compare the resulting signal with the k-clock signal from the original sweep, we would expect the zero-crossing intervals to be progressively shortened towards the end of the laser sweep. Thus, by adjusting the zero-crossing timings from the k-clock signal of the original sweep, we can estimate what the clock signal would be for the buffered sweep. A description of this transformation follows.

The zero-crossing timings from the original clock processing were modified by applying a polynomial delay function as follows:

$$T_2[n] - delay = T_1[n] + b_0 + b_1n + b_2n^2 + b_3n^3 \dots \quad (4.1.1)$$

Here,  $T_2$  is a vector of estimated zero-crossing timings for the buffered sweep,  $n$  is the index of the zero-crossing (between 1 and 1376),  $delay$  is the delay between the original and buffered sweeps (4.911  $\mu$ s),  $T_1$  is the vector of the zero-crossing timing from the

original sweep, and the  $b$  coefficients are fitting parameters. This technique is very similar to the dispersion compensation techniques described in [107, 176] and in section 3.2.2 above. Thus, a similar optimization approach can be used to find the  $b$  coefficients as was used to find the  $a$  coefficients in section 3.2.2, using an A-scan of a mirror.

However, to ensure that the fitting of the  $b$  coefficients is correcting for wavenumber recalibration only and not dispersion, it is important to minimize dispersion between the mirrors in the sample and reference arm, or to account for the dispersion in the optimization. This latter technique works because the dispersion parameters should be identical between the original sweep and the buffered sweep.

Using this technique, we were able to achieve identical sensitivity and axial resolution between the original sweep and buffered sweep using only two  $b$  coefficients ( $b_0$  and  $b_1$ ). Here, the  $b_0$  term adjusts the buffer delay computed by the cross-correlation, while the  $b_1$  applies a linear ramp to the delay timings over the course of the laser sweep.

Three plots of an A-scan of a mirror are shown in Figure 4.6. Part A shows the A-scan from the original sweep, part B shows the A-scan from the buffered sweep processed with the unmodified clock (i.e. the clock simply delayed by 4911), and part C shows the A-scan from the buffered sweep processed with the optimized  $b$  coefficients. Thus, processing the buffered sweep with the modified clock provides a very similar axial PSF, in terms of peak height and sidelobe suppression, as the original sweep. The

very slight difference between the plots in A and C is likely due to residual PMD that was not corrected by the polarization controllers.

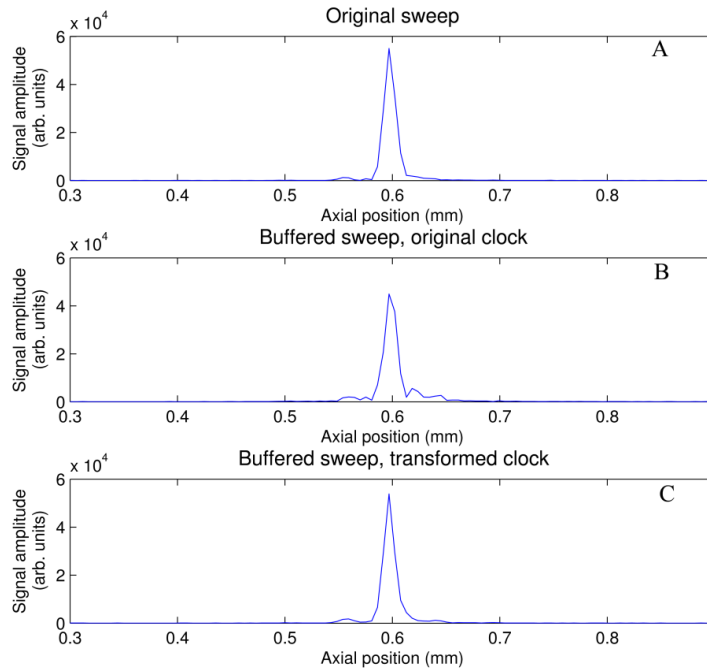


**Figure 4.6: A-scans of a mirror using (A) the original sweep, (B) the buffered sweep processed with the original clock, and (C) the buffered sweep processed with the transformed clock**

### *In vivo* retinal imaging

To demonstrate the feasibility and performance of this buffered SSOCT system, we acquired images of the posterior eye from healthy human volunteers. To manage PMD, the system was optimized as above with a mirror placed in the reference arm. Then, during patient alignment, only the reference arm polarization controller was adjusted while looking at a bright layer in the resulting image (usually the RNFL). The

polarization was adjusted until this layer appeared as bright and sharp as possible with minimal “ringing” artifacts. B-scans were then acquired with 1600 A-scans per B-scan at a frame rate of 125Hz.

### **4.1.3. Results**

#### Peak Sensitivity and Sensitivity Fall-off

The system’s peak sensitivity and sensitivity fall-off were measured, using techniques that have been described previously in section 3.2.2. The sensitivity was measured at a depth of approximately 500  $\mu\text{m}$  and found to be 97 dB with 1.8mW on the sample (the ANSI limit [159] at this wavelength), as compared to a theoretical sensitivity of 102 dB. The 5 dB discrepancy is attributed to coupling losses and residual RIN. The sensitivity fall-off profile was measured and had a 6dB fall-off range of 5.5mm.

Although not shown here, the fall-off performance was nearly identical to the results shown in section 3.2.2 (Figure 3.7). Furthermore, both the peak sensitivity and 6dB fall-off distance were identical for the forward and buffered sweeps, once the wavenumber recalibration and polarization control techniques described above had been implemented.

## Imaging results

Representative B-scans of the foveal region of the retina from a healthy human volunteer are shown below. These images were acquired at a 200 kHz A-scan rate using the buffered system described in the previous section. Each frame consisted of 800 A-scan pairs, for a total of 1600 A-scans. Acquisition time for each frame was 8ms (corresponding to 125Hz), and thus the 5x averaged frames shown below represent the image quality achievable at “video rate” (25Hz).

Figure 4.7, and its enlargement in Figure 4.8, show the typical image quality achieved before fine tuning of the reference arm polarization controller (but after optimizing the controller on a mirror reflector). Some ringing artifacts can be seen above the bright RNFL boundary (see enlargement in Figure 4.8), but these artifacts are much weaker than the peak signal, and do not appear surrounding the dimmer layers. These artifacts disappear when the polarization controller is adjusted, as shown in the B-scan in Figure 4.9 and its enlargement in Figure 4.10.

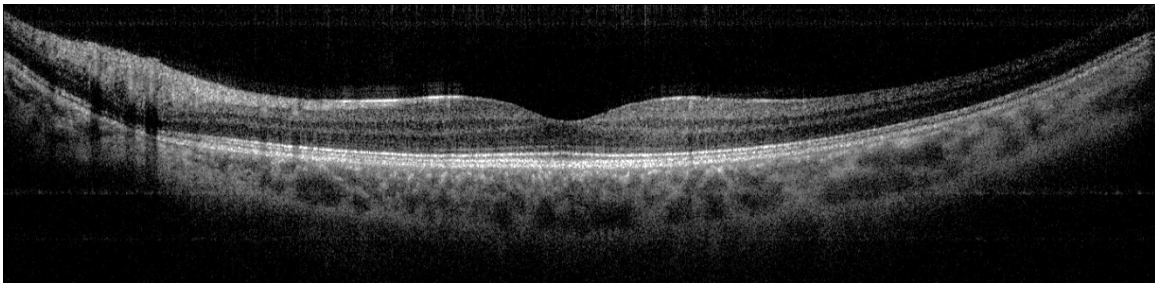


**Figure 4.7: *In vivo* B-scan of fovea acquired before optimization of polarization controller. Image consists of 1600 A-scans x 5 averaged frames. Total acquisition time was 40msec.**

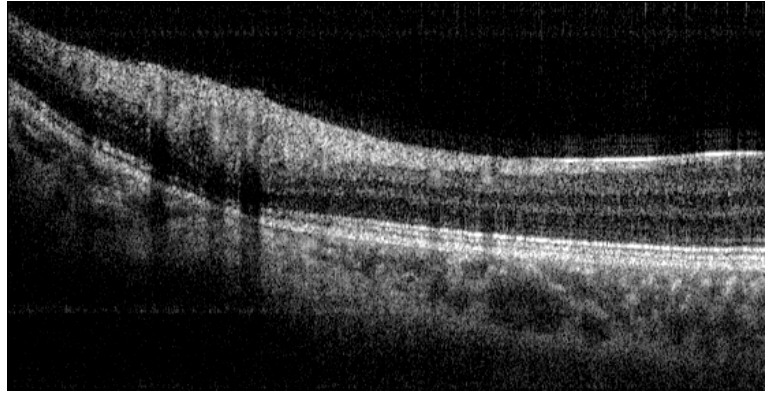


**Figure 4.8:** Enlargement of top left corner of Figure 4.7

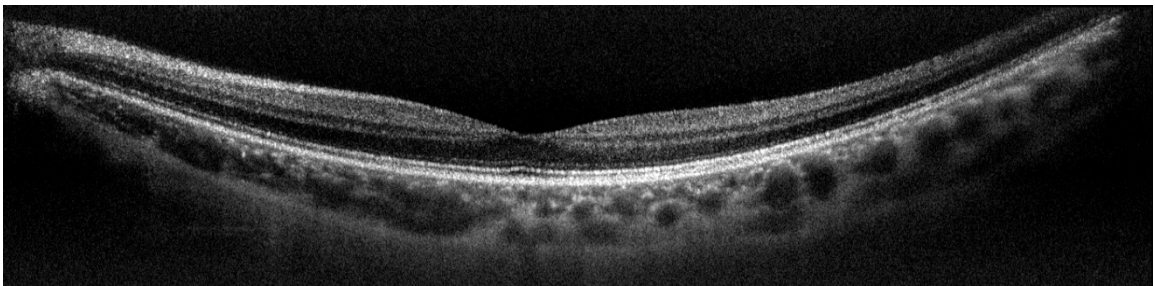


**Figure 4.9:** In vivo B-scan of fovea acquired after optimization of polarization controller. Image consists of 1600 A-scans x 5 averaged frames. Total acquisition time was 40msec.

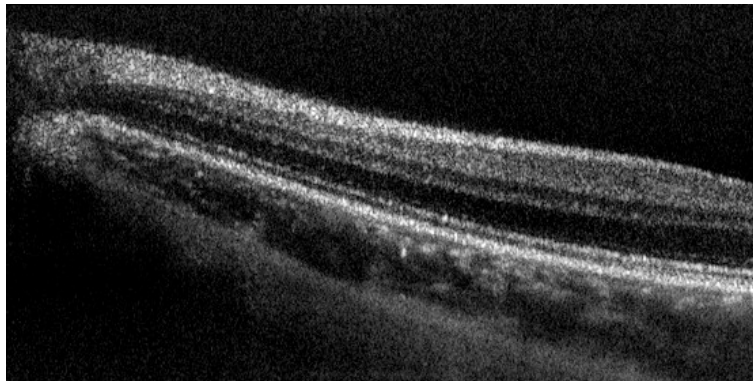


**Figure 4.10:** Enlargement of top left corner of Figure 4.9

#### 4.1.4. Discussion

We have demonstrated the development of a novel buffering strategy for increasing the imaging speed of SSOCT systems that employ duty cycles of 50% or less. This technique has numerous advantages over previously described buffering techniques. First, it is very power efficient, with roughly 60% of the source power being transmitted through the buffering stage after accounting for all insertion losses. It also exhibits superior sensitivity because the patient eye is not exposed to light that is not used for imaging, at the tails of the SSOCT sweep. Lastly, the system employs numerical methods that allow the use of the original sweep's calibration signal for recalibration of the buffered sweep. This dramatically simplifies the implementation of buffering with turnkey systems that contain integrated k-clocks. While the presence of PMD in the source arm can result in the generation of image artifacts, we have demonstrated that these artifacts can be mitigated by careful manipulation of fiber polarization controllers.

In addition, the buffering system described here is completely compatible with coherence revival-based heterodyne SSOCT described in chapter 3. The combination of these techniques would result in an SSOCT system with twice the imaging speed and nearly twice the imaging depth of conventional SSOCT systems employing the same source. In the next section, we describe such a combination system, and demonstrate its increased speed and enhanced depth imaging.

## 4.2. Sweep Buffering and Coherence Revival

### 4.2.1. Methods

To demonstrate the feasibility of combining sweep buffering with coherence revival, we modified the SSOCT system presented above to enable extended depth imaging of the anterior segment. Coherence revival was used in a +1 cavity length offset configuration (i.e. with the sample arm one cavity length longer than the reference). Other changes to the system included replacing the aiming laser with a power meter (to monitor reference arm power) and replacing the NewFocus balanced receiver with a Wieserlabs receiver (WL-BPD1GA) which had substantially higher bandwidth (1 GHz). Due to the low transimpedance gain of the Wieserlabs receiver, an RF amplifier (HD24388, HD Communications Corp.) was also used. A schematic of the buffered, extended-depth SSOCT system is shown Figure 4.11.

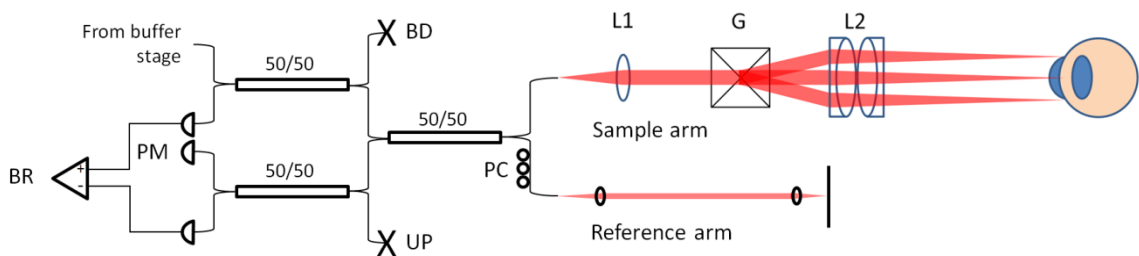


Figure 4.11: Schematic of buffered, extended-depth SSOCT system. BR: Balanced receiver. BD: Beam dump. UP: Unused port. PC: Polarization controller. L1, L2: Lenses. G: Galvanometers.

## 4.2.2. Results

### Peak Sensitivity and Sensitivity Fall-off

The system's peak sensitivity and sensitivity fall-off were measured, using techniques that have been described previously in section 3.2.2. The peak sensitivity was located at a depth of approximately 6mm and found to be 94 dB with 1.8mW on the sample, as compared to a theoretical shot-noise limited sensitivity of 102 dB. The 5 dB discrepancy is attributed to coherence revival sensitivity penalty, amplification noise, coupling losses and residual RIN. Although not shown here, the fall-off performance was nearly identical to the coherence results shown in section 3.2.2 (Figure 3.7), with a 9mm 6dB-imaging range spanning from 1.5mm to 10.5mm. Furthermore, both the peak sensitivity and 6dB-imaging range were identical for the forward and buffered sweeps.

### Imaging Results

Figure 4.12 shows a representative B-scan of the anterior segment of a healthy human volunteer. As before, each B-scans consisted of 800 A-scan pairs (1600 A-scans) and was acquired in 8 ms, supporting a framerate of 125 Hz. The image in Figure 4.12 represents 5 averaged frames, demonstrating the image quality that can be achieved at video rate, i.e. a frame rate of 25Hz. Figure 4.13 shows an enlargement of the apex of the cornea, and Figure 4.14 shows an enlargement of the iris and anterior surface of the crystalline lens.

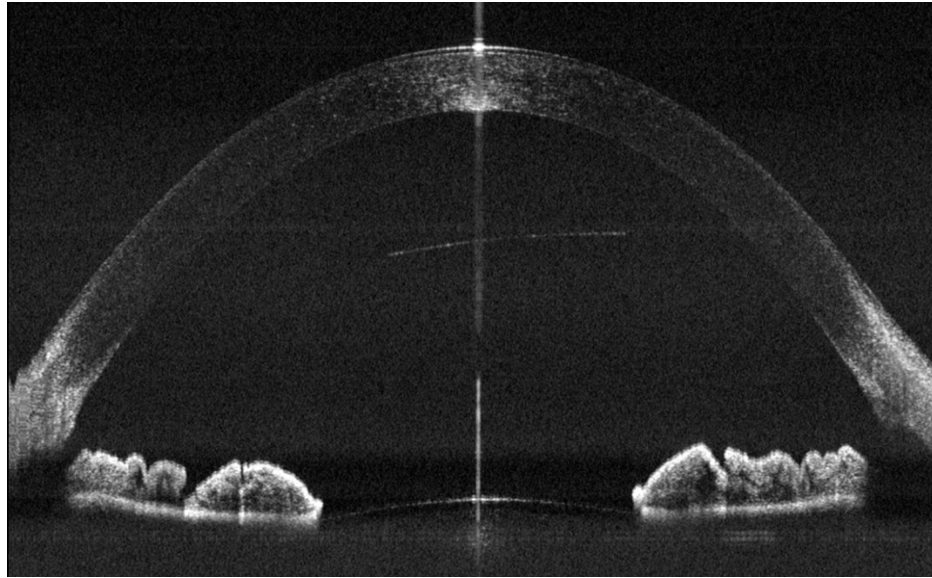


**Figure 4.12: In vivo B-scan of anterior segment. Image consists of 1600 A-scans x 5 averaged frames. Total acquisition time was 40msec.**

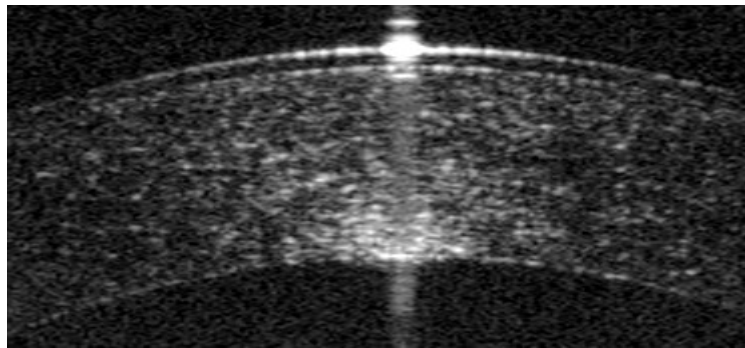


**Figure 4.13: Enlargement of apex of cornea from Figure 4.12**

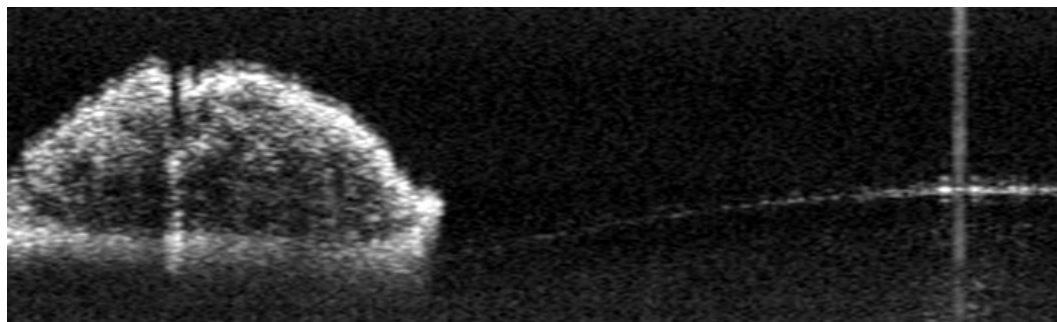


**Figure 4.14: Enlargement of iris and anterior lens from Figure 4.12**

### 4.2.3. Discussion

The artifact in the anterior chamber of the image in Figure 4.12 is a lens reflection that appeared due to coherence revival. Although not performed on this image, these lens reflection artifacts can be removed by background subtraction.

One potential concern with using the PMD compensation strategy described above is that, while it works well for imaging *through* birefringent tissues, it may not perform well for imaging *of* birefringent samples, as the polarization controller in the reference arm cannot compensate for polarization along the depth scan. Fortunately, it appears that the birefringence of the cornea does not produce significant artifacts in the images of the iris or anterior lens, as Figure 4.12 demonstrates artifact free imaging of the cornea and iris simultaneously. Furthermore, because there are no birefringent tissues in front of the cornea, as there are when imaging retina, the reference arm polarization controller would need to be optimized far less frequently, as long as no significant bending or twisting forces are applied to the fiber in the sample arm.

In summary, we have demonstrated that the previously described buffering technique is compatible with coherence revival-based heterodyne SSOCT, and demonstrated the simultaneous improvement of both the imaging speed and imaging depth of an SSOCT system based upon a turnkey, commercially available laser.

## 5. Towards “Whole-Eye” OCT

Whole-eye OCT refers to the use of OCT to image the entire optical system of the human eye, from the anterior surface of the cornea through to the choroidal-scleral interface. The motivation for the development of this technology is the ability to create customized, ray-traced optical models of patient eyes. These models could potentially enhance intraocular lens customization and refractive surgical interventions, and also facilitate the correction of optical distortions due to the cornea and crystalline lens in conventional retinal OCT diagnostics.

The ideal whole-eye OCT system would be able to acquire high resolution, motion-artifact free images of the anterior eye for anterior segment biometry, simultaneously with high resolution, wide-field, anatomically accurate images of the posterior eye. This lofty goal requires state-of-the-art OCT technology with optimal speed, sensitivity and resolution, as well as advanced image processing algorithms.

In section 5.1, the numerous challenges associated with realizing whole-eye OCT are outlined and discussed. In section 5.2, a technique that enables simultaneous, high speed and high resolution imaging of the anterior and posterior eye with a single SSOCT system is presented.

Theresa Bustamante contributed to the development of the dual-depth imaging system, constructing the sample arm of the first prototype dual-depth system. Derek

Nankivil contributed to the construction of later systems and also aided with data acquisition. Dr. Anthony Kuo provided valuable insights into the motivations and applications of the techniques developed in this chapter, and aided in the preparation of the related published manuscripts [124, 219].

## **5.1. Challenges in Realizing Whole-Eye OCT**

### **5.1.1. Imaging Depth**

Of course, the first challenge to realizing whole-eye OCT is an extension of the imaging depth. To facilitate imaging of the entire axial range of the eye, the inherent imaging depth be significantly extended from the typical 1~8 mm of existing clinical imaging systems. However, while the human eye extends over approximately 24mm of physical pathlength (32mm optical pathlength), a large portion of this axial length consists of optically transparent and relatively uninteresting vitreous gel. Thus, only a portion of this axial length must be imaged to provide a complete characterization of the optical system of the eye. These regions are shown in Figure 5.1. The anterior segment, which extends from the anterior cornea to the posterior lens, extends approximately 8mm in physical length [165], or 11mm in optical pathlength. The requirements for retinal imaging are somewhat more complicated, as the region of interest for imaging the retina is the inner surface of the globe of eye. However, as common practice with retinal OCT systems, the scanning mirrors can be imaged into the pupil of the eye, thereby using the

optics of the eye to perform a sector scan along the back of the eye (see section 5.1.3). Using this approach, a depth range of only ~2mm of optical pathlength is required to image the posterior eye.

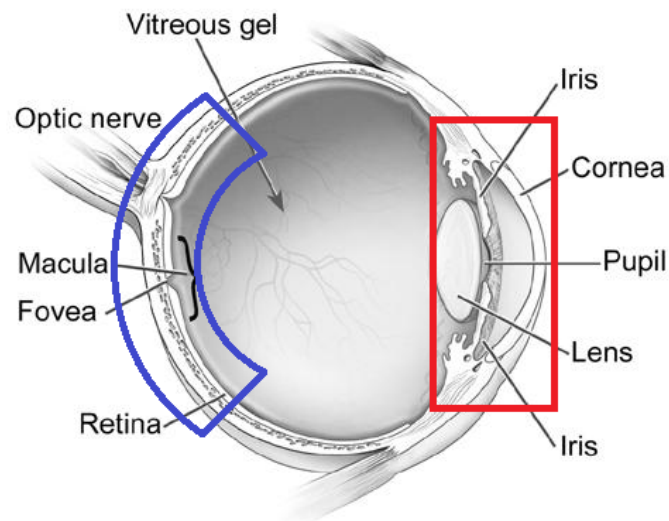


**Figure 5.1: Schematic of human eye showing regions of interest for whole-eye OCT. Anterior segment (red) and posterior eye (blue). Modified from [220]**

Thus, rather than imaging over 30+ mm of optical pathlength, an OCT system needs only ~15mm of optical pathlength imaging range if this range can be divided appropriately. We have demonstrated coherence revival-based OCT, which in theory could support imaging ranges exceeding 15mm if multiple cavity length offsets are used simultaneously. This idea will be further developed in the next section.

### 5.1.2. Imaging Speed

A second requirement of whole-eye OCT is that the imaging speed must be sufficiently fast to preclude image artifacts and errors in biometric measurements due to patient motion (discussed in section 1.5). We have demonstrated a high-speed and extended-depth imaging technique that enables A-scan rates of 200kHz (Chapter 4); other recent advances have also demonstrated extended-depth imaging at high speed using either strategies for extending the coherence length of FDML's [221], or next-generation MEMS-based VCSEL's lasers [88]. These advanced systems, operate at imaging rates approaching (or even exceeding) 1MHz, which is sufficiently fast to enable motion-artifact free volumetric imaging when combined with existing motion compensation strategies [178, 222]. However, these systems are currently pushing the limits of digitization and computer technology. For example, consider an OCT imaging system operating at 1MHz, with an optimal imaging depth range of 15mm and axial resolution of 5 microns. This system would produce data at a rate of 3GVoxels/s, and therefore require a digitization rate of 6 GHz (an extra factor of 2 is due to the complex conjugate). These data rates are currently pushing the limits of available digitization technology, as well as the limits of computer bus speeds and solid state drive write speeds. Thus, the biggest obstacle towards realizing megahertz (or even just hundreds of kilohertz) imaging speeds over the depth ranges required for whole-eye OCT is not

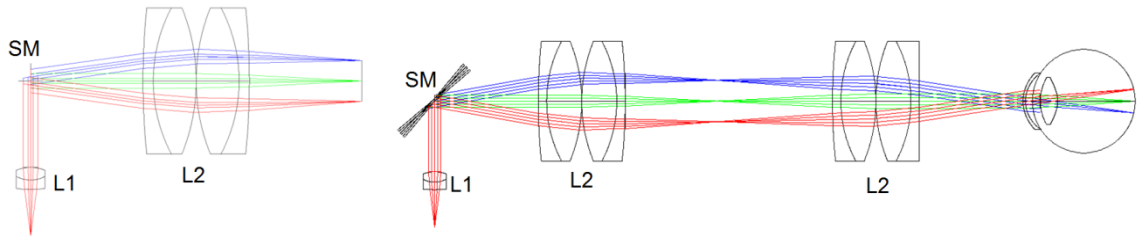
limitations of source or detector technology, but rather digitization and data streaming capabilities.

### **5.1.3. Optical Design**

The design of an optical system that can image the two regions of the eye highlighted in Figure 5.1, with sufficient resolution to be of clinical value, is a substantial challenge. Fortunately, the axial resolution in OCT is determined only by the properties of the source, and thus only the lateral resolution factors into the optical design. Nevertheless, the design of an optical system that can achieve the desired 30~50 micron lateral resolution in the anterior eye simultaneously with the 5~15 micron resolution in the posterior eye is a non-trivial problem.

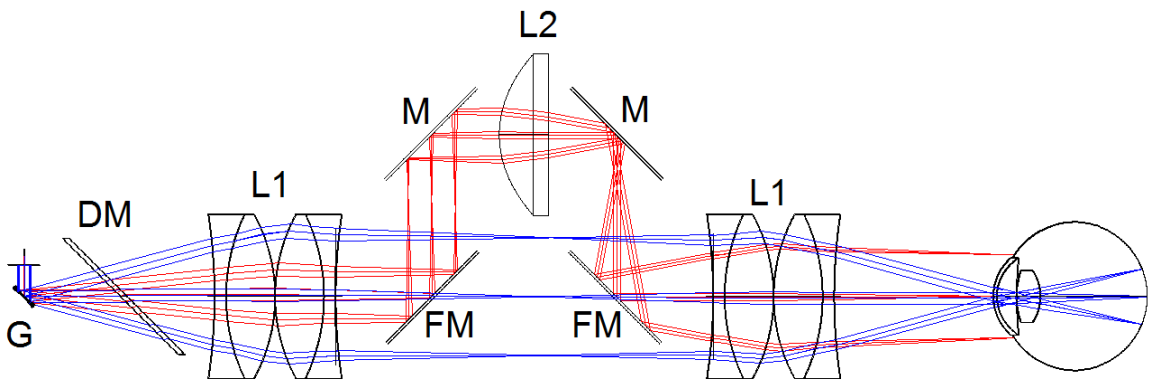
Of all the extended imaging range techniques introduced in section 1.3.5, the multiple focal plane techniques are perhaps the most promising. Thus, one potential solution for extending achieving high lateral resolution in the anterior and posterior eye is to use a multiple focal plane approach. Figure 5.2 shows schematics of the typical optical designs used for OCT imaging of the anterior and posterior eye. For anterior segment imaging, a “telecentric” configuration is typically used, where the scanning mirrors are placed a focal length away from the objective lens, and the object plane lies a focal length away on the opposite side. For retinal imaging, a 4F system is used to

image the scanning mirrors into the pupil of the patient eye, resulting in a “sector scan” that produces a curved focal plane on the retina.



**Figure 5.2: Schematics of optical designs typically used for OCT imaging of the anterior segment (left) and retina (right). SM: scanning mirror. L1,L2: lenses.**

To demonstrate how these two optical designs can be combined to image the anterior and posterior eye in a single system, we designed the OCT sample arm depicted in Figure 5.3.



**Figure 5.3: Sample arm design of sequential imaging of anterior (red) and posterior eye (blue). G: galvanometers. DM: dichroic mirror for fixation target (not shown). L1: Identical compound achromatic lenses. L2: Aspherical lens. M: Fixed mirrors. FM: Flip mirrors.**

In this design, a pair of “flip mirrors” can be slid into and out of the optical path. With the mirrors in place, the rays drawn in red demonstrate how a telecentric scan over the entire lateral range of interest of the anterior segment could be achieved. With the mirrors removed, the blue rays demonstrate the common sector-scanning approach to imaging the retina, where the scanning mirrors have been imaged into the pupil plane. This system also allows for the optical design to be optimized for each imaging depth. That is, the lateral resolution and axial depth-of-field trade-off can be managed separately for each depth. Of course, the major drawback of this design is that the anterior and posterior scans must be performed sequentially. In the next section, we demonstrate an extension of this optical design that enables simultaneous, as opposed to sequential, imaging of the anterior and posterior eye.

#### **5.1.4. Image Processing and Analysis**

Assuming that the imaging depth, imaging speed and optical design challenges can be met, the final challenge that must be addressed is the correction of the acquired images and the extraction of biometric parameters from the anterior eye. Significant progress has been made in these areas, with advanced algorithms for motion correction [178, 223], segmentation [181, 194], non-telecentric scan correction [168], refraction correction [168, 180], and extraction of corneal power and topography [163, 164, 170, 179, 182, 183]. However, considerable work remains to be done to validate these biometric

measurements against existing clinical standards, as well as to extend the characterization that has been performed on the cornea to the crystalline lens.

In addition to anterior eye biometry, whole-eye OCT also has the potential to correct artifacts and distortions in the retinal OCT images using parameters measured from the simultaneously acquired anterior segment images. To date, little has been published on this application, though it is an active area of research<sup>3</sup>.

## **5.2. *Simultaneous SSOCT of the Anterior and Posterior Eye***

### **5.2.1. Introduction**

As OCT develops into an important tool for anterior segment characterization, the ability to use a single system for both anterior and posterior imaging becomes a desirable feature for clinical systems. Several commercial ophthalmic OCT systems are capable of switching between anterior segment and retinal imaging modes, allowing a single system to function in both capacities. However, switching between modes requires the addition or removal of optics from the sample path and adjustment to the length of the reference path. Also, as these systems are designed primarily for retinal imaging, anterior segment imaging performance (particularly axial and lateral field of view) is typically suboptimal.

---

<sup>3</sup> Dr. Anthony Kuo has performed substantial work towards understanding the effect that patient alignment and patient optics have on retinal image quality, including ray tracing models and experimental validation.

In addition, a few research systems have been developed to demonstrate whole eye-OCT [123, 158, 172]. However, these systems have all made sacrifices in imaging speed, transverse resolution and/or field-of-view to achieve the large axial field-of-view. Here, we present a novel OCT system that avoids the depth-of-field and lateral resolution trade-off of traditional, single-depth OCT systems, enabling simultaneous, high resolution imaging of the both the anterior and posterior eye. Simultaneous imaging is achieved by combining coherence-revival based SSOCT with a polarization-encoded sample arm. To demonstrate the feasibility of this technique for *in vivo* ophthalmic imaging, the system was used to simultaneously image the anterior segments and retinas of healthy human volunteers.

### **5.2.2. Methods**

We describe an extension of the coherence revival based heterodyne SSOCT that enables simultaneous imaging of two different regions of the eye. This was achieved through the use of a dual-channel sample arm that simultaneously scanned the anterior segment and retina. The path through the sample arm that imaged the retina (the “retinal path”) was matched to the reference arm pathlength, encoding the retinal image at the baseband for conventional SSOCT imaging. The “anterior segment path” was offset from the reference arm pathlength by a distance equal to the laser cavity length, which encoded the anterior segment interferogram with a carrier frequency. As a result, after inverse

Fourier transformation of the acquired spectral interferogram, the retinal image appeared near DC while the anterior segment image appeared shifted in depth. This precluded overlap of the two images while also resolving the complex conjugate artifact for the anterior segment image.

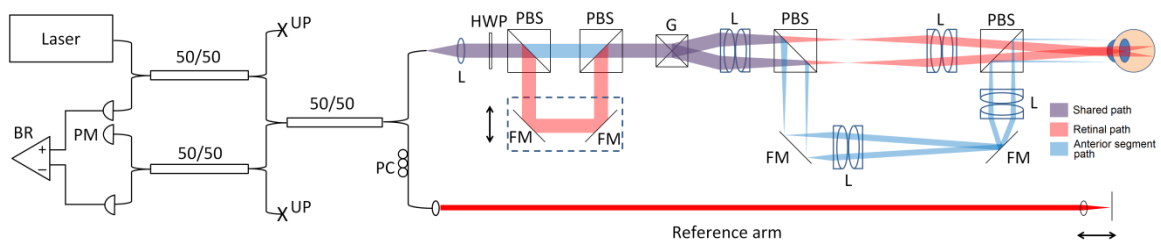


**Figure 5.4: SSOCT system schematic. BR: Balanced receiver. PM: power meter. UP: Unused ports, PC: polarization controller. Sample arm: Red and blue lines depict the retinal and anterior segment imaging paths, respectively. Overlapping paths are shown in purple. L: Lens. HWP: half-wave plate. PBS: Polarizing beamsplitter. FM: fold mirror. G: Galvanometers**

A schematic of the dual-channel sample arm is shown in Figure 5.4. The incoming polarization was controlled by the half-wave plate (HWP) before reaching the first PBS. Light emerging from the single mode fiber was partially polarized, such that rotation of the wave plate could direct as much as 83% of the incident light to either path. This implies that the degree of polarization of the source was 66%. The transmitted polarization experienced a fixed delay, whereas the reflected polarization experienced a longer and variable delay that could be adjusted via a translation stage (dashed box in Figure 5.4). The two polarizations were then recombined at the second PBS and scanned by a pair of orthogonal galvanometer mirrors. Reflections at the galvanometer mirrors

resulted in a rotation of the polarization, such that the P and S polarizations were switched. When the scanned beams reached the third PBS, the polarization state that had initially been reflected was then transmitted, and vice versa. Following this second split, each path contained carefully designed optics optimized for either anterior segment or retinal imaging, allowing for the acquisition of images of both regions of the subject's eye with no adjustment of the sample arm optics. The two paths were then recombined at the fourth PBS and directed to the patient eye.

Sample arm optics were optimized in Zemax to provide the optimal trade-off between resolution, aberration and depth of focus for each imaging depth using off-the-shelf achromatic doublets. The retinal imaging optics were optimized using an eye model with a gradient index lens [83], and designed to scan a 2.6 mm beam incident on the cornea, pivoting through the pupil about a 17.4 degree scan range. The anterior segment path was designed to have a lateral resolution of 30  $\mu\text{m}$  (defined as the FWHM of the PSF), and a 15.1 mm lateral scan range. This lower lateral resolution allowed for a much longer depth of field to permit imaging through the entire anterior chamber. The axial resolution for both paths was < 10  $\mu\text{m}$ , limited by the spectral shaping window applied in processing.

Key features of the combined polarization and depth encoding schemes used in this system are optimal optical power conservation and crosstalk rejection. The two sets of PBS cubes effectively created two polarization channels. Neglecting the finite

extinction ratios of the PBS cubes, all of the light whose polarization was not modified in the sample returned in the appropriate polarization channel, thereby limiting the sensitivity loss in each channel for dual-channel imaging to a single factor of -3 dB. Returning light whose polarization was modified either by depolarization or birefringence in the sample (and thus contaminated the wrong polarization channel) was also depth encoded and thus lost to imaging, but did not degrade the other image.

The SSOCCT system topology is also shown in Figure 5.4. An external cavity tunable laser (Axsun Technologies) operating at a 100 kHz sweep rate, output power of 22 mW, central wavelength of 1040 nm, and bandwidth of 100 nm was used as the source. A spectrally balanced Michelson fiber interferometer design [151] was used. While this interferometer design contains an inherent 3dB inefficiency, it provides near-ideal spectrally balanced detection, which significantly reduces relative intensity noise (RIN) from the source. The power incident on the patient eye was 900  $\mu$ W per channel, for a total of 1.8 mW. This is in compliance with the most stringent interpretation of the ANSI Z136.1 standard [159]. Light returning from the interferometer was detected on a 1 GHz InGaAs balanced receiver (WL-BPD1GA, Wieserlabs) and digitized at 1 GS/s on an 8-bit (6.7-ENOB), 500 MHz bandwidth digitizer (ATS9870, Alazar Tech). Data acquisition and processing were performed in LabVIEW and C. Separate dispersion compensation algorithms were applied for each depth, which is a requirement of the coherence revival technique [107].

### 5.2.3. System performance

For each channel of the sample arm, power efficiency, peak sensitivity and sensitivity fall-off profiles were measured. Power efficiency measurements were made by placing a mirror in the sample arm and measuring the optical power returning in the power meter channel as a fraction of the power incident on the sample. The retinal channel power efficiency was measured to be 40%, whereas the anterior segment channel efficiency was measured to be 38%.

Peak sensitivity and sensitivity fall-off profiles were measured by placing a -48 dB calibrated reflector in the sample arm and translating the reference mirror. Sensitivity was then computed as the ratio of the peak of the A-scan to the standard deviation of the noise floor measured with the sample arm blocked. The peak sensitivity was 96 dB for retinal imaging and 95 dB for anterior segment imaging; the 1 dB difference is a consequence of the coherence revival fall-off envelope [107]. The theoretical, shot-noise limited sensitivity was computed, as described in [51], to be 102 dB for each channel; this value includes the inherent 3 dB inefficiency of the spectrally balanced interferometer. The discrepancy between the theoretical and measured sensitivities can be partially explained by optical losses (4 dB). The remaining 2 dB discrepancy was likely due to digitization noise and residual RIN not rejected by spectral balancing.

#### 5.2.4. Results

Sensitivity fall-off profiles for each imaging channel are shown in Figure 5.5. For the retinal channel, we observed an imaging range of 5.2 mm in air (3.9 mm in tissue), defined as the region over which the sensitivity loss measured from the zero pathlength difference (ZPD) position was less than 6 dB. For anterior segment imaging, the peak sensitivity position appeared at approximately 6 mm in depth, and the anterior segment imaging region spanned approximately 8.5 mm (6.4 mm in tissue) from 1.5 mm to 10 mm. A full doubling of the 5.2 mm imaging depth was not achieved due to limited electronic bandwidth of the digitizer.

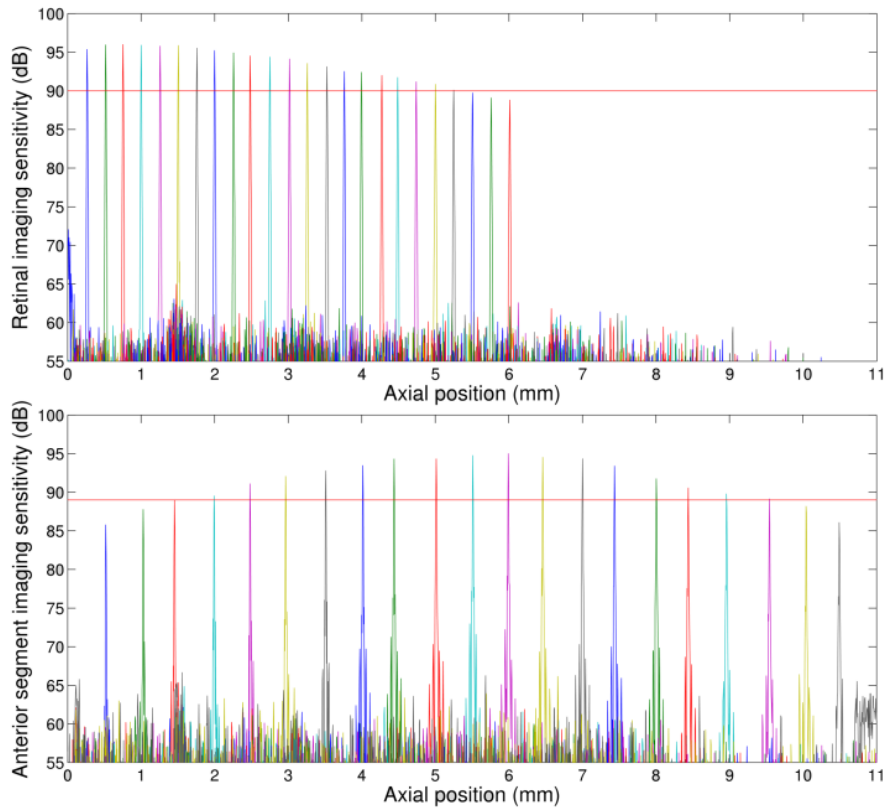


**Figure 5.5: Sensitivity fall-off profiles for the retinal (top) and anterior segment (bottom) imaging channels. Red horizontal lines are drawn at -6dB sensitivity from the peak.**

Thus, there existed a 1.5 mm region in which the retina could be imaged without limiting the imaging range of the anterior segment. While it is possible for faint anterior segment structures to appear in this 1.5mm region, this was avoided by managing the orientation of each image, as described below. This 1.5 mm retinal imaging range is comparable to the imaging depth of clinical SDOCT systems, and could be extended at the expense of anterior segment imaging range if necessary.

To demonstrate feasibility *in vivo*, images were acquired from three healthy human volunteers. Dual-depth B-scans were acquired at 50 Hz for 2000 (lateral) x 2304 (axial) pixel images. Figure 5.6A shows a typical B-scan as observed during acquisition. The retina appears “above” the anterior segment, and both images are upright. This orientation was chosen as it precludes the possibility of crosstalk between deeper structures in the anterior segment and the retinal image. Figure 5.6B and C show images from the same data set after further processing, including dispersion compensation for the anterior segment image, cropping, scaling, and averaging. Finally, Figure 5.7 shows 3D renderings of simultaneously acquired volumes of the anterior and posterior eye.

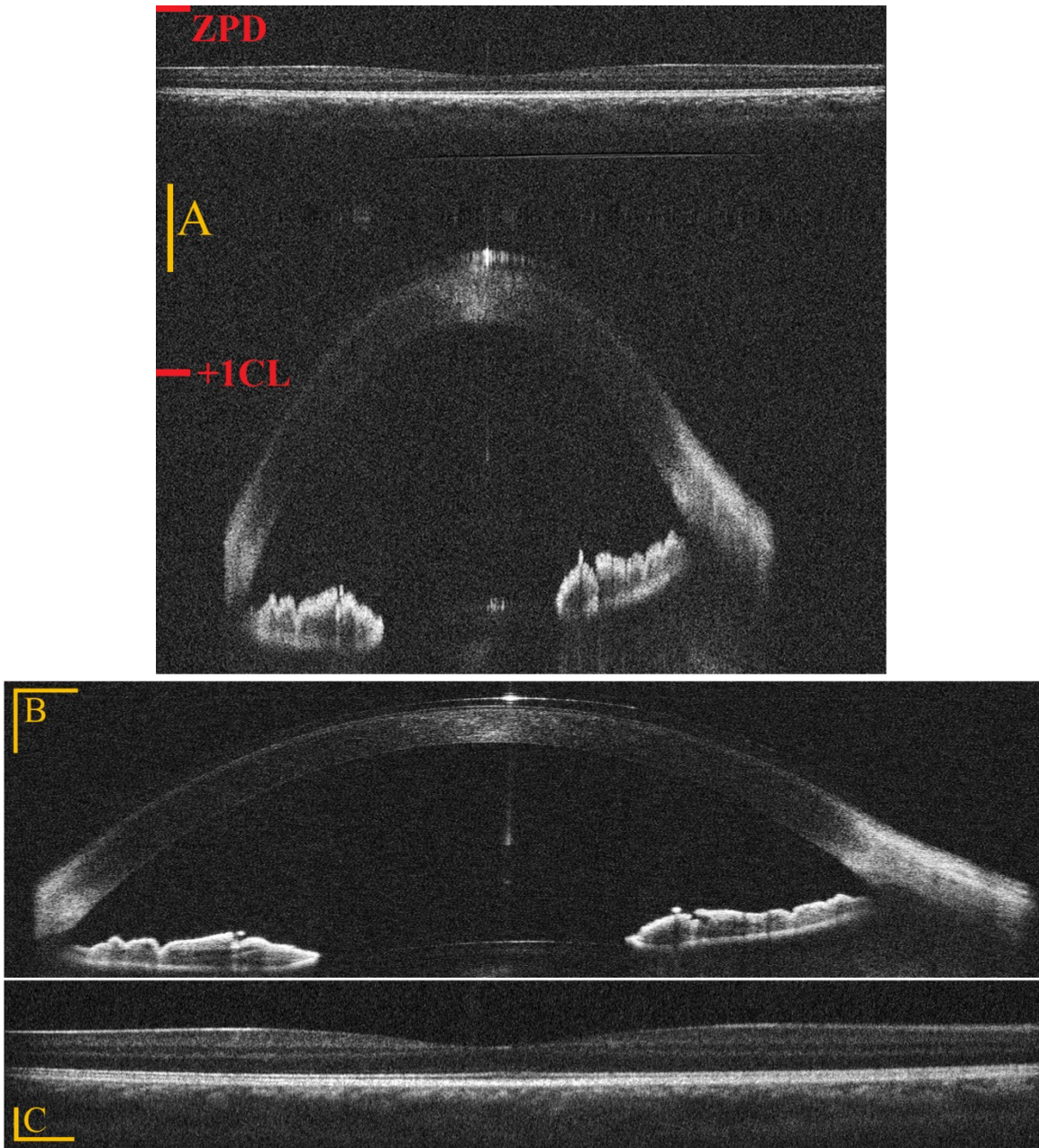
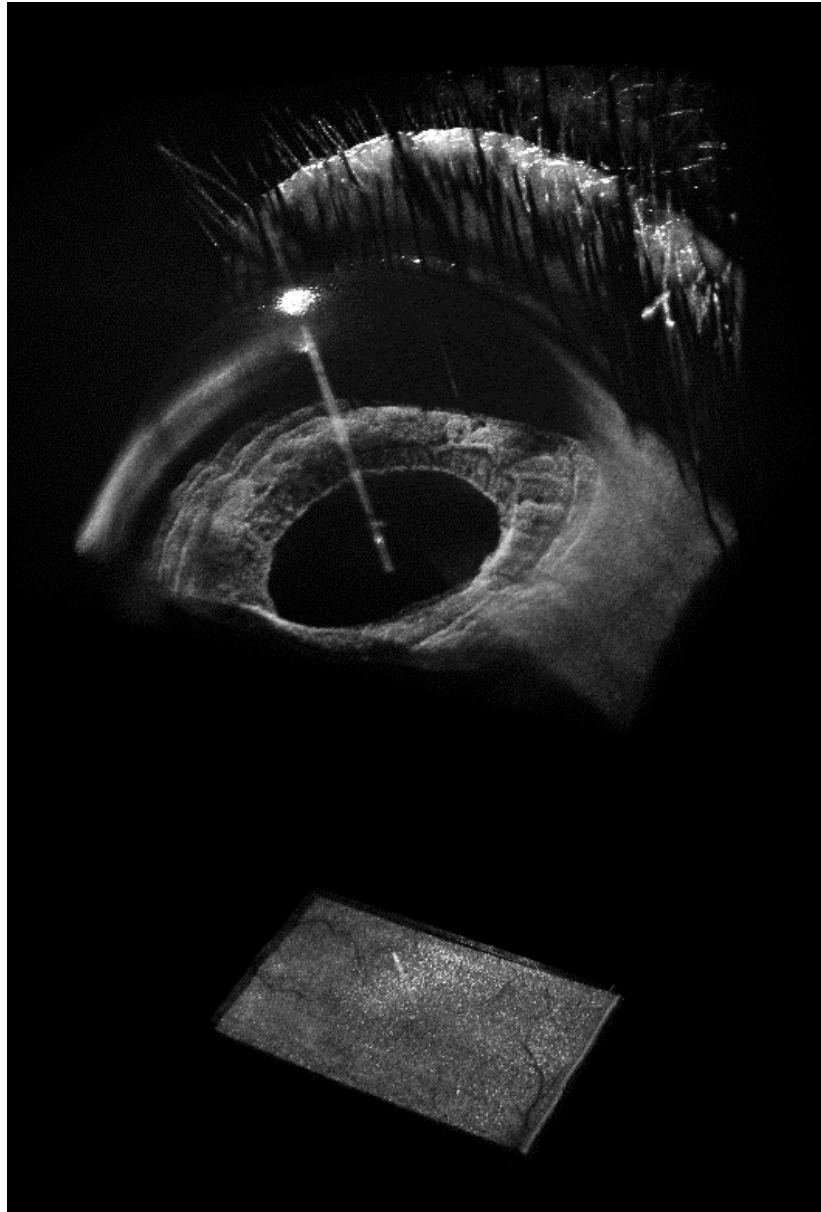
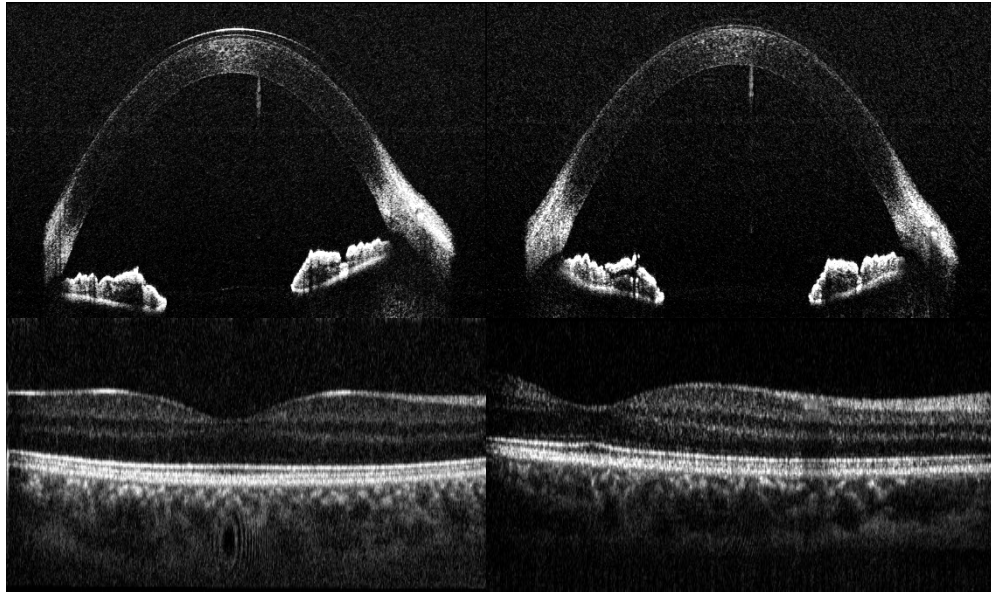


Figure 5.6: Simultaneously acquired anterior segment and retinal images. A: A single frame as acquired before cropping and dispersion compensation, consisting of 2000 (lateral) x 2304 (axial) samples, acquired in 20msec. ZPD: Zero pathlength difference position, +1CL: Cavity length offset position. B and C: Separated anterior segment and retinal images, averaged over 5 frames. Scale bars are 1mm, 1mm x 1mm and 250  $\mu\text{m}$  x  $1^\circ$  in A, B and C, respectively.



**Figure 5.7: 3D rendering of simultaneously acquired anterior segment and retinal volumes.**  
Total acquisition consisted of 2304 x 500 x 200 samples, acquired in 1 s.



**Figure 5.8: SSOCT B-scans taken with the OCT system aligned with the volunteer's visual axis (left) and optical axis (right). Each pair of images consists of 1600 (lateral) by 2304 (axial) samples x 5 averaged frames, acquired in 40 msec each.**

In Figure 5.6, the anterior segment image appears slightly angled because the optical axis of the system was aligned with the volunteer's visual axis, and thus offset from the optical axis of the eye by a few degrees. As a result, the fovea was centered in the retinal image, but the anterior segment was angled. The distinction between the optical and visual axes is portrayed in Figure 5.8. The two images on left were acquired simultaneously, with the SSOCT system aligned with the patient visual axis. Thus, the fovea is again centered in the image, but the anterior segment is skewed. The two images on the right were acquired with the SSOCT system aligned with the volunteer's optical axis. Here, the anterior segment image appears upright, but the fovea is off-center.

### **5.2.5. Summary**

We have reported on an SSOCT system design that enables simultaneous imaging of the retina and anterior segment. This design employs polarization encoding and coherence revival to discriminate each imaging depth, and allows for the optical design of each sample path to be optimized independently. While coherence revival-based frequency encoding is only applicable to certain sources, the polarization encoded sample arm design is applicable to any extended depth SSOCT system, provided that the relative delay between the two sample paths is adjusted accordingly.

## 6. Conclusions and Future Directions

In the preceding chapters, we have discussed recent advancements in the imaging speed and imaging depth of SSOCT techniques. These developments, in addition to other recent advancements in FDML technologies [73, 151, 221, 224], and especially vertical cavity surface emitting lasers (VCSEL's) [88] have enabled high speed and extended depth SSOCT technology to the extent that the imaging speed and inherent imaging range limitations (i.e. sensitivity fall-off and the complex conjugate) no longer restrict the applicability of these systems. However, system designs taking advantage of these advanced capabilities are still in development. In the following sections, we present on-going and proposed future projects that make use of the technologies described in the preceding chapters.

## **6.1. Field-Deployable, Handheld SSOCT System for Sequential Anterior/Posterior Ocular Imaging**

### **6.1.1. Motivation**

A common adage used in the triage of injuries is “life, limb, or eyesight.” Injuries that threaten any of these three have severe long-term consequences for the affected individual, military/veteran health care organizations, and society as a whole. Hence, injuries to “life, limb, or eyesight” need to be quickly identified and prioritized during triage. The incidence of combat related ocular injuries in modern warfare is unfortunately not uncommon, and was reported to be 13% in a recent analysis of combat related ocular trauma during portions of the Iraqi conflicts [225]. While combat related ocular injuries from close-range explosive munitions in recent conflicts were readily recognized by most medical personnel and quickly evacuated [225, 226], less dramatic presentations of ocular trauma can be difficult for non-specialist personnel to properly and quickly diagnose, or to distinguish between the various pathologies that can affect eyesight. In theatre, such scenarios can result from activities ranging from combat (e.g. guns/explosives handling), to training (e.g., transport, falls), to leisure (sports, horseplay) [227].

A presenting complaint as apparently simple as blurry vision can be a result of pathologies ranging from the vision-threatening (corneal ulcer, laceration) to the mundane (dry eye, need for glasses). A review of individuals evacuated out of theatre solely for ocular conditions in Iraq and Afghanistan from 2003-2004 showed that only

11% had truly acute, vision-threatening conditions [228]. The majority of the rest had chronic conditions which in some cases had existed even prior to deployment. As specialist physicians are generally in limited supply, a system and/or device to help non-ophthalmic medical personnel examine the eye and help distinguish between the mundane and the truly vision-threatening for triage has the potential to maximize use of available resources.

OCT generates high resolution images that provide more anatomic information than is available from the standard slit-lamp biomicroscope and ophthalmoscope. Furthermore, in contrast to the slit lamp biomicroscope and especially the ophthalmoscope – both of which may be difficult for the non-eye care specialist to use with proficiency – OCT is typically operated in the civilian setting by trained non-medical personnel (i.e., ophthalmic photographers). For the military setting, whether at the field, battalion aid stations, theater hospitals, base clinics, or other clinical settings, a ruggedized, portable OCT system could potentially be utilized by any lightly trained provider – physicians and nonphysicians – to examine and assist in the triage of ocular pathology.

Furthermore, as a digital platform, OCT examinations are stored and can be transmitted for review with consultants without subjecting the patient to reexamination, a particularly useful benefit when repeated examination may cause discomfort to the patient. A faithful digital volumetric representation of the entire eye as obtained with

the proposed OCT system would be valuable for teleconsultation with tertiary specialists. In addition, given the current average 5 hour response time in teleconsultation programs, initial screening of the OCT images with specialized software would give deployed providers immediate feedback, decision support, and case prioritization at the point of care.

### **6.1.2. System design**

The system proposed here employs an Axsun Technologies ECTL, operating at 100kHz sweep rate with a central wavelength of 1040nm and tuning bandwidth of 100nm. The single-sided imaging range of this laser is approximately 5mm, and will be doubled (as we have already demonstrated, discussed in chapter 3) using coherence revival to approximately 10mm. To achieve rapidly switchable imaging of two different imaging depths (the anterior segment and retina) the location of this 10mm imaging region must be changed to match the optical path delay of the desired imaging depth.

Existing convertible anterior/posterior commercial SDOCT systems switch the imaging region by physically replacing some portion of the sample arm optics and translating the reference mirror over a long distance, a slow process that requires the use of very long travel linear translators and is particularly susceptible to misalignment. Our proposed approach for much more rapid and robust optical switching between anterior and posterior segment imaging in the sample arm is the subject of the next section. To

similarly switch the reference arm delay, we propose to employ a MEMS fiber optic switch (e.g. OSW12-980- SM, Thorlabs Inc.) to switch between two pre-set reference delays, as depicted in Figure 6.1. It should be noted that, in contrast to the fast optical switch described in chapter 4, which split the incoming light by polarization and employed the electro-optic effect, this switch is MEMS-based, and thus does not result in the generation of PMD.

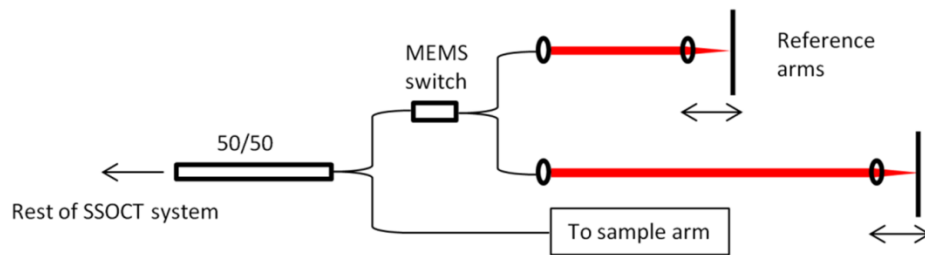


**Figure 6.1: Schematic of rapidly switchable dual reference arm configuration based on a MEMS fiber optic switch**

This switch supports switching times that are very fast compared to a B-scan ( $< 1\text{ms}$ ), and its operation involves no physical modification potentially introducing misalignment to the bulk optic component of either reference delay. Furthermore, because the system uses two relatively short reference arms, as compared to a single long travel reference arm, it is inherently robust against misalignment due to system drift or acute mechanical shock.

As discussed in section 5.1.3, the design of an OCT sample arm that can rapidly switch between states that efficiently focus light onto either the anterior or posterior segments of the human eye is a non-trivial problem. Constructing such a system with a sufficiently small form factor to be used as either a handheld or tabletop device further constrains the design. Conventional retinal OCT scanning schemes require imaging the scanning mirrors into the pupil plane of the patient eye in a 4F configuration, with an optimal beam size of ~3mm to achieve maximum lateral resolution on the retina of ~15 microns spot size limited by the patient's own optics [229]. Anterior segment scanning schemes depend strongly on the trade-off between lateral resolution and axial depth-of-field [87]. For the anterior segment scanning optics, a target 34 micron spot size (Gaussian spot waist) provides a depth of field (confocal parameter) of 7.4mm, corresponding well to the proposed system's 10mm imaging range, after correcting for refractive index, while still providing sufficient resolution for the characterization of refractive interfaces.

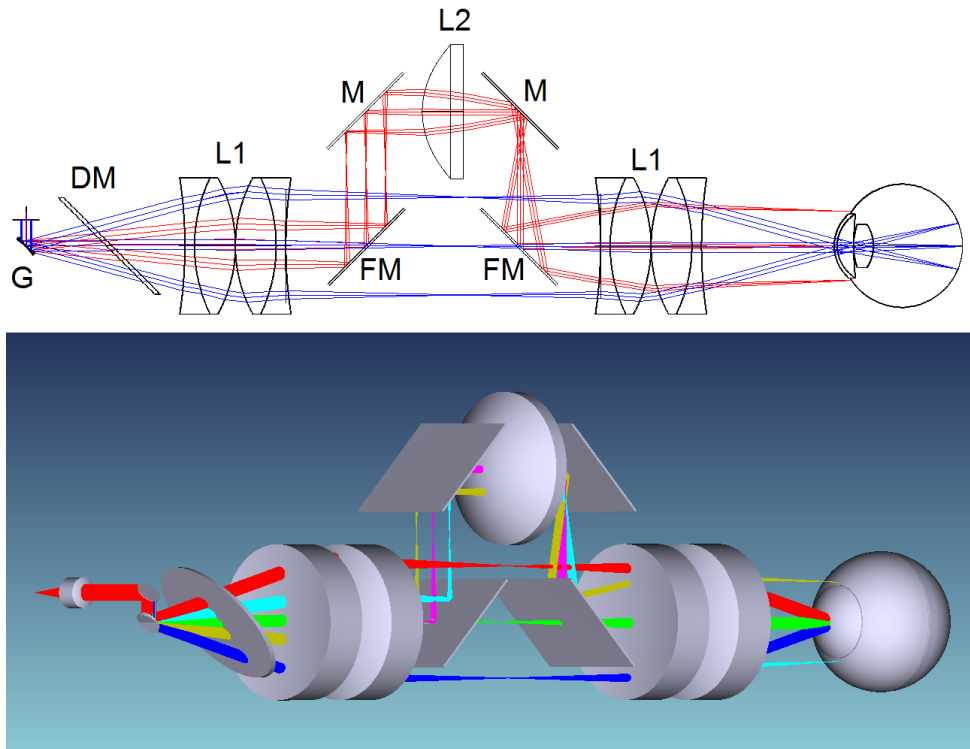


**Figure 6.2: Top: Schematic of a switchable sample arm design showing retinal imaging (blue) and anterior segment imaging (red) states. G: Galvanometers. DM: Dichroic mirror (for fixation target, not shown). L1: Compound achromatic lenses. L2: Aspherical lens. M: Fixed mirrors. FM: Flip mirrors. Bottom: 3D rendering of the same sample arm design.**

The proposed rapidly-convertible sample arm design, depicted in Figure 6.2, employs two “flip mirrors” that allow the system to be rapidly switched between retinal and anterior segment imaging modes. These commercially available motorized flip mounts (MFF001, Thorlabs Inc.) provide precise and repeatable removal and repositioning of mirrors in the beam path, with response times <500ms. A single electrical trigger will initiate a state change of the two flip mirrors in the sample arm as well as the MEMS switch in the reference arm (Figure 6.1). Light emerging from the sample arm fiber is collimated to a 2.6 mm diameter beam, which is then scanned in the

X and Y dimensions by a galvanometer mirror pair. The scanned beam is then refracted by a pair of matched 1" diameter 75mm achromatic lenses that are common to both paths. The anterior segment path is active when the flip mirrors are positioned in the beam path, and is illustrated in red in the schematic in Figure 6.2. In this path, a very large F-number aspheric lens (1" diameter, 20mm focal length) forms an image of the galvanometer mirrors in a 4F configuration. This galvanometer image is then used to create a 2F telecentric scanning system using a second matched pair of 1" diameter 75mm achromatic lenses. This system design produces a 30Mm spot in the anterior chamber of the patient's eye (defined as the FWHM of the lateral PSF), which corresponds to a  $\sim 35\mu\text{m}$  Gaussian spot waist and 7.5mm imaging range (confocal parameter), allowing full use of the depth afforded by the SSOCT engine. Note that imaging the entire depth of the anterior segment at once, as mandated by the requirements of the proposed device, necessitates a tradeoff from the single micronscale lateral resolution typically desired in OCT. However, this resolution still generates excellent quality images of all structures including cornea and iris (e.g., Figure 3.9). The lateral scan range across the anterior segment is approximately 15mmx15mm for diffraction limited performance; scan ranges exceeding 20mmx20mm can be achieved with some loss of resolution. The retinal path is active when the flip mirrors are positioned out of the beam path, and is illustrated in blue in the schematic in Figure 6.2. In this configuration, the two pairs of 75mm achromatic lenses form an image of the

galvanometer mirrors in a 4F configuration in the pupil plane of the patient. The beam pivoting in the patient's pupil is 2.6mm in diameter. Assuming (optimistically) the patient's eye has diffraction limited performance over that aperture, a spot size of  $7.7\mu\text{m}$  is produced on the retina. Neglecting the refractive index change, the beam pivots through an optical angle of approximately 30 degrees through the pupil. Finally, in addition to providing excellent imaging performance for both anterior segment and retinal imaging, this design is extremely compact, spanning only 5" x 2" (excluding working distance to the patient eye). This compact design is possible due to the use of matched pairs of achromatic lenses as well as a large F-number asphere.

## **6.2. Intrasurgical OCT imaging with extended-depth SSOCT**

Real-time 3D visualization of vitreoretinal surgery has the potential to improve patient outcomes by providing surgeons with immediate visual feedback on complex surgical maneuvers. Among the most challenging aspects of these surgeries are the difficulty in distinguishing tissues with subtle contrast and the uncertainty in the judgment of distances and relative positions within the patient eye [230]. First-line techniques to improve visualization pose potential hazards to patients; increasing the optical power emitted by endoilluminators used for wide-field illumination increases already elevated risks of photothermal/photochemical toxicity [231], while the use of fluorescent stains such as indocyanine green has been shown to cause reduced visual acuity and peripheral visual field loss [232].

Optical coherence tomography is an ideal candidate for intrasurgical visualization of vitreoretinal surgery, given its proven track record of providing high-speed, high resolution, and high contrast volumetric images of retinal tissue *in vivo* within safe optical exposure limits [159]. The recent demonstration of an SDOCT system integrated into a surgical microscope has established the feasibility of such systems [233-236], yielding high resolution (12 $\mu$ m lateral and 6.5  $\mu$ m axial) and high sensitivity (112 dB) OCT imaging with only 700 $\mu$ W of optical power incident on the patient eye. A schematic of an existing intrasurgical SDOCT system is shown in Figure 6.3.

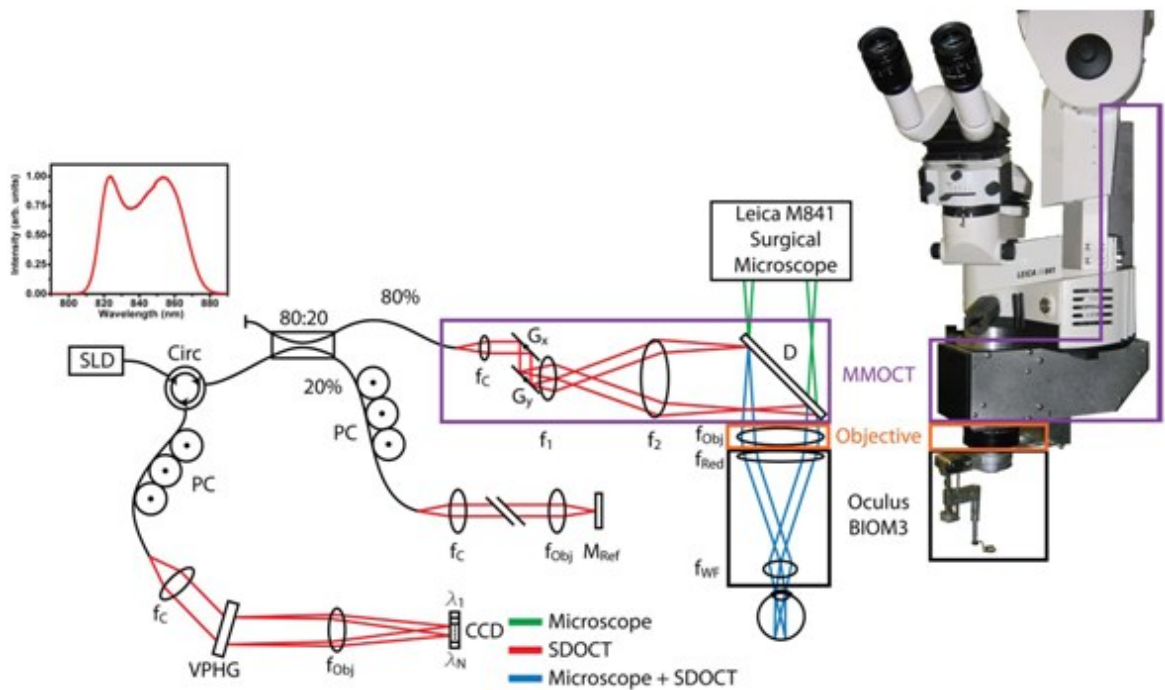


Figure 6.3: Existing design of the intrasurgical MM-SDOCT system, from [233].

The OCT engine used in this system is somewhat outdated, especially with respect to its relatively slow imaging speed (20kHz A-scan rate) and limited axial imaging range (1.45mm). Application of the techniques described in the preceding chapters would enable significantly improved imaging speed and imaging depth. In fact, implementation of the buffered, complex conjugate resolved SSOCT system described in section 4.2 would provide a 10-fold improvement in imaging speed and more than a 5-fold improvement in imaging depth. The increased imaging speed could provide significantly more information to the surgeon, for example, by enabling simultaneous visualization of multiple orthogonal views, or multiple parallel views staggered around

a region of interest. The increased imaging range would greatly simplify initial alignment of the system prior to each procedure and would offer a significant increase in system robustness to misalignment during complicated surgical procedures.

Of course, these improvements come at a price, specifically a substantial loss in imaging sensitivity (from 112dB to 98dB). However, much of this sensitivity loss could be compensated for by dense scanning and frame averaging, which are facilitated by the substantially improved imaging speed. It should be noted that, despite the difference in operating wavelength, both the system described [233] and the system described in section 4.2 have comparable axial resolution ( $\sim 7 \mu\text{m}$  in air,  $\sim 5 \mu\text{m}$  in tissue).

Constructing a SSOCT intrasurgical microscope based on the SSOCT engine described in section 4.2 and the existing intrasurgical SDOCT system shown in Figure 6.3 can be accomplished as follows. Of course, the SLD and spectrometer would be replaced by an appropriate swept source laser and balanced receiver. Beyond that, most of the required changes arise because of the difference in operating wavelength; while the existing SDOCT system operates around 840nm, the proposed SSOCT engine operates at 1040nm. Thus, the fiber interferometer and the dichroic mirror (denoted "D" in Figure 6.3) would be different. Fortunately, the so-called "B-coated" optics (in reference to Thorlabs' model numbers for optics with an NIR coating) used in the existing system work reasonably well around 1040nm, and thus the same optical design

could be reused, although re-optimization (to account for the slight variance in glass index of refraction) should be performed.

A significant obstacle that must be addressed before intrasurgical OCT can reach its full potential is the development of technology for real time display. Display technologies have lagged significantly behind the technological advancements in high speed FDOCT, to the extent that most high speed systems are capable of displaying in real-time only a subset of the information that is acquired. While this is not problematic for most clinical applications, where viewing the data after post-processing is feasible, this is clearly not the case for intrasurgical applications. As such, the development of hardware and algorithms that enable real time processing is critical.

Recently, the use of two alternative processing technologies for processing of OCT data has been explored: graphical programming units (GPU's) [237] and field programmable gate arrays (FPGA's) [238]. The implementation of either, or both, of these technologies will be critical to the implementation of high speed OCT systems in surgery, as without the capability for real-time processing and display, the improved imaging speed of the proposed SSOCT system would be for naught.

### **6.3. *Time and polarization–encoded dual depth SSOCT***

The dual-depth OCT system described in Chapter 4 employed both polarization-encoding and coherence revival-based frequency encoding to enable simultaneous imaging of the anterior segment and retina. While coherence revival-based frequency encoding is only applicable to sources that exhibit this behavior, the polarization encoded sample arm design is more widely applicable. For example, the sample arm design is compatible with any extended depth SSOCT system, provided that source has sufficient coherence length and the relative delay between the two sample paths is adjusted accordingly. Alternatively, the sample arm design can also be combined with an optical switch to enable time- and polarization-encoded imaging of multiple depths within a sample. One potential embodiment of a time- and polarization-encoded dual depth SSOCT system is described here.

Dual depth imaging can be achieved by combining a standard SSOCT system with a polarization encoded sample arm, and by placing fast optical switches in both the sample and reference arms. A schematic of such a system is shown in Figure 6.4.

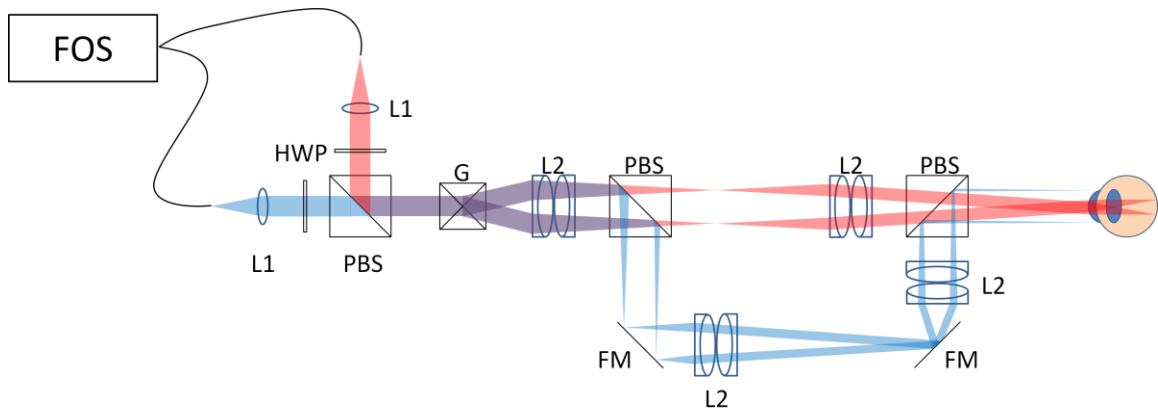


**Figure 6.4: Schematic of a time and polarization encoded dual-depth sample arm. Red and blue lines depict the retinal and anterior segment imaging paths, respectively. Overlapping paths are shown in purple. FOS: Fast optical switch. L: Lens. HWP: half-wave plate. PBS: Polarizing beamsplitter. FM: fold mirror. G: Galvanometers**

Here, the half wave plates (HWP) in the sample arm are adjusted to direct the desired amount of optical power to each path. The incoming light does not need to be polarized, although use of polarized light would increase throughput. The remainder of the system is identical to the system described in Chapter 4, and thus confers the same advantages, including allowing the trade-off between lateral resolution and axial field-of-view to be optimized for each path. Crosstalk between the two channels is precluded by temporal encoding, and because returning light whose polarization is modified in the sample (either by depolarization or birefringence) will return in the wrong channel and thus be rejected by the optical switch.

It should be noted that a reference arm with a fast optical switch that alternates between two delays, similar to the one shown in Figure 6.1, would also be required for

this system. The two fast optical switches can be driven with any arbitrary waveform to enable simultaneous (alternating A-scans) or sequential imaging (alternating B-scans) of the anterior and posterior eye. The switch used in the experiments described in Chapter 4 had a response time of 60ns, and thus would support alternating A-scans for lasers with sweep rates up to 1.67MHz (assuming a 90% duty cycle is desired).

This system can also be used in conjunction with a buffered SSOC system, even buffered systems employing fast optical switches in the source arm. In fact, integration of the three switches in such a system would be simplified by the fact that all three would require exactly the same drive waveform.

This system would enable both simultaneous and sequential imaging of the anterior and posterior eye with any SSOC laser, not just lasers exhibiting coherence revival. Furthermore, as with the system described in Chapter 4, the lateral resolution and axial field-of-view trade-off can be optimized for each path. However, the design does have certain drawbacks in terms of cost and complexity, as at least two optical switches are required. Furthermore, insertion losses in the switch may also reduce system sensitivity, as would any birefringence in the sample.

#### **6.4. Design of an optimal coherence revival laser**

It is worth noting that, in the coherence revival experiments presented in Chapter 3, the phase modulations used to generate all of the experimental data were generated as an unintended by-product of the designs of the two lasers used. One could envision a laser deliberately designed to create a cavity length variation that would exhibit significantly better performance. An ideal laser would create a pure, linear-in-wavelength cavity length variation (and thus create fewer, if any, ghost image artifacts), would have a high finesse (ensuring that the sensitivity loss with increasing cavity length offset is minimized), and might even allow for user control of the axial position shift (by adjusting the slope of the cavity length variation). Such a laser would be valuable for extended depth SSOCT imaging applications, and would even further simplify this technique for resolving the complex conjugate ambiguity in SSOCT.

An optimized coherence revival laser could be achieved by simply adding a phase modulator, such as an AOM, into the cavity of an external cavity tunable laser. The drawbacks generally associated with placing an AOM in the OCT interferometer can be mitigated in this configuration as the gain in the laser cavity can be used to compensate the spectrally-dependent insertion losses of the modulator. This design would allow for the axial position shift to be adjusted by simply tuning the modulation frequency of the modulator. As ECTL's generally have non-linear wavelength vs. time profiles, driving the AOM with a pure tone would likely result in the creation of

dispersion-like PSF degradation discussed in Chapter 3. However, by driving the modulator with an optimized, non-linear drive waveform, the modulation frequency could be dynamically adjusted to compensate for the non-linear sweep of the laser, thereby creating a pure axial position shift with little or no PSF degradation.

### **6.5. Ultrahigh resolution SDOCT using supercontinuum lasers**

Ultrahigh resolution SDOCT systems employing very broad bandwidth supercontinuum sources have been demonstrated [116, 138, 239-243] and in many cases have achieved sub-micron axial resolution. One drawback of these techniques, however, is the dynamic amplitude noise introduced by power and spectral fluctuations of supercontinuum sources, which are discussed in detail in [244, 245]. While this amplitude noise can be reduced by careful optimization of the source, shot-noise limited performance is still difficult to achieve.

One potential solution for removing this amplitude noise is to use a balanced detection scheme [246, 247], which is commonly used in SSOCT systems. Balanced detection is not commonly used in SDOCT because of the relatively low RIN associated with SLD's [49, 248], and because, for optimal balancing, co-alignment of the two spectrometers is critical, which is difficult to achieve in practice.

One potential solution for simplifying the co-alignment, and increasing the imaging of depth of the system at the same time, is to use a source with a comb spectrum, as has been previously suggested by Izatt et al, [249] and later demonstrated by Bajraszewski et al [250]. This can be realized by using a source that inherently has a comb-like spectrum (such as a mode-locked laser), or by filtering a continuous spectrum source with a periodic optical filter. This latter technique is, of course, extremely

inefficient, but is compatible with supercontinuum lasers for use in OCT due to their inherently high optical power.

This technique is optimized if the number of comb “teeth” per pixel is limited to one across the entire imaging range. This requires that the free spectral range (FSR) of the periodic filter match the pixel spacing in spectrum. Furthermore, because periodic filters, such as Fabry-Perot filters, are most commonly evenly spaced in wavenumber, and spectrometers are ordinarily (fairly) linear in wavelength, the comb spacing may change across the spectrometer. One potential solution to this problem is to employ a linear-in-wavenumber spectrometer, which has been previously demonstrated for use in OCT [251]. This design has the added advantage of simplifying the processing of OCT data, by not requiring hardware resampling.

It is important to note, however, that the improvement in both imaging depth and ease of alignment with comb sources is only realized if the spectral bandwidth corresponding to each pixel on the spectrometer is limited by the continuous nature of the light source spectrum, and not by diffraction or aberrations in the spectrometer optics. That is, after comb filtering, the spot size of each comb “tooth” on the spectrometer camera must be smaller than a pixel, which requires careful design of the optics of the spectrometer. Assuming this can be achieved, co-alignment of two such spectrometers can be easily realized, as small misalignments between the two

spectrometers will not affect the co-alignment, as long as these misalignments do not cause a the comb “teeth” to be shifter onto adjacent pixels.

In summary, the use of a pair of co-aligned, linear-in-wavenumber spectrometers, while potentially complicated in design and implementation, would enable shot-noise limited performance of ultrahigh resolution SDOCT systems employing supercontinuum sources. Of course, in this implementation, balancing is performed digitally and thus common-mode noise can only be suppressed to the same level as digitization noise. However, in typical shot-noise limited SDOCT systems, shot-noise will dominate over digitization noise, and thus this technique would still enable shot-noise limited performance.

## References

- 1 Huang, D., E. A. Swanson, C. P. Lin, J. S. Schuman, W. G. Stinson, W. Chang, M. R. Hee, T. Flotte, K. Gregory, C. A. Puliafito, and J. G. Fujimoto. "Optical Coherence Tomography." *Science* 254, no. 5035 (1991): 1178-1181.
- 2 Swanson, E. A., J. A. Izatt, M. R. Hee, D. Huang, C. P. Lin, J. S. Schuman, C. A. Puliafito, and J. G. Fujimoto. "In-Vivo Retinal Imaging by Optical Coherence Tomography." *Optics Letters* 18, no. 21 (1993): 1864-1866.
- 3 Hee, M. R., J. A. Izatt, E. A. Swanson, D. Huang, J. S. Schuman, C. P. Lin, C. A. Puliafito, and J. G. Fujimoto. "Optical Coherence Tomography of the Human Retina." *Archives of ophthalmology* 113, no. 3 (1995): 325-332.
- 4 Fercher, A. F., C. K. Hitzenberger, W. Drexler, G. Kamp, and H. Sattmann. "In-Vivo Optical Coherence Tomography." *American Journal of Ophthalmology* 116, no. 1 (1993): 113-115.
- 5 Puliafito, C. A., M. R. Hee, C. P. Lin, E. Reichel, J. S. Schuman, J. S. Duker, J. A. Izatt, E. A. Swanson, and J. G. Fujimoto. "Imaging of Macular Diseases with Optical Coherence Tomography." *Ophthalmology* 102, no. 2 (1995): 217-229.
- 6 Hee Mr, Puliafito C. A. Wong C. and et al. "Quantitative Assessment of Macular Edema with Optical Coherence Tomography." *Archives of ophthalmology* 113, no. 8 (1995): 1019-1029.
- 7 Hee, Michael R., Carmen A. Puliafito, Jay S. Duker, Elias Reichel, Jeffrey G. Coker, Jason R. Wilkins, Joel S. Schuman, Eric A. Swanson, and James G. Fujimoto. "Topography of Diabetic Macular Edema with Optical Coherence Tomography." *Ophthalmology* 105, no. 2 (1998): 360-370.
- 8 Izatt, Joseph A., Michael R. Hee, Eric A. Swanson, Charles P. Lin, David Huang, Joel S. Schuman, Carmen A. Puliafito, and James G. Fujimoto. "Micrometer-Scale Resolution Imaging of the Anterior Eye in Vivo with Optical Coherence Tomography." *Arch Ophthalmol* 112, no. 12 (1994): 1584-1589.

- 9 Drexler, W., A. Baumgartner, O. Findl, C. K. Hitzenberger, H. Sattmann, and A. F. Fercher. "Submicrometer Precision Biometry of the Anterior Segment of the Human Eye." *Investigative Ophthalmology & Visual Science* 38, no. 7 (1997): 1304-1313.
- 10 Maldonado, M. J., L. Ruiz-Oblitas, J. M. Munuera, D. Aliseda, A. Garcia-Layana, and J. Moreno-Montanes. "Optical Coherence Tomography Evaluation of the Corneal Cap and Stromal Bed Features after Laser in Situ Keratomileusis for High Myopia and Astigmatism." *Ophthalmology* 107, no. 1 (2000): 81-87.
- 11 Radhakrishnan, S., A. M. Rollins, J. E. Roth, S. Yazdanfar, V. Westphal, D. S. Bardenstein, and J. A. Izatt. "Real-Time Optical Coherence Tomography of the Anterior Segment at 1310 Nm." *Archives of ophthalmology* 119, no. 8 (2001): 1179-1185.
- 12 Tearney, G. J., M. E. Brezinski, B. E. Bouma, S. A. Boppart, C. Pitris, J. F. Southern, and J. G. Fujimoto. "In Vivo Endoscopic Optical Biopsy with Optical Coherence Tomography." *Science* 276, no. 5321 (1997): 2037-2039.
- 13 Rollins, A. M., R. Ung-arunyawee, A. Chak, R. C. K. Wong, K. Kobayashi, M. V. Sivak, and J. A. Izatt. "Real-Time in Vivo Imaging of Human Gastrointestinal Ultrastructure by Use of Endoscopic Optical Coherence Tomography with a Novel Efficient Interferometer Design." *Optics Letters* 24, no. 19 (1999): 1358-1360.
- 14 Li, X. D., S. A. Boppart, J. Van Dam, H. Mashimo, M. Mutinga, W. Drexler, M. Klein, C. Pitris, M. L. Krinsky, M. E. Brezinski, and J. G. Fujimoto. "Optical Coherence Tomography: Advanced Technology for the Endoscopic Imaging of Barrett's Esophagus." *Endoscopy* 32, no. 12 (2000): 921-930.
- 15 Rothenberg, F., A. M. Davis, and J. A. Izatt. "Non-Invasive Investigations of Early Embryonic Cardiac Blood Flow with Optical Coherence Tomography." *Faseb Journal* 20, no. 4 (2006): A451-A451.
- 16 Davis, A. M., F. Rothenberg, and J. A. Izatt. "Optical Coherence Tomography: An Emerging Technology for Functional Imaging in Embryonic Cardiovasculature." *Faseb Journal* 21, no. 5 (2007): A88-A88.

- 17 Davis, A. M., F. G. Rothenberg, N. Shepherd, and J. A. Izatt. "In Vivo Spectral Domain Optical Coherence Tomography Volumetric Imaging and Spectral Doppler Velocimetry of Early Stage Embryonic Chicken Heart Development." *Journal of the Optical Society of America a-Optics Image Science and Vision* 25, no. 12 (2008): 3134-3143.
- 18 Fujimoto, J. G., M. E. Brezinski, G. J. Tearney, S. A. Boppart, B. Bouma, M. R. Hee, J. F. Southern, and E. A. Swanson. "Optical Biopsy and Imaging Using Optical Coherence Tomography." *Nature Medicine* 1, no. 9 (1995): 970-972.
- 19 Brezinski, M. E., G. J. Tearney, B. E. Bouma, J. A. Izatt, M. R. Hee, E. A. Swanson, J. F. Southern, and J. G. Fujimoto. "Optical Coherence Tomography for Optical Biopsy - Properties and Demonstration of Vascular Pathology." *Circulation* 93, no. 6 (1996): 1206-1213.
- 20 Fujimoto, J. G., S. A. Boppart, G. J. Tearney, B. E. Bouma, C. Pitris, and M. E. Brezinski. "High Resolution in Vivo Intra-Arterial Imaging with Optical Coherence Tomography." *Heart* 82, no. 2 (1999): 128-133.
- 21 Jang, I. K., G. J. Tearney, B. MacNeill, M. Takano, F. Moselewski, N. Iftima, M. Shishkov, S. Houser, H. T. Aretz, E. F. Halpern, and B. E. Bouma. "In Vivo Characterization of Coronary Atherosclerotic Plaque by Use of Optical Coherence Tomography." *Circulation* 111, no. 12 (2005): 1551-1555.
- 22 Yabushita, H., B. E. Bouma, S. L. Houser, T. Aretz, I. K. Jang, K. H. Schlendorf, C. R. Kauffman, M. Shishkov, D. H. Kang, E. F. Halpern, and G. J. Tearney. "Characterization of Human Atherosclerosis by Optical Coherence Tomography." *Circulation* 106, no. 13 (2002): 1640-1645.
- 23 Jang, I. K., B. E. Bouma, D. H. Kang, S. J. Park, S. W. Park, K. B. Seung, K. B. Choi, M. Shishkov, K. Schlendorf, E. Pomerantsev, S. L. Houser, H. T. Aretz, and G. J. Tearney. "Visualization of Coronary Atherosclerotic Plaques in Patients Using Optical Coherence Tomography: Comparison with Intravascular Ultrasound." *Journal of the American College of Cardiology* 39, no. 4 (2002): 604-609.

- 24 Adler, Desmond C., Jens Stenger, Iwona Gorczynska, Henry Lie, Teri Hensick, Ron Spronk, Stephan Wolohojian, Narayan Khandekar, James Y. Jiang, Scott Barry, Alex E. Cable, Robert Huber, and James G. Fujimoto. "Comparison of Three-Dimensional Optical Coherence Tomography and High Resolution Photography for Art Conservation Studies." *Optics Express* 15, no. 24 (2007): 15972-15986.
- 25 Arecchi, T., M. Bellini, C. Corsi, R. Fontana, M. Materazzi, L. Pezzati, and A. Tortora. "A New Tool for Painting Diagnostics: Optical Coherence Tomography." *Optics and Spectroscopy* 101, no. 1 (2006): 23-26.
- 26 Targowski, P., B. Rouba, M. Gora, L. Tyminska-Widmer, J. Marczak, and A. Kowalczyk. "Optical Coherence Tomography in Art Diagnostics and Restoration." *Applied Physics a-Materials Science & Processing* 92, no. 1 (2008): 1-9.
- 27 Cheng, Y. Z. and K. V. Larin. "Artificial Fingerprint Recognition by Using Optical Coherence Tomography with Autocorrelation Analysis." *Applied Optics* 45, no. 36 (2006): 9238-9245.
- 28 Dubey, S. K., T. Anna, C. Shakher, and D. S. Mehta. "Fingerprint Detection Using Full-Field Swept-Source Optical Coherence Tomography." *Applied Physics Letters* 91, no. 18 (2007).
- 29 Cheng, Y. and K. V. Larin. "In Vivo Two- and Three-Dimensional Imaging of Artificial and Real Fingerprints with, Optical Coherence Tomography." *IEEE Photonics Technology Letters* 19, no. 17-20 (2007): 1634-1636.
- 30 Anna, T., C. Shakher, and D. S. Mehta. "Simultaneous Tomography and Topography of Silicon Integrated Circuits Using Full-Field Swept-Source Optical Coherence Tomography." *Journal of Optics a-Pure and Applied Optics* 11, no. 4 (2009).
- 31 Serrels, K. A., M. K. Renner, and D. T. Reid. "Optical Coherence Tomography for Non-Destructive Investigation of Silicon Integrated-Circuits." *Microelectronic Engineering* 87, no. 9 (2010): 1785-1791.

- 32 Tearney, G. J., B. E. Bouma, and J. G. Fujimoto. "High-Speed Phase- and Group-Delay Scanning with a Grating-Based Phase Control Delay Line." *Opt. Lett.* 22, no. 23 (1997): 1811-1813.
- 33 Rollins, Andrew, Siavash Yazdanfar, Manish Kulkarni, Rujchai Ung-Arunyawee, and Joseph Izatt. "In Vivo Video Rate Optical Coherence Tomography." *Opt. Express* 3, no. 6 (1998): 219-229.
- 34 Martinez, O. "Design of High-Power Ultrashort Pulse Amplifiers by Expansion and Recompression." *Quantum Electronics, IEEE Journal of* 23, no. 8 (1987): 1385-1387.
- 35 Martinez, O. "3000 Times Grating Compressor with Positive Group Velocity Dispersion: Application to Fiber Compensation in 1.3-1.6  $\mu\text{M}$  Region." *Quantum Electronics, IEEE Journal of* 23, no. 1 (1987): 59-64.
- 36 Weiner, A. M., D. E. Leaird, J. S. Patel, and J. R. Wullert. "Programmable Femtosecond Pulse Shaping by Use of a Multielement Liquid-Crystal Phase Modulator." *Optics Letters* 15, no. 6 (1990): 326-328.
- 37 Kwong, K. F., D. Yankelevich, K. C. Chu, J. P. Heritage, and A. Dienes. "400-Hz Mechanical Scanning Optical Delay-Line." *Optics Letters* 18, no. 7 (1993): 558-560.
- 38 Wong, Victor and Ian A. Walmsley. "Analysis of Ultrashort Pulse-Shape Measurement Using Linear Interferometers." *Opt. Lett.* 19, no. 4 (1994): 287-289.
- 39 Fercher, A. F., C. K. Hitzenberger, G. Kamp, and S. Y. El-Zaiat. "Measurement of Intraocular Distances by Backscattering Spectral Interferometry." *Optics Communications* 117, no. 1-2 (1995): 43-48.
- 40 Wojtkowski, M., R. Leitgeb, A. Kowalczyk, T. Bajraszewski, and A. F. Fercher. "In Vivo Human Retinal Imaging by Fourier Domain Optical Coherence Tomography." *Journal of Biomedical Optics* 7, no. 3 (2002): 457-463.

- 41 Hausler, Gerd and Michael Walter Lindner. "``Coherence Radar" and ``Spectral Radar"---New Tools for Dermatological Diagnosis." *Journal of Biomedical Optics* 3, no. 1 (1998): 21-31.
- 42 Wojtkowski, M., A. Kowalczyk, R. Leitgeb, and A. F. Fercher. "Full Range Complex Spectral Optical Coherence Tomography Technique in Eye Imaging." *Opt. Lett.* 27, no. 16 (2002): 1415-1417.
- 43 Golubovic, B., B. E. Bouma, G. J. Tearney, and J. G. Fujimoto. "Optical Frequency-Domain Reflectometry Using Rapid Wavelength Tuning of a Cr<sup>4+</sup>:Forsterite Laser." *Opt. Lett.* 22, no. 22 (1997): 1704-1706.
- 44 Chinn, S. R., E. A. Swanson, and J. G. Fujimoto. "Optical Coherence Tomography Using a Frequency-Tunable Optical Source." *Opt. Lett.* 22, no. 5 (1997): 340-342.
- 45 Lexer, F., C. K. Hitzenberger, A. F. Fercher, and M. Kulhavy. "Wavelength-Tuning Interferometry of Intraocular Distances." *Appl. Opt.* 36, no. 25 (1997): 6548-6553.
- 46 Haberland, U. H. P., V. Blazek, and H. J. Schmitt. "Chirp Optical Coherence Tomography of Layered Scattering Media." *Journal of Biomedical Optics* 3, no. 3 (1998): 259-266.
- 47 Andretzky, P., M. W. Lindner, J. M. Herrmann, A. Schultz, M. Konzog, F. Kiesewetter, and G. Hausler. "Optical Coherence Tomography by "Spectral Radar": Dynamic Range Estimation and in Vivo Measurements of Skin." In *Optical and Imaging Techniques for Biomonitoring Iv, Proceedings Of*, edited by M. DalFante, H. J. Foth, N. Krasner, R. Marchesini, H. Podbielska, and A. Katzir, 3567, 78-87. Bellingham: Spie-Int Soc Optical Engineering, 1999.
- 48 Mitsui, Takahisa. "Dynamic Range of Optical Reflectometry with Spectral Interferometry." *Japanese Journal of Applied Physics* 38, no. Copyright (C) 1999 Publication Board, Japanese Journal of Applied Physics (1999): 6133.

- 49 Leitgeb, R., C. Hitzenberger, and Adolf Fercher. "Performance of Fourier Domain Vs. Time Domain Optical Coherence Tomography." *Optics Express* 11, no. 8 (2003): 889-894.
- 50 de Boer, Johannes F., Barry Cense, B. Hyle Park, Mark C. Pierce, Guillermo J. Tearney, and Brett E. Bouma. "Improved Signal-to-Noise Ratio in Spectral-Domain Compared with Time-Domain Optical Coherence Tomography." *Opt. Lett.* 28, no. 21 (2003): 2067-2069.
- 51 Choma, Michael, Marinko Sarunic, Changhuei Yang, and Joseph Izatt. "Sensitivity Advantage of Swept Source and Fourier Domain Optical Coherence Tomography." *Optics Express* 11, no. 18 (2003): 2183-2189.
- 52 Wiener, Norbert. "Generalized Harmonic Analysis." *ACTA MATHEMATICA* 55, no. 1 (1930): 117-258.
- 53 Khintchine, Alexander. "Korrelationstheorie Der Stationären Stochastischen Prozesse." *Mathematische Annalen* 109, no. 604 (1934).
- 54 Stoilov, G. and T. Dragostinov. "Phase-Stepping Interferometry: Five-Frame Algorithm with an Arbitrary Step." *Optics and Lasers in Engineering* 28, no. 1 (1997): 61-69.
- 55 Beaulieu, E., A. C. Boccara, M. Lebec, L. Blanchot, and H. Saint-Jalmes. "Full-Field Optical Coherence Microscopy." *Opt. Lett.* 23, no. 4 (1998): 244-246.
- 56 Dyson, J. "An Interferometer Microscope." *Proceedings of the Royal Society of London. Series A. Mathematical and Physical Sciences* 204, no. 1077 (1950): 170-187.
- 57 Kino, Gordon S. and Stanley S. C. Chim. "Mirau Correlation Microscope." *Appl. Opt.* 29, no. 26 (1990): 3775-3783.
- 58 Dubois, A., K. Grieve, G. Moneron, R. Lecaque, L. Vabre, and C. Boccara. "Ultrahigh-Resolution Full-Field Optical Coherence Tomography." *Applied Optics* 43, no. 14 (2004): 2874-2883.

- 59 Dubois, Arnaud, Laurent Vabre, Albert-Claude Boccara, and Emmanuel Beaurepaire. "High-Resolution Full-Field Optical Coherence Tomography with a Linnik Microscope." *Appl. Opt.* 41, no. 4 (2002): 805-812.
- 60 Vabre, L., A. Dubois, and A. C. Boccara. "Thermal-Light Full-Field Optical Coherence Tomography." *Optics Letters* 27, no. 7 (2002): 530-532.
- 61 Laude, Blandine, Antonello De Martino, Bernard Drévillon, Laurence Benattar, and Laurent Schwartz. "Full-Field Optical Coherence Tomography with Thermal Light." *Applied Optics* 41, no. 31 (2002): 6637-6637.
- 62 Dubois, A., G. Moneron, K. Grieve, and A. C. Boccara. "Three-Dimensional Cellular-Level Imaging Using Full-Field Optical Coherence Tomography." *Physics in Medicine and Biology* 49, no. 7 (2004): 1227-1234.
- 63 Grieve, K., M. Paques, A. Dubois, J. Sahel, C. Boccara, and J. F. Le Gargasson. "Ocular Tissue Imaging Using Ultrahigh-Resolution, Full-Field Optical Coherence Tomography." *Investigative Ophthalmology & Visual Science* 45, no. 11 (2004): 4126-4131.
- 64 Grieve, K., A. Dubois, M. Simonutti, M. Paques, J. Sahel, J. F. Le Gargasson, and C. Boccara. "In Vivo Anterior Segment Imaging in the Rat Eye with High Speed White Light Full-Field Optical Coherence Tomography." *Optics Express* 13, no. 16 (2005): 6286-6295.
- 65 Karamata, B., M. Leutenegger, M. Laubscher, S. Bourquin, T. Lasser, and P. Lambelet. "Multiple Scattering in Optical Coherence Tomography. Ii. Experimental and Theoretical Investigation of Cross Talk in Wide-Field Optical Coherence Tomography." *Journal of the Optical Society of America a-Optics Image Science and Vision* 22, no. 7 (2005): 1380-1388.
- 66 Goodman, Joseph W. "Frequency Analysis of Optical Imaging Systems." In *Introduction to Fourier Optics*, 121-172. Englewood, CO: Roberts & Co., 2005.

- 67 Karamata, B., P. Lambelet, M. Laubscher, R. P. Salathe, and T. Lasser. "Spatially Incoherent Illumination as a Mechanism for Cross-Talk Suppression in Wide-Field Optical Coherence Tomography." *Optics Letters* 29, no. 7 (2004): 736-738.
- 68 Mandel, L and E Wolf. *Optical Coherence and Quantum Optics*. Cambridge, UK: Cambridge University Press, 1995.
- 69 Fercher, A. F., C. K. Hitzenberger, M. Sticker, E. Moreno-Barriuso, R. Leitgeb, W. Drexler, and H. Sattmann. "A Thermal Light Source Technique for Optical Coherence Tomography." *Optics Communications* 185, no. 1-3 (2000): 57-64.
- 70 Kim, J., D. T. Miller, E. Kim, S. Oh, J. Oh, and T. E. Milner. "Optical Coherence Tomography Speckle Reduction by a Partially Spatially Coherent Source." *Journal of Biomedical Optics* 10, no. 6 (2005): 064034.
- 71 Marks, Daniel L., Brynmor J. Davis, Stephen a Boppart, and P. Scott Carney. "Partially Coherent Illumination in Full-Field Interferometric Synthetic Aperture Microscopy." *Journal of the Optical Society of America. A, Optics, image science, and vision* 26, no. 2 (2009): 376-386.
- 72 Wolfgang, Wieser, R. Biedermann Benjamin, Klein Thomas, M. Eigenwillig Christoph, and Huber Robert, "Multimegahertz Optical Coherence Tomography: High Quality Biomedical Imaging Beyond 1 Million a-Scans Per Second," in OSA Technical Digest (CD) (Optical Society of America, 2010), BSuC1.
- 73 Wieser, Wolfgang, Benjamin R. Biedermann, Thomas Klein, Christoph M. Eigenwillig, and Robert Huber. "Multi-Megahertz Oct: High Quality 3d Imaging at 20 Million a-Scans and 4.5 Gvoxels Per Second." *Opt. Express* 18, no. 14 (2010): 14685-14704.
- 74 Ohbayashi, K., D. Choi, H. Hiro-Oka, H. Furukawa, R. Yoshimura, M. Nakanishi, and K. Shimizu, "60 Mhz a-Line Rate Ultra-High Speed Fourier-Domain Optical Coherence Tomography," in (SPIE, 2008), 68470M-68475.

- 75 Grajciar, Branislav, Michael Pircher, Adolf Fercher, and Rainer Leitgeb. "Parallel Fourier Domain Optical Coherence Tomography for in Vivo Measurement of the Human Eye." *Opt. Express* 13, no. 4 (2005): 1131-1137.
- 76 Nakamura, Yoshifumi, Shuichi Makita, Masahiro Yamanari, Masahide Itoh, Toyohiko Yatagai, and Yoshiaki Yasuno. "High-Speed Three-Dimensional Human Retinal Imaging by Line-Field Spectraldomain Optical Coherence Tomography." *Opt. Express* 15, no. 12 (2007): 7103-7116.
- 77 Yaqoob, Zahid, Wonshik Choi, Seungeun Oh, Niyom Lue, Yongkeun Park, Christopher Fang-Yen, Ramachandra R. Dasari, Kamran Badizadegan, and Michael S. Feld. "Improved Phase Sensitivity in Spectral Domain Phase Microscopy Using Line-Field Illumination and Self Phase-Referencing." *Opt. Express* 17, no. 13 (2009): 10681-10687.
- 78 Sarunic, M. V., S. Weinberg, and J. A. Izatt. "Full-Field Swept-Source Phase Microscopy." *Optics Letters* 31, no. 10 (2006): 1462-1464.
- 79 Povazay, Boris, Angelika Unterhuber, Boris Hermann, Harald Sattmann, Holger Arthaber, and Wolfgang Drexler. "Full-Field Time-Encoded Frequency-Domain Optical Coherence Tomography." *Optics Express* 14, no. 17 (2006): 7661-7669.
- 80 Ramos, Jose Luiz Branco, Yan Li, and David Huang. "Clinical and Research Applications of Anterior Segment Optical Coherence Tomography – a Review." *Clinical & Experimental Ophthalmology* 37, no. 1 (2009): 81-89.
- 81 Hermann, B., E. J. Fernández, A. Unterhuber, H. Sattmann, A. F. Fercher, W. Drexler, P. M. Prieto, and P. Artal. "Adaptive-Optics Ultrahigh-Resolution Optical Coherencetomography." *Opt. Lett.* 29, no. 18 (2004): 2142-2144.
- 82 Zawadzki, Robert, Steven Jones, Scot Olivier, Mingtao Zhao, Bradley Bower, Joseph Izatt, Stacey Choi, Sophie Laut, and John Werner. "Adaptive-Optics Optical Coherence Tomography for High-Resolution and High-Speed 3d Retinal in Vivo Imaging." *Opt. Express* 13, no. 21 (2005): 8532-8546.

- 83 Goncharov, Alexander V. and Chris Dainty. "Wide-Field Schematic Eye Models with Gradient-Index Lens." *J. Opt. Soc. Am. A* 24, no. 8 (2007): 2157-2174.
- 84 Torti, C., B. Povazay, B. Hofer, A. Unterhuber, J. Carroll, P. K. Ahnelt, and W. Drexler. "Adaptive Optics Optical Coherence Tomography at 120,000 Depth Scans/S for Non-Invasive Cellular Phenotyping of the Living Human Retina." *Optics Express* 17, no. 22 (2009): 19382-19400.
- 85 Grulkowski, I., M. Gora, M. Szkulmowski, I. Gorczynska, D. Szlag, S. Marcos, A. Kowalczyk, and M. Wojtkowski. "Anterior Segment Imaging with Spectral Oct System Using a High-Speed Cmos Camera." *Optics Express* 17, no. 6 (2009): 4842-4858.
- 86 Gora, Michalina, Karol Karnowski, Maciej Szkulmowski, Bartłomiej J. Kaluzny, Robert Huber, Andrzej Kowalczyk, and Maciej Wojtkowski. "Ultra High-Speed Swept Source Oct Imaging of the Anterior Segment of Human Eye at 200 Khz with Adjustable Imaging Range." *Opt. Express* 17, no. 17 (2009): 14880-14894.
- 87 Dhalla, Al-Hafeez and Joseph A Izatt. "Complete Complex Conjugate Resolved Heterodyne Swept Source Optical Coherence Tomography Using a Dispersive Optical Delay Line." *Biomedical Optics Express* 2, no. 5 (2011): 1218-1232.
- 88 Potsaid, Benjamin, Vijaysekhar Jayaraman, James G. Fujimoto, James Jiang, Peter J. S. Heim, and Alex E. Cable, "Mems Tunable Vcsel Light Source for Ultrahigh Speed 60khz - 1mhz Axial Scan Rate and Long Range Centimeter Class Oct Imaging," in (SPIE, 2012), 82130M-82138.
- 89 Izatt, Joseph A and Michael A Choma. "Theory of Optical Coherence Tomography." In *Optical Coherence Tomography: Technology and Applications*, edited by Wolfgang Drexler and James Fujimoto, 47-72. New York: Springer, 2008.
- 90 Yun, S., G. Tearney, J. de Boer, and B. Bouma. "Removing the Depth-Degeneracy in Optical Frequency Domain Imaging with Frequency Shifting." *Opt. Express* 12, no. 20 (2004): 4822-4828.

- 91 Davis, Anjul M., Michael A. Choma, and Joseph A. Izatt. "Heterodyne Swept-Source Optical Coherence Tomography for Complete Complex Conjugate Ambiguity Removal." *Journal of Biomedical Optics* 10, no. 6 (2005): 064005-064006.
- 92 Götzinger, Erich, Michael Pircher, Rainer Leitgeb, and Christoph Hitzenberger. "High Speed Full Range Complex Spectral Domain Optical Coherence Tomography." *Opt. Express* 13, no. 2 (2005): 583-594.
- 93 Zhang, Jun, J. Stuart Nelson, and Zhongping Chen. "Removal of a Mirror Image and Enhancement of the Signal-to-Noise Ratio in Fourier-Domain Optical Coherence Tomography Using an Electro-Optic Phasemodulator." *Opt. Lett.* 30, no. 2 (2005): 147-149.
- 94 Bachmann, Adrian, Rainer Leitgeb, and Theo Lasser. "Heterodyne Fourier Domain Optical Coherence Tomography for Full Range Probing with High Axial Resolution." *Opt. Express* 14, no. 4 (2006): 1487-1496.
- 95 Sarunic, Marinko V., Brian E. Applegate, and Joseph A. Izatt. "Real-Time Quadrature Projection Complex Conjugate Resolved Fourier Domain Optical Coherence Tomography." *Opt. Lett.* 31, no. 16 (2006): 2426-2428.
- 96 Vakhtin, Andrei B., Kristen A. Peterson, and Daniel J. Kane. "Resolving the Complex Conjugate Ambiguity in Fourier-Domain OCT by Harmonic Lock-in Detection of the Spectral Interferogram." *Opt. Lett.* 31, no. 9 (2006): 1271-1273.
- 97 Vakoc, B. J., S. H. Yun, G. J. Tearney, and B. E. Bouma. "Elimination of Depth Degeneracy in Optical Frequency-Domain Imaging through Polarization-Based Optical Demodulation." *Opt. Lett.* 31, no. 3 (2006): 362-364.
- 98 Yasuno, Y., S. Makita, T. Endo, G. Aoki, M. Itoh, and T. Yatagai. "Simultaneous B-M-Mode Scanning Method for Real-Time Full-Range Fourier Domain Optical Coherence Tomography." *Applied Optics* 45, no. 8 (2006): 1861-1865.

- 99 An, L. and R. K. Wang. "Use of a Scanner to Modulate Spatial Interferograms for in Vivo Full-Range Fourier-Domain Optical Coherence Tomography." *Optics Letters* 32, no. 23 (2007): 3423-3425.
- 100 Leitgeb, R. A., R. Michaely, T. Lasser, and S. C. Sekhar. "Complex Ambiguity-Free Fourier Domain Optical Coherence Tomography through Transverse Scanning." *Optics Letters* 32, no. 23 (2007): 3453-3455.
- 101 Tao, Yuankai K., Mingtao Zhao, and Joseph A. Izatt. "High-Speed Complex Conjugate Resolved Retinal Spectral Domain Optical Coherence Tomography Using Sinusoidal Phase Modulation." *Opt. Lett.* 32, no. 20 (2007): 2918-2920.
- 102 Wang, R. K. "In Vivo Full Range Complex Fourier Domain Optical Coherence Tomography." *Applied Physics Letters* 90, no. 5 (2007): 054103
- 103 Wang, Hui, Yinsheng Pan, and Andrew M. Rollins. "Extending the Effective Imaging Range of Fourier-Domain Optical Coherence Tomography Using a Fiber Optic Switch." *Opt. Lett.* 33, no. 22 (2008): 2632-2634.
- 104 Hofer, B., B. Povazay, B. Hermann, A. Unterhuber, G. Matz, and W. Drexler. "Dispersion Encoded Full Range Frequency Domain Optical Coherence Tomography." *Optics Express* 17, no. 1 (2009): 7-24.
- 105 Wang, Ruikang K. "Fourier Domain Optical Coherence Tomography Achieves Full Range Complex Imaging in Vivo by Introducing a Carrier Frequency During Scanning." *Phys. Med. Biol.* 52, (2007): 5897.
- 106 Hofer, B., B. Povazay, A. Unterhuber, L. Wang, B. Hermann, S. Rey, G. Matz, and W. Drexler. "Fast Dispersion Encoded Full Range Optical Coherence Tomography for Retinal Imaging at 800 Nm and 1060 Nm." *Optics Express* 18, no. 5 (2010): 4898-4919.
- 107 Dhalla, Al-Hafeez, Derek Nankivil, and Joseph A Izatt. "Complex Conjugate Resolved Heterodyne Swept Source Optical Coherence Tomography Using Coherence Revival." *Biomed. Opt. Express* 3, no. 3 (2012): 633-649.

- 108 Wilson, Tony. *Confocal Microscopy*. London: Academic Press, 1990.
- 109 Drexler, Wolfgang and James G. Fujimoto, eds. *Optical Coherence Tomography: Technology and Applications*. Cardiff, UK: Springer, 2008.
- 110 Izatt, Joseph A., Michael R. Hee, Gabrielle M. Owen, Eric A. Swanson, and James G. Fujimoto. "Optical Coherence Microscopy in Scattering Media." *Opt. Lett.* 19, no. 8 (1994): 590-592.
- 111 Schmitt, J. M., M. J. Yadlowsky, and R. F. Bonner. "Subsurface Imaging of Living Skin with Optical Coherence Microscopy." *Dermatology* 191, no. 2 (1995): 93-98.
- 112 Choma, Michael a, Audrey K. Ellerbee, Changhuei Yang, Tony L. Creazzo, and Joseph a Izatt. "Spectral-Domain Phase Microscopy." *Optics Letters* 30, no. 10 (2005): 1162-1164.
- 113 Huang, Shu-Wei, Aaron D. Aguirre, Robert A. Huber, Desmond C. Adler, and James G. Fujimoto. "Swept Source Optical Coherence Microscopy Using a Fourier Domain Mode-Locked Laser." *Opt. Express* 15, no. 10 (2007): 6210-6217.
- 114 Tearney, G. J., M. E. Brezinski, J. F. Southern, B. E. Bouma, M. R. Hee, and J. G. Fujimoto. "Determination of the Refractive Index of Highly Scattering Human Tissue by Optical Coherence Tomography." *Opt. Lett.* 20, no. 21 (1995): 2258-2260.
- 115 Chen, Zhongping, Thomas E. Milner, Digant Dave, and J. Stuart Nelson. "Optical Doppler Tomographic Imaging of Fluid Flow Velocity in Highly Scattering Media." *Opt. Lett.* 22, no. 1 (1997): 64-66.
- 116 Wang, Yimin, Yonghua Zhao, J. S. Nelson, Zhongping Chen, and Robert S. Windeler. "Ultrahigh-Resolution Optical Coherence Tomography by Broadband Continuum Generation from a Photonic Crystal Fiber." *Opt. Lett.* 28, no. 3 (2003): 182-184.
- 117 Qi, Bing, A. Phillip Himmer, L. Maggie Gordon, X. D. Victor Yang, L. David Dickensheets, and I. Alex Vitkin. "Dynamic Focus Control in High-Speed Optical

- Coherence Tomography Based on a Microelectromechanical Mirror." *Optics Communications* 232, no. 1–6 (2004): 123-128.
- 118 Cobb, Michael J., Xiumei Liu, and Xingde Li. "Continuous Focus Tracking for Real-Time Optical Coherence Tomography." *Opt. Lett.* 30, no. 13 (2005): 1680-1682.
- 119 Drexler, W., U. Morgner, F. X. Kartner, C. Pitris, S. A. Boppart, X. D. Li, E. P. Ippen, and J. G. Fujimoto. "In Vivo Ultrahigh-Resolution Optical Coherence Tomography." *Optics Letters* 24, no. 17 (1999): 1221-1223.
- 120 Gloesmann, Martin, Boris Hermann, Christian Schubert, Harald Sattmann, Peter K. Ahnelt, and Wolfgang Drexler. "Histologic Correlation of Pig Retina Radial Stratification with Ultrahigh-Resolution Optical Coherence Tomography." *Investigative Ophthalmology & Visual Science* 44, no. 4 (2003): 1696-1703.
- 121 Xie, Tuqiang, Shuguang Guo, Zhongping Chen, David Mukai, and Matthew Brenner. "Grin Lens Rod Based Probe for Endoscopic Spectral Domain Optical Coherence Tomography with Fast Dynamic Focus Tracking." *Opt. Express* 14, no. 8 (2006): 3238-3246.
- 122 Zhou, Chuanqing, Jianhua Wang, and Shuliang Jiao. "Dual Channel Dual Focus Optical Coherence Tomography for Imaging Accommodation of the Eye." *Opt. Express* 17, no. 11 (2009): 8947-8955.
- 123 Dai, Cuixia, Chuanqing Zhou, Shanhui Fan, Zhe Chen, Xinyu Chai, Qiushi Ren, and Shuliang Jiao. "Optical Coherence Tomography for Whole Eye Segment Imaging." *Opt. Express* 20, no. 6 (2012): 6109-6115.
- 124 Dhalla, Al-Hafeez, Derek Nankivil, Theresa Bustamante, Anthony Kuo, and Joseph A. Izatt. "Simultaneous Swept Source Optical Coherence Tomography of the Anterior Segment and Retina Using Coherence Revival." *Opt. Lett.* 37, no. 11 (2012): 1883-1885.

- 125 Nowack, Robert. "A Tale of Two Beams: An Elementary Overview of Gaussian Beams and Bessel Beams." *Studia Geophysica et Geodaetica* 56, no. 2 (2012): 355-372.
- 126 Lu, Jian-Yu. "Ultrasonic Imaging with Limited-Diffraction Beams." In *Localized Waves*, 97-128: John Wiley & Sons, Inc., 2007.
- 127 McGloin, D. and K. Dholakia. "Bessel Beams: Diffraction in a New Light." *Contemporary Physics* 46, no. 1 (2005): 15-28.
- 128 Durnin, J., J. J. Miceli, and J. H. Eberly. "Diffraction-Free Beams." In *J. Opt. Soc. Am. A*, 3, P128. Seattle, WA: OSA, 1986.
- 129 Durnin, J. "Exact Solutions for Nondiffracting Beams. I. The Scalar Theory." *J. Opt. Soc. Am. A* 4, no. 4 (1987): 651-654.
- 130 Durnin, J., J. J. Miceli, Jr., and J. H. Eberly. "Diffraction-Free Beams." *Physical Review Letters* 58, no. 15 (1987): 1499-1501.
- 131 Lin, Y., W. Seka, J. H. Eberly, H. Huang, and D. L. Brown. "Experimental Investigation of Bessel Beam Characteristics." *Appl. Opt.* 31, no. 15 (1992): 2708-2713.
- 132 Leitgeb, R. A., M. Villiger, A. H. Bachmann, L. Steinmann, and T. Lasser. "Extended Focus Depth for Fourier Domain Optical Coherence Microscopy." *Opt. Lett.* 31, no. 16 (2006): 2450-2452.
- 133 McLeod, John H. "The Axicon: A New Type of Optical Element." *J. Opt. Soc. Am.* 44, no. 8 (1954): 592-592.
- 134 Ding, Zhihua, Hongwu Ren, Yonghua Zhao, J. Stuart Nelson, and Zhongping Chen. "High-Resolution Optical Coherence Tomography over a Large Depth Range with an Axicon Lens." *Opt. Lett.* 27, no. 4 (2002): 243-245.

- 135 Lee, Kye-Sung and Jannick P. Rolland. "Bessel Beam Spectral-Domain High-Resolution Optical Coherence Tomography with Micro-Optic Axicon Providing Extended Focusing Range." *Opt. Lett.* 33, no. 15 (2008): 1696-1698.
- 136 Blatter, Cedric, Branislav Grajciar, Christoph M. Eigenwillig, Wolfgang Wieser, Benjamin R. Biedermann, Robert Huber, and Rainer A. Leitgeb. "Extended Focus High-Speed Swept Source OCT with Self-Reconstructive Illumination." *Opt. Express* 19, no. 13 (2011): 12141-12155.
- 137 Zlotnik, Alex, Yoed Abraham, Lior Liraz, Ibrahim Abdulhalim, and Zeev Zalevsky. "Improved Extended Depth of Focus Full Field Spectral Domain Optical Coherence Tomography." *Optics Communications* 283, no. 24 (2010): 4963-4968.
- 138 Liu, Linbo, Joseph A. Gardecki, Seemantini K. Nadkarni, Jimmy D. Toussaint, Yukako Yagi, Brett E. Bouma, and Guillermo J. Tearney. "Imaging the Subcellular Structure of Human Coronary Atherosclerosis Using Micro-Optical Coherence Tomography." *Nat Med* 17, no. 8 (2011): 1010-1014.
- 139 Ralston, T. S., D. L. Marks, F. Kamalabadi, and S. A. Boppart. "Deconvolution Methods for Mitigation of Transverse Blurring in Optical Coherence Tomography." *Image Processing, IEEE Transactions on* 14, no. 9 (2005): 1254-1264.
- 140 Yasuno, Yoshiaki, Jun-ichiro Sugisaka, Yusuke Sando, Yoshifumi Nakamura, Shuichi Makita, Masahide Itoh, and Toyohiko Yatagai. "Non-Iterative Numerical Method for Laterally Superresolving Fourier Domain Optical Coherence Tomography." *Opt. Express* 14, no. 3 (2006): 1006-1020.
- 141 Yasuno, Yoshiaki, Yusuke Sando, Jun-ichiro Sugisaka, Takashi Endo, Shuichi Makita, Gouki Aoki, Masahide Itoh, and Toyohiko Yatagai. "In-Focus Fourier-Domain Optical Coherence Tomography by Complex Numerical Method." *Optical and Quantum Electronics* 37, no. 13 (2005): 1185-1189.
- 142 Liu, Guozhong, Siavash Yousefi, Zhongwei Zhi, and Ruikang K. Wang. "Automatic Estimation of Point-Spread-Function for Deconvoluting out-of-Focus

- Optical Coherence Tomographic Images Using Information Entropy-Based Approach." *Opt. Express* 19, no. 19 (2011): 18135-18148.
- 143 Yu, Lingfeng, Bin Rao, Jun Zhang, Jianping Su, Qiang Wang, Shuguang Guo, and Zhongping Chen. "Improved Lateral Resolution in Optical Coherence Tomography by Digital Focusing Using Two-Dimensional Numerical Diffraction Method." *Opt. Express* 15, no. 12 (2007): 7634-7641.
- 144 Ralston, Tyler S., Daniel L. Marks, P. Scott Carney, and Stephen A. Boppart. "Interferometric Synthetic Aperture Microscopy." *Nat Phys* 3, no. 2 (2007): 129-134.
- 145 Davis, Brynmor J., Simon C. Schlachter, Daniel L. Marks, Tyler S. Ralston, Stephen A. Boppart, and P. Scott Carney. "Nonparaxial Vector-Field Modeling of Optical Coherence Tomography and Interferometric Synthetic Aperture Microscopy." *J. Opt. Soc. Am. A* 24, no. 9 (2007): 2527-2542.
- 146 Ralston, Tyler S., Daniel L. Marks, P. S. Carney, and Stephen A. Boppart. "Real-Time Interferometric Synthetic Aperture Microscopy." *Opt. Express* 16, no. 4 (2008): 2555-2569.
- 147 Hillmann, Dierck, Christian Lühns, Tim Bonin, Peter Koch, and Gereon Hüttmann. "Holoscopy - Holographic Optical Coherence Tomography." *Opt. Lett.* 36, no. 13 (2011): 2390-2392.
- 148 Huber, R., M. Wojtkowski, and J. G. Fujimoto. "Fourier Domain Mode Locking (Fdm): A New Laser Operating Regime and Applications for Optical Coherence Tomography." *Opt. Express* 14, no. 8 (2006): 3225-3237.
- 149 Huber, Robert, Desmond C. Adler, and James G. Fujimoto. "Buffered Fourier Domain Mode Locking: Unidirectional Swept Laser Sources for Optical Coherence Tomography Imaging at 370,000 Lines/S." *Opt. Lett.* 31, no. 20 (2006): 2975-2977.

- 150 Kuznetsov, M., W. Atia, B. Johnson, and D. Flanders. "Compact Ultrafast Reflective Fabry-Perot Tunable Lasers for Oct Imaging Applications." In *Optical Coherence Tomography and Coherence Domain Optical Methods in Biomedicine Xiv*, edited by J. A. Izatt, J. G. Fujimoto, and V. V. Tuchin, 7554. Bellingham: Spie-Int Soc Optical Engineering, 2010.
- 151 Klein, Thomas, Wolfgang Wieser, Christoph M. Eigenwillig, Benjamin R. Biedermann, and Robert Huber. "Megahertz Oct for Ultrawide-Field Retinal Imaging with a 1050nm Fourier Domain Mode-Locked Laser." *Opt. Express* 19, no. 4 (2011): 3044-3062.
- 152 Adler, D. C., R. Huber, and J. G. Fujimoto. "Phase-Sensitive Optical Coherence Tomography at up to 370,000 Lines Per Second Using Buffered Fourier Domain Mode-Locked Lasers." *Optics Letters* 32, no. 6 (2007): 626-628.
- 153 Huber, R., D. C. Adler, V. J. Srinivasan, and J. G. Fujimoto. "Fourier Domain Mode Locking at 1050 Nm for Ultra-High-Speed Optical Coherence Tomography of the Human Retina at 236,000 Axial Scans Per Second." *Opt. Lett.* 32, no. 14 (2007): 2049-2051.
- 154 Jenkins, M. W., D. C. Adler, M. Gargesha, R. Huber, F. Rothenberg, J. Belding, M. Watanabe, D. L. Wilson, J. G. Fujimoto, and A. M. Rollins. "Ultrahigh-Speed Optical Coherence Tomography Imaging and Visualization of the Embryonic Avian Heart Using a Buffered Fourier Domain Mode Locked Laser." *Opt. Express* 15, no. 10 (2007): 6251-6267.
- 155 Srinivasan, V. J., D. C. Adler, Y. L. Chen, I. Gorczynska, R. Huber, J. S. Duker, J. S. Schuman, and J. G. Fujimoto. "Ultrahigh-Speed Optical Coherence Tomography for Three-Dimensional and En Face Imaging of the Retina and Optic Nerve Head." *Investigative Ophthalmology & Visual Science* 49, no. 11 (2008): 5103-5110.
- 156 Wieser, W., B. R. Biedermann, C. M. Eigenwillig, T. Klein, and R. A. Huber. "Fdmf Based Multi-Spot Oct at 4,100,000 a-Scans and 4 Gvoxels Per Second." In *SPIE Photonics West*. San Francisco, CA, 2010.

- 157 Klein, Thomas, Wolfgang Wieser, Benjamin R. Biedermann, Christoph M. Eigenwillig, and Robert A. Huber. "Megahertz Retinal Oct Imaging at 1050 Nm and up to 1,400,000 a-Scans Per Second Using an Fdml Laser." San Francisco, CA: SPIE, 2011.
- 158 Potsaid, Benjamin, Bernhard Baumann, David Huang, Scott Barry, Alex E. Cable, Joel S. Schuman, Jay S. Duker, and James G. Fujimoto. "Ultrahigh Speed 1050nm Swept Source / Fourier Domain Oct Retinal and Anterior Segment Imaging at 100,000 to 400,000 Axial Scans Per Second." *Opt. Express* 18, no. 19 (2010): 20029-20048.
- 159 ANSI. "Ansi Z136.1 - American National Standard for Safe Use of Lasers." Orlando, FL: Laser Institute of America, 2007.
- 160 Baumann, Bernhard, Benjamin Potsaid, Martin F. Kraus, Jonathan J. Liu, David Huang, Joachim Hornegger, Alex E. Cable, Jay S. Duker, and James G. Fujimoto. "Total Retinal Blood Flow Measurement with Ultrahigh Speed Swept Source/Fourier Domain Oct." *Biomed. Opt. Express* 2, no. 6 (2011): 1539-1552.
- 161 Oh, Wang-Yuhl, Benjamin J. Vakoc, Milen Shishkov, Guillermo J. Tearney, and Brett E. Bouma. ">400 Khz Repetition Rate Wavelength-Swept Laser and Application to High-Speed Optical Frequency Domain Imaging." *Opt. Lett.* 35, no. 17 (2010): 2919-2921.
- 162 Sakata, Lisandro M., Julio DeLeon-Ortega, Viviane Sakata, and Christopher A. Girkin. "Optical Coherence Tomography of the Retina and Optic Nerve – a Review." *Clinical & Experimental Ophthalmology* 37, no. 1 (2009): 90-99.
- 163 Tang, Maolong, Yan Li, Mariana Avila, and David Huang. "Measuring Total Corneal Power before and after Laser in Situ Keratomileusis with High-Speed Optical Coherence Tomography." *Journal of Cataract & Refractive Surgery* 32, no. 11 (2006): 1843-1850.
- 164 Kuo, Anthony N., Ryan P. McNabb, Mingtao Zhao, Francesco LaRocca, Sandra S. Stinnett, Sina Farsiu, and Joseph A. Izatt. "Corneal Biometry from Volumetric

- Sdoct and Comparison with Existing Clinical Modalities." *Biomed. Opt. Express* 3, no. 6 (2012): 1279-1290.
- 165 Koretz, Jane F., Paul L. Kaufman, Michael W. Neider, and Patrick A. Goeckner. "Accommodation and Presbyopia in the Human Eye—Aging of the Anterior Segment." *Vision Research* 29, no. 12 (1989): 1685-1692.
- 166 Radhakrishnan, Sunita, Jason Goldsmith, David Huang, Volker Westphal, David K. Dueker, Andrew M. Rollins, Joseph A. Izatt, and Scott D. Smith. "Comparison of Optical Coherence Tomography and Ultrasound Biomicroscopy for Detection of Narrow Anterior Chamber Angles." *Arch Ophthalmol* 123, no. 8 (2005): 1053-1059.
- 167 Lehman, Bret M., David A. Berntsen, Melissa D. Bailey, and Karla Zadnik. "Validation of Optical Coherence Tomography-Based Crystalline Lens Thickness Measurements in Children." *Optometry and Vision Science* 86, no. 3 (2009): 181-187.
- 168 Zhao, Mingtao, Anthony N. Kuo, and Joseph A. Izatt. "3d Refraction Correction and Extraction of Clinical Parameters from Spectral Domain Optical Coherence Tomography of the Cornea." *Opt. Express* 18, no. 9 (2010): 8923-8936.
- 169 Ortiz, Sergio, Damian Siedlecki, Ireneusz Grulkowski, Laura Remon, Daniel Pascual, Maciej Wojtkowski, and Susana Marcos. "Optical Distortion Correction in Optical Coherence Tomography for Quantitative Ocular Anterior Segment by Three-Dimensional Imaging." *Opt. Express* 18, no. 3 (2010): 2782-2796.
- 170 Tang, Maolong, Alex Chen, Yan Li, and David Huang. "Corneal Power Measurement with Fourier-Domain Optical Coherence Tomography." *Journal of Cataract & Refractive Surgery* 36, no. 12 (2010): 2115-2122.
- 171 Maceo, Bianca M., Fabrice Manns, David Borja, Derek Nankivil, Stephen Uhlhorn, Esdras Arrieta, Arthur Ho, Robert C. Augusteyn, and Jean-Marie Parel. "Contribution of the Crystalline Lens Gradient Refractive Index to the Accommodation Amplitude in Non-Human Primates: In Vitro Studies." *Journal of Vision* 11, no. 13 (2011).

- 172 Ruggeri, Marco, Stephen R. Uhlhorn, Carolina De Freitas, Arthur Ho, Fabrice Manns, and Jean-Marie Parel. "Imaging and Full-Length Biometry of the Eye During Accommodation Using Spectral Domain Oct with an Optical Switch." *Biomed. Opt. Express* 3, no. 7 (2012): 1506-1520.
- 173 Ratliff, F. and L. A. Riggs. "Involuntary Motions of the Eye During Monocular Fixation." *J Exp Psychol* 40, no. 6 (1950): 687-701.
- 174 Otero-Millan, Jorge, Xoana G. Troncoso, Stephen L. Macknik, Ignacio Serrano-Pedraza, and Susana Martinez-Conde. "Saccades and Microsaccades During Visual Fixation, Exploration, and Search: Foundations for a Common Saccadic Generator." *Journal of Vision* 8, no. 14 (2008).
- 175 McNabb, Ryan P., Francesco LaRocca, Sina Farsiu, Anthony N. Kuo, and Joseph A. Izatt. "Distributed Scanning Volumetric Sdoct for Motion Corrected Corneal Biometry." *Biomed. Opt. Express* In Press, (2012).
- 176 Wojtkowski, Maciej, Vivek J. Srinivasan, Tony H. Ko, James G. Fujimoto, Andrzej Kowalczyk, and Jay S. Duker. "Ultrahigh-Resolution, High-Speed, Fourier Domain Optical Coherence Tomography and Methods for Dispersion Compensation." *Optics Express* 12, no. 11 (2004): 707-709.
- 177 Tao, Y., B. Bower, J. Mahood, and J. A. Izatt. "Scanning Spectrometer Based Sdoct for Ultra-High-Speed Imaging at 500khz a-Scan Rate." San Jose, CA, 2008.
- 178 Kraus, Martin F., Benjamin Potsaid, Markus A. Mayer, Ruediger Bock, Bernhard Baumann, Jonathan J. Liu, Joachim Hornegger, and James G. Fujimoto. "Motion Correction in Optical Coherence Tomography Volumes on a Per a-Scan Basis Using Orthogonal Scan Patterns." *Biomed. Opt. Express* 3, no. 6 (2012): 1182-1199.
- 179 McNabb, Ryan P., Francesco LaRocca, Sina Farsiu, Anthony Kuo, and Joseph Izatt, "Distributed Scan Sdoct Improves Post Refractive Surgery Corneal Biometry," in OSA Technical Digest (Optical Society of America, 2012), JM3A.65.

- 180 Westphal, Volker, Andrew Rollins, Sunita Radhakrishnan, and Joseph Izatt. "Correction of Geometric and Refractive Image Distortions in Optical Coherence Tomography Applying Fermat's Principle." *Opt. Express* 10, no. 9 (2002): 397-404.
- 181 LaRocca, Francesco, Stephanie J. Chiu, Ryan P. McNabb, Anthony N. Kuo, Joseph A. Izatt, and Sina Farsi. "Robust Automatic Segmentation of Corneal Layer Boundaries in Sdoct Images Using Graph Theory and Dynamic Programming." *Biomed. Opt. Express* 2, no. 6 (2011): 1524-1538.
- 182 Karnowski, Karol, Bartłomiej J. Kaluzny, Maciej Szkulmowski, Michalina Gora, and Maciej Wojtkowski. "Corneal Topography with High-Speed Swept Source Oct in Clinical Examination." *Biomed. Opt. Express* 2, no. 9 (2011): 2709-2720.
- 183 Ortiz, Sergio, Damian Siedlecki, Pablo Pérez-Merino, Noelia Chia, Alberto de Castro, Maciej Szkulmowski, Maciej Wojtkowski, and Susana Marcos. "Corneal Topography from Spectral Optical Coherence Tomography (Soct)." *Biomed. Opt. Express* 2, no. 12 (2011): 3232-3247.
- 184 Akiba, M., K. P. Chan, and N. Tanno. "Full-Field Optical Coherence Tomography by Two-Dimensional Heterodyne Detection with a Pair of Ccd Cameras." *Optics Letters* 28, no. 10 (2003): 816-818.
- 185 Moneron, G., A. C. Boccara, and A. Dubois. "Stroboscopic Ultrahigh-Resolution Full-Field Optical Coherence Tomography." *Optics Letters* 30, no. 11 (2005): 1351-1353.
- 186 Abdullaev, S. S. "Spatial Coherence of the Optical-Field in Multimode Waveguides." *Kvantovaya Elektronika* 11, no. 5 (1984): 904-912.
- 187 Sharma, KK. *Optics: Principles and Applications*. 1 ed.: Academic Press, 2006.
- 188 Manni, Jeffrey G. and Joseph W. Goodman. "Versatile Method for Achieving 1% Speckle Contrast in Large-Venue Laser Projection Displays Using a Stationary Multimode Optical Fiber." *Opt. Express* 20, no. 10 (2012): 11288-11315.

- 189 Savovi, Svetislav, Alexandar Djordjevich, Ana Simovi, and Branko Drlja?a. "Equilibrium Mode Distribution and Steady-State Distribution in 100?400??M Core Step-Index Silica Optical Fibers." *Appl. Opt.* 50, no. 21 (2011): 4170-4173.
- 190 Liu, Jia-Ming *Photonic Devices*. Cambridge: Cambridge University Press, 2005.
- 191 Born, Max and Emil Wolf. *Principles of Optics*. 7th ed.: Cambridge University Press, 1999.
- 192 Dhalla, A. H., J. V. Migacz, and J. A. Izatt. "Crosstalk Rejection in Parallel Optical Coherence Tomography Using Spatially Incoherent Illumination with Partially Coherent Sources." *Optics Letters* 35, no. 13 (2010): 2305-2307.
- 193 Redding, Brandon, Michael A. Choma, and Hui Cao. "Speckle-Free Laser Imaging Using Random Laser Illumination." *Nat Photon* 6, no. 6 (2012): 355-359.
- 194 Chiu, Stephanie J., Xiao T. Li, Peter Nicholas, Cynthia A. Toth, Joseph A. Izatt, and Sina Farsiu. "Automatic Segmentation of Seven Retinal Layers in Sdoct Images Congruent with Expert Manual Segmentation." *Opt. Express* 18, no. 18 (2010): 19413-19428.
- 195 Hee, Michael R. "Optical Coherence Tomography: Theory." In *Handbook of Optical Coherence Tomography*, edited by Brett Bouma and Guillermo Tearney. New York, NY: Marcel Dekker, Inc., 2002.
- 196 Baek, So-Young, Osung Kwon, and Yoon-Ho Kim. "High-Resolution Mode-Spacing Measurement of the Blue-Violet Diode Laser Using Interference of Fields Created with Time Delays Greater Than the Coherence Time." *Japanese Journal of Applied Physics* 46, no. Copyright (C) 2007 The Japan Society of Applied Physics (2007): 7720-7723.
- 197 Siegman, A. E. *Lasers*. Mill Valley, CA.: University Science Books, 1986.
- 198 Jiang, H. X. and J. Y. Lin. "Mode Spacing ``Anomaly" in Ingan Blue Lasers." *Applied Physics Letters* 74, no. 8 (1999): 1066-1068.

- 199 Dhalla, Al-Hafeez and Joseph A Izatt. "Complete Complex Conjugate Resolved Heterodyne Swept Source Optical Coherence Tomography Using a Dispersive Optical Delay Line: Erratum." *Biomed. Opt. Express* 3, no. 3 (2012): 630-632.
- 200 Saleh, Bahaa E. A. and Malvin Carl Teich. *Fundamentals of Photonics*. 2 ed. New York, NY: Wiley-Interscience, 2007.
- 201 Diddams, Scott and Jean-Claude Diels. "Dispersion Measurements with White-Light Interferometry." *J. Opt. Soc. Am. B* 13, no. 6 (1996): 1120-1129.
- 202 Goldberg, Brian D., Benjamin J. Vakoc, Wang-Yuhl Oh, Melissa J. Suter, Sergio Waxman, Mark I. Freilich, Brett E. Bouma, and Guillermo J. Tearney. "Performance of Reduced Bit-Depth Acquisition for Optical Frequency Domain Imaging." *Opt. Express* 17, no. 19 (2009): 16957-16968.
- 203 Fork, R. L., C. H. Brito Cruz, P. C. Becker, and C. V. Shank. "Compression of Optical Pulses to Six Femtoseconds by Using Cubic Phase Compensation." *Opt. Lett.* 12, no. 7 (1987): 483-485.
- 204 Tearney, Guillermo J. "Optical Biopsy of in Vivo Tissue Using Optical Coherence Tomography." MIT, 1997.
- 205 Izatt, Joseph A., Manish D. Kulkarni, Kenji Kobayashi, Michael V. Sivak, Jennifer K. Barton, and Ashley J. Welch. "Optical Coherence Tomography for Biodiagnostics." *Opt. Photon. News* 8, no. 5 (1997): 41.
- 206 Izatt, J. a, M. D. Kulkarni, S. Yazdanfar, J. K. Barton, and a J. Welch. "In Vivo Bidirectional Color Doppler Flow Imaging of Picoliter Blood Volumes Using Optical Coherence Tomography." *Optics Letters* 22, no. 18 (1997): 1439-1441.
- 207 Chen, Zhongping, Thomas E. Milner, Shyam Srinivas, Xiaojun Wang, Arash Malekafzali, Martin J. C. van Gemert, and J. Stuart Nelson. "Noninvasive Imaging of in Vivo Blood Flow Velocity Using Optical Doppler Tomography." *Opt. Lett.* 22, no. 14 (1997): 1119-1121.

- 208 Zhao, Yonghua, Zhongping Chen, Christopher Saxer, Shaohua Xiang, Johannes F. de Boer, and J. Stuart Nelson. "Phase-Resolved Optical Coherence Tomography and Optical Doppler Tomography for Imaging Blood Flow in Human Skin with Fast Scanning Speed and High Velocity Sensitivity." *Opt. Lett.* 25, no. 2 (2000): 114-116.
- 209 Yazdanfar, Siavash, Andrew M. Rollins, and Joseph A. Izatt. "Imaging and Velocimetry of the Human Retinal Circulation with Color Doppler Optical Coherence Tomography." *Opt. Lett.* 25, no. 19 (2000): 1448-1450.
- 210 Yazdanfar, S., A. M. Rollins, and J. A. Izatt. "In Vivo Imaging of Human Retinal Flow Dynamics by Color Doppler Optical Coherence Tomography." *Archives of ophthalmology* 121, no. 2 (2003): 235-239.
- 211 Leitgeb, R. A., L. Schmetterer, W. Drexler, A. F. Fercher, R. J. Zawadzki, and T. Bajraszewski. "Real-Time Assessment of Retinal Blood Flow with Ultrafast Acquisition by Color Doppler Fourier Domain Optical Coherence Tomography." *Optics Express* 11, no. 23 (2003): 3116-3121.
- 212 Tao, Yuankai K., Kristen M. Kennedy, and Joseph A. Izatt. "Velocity-Resolved 3d Retinal Microvessel Imaging Using Single-Pass Flow Imaging Spectral Domain Optical Coherence Tomography." *Opt. Express* 17, no. 5 (2009): 4177-4188.
- 213 Tao, Yuankai K., Anjul M. Davis, and Joseph A. Izatt. "Single-Pass Volumetric Bidirectional Blood Flow Imaging Spectral Domain Optical Coherence Tomography Using a Modified Hilbert Transform." *Opt. Express* 16, no. 16 (2008): 12350-12361.
- 214 Hendargo, Hansford C., Ryan P. McNabb, Al-Hafeez Dhalla, Neal Shepherd, and Joseph A. Izatt. "Doppler Velocity Detection Limitations in Spectrometer-Based Versus Swept-Source Optical Coherence Tomography." *Biomed. Opt. Express* 2, no. 8 (2011): 2175-2188.
- 215 Huber, R., M. Wojtkowski, K. Taira, J. Fujimoto, and K. Hsu. "Amplified, Frequency Swept Lasers for Frequency Domain Reflectometry and Oct Imaging: Design and Scaling Principles." *Opt. Express* 13, no. 9 (2005): 3513-3528.

- 216 Choma, Michael A., Kevin Hsu, and Joseph A. Izatt. "Swept Source Optical Coherence Tomography Using an All-Fiber 1300-Nm Ring Laser Source." *Journal of Biomedical Optics* 10, no. 4 (2005): 044009-044006.
- 217 Srinivasan, V. J., R. Huber, I. Gorczynska, J. G. Fujimoto, J. Y. Jiang, P. Reisen, and A. E. Cable. "High-Speed, High-Resolution Optical Coherence Tomography Retinal Imaging with a Frequency-Swept Laser at 850 Nm." *Opt. Lett.* 32, no. 4 (2007): 361-363.
- 218 Jiang, Hua, Y. K. Zou, Q. Chen, K. K. Li, R. Zhang, Y. Wang, H. Ming, and Zhiqiang Zheng, "Transparent Electro-Optic Ceramics and Devices," in (SPIE, 2005), 380-394.
- 219 Dhalla, Al-Hafeez, Theresa Bustamante, Derek Nanikivil, Hansford Hendargo, Ryan McNabb, Anthony Kuo, and Joseph A. Izatt. "Dual-Depth Ssoct for Simultaneous Complex Resolved Anterior Segment and Conventional Retinal Imaging." *Proc. SPIE* 8213, (2012): 82131G.
- 220 "Diagram of the Eye", National Eye Institute  
<http://www.nei.nih.gov/health/eyediagram/> (accessed 6/1/2012).
- 221 Wieser, Wolfgang, Thomas Klein, Desmond C. Adler, Francois Trépanier, Christoph Eigenwillig, Sebastian Karpf, Joseph M. Schmitt, and Robert A. Huber, "Extended Coherence Range Megahertz Fdml Laser for Imaging the Human Anterior Segment," in OSA Technical Digest (Optical Society of America, 2012), BTu2B.2.
- 222 Klein, Thomas, Wolfgang Wieser, Raphael Andre, Tom Pfeiffer, Christoph M. Eigenwillig, and Robert Huber, "Multi-Mhz Fdml Oct: Snapshot Retinal Imaging at 6.7 Million Axial-Scans Per Second," in (SPIE, 2012), 82131E-82136.
- 223 McNabb, R. P., F. LaRocca, S. Farsiu, A. N. Kuo, and J. A. Izatt. "Distributed Scanning Volumetric Sdoct for Motion Corrected Corneal Biometry." *Biomed. Opt. Express* submitted, (2012).

- 224 Wieser, Wolfgang, Thomas Klein, Desmond C. Adler, Francois Trépanier, Sebastian Karpf, Christoph Eigenwillig, Joseph M. Schmitt, and Robert Huber, "Dispersion Compensated Megahertz Fdml Laser for Imaging of the Anterior Segment," in OSA Technical Digest (online) (Optical Society of America, 2012), JTh3J.2.
- 225 Weichel, Eric D., Marcus H. Colyer, Spencer E. Ludlow, Kraig S. Bower, and Andrew S. Eiseman. "Combat Ocular Trauma Visual Outcomes During Operations Iraqi and Enduring Freedom." *Ophthalmology* 115, no. 12 (2008): 2235-2245.
- 226 Mader, Thomas H., Robert D. Carroll, Clifton S. Slade, Roger K. George, J. Phillip Ritchey, and S. Page Neville. "Ocular War Injuries of the Iraqi Insurgency, January–September 2004." *Ophthalmology* 113, no. 1 (2006): 97-104.
- 227 Hilber, David, Timothy A. Mitchener, James Stout, Brian Hatch, and Michelle Canham-Chervak. "Eye Injury Surveillance in the U.S. Department of Defense, 1996–2005." *American journal of preventive medicine* 38, no. 1 (2010): S78-S85.
- 228 Ari, Adrienne B. "Eye Injuries on the Battlefields of Iraq and Afghanistan: Public Health Implications." *Optometry (St. Louis, Mo.)* 77, no. 7 (2006): 329-339.
- 229 Bower, Bradley a, Mingtao Zhao, Robert J. Zawadzki, and Joseph a Izatt. "Real-Time Spectral Domain Doppler Optical Coherence Tomography and Investigation of Human Retinal Vessel Autoregulation." *Journal of Biomedical Optics* 12, no. 4 (2007): 041214-041214.
- 230 Virata, S. R., J. A. Kylstra, and H. T. Singh. "Corneal Epithelial Defects Following Vitrectomy Surgery Using Hand-Held, Sew-on, and Noncontact Viewing Lenses." *Retina-the Journal of Retinal and Vitreous Diseases* 19, no. 4 (1999): 287-290.
- 231 Charles, Steve. "Illumination and Phototoxicity Issues in Vitreoretinal Surgery." *RETINA* 28, no. 1 (2008): 1-4 10.1097/IAE.1090b1013e318156e318015.

- 232 Ando, Fumitaka, Kumiko Sasano, Norio Ohba, Hiroshi Hirose, and Osamu Yasui. "Anatomic and Visual Outcomes after Indocyanine Green-Assisted Peeling of the Retinal Internal Limiting Membrane in Idiopathic Macular Hole Surgery." *American Journal of Ophthalmology* 137, no. 4 (2004): 609-614.
- 233 Tao, Y. K. K., J. P. Ehlers, C. A. Toth, and J. A. Izatt. "Intraoperative Spectral Domain Optical Coherence Tomography for Vitreoretinal Surgery." *Optics Letters* 35, no. 20 (2010): 3315-3317.
- 234 Ehlers, Justis P., Yuankai K. Tao, Sina Farsiu, Ramiro Maldonado, Joseph A. Izatt, and Cynthia A. Toth. "Integration of a Spectral Domain Optical Coherence Tomography System into a Surgical Microscope for Intraoperative Imaging." *Investigative Ophthalmology & Visual Science* 52, no. 6 (2011): 3153-3159.
- 235 Izatt, Joseph, "Intraoperative Oct for Vitreoretinal Surgery," in OSA Technical Digest (Optical Society of America, 2012), BTu2B.1.
- 236 Hahn, Paul, Justin Migacz, Rachelle O'Connell, Joseph Izatt, and Cynthia Toth. "Unprocessed Real-Time Imaging of Vitreoretinal Surgical Maneuvers Using a Microscope-Integrated Spectral-Domain Optical Coherence Tomography System." *Graefe's Archive for Clinical and Experimental Ophthalmology*, (2012): 1-8.
- 237 Zhang, Kang and Jin U. Kang. "Graphics Processing Unit Accelerated Non-Uniform Fast Fourier Transform for Ultrahigh-Speed, Real-Time Fourier-Domain Oct." *Opt. Express* 18, no. 22 (2010): 23472-23487.
- 238 Schaefer, A. W., J. J. Reynolds, D. L. Marks, and S. A. Boppart. "Real-Time Digital Signal Processing-Based Optical Coherence Tomography and Doppler Optical Coherence Tomography." *Biomedical Engineering, IEEE Transactions on* 51, no. 1 (2004): 186-190.
- 239 Marks, Daniel L., Amy L. Oldenburg, J. Joshua Reynolds, and Stephen A. Boppart. "Study of an Ultrahigh-Numerical-Aperture Fiber Continuum Generation Source for Optical Coherence Tomography." *Opt. Lett.* 27, no. 22 (2002): 2010-2012.

- 240 Nishizawa, N., Y. Chen, P. Hsiung, E. P. Ippen, and J. G. Fujimoto. "Real-Time, Ultrahigh-Resolution, Optical Coherence Tomography With an All-Fiber, Femtosecond Fiber Laser Continuum at 1.5  $\mu$ m." *Opt. Lett.* 29, no. 24 (2004): 2846-2848.
- 241 Moon, Su-bei and Dug Young Kim. "Ultra-High-Speed Optical Coherence Tomography with a Stretched Pulse Supercontinuum Source." *Opt. Express* 14, no. 24 (2006): 11575-11584.
- 242 Aguirre, Aaron, Norihiko Nishizawa, James Fujimoto, Wolfgang Seitz, Max Lederer, and Daniel Kopf. "Continuum Generation in a Novel Photonic Crystal Fiber for Ultrahigh Resolution Optical Coherence Tomography at 800 nm and 1300 nm." *Opt. Express* 14, no. 3 (2006): 1145-1160.
- 243 Humbert, G., W. Wadsworth, S. Leon-Saval, J. Knight, T. Birks, P. St. J. Russell, M. Lederer, D. Kopf, K. Wiesauer, E. Breuer, and D. Stifter. "Supercontinuum Generation System for Optical Coherence Tomography Based on Tapered Photonic Crystal Fibre." *Opt. Express* 14, no. 4 (2006): 1596-1603.
- 244 Newbury, N. R., B. R. Washburn, K. L. Corwin, and R. S. Windeler. "Noise Amplification During Supercontinuum Generation in Microstructure Fiber." *Opt. Lett.* 28, no. 11 (2003): 944-946.
- 245 Corwin, K. L., N. R. Newbury, J. M. Dudley, S. Coen, S. A. Diddams, K. Weber, and R. S. Windeler. "Fundamental Noise Limitations to Supercontinuum Generation in Microstructure Fiber." *Physical Review Letters* 90, no. 11 (2003): 113904.
- 246 Chen, Yueli, Daniel M. de Bruin, Charles Kerbage, and Johannes F. de Boer. "Spectrally Balanced Detection for Optical Frequency Domain Imaging." *Opt. Express* 15, no. 25 (2007): 16390-16399.
- 247 Rollins, Andrew M. and Joseph A. Izatt. "Optimal Interferometer Designs for Optical Coherence Tomography." *Opt. Lett.* 24, no. 21 (1999): 1484-1486.

- 248 Morkel, P. R., R. I. Laming, and D. N. Payne. "Noise Characteristics of High-Power Doped-Fibre Superluminescent Sources." *Electronics Letters* 26, no. 2 (1990): 96-98.
- 249 Izatt, Joseph A., Eric L. Buckland, and William J. Brown, "Optical Coherence Imaging Systems Having a Reduced Effective Linewidth and Methods of Using the Same " US 2011/0249271 A1 (2011).
- 250 Bajraszewski, Tomasz, Maciej Wojtkowski, Maciej Szkulmowski, Anna Szkulmowska, Robert Huber, and Andrzej Kowalczyk. "Improved Spectral Optical Coherence Tomography Using Optical Frequency Comb." *Opt. Express* 16, no. 6 (2008): 4163-4176.
- 251 Hu, Zhilin and Andrew M. Rollins. "Fourier Domain Optical Coherence Tomography with a Linear-in-Wavenumber Spectrometer." *Opt. Lett.* 32, no. 24 (2007): 3525-3527.

## Biography

Al-Hafeez Dhalla was born in Toronto, Ontario on June 4<sup>th</sup>, 1985. He received his Bachelor's of Science in Engineering with Distinction from Duke University in 2007, majoring in Biomedical Engineering with a minor in Arabic. He continued his studies at Duke University, earning a Master's in Biomedical Engineering in 2010 and a Ph.D. in Biomedical Engineering in 2012. He has authored or co-authored eight peer-reviewed journal publications (with two additional publications in preparation), three conference proceedings papers, and is currently contributing to two book chapters. He has also given oral and poster presentations at thirteen optical imaging and ophthalmology conferences, and was a co-author on eight other conference presentations. In addition, he is listed as an inventor on two patents. A list of publications, conference presentations and patents follows.

### PEER-REVIEWED PUBLICATIONS

Bing Yu, Elizabeth S. Burnside, Gale A. Sisney, Josephine M. Harter, Changfang Zhu, Al-Hafeez Dhalla, Nirmala Ramanujam, "Feasibility of near-infrared diffuse optical spectroscopy on patients undergoing image-guided core-needle biopsy," *Optics Express* 15, 7335-7350 (2007)

Al-Hafeez Dhalla, Justin Migacz, Joseph A. Izatt, "Crosstalk rejection in parallel optical coherence tomography using spatially incoherent illumination with partially coherent sources," *Opt. Lett.* 35, 2305-2307 (2010)

Al-Hafeez Dhalla, Joseph A. Izatt, "Complete complex conjugate resolved heterodyne swept-source optical coherence tomography using a dispersive optical delay line," Biomed. Opt. Express 2, 1218-1232 (2011)

Hansford C. Hendargo, Ryan McNabb, Al-Hafeez Dhalla, Neal Shepherd, Joseph A. Izatt, "Doppler velocity detection limitations in spectrometer-based versus swept-source optical coherence tomography," Biomed. Opt. Express 2, 2175-2188 (2011)

Al-Hafeez Dhalla, Derek Nankivil, Joseph A. Izatt, "Complex conjugate resolved heterodyne swept source optical coherence tomography using coherence revival," Biomed. Opt. Express 3, 633-649 (2012).

Al-Hafeez Dhalla, Derek Nankivil, Theresa Bustamante, Anthony Kuo, Joseph A. Izatt, "Simultaneous Swept Source Optical Coherence Tomography of the Anterior Segment and Retina using Coherence Revival," Opt. Lett. 37, 1883-1885 (2012).

Shwetadwip Chowdhury, Al-Hafeez Dhalla, Joseph Izatt, "Structured Oblique Illumination Microscopy for Enhanced Resolution Imaging of Non-Fluorescent, Coherently Scattering Samples", Biomed. Opt. Express. 3, 1841-1854 (2012).

Francesco LaRocca, Al-Hafeez Dhalla, Sina Farsiu, Joseph Izatt, "Optimization of Confocal Scanning Laser Ophthalmoscope Design", Biomed. Opt. Express. *Submitted*.

Al-Hafeez Dhalla, Kevin Shia, Joseph Izatt, "Efficient sweep buffering in swept source optical coherence tomography using a fast optical switch", Biomed. Opt. Express. *In preparation*.

Al-Hafeez Dhalla, Kevin Shia, Joseph Izatt, "Theoretical Development of Fourier Domain Optical Coherence Tomography in Dispersive Media", *In preparation*.

## CONFERENCE PRESENTATIONS AND PROCEEDINGS

Al-Hafeez Dhalla, Joseph A. Izatt, "Signal-to-Noise Ratio and Phase Stability Analysis in Spectral Domain Phase Microscopy," SPIE Photonics West, 7168-90, San Jose, CA. January 2009.

Al-Hafeez Dhalla, Justin V. Migacz, Joseph A. Izatt, "Crosstalk rejection in full-field optical coherence tomography using spatially incoherent illumination with a partially coherent source," SPIE Photonics West, 7554-79, San Francisco, CA. January 2010.

Al-Hafeez Dhalla, Justin Migacz and Joseph A. Izatt, "Crosstalk rejection in full-field optical coherence tomography using spatially incoherent illumination with a partially coherent source", Proc. SPIE 7554, 755427 (2010).

Hansford C. Hendargo, Ryan P. McNabb, Al-Hafeez Dhalla, Neal Shepherd and Joseph A. Izatt, "Doppler velocity detection limitations in spectrometer and swept-source Fourier-domain optical coherence tomography," SPIE Photonics West, 7889-36, San Francisco, CA. January 2011.

Al-Hafeez Dhalla, Joseph A. Izatt, "Heterodyne SSOCT complex conjugate artifact removal at 100kHz line rate using a novel phase modulator," SPIE Photonics West, 7889-63, San Francisco, CA. January 2011.

Hansford C. Hendargo, Ryan P. McNabb, Al-Hafeez Dhalla, Neal Shepherd and Joseph A. Izatt, "Doppler velocity detection limitations in spectrometer and swept-source Fourier-domain optical coherence tomography", Proc. SPIE 7889, 788911 (2011).

Al-Hafeez Dhalla, Anthony N. Kuo, Ryan P. McNabb, Joseph A. Izatt, "Full-range, High Speed Anterior Segment Imaging At 1040nm With Complete Complex Conjugate Artifact Removal," ARVO 2011 Annual Meeting, 1756/A220, Ft. Lauderdale, FL. May 2011.

Xinyu Song, Rolando Estrada, Stephanie J. Chiu, Al-Hafeez Dhalla, Cynthia A. Toth, Joseph A. Izatt, Sina Farsiu, "Segmentation-Based Registration of Retinal Optical Coherence Tomography Images with Pathology," ARVO 2011 Annual Meeting, 1309/A246, Ft. Lauderdale, FL. May 2011.

Hansford C. Hendargo, Al-Hafeez Dhalla, Ryan P. McNabb, Joseph A. Izatt, "Overcoming High Flow Rate Imaging Limitations in Doppler Optical Coherence Tomography," ARVO 2011 Annual Meeting, 1756-A234, Ft. Lauderdale, FL. May 2011.

Al-Hafeez Dhalla, Theresa Bustamante, Hansford C. Hendargo, Ryan P. McNabb, Anthony N. Kuo, Joseph A. Izatt, "Dual-depth SSOCT for simultaneous complex conjugate resolved anterior segment and conventional retinal imaging," SPIE Photonics West, 8213-51, San Francisco, CA. January 2012.

Hansford C. Hendargo, Al-Hafeez Dhalla, Joseph A. Izatt, "Real-time, angle-insensitive total axial flow measurement using transversal scanning Doppler OCT," SPIE Photonics West, 8213-36, San Francisco, CA. January 2012.

Shwetadwip Chowdhury, Al-Hafeez Dhalla, Joseph A. Izatt, "Spatial coherence and transfer function analysis of structured illumination super-resolution microscopy," SPIE Photonics West, 8227-57, San Francisco, CA. January 2012.

Francesco LaRocca, Al-Hafeez Dhalla, Sina Farsiu, Joseph A. Izatt, "Optimization of CSLO design," SPIE Photonics West, 8209-37, San Francisco, CA. January 2012.

Al-Hafeez Dhalla, Theresa Bustamante, Derek Nanikivil, Hansford Hendargo, Ryan McNabb, Anthony Kuo and Joseph A. Izatt, "Dual-depth SSOCT for simultaneous complex resolved anterior segment and conventional retinal imaging", Proc. SPIE 8213, 82131G (2012)

Al-Hafeez Dhalla, Derek Nankivil, Theresa Bustamante, Anthony N. Kuo, Joseph A. Izatt. "Simultaneous Swept Source Optical Coherence Tomography of the Anterior Segment and Retina," OSA BIOMED Topical Meeting, Miami, FL. April 2012.

Al-Hafeez Dhalla, Derek Nankivil, Theresa Bustamante, Anthony N. Kuo, Joseph A. Izatt, "Simultaneous Swept Source Optical Coherence Tomography of the Anterior Segment and Retina," in Biomedical Optics, OSA Technical Digest, paper BTu2B.3, April 2012.

Al-Hafeez Dhalla, Ryan P. McNabb, Anthony N. Kuo, Stephanie J. Chiu, Francesco LaRocca, Derek Nankivil, Theresa Bustamante, Sina Farsiu, Joseph A. Izatt. "Towards Whole Eye Optical Coherence Tomography," ARVO/ISIE Imaging Conference, Ft. Lauderdale, FL. May 2012.

Al-Hafeez Dhalla, Derek Nankivil, Theresa Bustamante, Hansford C. Hendargo, Ryan P. McNabb, Anthony N. Kuo, Joseph A. Izatt. "Simultaneous Swept Source Optical Coherence Tomography of the Anterior Segment and Retina," ARVO Annual Meeting, Ft. Lauderdale, FL. May 2012.

Francesco LaRocca, Al-Hafeez Dhalla, Sina Farsiu, Joseph A. Izatt. "Optimization of compact cSLO design," ARVO Annual Meeting, Ft. Lauderdale, FL. May 2012.

Al-Hafeez Dhalla, Hansford C. Hendargo, Joseph A. Izatt. "15 Years of Doppler OCT," Association for Ocular Circulation Conference, Portland, OR. July 2012.

Al-Hafeez Dhalla, Kevin Shia, Joseph Izatt, "Efficient sweep buffering in swept source optical coherence tomography using a fast optical switch", SPIE Photonics West, San Francisco, CA. January 2013. *Submitted*.

Francesco LaRocca, Derek Nankivil, Al-Hafeez Dhalla, Ryan P. McNabb, Sina Farsiu, Joseph A. Izatt. "Design of a compact, hand-held simultaneous OCT/SLO," SPIE Photonics West, San Francisco, CA. January 2013. *Submitted*.

## **PATENTS**

Al-Hafeez Dhalla, Joseph A. Izatt, "Novel systems and methods for heterodyne swept source optical coherence tomography," US Patent Application 13/355381. Filed January 20<sup>th</sup>, 2012.

Shwetadwip Chowdhury, Al-Hafeez Dhalla, Joseph A. Izatt, "Novel techniques for super-resolution structured illumination microscopy" IDF filed.